MASTERARBEIT / MASTER'S THESIS

Titel der Masterarbeit / Title of the Master's Thesis

„Proglacial icing Rieperbreen: tracking the source of water with natural and artificial tracers"

verfasst von / submitted by

Sarah Elise Sapper, BSc

angestrebter akademischer Grad / in partial fulfilment of the requirements for the degree of

Master of Science (MSc)

Wien / Vienna, 2018

Studienkennzahl lt. Studienblatt / degree program code as it appears on the student record sheet:	A 066 855
Studienrichtung lt. Studienblatt / degree program as it appears on the student record sheet:	Master's degree Geography
Betreut von / Supervisor:	Univ.Prof. Dipl.-Geogr. Dr. Thomas Glade
Mitbetreut von / Co-Supervisor:	Prof. Andy Hodson

Erklärung

Hiermit versichere ich, dass:

- ich die vorliegende Masterarbeit selbstständig verfasst habe,
- ich keine anderen Quellen und Hilfsmittel benutzt habe als die angegebenen,
- ich mich keiner unerlaubten Hilfe bedient habe,
- ich dieses Masterarbeitsthema bisher weder im In- noch im Ausland in irgendeiner Form als Prüfungsarbeit vorgelegt habe,
- diese Arbeit mit der vom Begutachter beurteilten Arbeit inhaltlich vollständig übereinstimmt.

Declaration of Authorship

I hereby declare that:

- this thesis and the work presented in it is my independent work,
- I did not use any other sources and aids than those clearly stated,
- I have not used any unauthorized help,
- I have not yet submitted the subject of this master's thesis as an examination paper, neither in Austria nor abroad,
- The content of this thesis is in complete agreement with the work judged by the assessor.

Wien / Vienna, 15.5.2018

Sarah Elise Sapper

Abstract

In comparison to polythermal glaciers, little research has been conducted on the occurrence of proglacial icings adjacent to cold-based glaciers, wherefore considerable knowledge gaps exist regarding the origin of water forming these extrusive ice bodies, its flow pathways and residence time. This study examines the proglacial icing of the Rieperbreen glacier in Central Spitsbergen, Svalbard, and assesses the contribution of possible water sources, such as sub-glacially stored summer meltwater, water from a kettle lake, long residence sub-permafrost groundwater and surficially routed snowmelt and rain, in the formation of the ice body. The aim is to establish the source of water feeding icings next to cold-based glaciers. The provenance of the water and its routing is investigated through the analysis of natural tracers (major ions and stable water isotope ratios $\delta^{2}H$ and $\delta^{18}O$) of ice core and water samples and artificial (dye) tracer investigations of the present glacier drainage system. These methods are complemented by geophysical surveys of the icing with a high frequency ground-penetrating radar. Hydrochemical results strongly suggest snowmelt, from an unleached snowpack generated during winter warm spells, as the main source of water. Before surfacing about 1 km from the current glacier terminus and forming the up to 2 m thick icing, the meltwater is routed sub-surficially through a slow, pressurized and anoxic channel, characterised by restricted access to the atmosphere and high rock-water contact. The findings of this study challenge the most common theory of icing formation next to cold-based glaciers through slow winter discharge of sub-glacially stored summer meltwater by proposing another provenance and flow path configuration.

Kurzfassung

Im Vergleich zu polythermalen Gletschern wurde bisher wenig Forschung über die Entstehung von proglazialem Aufeis vor kalten Gletschern betrieben. Aus diesem Grund bestehen beträchtliche Wissenslücken hinsichtlich der Herkunft des Wassers, welches diese Eiskörper bildet, seiner Fließwege und der Verweilzeit. Diese Studie untersucht das proglaziale Aufeis des Rieperbreen-Gletschers, welcher sich im Zentrum der Insel Spitzbergen befindet. Mehrere Wasserquellen werden identifiziert, welche zur Bildung des Eiskörpers beitragen könnten. Dazu zählen subglazial gespeichertes Sommerschmelzwasser, Wasser aus einem See zwischen den Endmoränen, Grundwasser von unterhalb des Permafrosts mit einer langen Verweilzeit und oberflächlich geleitetes Schneeschmelzwasser sowie Regen. Ziel der Arbeit ist es, den Ursprung des Wassers herauszufinden, welches im Winter Aufeis vor kalten Gletschern ausformt. Die Herkunft des Wassers und dessen Fließwege wird durch die Quantifizierung von natürlichen Tracern wie die Ionenzusammensetzung und das Verhältnis stabiler Wasserstoff- ($\delta^{2}H$) und Sauerstoffisotope ($\delta^{18}O$) in Eisbohrkernen und Wasserproben sowie durch Färbeversuche des gegenwärtigen Gletscherabflusssystems mit künstlichen Tracern analysiert. Diese Methoden werden durch geophysikalische Untersuchungen des Aufeises mit einem hochfrequenten Georadar ergänzt. Hydrochemische Ergebnisse lassen vermuten, dass es sich beim Ursprung des Wassers um Schneeschmelzwasser aus einer nicht ausgewaschenen Schneedecke handelt. Dieses stammt von winterlichen Wärmeperioden. Bevor das Wasser etwa 1 km vor der heutigen Gletscherfront an die Oberfläche tritt, wird es unterirdisch mit langsamer Fließgeschwindigkeit durch einen unter Druck stehenden und anoxischen Kanal geleitet, der sich mit eingeschränkter Verbindung zur Atmosphäre und einem hohen Sediment-Wasser-Kontakt auszeichnet. Die Ergebnisse dieser Studie stellen die häufigste Theorie der Aufeisbildung vor kalten Gletschern durch den langsamen winterlichen Austritt von subglazial gespeichertem Sommerschmelzwasser in Frage, indem sie auf einen anderen Wasserursprung und eine andere Fließwegkonfiguration hindeuten.

Acknowledgements

Acknowledgements are in place for so many individuals helping me during the several steps of this thesis. A few of you are mentioned here by name and to all others: I know who you are!

First thanks to my supervisors. Thank you, Thomas Glade for supporting my fascination for Svalbard, and helping me to write my thesis there. Special thanks to Andy Hodson for first introducing me to icings, supervising me as external student and sharing your enthusiasm and knowledge. The time you put into helping with field work, lab work and discussions is highly appreciated. Thanks for letting me join your trips into the field. I learned a lot and could not have asked for a better mentor.

I am grateful for the generous financial support I received for field work, travel and living expenses. The Research Council of Norway is thanked for awarding the Arctic Field Grant (project 270008, RiS-ID 10642) and the University of Vienna for the Förderstipendium and the Short-term grant abroad (KWA, LNR: 000015). Further thanks to the Austrian Research Association on Geomorphology and Environmental Change of the Austrian Geographical Society and the University Centre in Svalbard for financial support to present preliminary and final results of this thesis at the European Geoscience Union General Assembly 2017 and 2018 as poster and PICO presentations.

The fieldwork of this thesis was made possible by eager and motivated field assistants. Thank you: Uschi, Flo, Clemens, Samuele, Erik, Joseph, Andrew, Andy, Marie, Fridrik, Max, Molly, Aga, Coco, Ugo, Laura B., Nico, Birte, Laura C., Tamsin, Emmy, Ben D., Joshua, Ben S., Will and Jan for coming out into the field with me, for letting me fill your backpacks with heavy equipment but mostly for your good spirit even at the end of sometimes very long and bitter cold field days (or at least as long as we could make the chocolate supply last – I understand!). Because of you, field work was successful and will be remembered as exciting days spent playing outdoors. Further thanks to the UNIS tech and logistic department for your help and advice regarding fieldwork safety, logistical support, trusting me with equipment, providing lab space, and especially to Dag, for always helping me find every last item on my list.

Mette Kusk Gillespie, Tris Irvine-Fynn, Brian Moorman, Phil Porter and Jacob Yde: thank you for your time, advice on field surveys, lending equipment, help with data processing and sound discussions. Thanks to the Laboratory of the Geography Department at the University of Sheffield, the Laboratory of the School of Earth and Environment at the University of Leeds and the Stable Isotope Laboratory of the University of East Anglia for chemical analyses.

A huge thanks to my friends, the old ones from back home and the new ones I met on the way, for making this time more than enjoyable. Thanks for all the tears you made me shed from laughing, the company during travels, hikes, ski tours and long sunny nights. I am happy to share so many great memories with you! Thanks for being my study buddies, partners in crime and for being the way you are!

My biggest thanks go to my family. You encourage me to follow my curiosity and to walk my own path, no matter how different it is from yours. Thank you for understanding that it makes me happy and sometimes takes me odd places and for making me know that I can count on your love and support no matter where I am, anytime.

Finally, Svalbard, you continue to amaze me and leave me with nothing but love for the nature and people at 78°N. It has been a pleasure, as always!

Table of Content

List of Figures

List of Tables

1 Introduction

Icings (also naled or Aufeis) are extrusive ice bodies which form during winter when water emerges to the surface and freezes under sub-zero atmospheric temperatures. Icings occur in many different situations with water emanating from various sources. After the water's provenance, Åkerman (1980) proposes a classification into spring-, pingo-, river- and glacier naled, whereas the first three are considered periglacial- and the last a paraglacial feature. Icings have been recognised to be a considerable temporary surface water storage component in Arctic regions (Kane & Slaughter 1972; Wanty et al. 2007; Yoshikawa et al. 2007), second in volume only behind snow cover in unglaciated watersheds (Yoshikawa et al. 2007). Since icings often survive longer than snow cover during the ablation season, they are an important source of water to rivers in the absence of glaciers or precipitation (French 2007; Kane & Slaughter 1972; Wanty et al. 2007). In this thesis, the emphasis lies on the last icing type: glacier icings. Glacier icings form in front of many glaciers (hence, proglacial icing), but seem especially abundant on the archipelago of Svalbard. While general agreement prevails concerning the source of water feeding groundwater-, spring- and river icings, considerable uncertainties and discussion exist in regard of the origin of water forming proglacial icings. The occurrence of proglacial icings has long been interpreted as evidence of a polythermal regime of the corresponding glacier and the release of subglacial water throughout the year. Recent studies however show, that proglacial icings also form in front of cold-based glaciers. Hence, questions about the origin of the water exist.

1.1 Literature Review of Proglacial Icings

Glacier icings have been studied in the High Arctic regions of Canada (Moorman & Michel 2000; Moorman 2003; Wainstein et al. 2008; Wainstein et al. 2014), Greenland (Yde & Knudsen 2005; Yde et al. 2005) and Svalbard where they seem to be especially abundant (Baranowski 1982; Hambrey 1984; Gokhman 1987; Hodgkins et al. 1998; Hodgkins & Tranter 1998; Wadham et al. 2000; Hodgkins et al. 2004; Bukowska-Jania & Szafraniec 2005; Grezés 2005; Bælum & Benn 2011; Yde et al. 2012; Sobota 2016; Stachnik et al. 2016). Due to their location adjacent to a glacier or some distance away in the glacier forefield, they are commonly referred to as proglacial icings.

The occurrence of icings in front of glaciers was used to infer the thermal regime of these ice bodies presuming that *"icings show whether a glacier is polar or subpolar"* (Liestøl 1977 p.10) since *"they are absent in the case of small glaciers which are frozen to their beds"* (Gokhman 1987 p. 249). The belief that proglacial icings are indicative of polythermal conditions was even communicated several decades later by Hagen et al. who concluded: *"since all the glaciers in Svalbard are either cold or polythermal, the presence of naled ice indicates that the glacier is a polythermal (subpolar) glacier"* (2003a p.146). Hence, proglacial icings have long been interpreted as evidence for polythermal glaciers with a (partly) warm base, the ability of subglacial water production and storage and its release throughout the year. Assumptions have been made that proglacial icings are also associated with surge- type glaciers, for example on Disko Island, Greenland, where icings were described to occur only in front of glaciers with known surging history both in their quiescent and surging phase (Yde & Knudsen 2005). Previous studies of proglacial icings were conducted to examine their distribution, morphology and morphological role (Baranowski 1982; Moorman & Michel 2000; Bukowska-Jania & Szafraniec 2005; Grezés 2005; Sobota 2016), the hydrologic system of the adjacent glacier (Moorman & Michel 2000; Wainstein et al. 2008), the activity of the subglacial drainage system during the accumulation season and subglacial chemical weathering processes (Wadham et al. 2000; Stachnik et al. 2016) but also the glacier-permafrost interactions (Moorman 2003; Wainstein et al. 2008, 2014).

Although a plethora of possible water sources forming proglacial icings is offered in the literature, no consensus exists between the authors, but most named sources have a glacial provenance in common. They can be grouped into: (i) sub-glacially produced or stored water, (ii) water percolating into subglacial talik and (iii) other sources:
(i) An often-named source is subglacial water (Bukowska-Jania & Szafraniec 2005; Sobota 2016). Some authors differentiated between sub-glacially produced meltwater through geothermal heat and friction (Liestøl 1977; Baranowski 1982; Stachnik et al. 2016; Wadham et al. 2000) and sub-glacially stored water in cavities (Bælum & Benn 2011; Bukowska-Jania & Szafraniec 2005; Sobota 2016; Wadham et al. 2000; Wainstein et al. 2008; Yde & Knudsen 2005), either produced sub-glacially or consists of meltwater from the end of the previous ablation season which is stored sub-glacially during winter (Wadham et al. 2000). Bælum & Benn (2011) further name en-glacially stored water as a possible source.

(ii) Early studies, such as Åkerman (1982), already acknowledged the possibility of an interaction between glaciers and permafrost in the formation of icings: *"most of the naled in front of the glaciers are not fed by water from the glacier itself, but rather from groundwater 'released' by the direct or indirect action of the glaciers"* (p.192). Since some areas of the bed of polythermal glaciers are at the pressure melting point, subglacial taliks are present and have been observed to extend beyond the glacier limits (Moorman 2003). In these areas, water can percolate into and move through the ground. The flow path in the proglacial area does not freeze for some distance due to friction heat produced by the movement of pressurized water (Wainstein et al. 2008). The contribution of water flowing through subglacial taliks in the formation of proglacial icings has been acknowledged by Gokhman (1987), Moorman (2003), Yde & Knudsen (2005), Liestøl (1977) and Wainstein et al. (2008).
(iii) Other sources besides water discharged directly from the glacier or water flowing through subglacial talik are rarely mentioned. The possibility of water originating from supraglacial or ice marginal ice dammed lakes routed through taliks is acknowledged by Moorman (2003), Wainstein et al. (2011) and Yde & Knudsen (2005). Through hydrochemical analyses, Wadham et al. (2000) deduced surficially routed water, originating from snowmelt during winter warm spells, as an additional source of water besides sub-glacially produced and stored summer meltwater. Liestøl (1977) further lists groundwater as source of water additionally to glacial groundwater (interpreted as water flowing through a subglacial talik) and sub-glacial meltwater.

Recent studies acknowledge that proglacial icings also form adjacent to cold-based glaciers. This discovery raises several questions regarding the source of water and flow paths connected to these icings. It further indicates that the presence of a proglacial icing cannot be used as solely indicator of a polythermal regime. While it is regarded plausible that proglacial icings adjacent to warm-based, polythermal glaciers are fed by subglacial meltwater throughout the year, this does not explain the occurrence of proglacial icings in front of cold-based glaciers. The bed of cold-based glaciers is below the pressure melting point and the glaciers are frozen to their bed. Hence, no subglacial water production takes place and subglacial taliks are believed absent. Traditionally it has been assumed that cold-based glaciers exhibit a simple drainage system with water routed supra-glacially only and englacial or subglacial flow paths being absent (Fountain & Walder 1998). Therefore, it appears comprehensible

that proglacial icings were interpreted as indicative for polythermal glaciers since some source of water is required throughout the winter and surface runoff is absent during this time of year (Hodgkins et al. 2004). Recent studies, however, have shown that even cold-based glaciers exhibit an englacial and subglacial drainage system possibly explaining the formation of icings (Bælum & Benn 2011; Naegeli et al. 2014). Supraglacial channels can evolve into englacial channels and even reach the bed through the process of cut-and-closure (Bælum & Benn 2011; Gulley et al. 2009; Naegeli et al. 2014).

Little research has been conducted on icings forming in front of cold glaciers so far since most studies have concentrated on large proglacial icings adjacent to polythermal glaciers. Scott Turnerbreen (Hodgkins et al. 1998, 2004) and Tellbreen (Bælum & Benn 2011; Naegeli et al. 2014), both in Central Spitsbergen, are the only cold-based glaciers where studies regarding the characteristics of their icing or the source of water are known to have been published. Due to the different thermal regime of cold-based glaciers, several plausible water origins and flow paths for polythermal glaciers are insufficient in explaining the formation of cold-based glacier icings. Hodgkins et al. (2004) discuss potential water origins of the icing forming adjacent to Scott Turnerbreen. Snowmelt during winter warm spells was discarded as source of water since it is believed that meltwater would rather form ice lenses within the snowpack than produce runoff. This is supported by Bælum & Benn (2011) who state that snowmelt could not explain the volume or the continuous growth of the icing throughout the winter. Further, the formation through groundwater is evaluated as unlikely since the glacier is underlain with at least 200 m of permafrost as obtained through ground-temperature modelling (Hodgkins et al. 2004). Studies at Scott Turnerbreen and Tellbreen suggest a glacial provenance of water feeding the icings. Hodgkins et al. (1998) propose a formation of proglacial icings adjacent to cold-based glaciers through stored summer meltwater in subglacial channels which is slowly released during the accumulation season. Hodgkins et al. (2004) adds the possibility of water percolating through thawed sediments beneath the channel during winter. Results from Bælum & Benn (2011), showing that water is stored sub-glacially in several channels located beneath the lower part of the Tellbreen glacier snout, seem to underline the theory of Hodgkins et al. (1998). These channels are linked to englacial channels which are fed by supraglacial meltwater during the summer.

1.2 Objectives of Study

Due to the small number of studies conducted on proglacial icings forming adjacent to cold-based glaciers, a considerable knowledge gap exists regarding the origin of the water, its flow paths and residence time as outlined by previous studies (Wadham et al. 2000; Bælum & Benn 2011). The objective of this study is to better the understanding of hydrological processes at and in front of cold-based glaciers by increasing the knowledge about the formation of proglacial icings adjacent to cold-based glaciers, the provenance of water during winter and flow paths in the glacier forefield. The proglacial icing annually forming in front of Rieperbreen, a cold-based glacier located in Bolterdalen, Central Spitsbergen, was selected as study site. This location was chosen due to its easy accessibility, allowing repeated field investigations, its vicinity to the only two previously studied icings forming adjacent to cold-based glaciers (Scott Turnerbreen and Tellbreen) and its similar size compared to Scott Turnerbreen. Investigations of the Rieperbreen icing aid to review previously proposed theories on water provenance and routing in cold-based glaciers in regard of the formation of proglacial icings.

1.2.1 Hypotheses and Research Questions

The occurrence of a proglacial icing indicates the emergence of liquid water during the accumulation season. This thesis therefore aims to establish the source of water feeding the Rieperbreen proglacial icing. The main research question is:

What is the origin of the water that annually forms a proglacial icing adjacent to Rieperbreen?

In conjunction with this question, four working hypotheses are outlined below exploring the responsibility of different water sources in the formation of the icing, followed by sub-questions (Q) formulated for each hypothesis.

Hypothesis 1:

The icing is fed by the slow winter discharge of sub-glacially stored summer meltwater.

- Q 1-1: Does the icing form adjacent to the glacier portal?
- Q 1-2: Does the ionic composition of water samples show a high abundance of crustally derived solutes?

- Q 1-3: Is a hydrologic connection present between the glacier and the area of icing formation during summer?

Previously conducted studies on proglacial icings forming in front of cold-based glaciers attribute these glaciers the ability of subglacial water storage and slow release of summer meltwater throughout the winter, presumably leading to the formation of proglacial icings (Bælum & Benn 2011; Hodgkins et al. 1998, 2004; Lysså & Lønne 2001).

Hypothesis 2:

The lower part of the icing is formed by water from a lake present within the moraine complex.

- Q 2-1: Are the dimensions of the lake sufficient to form a sub-lake talik through which water can percolate towards the icing?
- Q 2-2: Can two different sources of water, forming different parts of the icing, be distinguished through the analysis of the ionic and isotopic composition of ice core and water samples?
- Q 2-3: Do GPR surveys reveal a connection between all visible icing areas?

A kettle lake is present within the frontal moraine complex in close proximity to the lower areas of the proglacial icing and appears, from its location, as a plausible source of water feeding the icing. Since no surface connection between the lake and the area of icing formation is visible during winter or summer, water would be assumed to percolate through a zone of talik underneath the lake towards the icing. If the lower icing is fed by a different source than the upper areas, the isotopic composition of spring water samples are expected to differ significantly.

Hypothesis 3:

The icing is fed by long residence sub-permafrost groundwater and is therefore not a proglacial icing, but ascribed to another icing type.

- Q 3-1: Could groundwater be the source of water rather than water with a glacial or atmospheric provenance?

The emergence of groundwater springs has been reported throughout Svalbard (Åkerman 1980; Liestøl 1977). The possibility exists, that the studied icing, believed to be a proglacial icing related to Rieperbreen, is not a glacier icing but rather a spring

icing fed by long residence sub-permafrost groundwater. The chemical composition of old, sub-permafrost groundwater would be assumed to show a different signature than water of glacial- or atmospheric origin.

Hypothesis 4:

The icing is formed from surficially routed rain and snowmelt generated during winter warm spells.

- Q 4-1: Did days with positive air temperatures occur during the 2016/17 accumulation season?
- Q 4-2: Does the ionic composition of water samples reveal low concentrations of crustally derived solutes compared to atmospherically derived solutes?
- Q 4-3: Can rain and snowmelt explain the localized accumulation and continuous growth of an icing during winter?

If the icing is fed by rain or snowmelt routed on the surface, limited rock-water contact would result in a low concentration of crustally derived ions from chemical weathering in the icing and spring water.

1.2.2 Approach

In order to test the hypotheses and answer the research questions, several methods are utilised. The methodological approach encompasses geophysical investigations of the icing, hydrochemical and isotopic analyses of ice and water samples and tracer investigations of the hydrologic system of the glacier and its forefield. Some of these methods have commonly been used in the investigation of proglacial icings adjacent to polythermal glaciers but, not yet, to deduce the water's origin of cold-based glacier icings. This is the first known study of a proglacial icing forming adjacent to a cold-based glacier with such broad methodical range.

Field investigations and sampling were conducted from March to September 2017. Fieldwork during the accumulation season aimed to investigate the morphological and chemical characteristics of the icing. GPR surveys of the proglacial icing were performed to study the extent of the icing, its internal morphology and to locate the point of water emergence. In order to extract information, the icing itself and the water feeding the icing hold about the origin of the water and the flow paths it has been routed along, ice cores from the icing and spring water were sampled. Melted ice core water

was analysed for its hydrochemical composition to deduce the flow paths of the source water as well as effects of freezing on spatially variable icing chemistry. Emerging water from the springs feeding the icing was analysed for its chemical and isotopic composition to infer the water's origin and flow paths. At the end of the ablation season, dye tracing experiments were performed to investigate the routing of meltwater during the summer and to study the connection between the hydrologic system of Rieperbreen and the icing.

1.3 Outline of Thesis

Chapter 1 introduces the thesis and presents an overview of research previously conducted on proglacial icings (Section 1.1). Existing knowledge gaps are outlined in Section 1.2 leading to the purpose of this study, its research questions and hypotheses. The first part of Chapter 2 introduces the reader to icings, existing terms and definitions and characteristics of different icing types (Sections 2.1 and 2.2); the second part provides background knowledge on research methods applied in this study such as ground-penetrating radar, ionic and isotopic hydrochemistry and dye tracing (Sections 2.3 to 2.5). The study area is described in Chapter 3 with an emphasis upon the climatic and geologic settings, as well as the development of Rieperbreen and its proglacial area since the Little Ice Age. A step-by-step instruction of data collection during fieldwork and post-processing is provided in Chapter 4. Afterwards, results of GPR surveys, hydrochemical analyses, as well as dye tracing experiments are outlined in Chapter 5. Chapter 6 encompasses the interpretation and discussion of the results and returns to the formulated research question and hypotheses. A summary of this thesis's findings and an outlook on future research needs is presented in Chapter 7.

2 Theoretical and Methodological Background

This chapter is divided into a first, theoretical, and second, methodological part. The theoretical sections provide a compilation of existing terms and definitions of icings followed by an introduction of icings in regard of their distribution, dimensions, ice structure and chemical composition (Section 2.1). Characteristics of different types of icings such as ground, river, spring, pingo and glacier icings are described in Section 2.2. The second part encompasses an introduction of the research methods applied in this study: GPR, ionic and isotopic hydrochemistry and dye tracing as well as previous application of these methods in the study of glaciers and, where present, icings (Section 2.3 to 2.5).

2.1 Icings

2.1.1 Terms and Definitions

Extrusive ice bodies, abundant in arctic and sub-arctic regions, are referred to as *icings*, *naled* (pl. *naledi*) or *Aufeis*. The term first used in scientific literature, by von Middendorf (1859) to denote these phenomena, was *Aufeis* (Åkerman 1982). However, the original name of the extrusive ice bodies is believed to be the Russian *naled*, which was later translated into German as *Aufeis*, both meaning *on* or *upon ice* (Åkerman 1980; Carey 1973). All three terms, *icing*, *naled* and *Aufeis*, are found in the recent literature, the preferably used term differs geographically. In Russian literature, these ice bodies are exclusively referred to as *naled* whereas in studies from North America both, *icing* and *Aufeis,* are used. *Aufeis* was the original term in Europe. In current studies, however, it is more often named *icing* or *naled*. To add to the confusion, some authors do not use *icing*, *naled* and *Aufeis* synonymous, but refer to different features with these terms. (Åkerman 1980, 1982)

In this thesis, the studied ice body is further referred to with the English term *icing*. To avoid confusion, it is pointed out that *icing* describes several phenomena attributed to cold environments and the definitions hence vary. Carey (1973) divides these phenomena into two groups by the means of water reaching the site of icing formation. In the first group, icings are associated with water or water vapor that has been airborne before forming an icing. In this sense, it is a common term in aviation used to describe an ice layer forming on the outside of aircrafts from supercooled drops in

clouds, in shipping for the ice coating on the outside of ships when sea spray freezes or for ice on infrastructure such as antennas and powerlines from the freezing of water vapor (Carey 1973, Kumar 2011). The second group encompasses the type of icing that is subject to this study, formed by water originating either from the underground or the earth's surface.

Icing is not only used as a name of the feature, but also for the process of formation (Carey 1973) as outlined in a general definition presented by Kumar (2011, p.640) who defines an icing as:

"the freezing of water on exposed surface".

In a geomorphologic context, the term icing was first introduced by Muller (1947) to describe:

"a mass of surface ice formed during the winter by successive freezing of sheets of water that may seep from the ground, from a river, or from a spring" (Carey 1973, p.1).

Further definitions followed, specifying icings either in regard of the underlaying material on which they form:

"Icings are sheet-like masses of layered ice that form on either the ground surface or on river or lake ice" Pollard et al. (2005, p.52),

with a genetic background after the source of the water:

"Icings […] are formed by the freezing of water that seeps from the ground, flows from a spring or emerges from beneath a river bed or through fractures in river ice" (Woo 2012, p.95)

or a combination of both:

"A sheetlike mass of layered ice formed on the ground surface, or on river or lake ice, by freezing of successive flows of water that may seep from the ground, flow from a spring, or emerge from below river ice through fractures" (Permafrost Subcommittee 1988, p.52).

Evident from these definitions is the existence of several types of icings with water originating from different sources. To reduce confusion, a variety of classification systems have been proposed. Still widely used is the three-fold differentiation proposed by Carey (1973) who groups icings after the source of water into ground-spring- and river icings (Heldman et al. 2005; Pollard et al. 2005; Woo 2012; Pollard 2018). However, since this classification does not cover all known types of icings, especially in the study area Svalbard, the definition and classification proposed by Åkerman (1980) is regarded as improvement by including the whole spectrum of icing phenomena forming from underground or surface water. Åkerman (1980, p.152) defines naled as:

> *"a sheet of freshwater ice, formed during winter on top of an ice, snow or ground surface by the freezing of flowing water from the ground, a stream or a glacier and remaining during a considerable part of the summer season"*,

where water from the ground can be the seepage of groundwater but also the discharge of a spring. He further extends the classification with pingo-naled, glacier-naled and thermal spring-naled, when formed from thermal, rather than ordinary ground water springs.

2.1.2 Distribution and Dimensions

Occurrences of icings have mainly been reported from permafrost regions of the northern hemisphere such as Russia (Alekseyev & Tolstikhin 1973), Alaska (Carey 1973; Kane 1981; Kane & Slaughter 1972; Sloan et al. 1976; Wanty et al. 2007; Yoshikawa et al. 2003; Yoshikawa et al. 2007), Arctic Canada (Clark & Lauriol 1997; Heldmann et al. 2005; Moorman 2003; Moorman & Michel 2000; Pollard 2005; van Everdingen 1982a; van Everdingen 1982b; Wainstein et al. 2008; Wainstein et al. 2014), Svalbard (Åkerman 1980, 1982; Bælum & Benn 2011; Baranowski 1982; Bukowska-Jania 2007; Bukowska-Jania & Szafraniec 2005; Greześ 2005; Hodgkins et al. 2004; Liestøl 1977; Sobota 2016; Stachnik et al. 2016; Wadham et al. 2000; Yde et al. 2012), Greenland (Yde & Knudsen 2005; Yde et al. 2005) and Mongolia (Froehlich & Slupik 1982), but also Antarctica (Souchez et al. 2000). However, icings are not limited to permafrost regions. They can form wherever atmospheric temperatures are cold enough to freeze water that surfaces during winter.

The sizes and shapes of icings varies greatly. They can be small features with an extent of a few m², but also large ice bodies covering several km² (Woo 2012). Large icings are often reported in conjunction with rivers such as the icing forming in the Moma River valley with a length of 25 km, a width of 5,5 - 8 km and a thickness of up to 4 m (Carey 1973; Woo 2012). Ice thickness normally ranges between 1-3 m (Åkerman 1980), but can also significantly exceed this range as is the case of icings forming in a tributary valley of the Firth River which are up to 7 m thick (Clark & Lauriol 1997). Icings often form in the same location year after year whereas the size can vary. The size, shape and characteristics of icings are influenced by the discharged volume of water, mode of discharge, topography of the location, chemistry of the surfacing water, snow cover thickness and temperature of the water and air (Pollard 2005). The air temperature has a significant influence on the size and shape of icings whereas low temperatures result in fast freezing of surfaced water close to the exit point leading to a thick ice cover near the source and a small extent and milder conditions, to the formation of wide-spread but thin icings. Precipitation during winter further influences the size of icings since snow is incorporated into the ice body when deposited on the wet surface (Åkerman 1980). Precipitation during the summer, on the other hand, determines the volume of water supply of some icing types for the following winter, such as ground icings formed by supra-permafrost waters but also river icings (Carey 1973). Icings grow throughout the winter until temperatures rise above freezing or until the supply of water is exhausted. Most icings melt completely during the summer and are additionally eroded by meltwater rivers when located in a channel. Some icings, or parts of icings, can persist one or several ablation seasons due to cold summers, large volume or formation in a location sheltered from solar radiation and fluvial erosion and become semi-perennial features (Åkerman 1980).

2.1.3 Ice Structure and Chemical Characteristics

Characteristic for all types of icings is a laminated ice structure oriented parallel to the ground surface. Through this attribute, icings can easily be differentiated from other types of surface and ground ice (Åkerman 1980). The ice layers are formed by successive overflow events of thin sheets of water (<2mm thick) across the icing surface. Water on the surface travels only a short distance from the source before freezing, less than 2 m at the onset of an overflow event (Hu & Pollard 1998b). The distance can increase with further discharge, however, does not exceed intra-icing flow

where water moves along voids within the icing, protected by overlying ice from air temperatures, before surfacing farther away from the source (Heldmann et al. 2005; Hu & Pollard 1998b).

The different ice layers can be composed of transparent ice, which appears blue due to preferential absorption of longer wavelengths (Bohren 1983) or bubble-rich ice, white in colour. The transparent layers are made up of smaller ice crystals (0,08 - 0,25 cm) than those white in colour (up to 0,4 cm) (Åkerman 1980). Large candle (or needle) ice crystals have been observed to form either within the ice body during the ablation season when the crystallography of solid layers changes to needle structures (Stachnik et al. 2016, Yde et al. 2012), as characteristic surface feature during the ablation season (Hodgkins et al. 2004) or in relation to cavity mounds (Åkerman 1980). These ice crystals are hexagonal, composed of bubble-free ice and grow in direction of the freezing front (Åkerman 1980, Yde et al. 2012; Woo 2012). Yde et al. (2012) reported the formation of candle ice crystals up to 2,5 cm in diameter and 13 cm length oriented vertically within an icing. When forming on the surface, with no restrictions exerted by overlying ice, needle ice crystals up to 40 cm in length have been found to form on cavity mounds (Åkerman 1980).

The chemical composition of icings varies spatially. It is influenced by the presence of solutes in the water feeding the icing and by cryochemical effects during freezing (Wadham et al. 2000). Depending on the origin, the water may be rich in Na^+ and Cl^- and to a lesser degree SO_4^{2-} and Mg^{2+} when derived from rain, snow or ice-melt or rich in HCO_3^-, Ca^{2+}, SO_4^{2-}, Mg^{2+} and Na^+ when emanating from the ground due to weathering reactions. During freezing, the chemical composition of the ice may be altered compared to the source water through mineral precipitation (Wadham et al. 2000). Minerals insoluble in low temperatures precipitate from the water as it freezes. Some minerals, such as calcium carbonate ($CaCO_3$) and calcium sulphate ($CaSO_4$), precipitate soon from freezing water resulting in enrichment of these minerals close to the outlet and depletion of Ca^{2+} and HCO_3^- in ice at greater distance. Contrary, Na^+, Cl^-, Mg^{2+} and SO_4^{2-} remain in the solution longer resulting in enrichment at a greater distance from the spring (Åkerman 1980; Stachnik et al. 2016; Wadham et al. 2000). Mineral precipitation has not only been observed for icings fed by highly mineralized waters but to some degree for all icing types. Thin layers of precipitates accumulate on the surface (Bukowska-Jania 2007; Yde et al. 2012), at the bottom (Pollard 2005)

and within the icing (Yde et al. 2012; Yde & Knudsen 2005). Once the ice has melted, precipitates remain on the ground (Yde et al. 2012) and have been proposed to be usable to map the maximum extent of last winter's icing (Åkerman 1980; Yoshikawa et al. 2007). The presence of solutes in the source water can further result in a different colour of icings or individual ice layers. Ground icings, for example, are commonly yellowish or brown in colour due to dissolved minerals or organic compounds. Turbid ice further indicates the presence of soil or vegetation particles. The ice of spring icings can also be coloured due to dissolved minerals, however turbidity caused by larger particles is absent since the water is issued through well-defined flow paths (Carey 1973; Yoshikawa et al. 2007).

2.2 Characteristics of Different Icing Types

Icings can be divided into different types distinguished by their source of water. The commonly used classification from Carey (1973) groups icings into ground- spring and river icings. Here, this classification is extended with pingo- and glacier icings as proposed by Åkerman (1980).

2.2.1 Ground Icings

Ground icings are formed by groundwater seeping to the surface. This water can originate from below or above the permafrost whereas supra-permafrost water feeding the icing is more common, but also from the ground in non-permafrost areas. Due to the mode of water emergence from the ground, these icings are also referred to as seepage icings. (Carey 1973; Hu & Pollard 1998b; Yoshikawa et al. 2007) Ground icings are a rare type of icing. They most commonly occur in relation to disturbances caused by human activities. Naturally occurring icings can predominantly be found in the Subarctic where the ground exhibits a large enough water storage capacity. Ground icings originating from supra-permafrost water are hardly found in the Arctic since the shallow active layer does not permit sufficient water storage. (Carey 1973)

During winter, the refreezing active layer exhibits pressure on the stored water. This water is either expelled slowly to the surface through cracks in bedrock, fractures in the ground formed through frost action or along paths related to biological activity such as roots or animal tunnels. The water can also leave the ground in areas unfrozen from the insulating effects of snow or vegetation cover or it exits rapidly through the

formation of frost mounds. Water forming ground icings often seeps from several points which change their location during winter. (Carey 1973; Woo 2012)

Ground icings are not linked to certain features, as for example river, pingo and glacier icings, and can form anywhere. Their shape depends on the topography and migration of exit points during the accumulation season and their size on the amount of stored water. (Carey 1973; Hu & Pollard 1998b) Ground icings are generally smaller compared to other icing types such as river or spring icings because of limited water supply. They often stop growing during winter when water supply is depleted or flow paths are closed off due to freezing (Pollard 2005). Fast growing rates can be observed during warm spells or the onset of the melt season when the location of the icing allows the accumulation of meltwater which refreezes at night. During the ablation season, ground icings waste away slower than other types of icings, since they are often not dissected by meltwater streams. (Carey 1973)

2.2.2 Spring Icings

Spring icings are formed by water discharged from perennial groundwater springs whereas the water can originate from sub-permafrost reservoirs but also from supra-permafrost areas in regions where the permafrost is located at sufficient depth (Carey 1973). Since the origin of water can be the same as of ground icings, the distinction between these two icing types should not be based on the source of water, but rather on the mode of water discharge. While ground icings are formed by the seepage of water from the ground, water feeding spring icings follows more defined flow paths and forms distinct channels on the surface (Woo 2012). The sub-permafrost aquifers are fed by water percolating through taliks present underneath lakes, rivers and glaciers (Woo 2012; Åkerman 1980). Past ice cover, and fault zones have shown to influence the occurrence of spring icings. Yoshikawa et al. (2007) suggest, that spring icings forming in the Brook Range, Alaska, originate from a sub-permafrost aquifer that was recharged through taliks underneath warm-based glaciers and ice caps during the Wisconsonian and are issued to the surface along limestone outcrops.

Spring icings form earlier in the cold season than ground and river icings. The onset of spring icing formation is controlled by air temperatures. An icing starts to grow when air temperatures drop below the freezing point of the surfacing water. This temperature can vary from spring to spring depending on the mineral content of the water.

Heldmann et al. (2005) and Pollard (2005), studying spring icings on Axel Heiberg Island, Nunavut, Canada, show that the high salinity of spring water in this location depresses the freezing point. Freezing of a portion of the water further leads to fractionation in the water and enrichment of the residual brine which depresses the freezing point to as low as -20°C. This brine can remain liquid while flowing several hundred metres from the outlet. Successive overflow events result in the characteristic sheet-like ice structure and vertical and lateral expansion. Compared to other icing types, the location of the outlet does not shift during winter (Carey 1973). The icing forms close to the spring in case of ordinary springs or some distance away when fed by thermal springs due to the longer time needed to freeze thermal waters (Åkerman 1980). High mineral content of the water can further keep it from freezing leading to large lateral expansion of the ice body (Heldmann et al. 2005; Pollard 2005). Spring icings vary greatly in size depending on the volume of discharge (Åkerman 1980) and restrictions induced by the topography in the area of formation. Generally, spring icings grow to larger size than ground icings since water supply is continuous during winter. The icing growth continues as long as air temperatures are below 0°C or below the freezing point of the solution. Spring icings waste away faster than ground icings since spring discharge erodes channels into the icing. The erosional force of water flowing through these channels, however, is weaker than in river icings due to lower discharge (Carey 1973). Small spring icings are periodic features while springs with a high discharge can form large, perennial icings (Åkerman 1980).

2.2.3 River Icings

Icings form on and around many rivers in the Arctic and Subarctic during winter. The term river icing does not simply refer to the ice cover that forms at the onset of winter, but to layers of ice that start to accumulate on top of the frozen river surface and adjacent areas. River icings are supplied by winter streamflow and ground water flowing in taliks underneath rivers (Kane & Slaughter 1972). Contrary to ground icings, also formed by groundwater, the occurrence of taliks is related to the presence of the river.

Hu & Pollard (1998a) define three stages leading to the formation of river icings: freeze-up, obstruction and overflow. At the onset of winter, the surface of rivers in cold regions and the surrounding ground freezes. Even though river recharge by surface water ceases, some water remains in the channel. Due to the thermal effect of rivers,

unfrozen ground can be present underneath and to the sides of channels. In these sub-river taliks, groundwater flow can be sustained even during winter (Carey 1973). With the continuance of winter, the ice cover in the channel thickens with snow accumulation adding additional weight onto the ice. Decreasing cross section and overlying weight induces pressure on the water in the river channel. Once the pressure head is above the ice cover, fractures develop in the ice through which water is expelled to the surface (Kane 1981; Woo 2012). Due to sub-zero temperatures, it freezes quickly as thin sheets onto the existing ice. River icings can double or triple the thickness of the original ice cover. The icing thickness can be several times larger than the water depth during summer (Kane 1981). With increasing thickness, the ice cover starts to extend laterally over the river banks onto the river plain as long as water supply is sustained. Additionally, increased pressure exerted by the freezing of the ground can force groundwater to the surface along unfrozen river banks adding to the lateral growth of river icings. (Carey 1973)

As with ground icings, the size of river icings depends on the source of water and whether the supply becomes depleted during winter. Rivers mainly fed by surface or supra-permafrost water form small icings in the river channels due to the termination of growth during winter. Rivers receiving inflow from groundwater present in taliks underneath the river or from perennial sub-permafrost springs form extensive icings. These water sources can sustain icing growth throughout the winter, leading to the formation of river icings that extend beyond the river channel and cover large areas on the flood plain. (Carey 1973; Woo 2012) River icings seldom occur along large rivers with deep channels but are more common features along shallow and braided rivers (Carey 1973; Sloan et al. 1976). They can develop thicknesses of several metres and extend for several kilometres to the sides of the channel (Kane & Slaughter 1972). The icing in the channel is eroded quickly at the onset of the melt season due to the erosional force of the river while icing areas developed on the floodplain waste away slower.

2.2.4 Pingo Icings

Compared to other classifications of icing types such as the one proposed by Carey (1973), Åkerman 1980 refers to pingo-naled as a discrete type. The Permafrost Subcommittee defines a pingo as: “*perennial frost mound consisting of a core of massive ice, produced primarily by injection of water, and covered with soil and*

vegetation" (1988, p.71). Two types of pingos are differentiated after the source of water and their formation: open-system and closed-system pingos. Pingo icings are associated with the open-system type where water originates from perennial springs fed by sub- or intra-permafrost groundwater (Åkerman 1980; Ballantyne 2018; French 2007). Since the discharge does not abate during winter, surfaced water freezes once in contact with sub-zero air temperatures. The required conditions for the onset of icing formation and growth are similar to spring icings. Compared to other icing types, pingo icings are relatively small in size. The size and location of formation mainly depends on the discharged water volume and the water temperature. An icing forms on top of the pingo or on the slopes when both, discharge and water temperature, are low. Higher discharge and water temperatures result in water remaining liquid over a longer distance. Under these conditions, the largest icing growth is observed on the flat ground surrounding the pingo (Åkerman 1980).

2.2.5 Glacier Icings

Glacier icings are referred to with several different terms in the literature such as: *naled* (Wadham et al. 2000; Yde & Knudsen 2005), *glacier naled* (Åkerman 1980, 1982; Stachnik et al. 2016; Yde et al. 2012), *naled ice* (Baranowski 1982), *icing* (Moorman 2003; Sobota 2016; Wadham et al. 2000), *icing fields* (Bukowska-Jania 2007; Bukowska-Jania & Szafraniec 2005; Sobota 2016) or *Aufeis* (Hambrey 1984), whereas *proglacial icing* is the most common term in recent literature (Bælum & Benn 2011; Hodgkins & Tranter 1998; Hodgkins 2004; Wainstein et al. 2008, 2014; Whitehead et al. 2013). Proglacial icings are the icing type with the widest distribution in areas with continuous permafrost (Åkerman 1982; Pollard 2018; Wainstein et al. 2014). While general agreement prevails concerning the source of water feeding groundwater-, spring- and river icings, considerable uncertainties and discussion exist in regard of the origin of water forming proglacial icings. A review of existing theories is compiled in Chapter 1.1.

Proglacial icings form, as the name suggests, in front of glaciers but their exact location in regard and distance from the glacier can vary greatly. The ice masses form either directly adjacent to the glacier snout, on the outwash plain between the glacier and the terminal moraine or outside the terminal moraine (Åkerman 1982; Bukowska-Jania & Szafraniec 2005).

Proglacial icings exhibit a large range of shapes and sizes. On Svalbard, the largest reported dimensions were a thickness of >5 m and an area of up to 2,5 km² (Baranowski 1982; Liestøl 1977). Bukowska-Jania & Szafraniec (2005) estimate the average thickness of proglacial icings to be 1,5 m. However, none of these numbers can compare to the proglacial icing forming in front of Fountain Glacier, Bylot Island in Arctic Canada which has been reported to be 11 km long, up to 500 m wide and 12 m thick (Moorman & Michel 2000; Moorman 2003). Due to the interplay of several determining factors, the size and volume of proglacial icings varies from year to year. The most commonly listed ones are: the glacier size (Bukowska-Jania & Szafraniec 2005; Grezés 2005; Stachnik et al. 2016), the volume of stored water within the glacier and hence the amount of winter discharge from the glacier (Bukowska-Jania & Szafraniec 2005; Pollard 2018), the topography of the forefield (Bukowska-Jania & Szafraniec 2005; Gokham 1987; Sobota 2016; Stachnik et al. 2016; Wainstein et al. 2014) and the air temperature (Bukowska-Jania & Szafraniec 2005; Sobota 2016, Wainstein et al. 2014). But also, the presence of ridges in bedrock (Olszewski 1982; Stachnik et al. 2016) and the precipitation in a given year (Sobota 2016). A gradual long-term change of the extent of an icing could, on the other hand, indicate a change in the hydrologic system and/or the glacier-permafrost interaction. The array of mentioned factors and the general disagreement on the ones determining the size of icings is believed to originate from the lack of knowledge regarding the source of water forming this icing type.

Proglacial icings are dome- or cone shaped (Stachnik et al. 2016) and, as the other icing types, composed of stratified ice. Through the analyses of ion concentration in ice cores, Stachnik et al. (2016) show that icings do not only grow through successive overflow events, but also through ice accretion at the bottom of the icing. Icings mainly growing from the bottom are predominantly composed of transparent ice, while icings formed through ice accretion on the top also exhibit white, bubble-rich ice layers believed to indicate either the incorporation of snow or fast freezing processes (Åkerman 1980; Moorman & Michel 2000). Given the second type of formation, snow can account for a considerable portion of the ice volume. Often described surface features of proglacial icings during winter are injection mounds which can be several meters to tens of meters in diameter and have been observed in the same location year after year (Hodgkins et al. 2004; Moorman & Michel 2000; Sobota 2016). They form above a water source (spring) or an internal water-filled channel through pressure

induced by water underneath the ice which forces the icing to bulge and, eventually, to rupture (Åkerman 1980; Moorman & Michel 2000), but it is not agreed that they indicate the maximum reach of an icing as suggested by Sobota (2016). In the field these features can be useful when trying to locate liquid water for sampling.

Most proglacial icings disappear during the melt season due to thermo-fluvial erosion. Glacial meltwater streams cut through the icing and significantly contribute to a fast disintegration. Sometimes parts of an icing persist throughout the ablation season due to its size such as a 300 m wide and 1,2 km long part of the icing in front of Fountain Glacier which has existed perennially since at least 1948 (Moorman 2003). Further, a layer of glacio-fluvial sediment deposited on top of an icing can protect the underlying ice from melting for several years in case the sediment layer is thick enough. Through irregular melting, the sediment covered patches form a hummocky terrain in the glacier forefield. Other small landforms in proglacial areas, related to icings rather than flowing ice, such as esker-like landforms or kame-like structures have been described in Åkerman (1982). Several authors have acknowledged icings as geomorphological agent modifying glacier outwash plains (Åkerman 1980, 1982; Bukowska-Jania & Szafraniec 2005; Hambrey 1984; Olszewski 1982).

2.3. Ground-Penetrating Radar

2.3.1 Principles of GPR

Ground-penetrating radar (GPR) is a non-destructive geophysical technique to image the subsurface. The central part of a GPR unit consists of an antenna containing transmitter and receiver. The most common survey design is the common-offset reflection survey (Figure 1). In this design, one transmitter and one receiver are used. The antenna is moved across the surface whereby the spacing between the transmitter and receiver remains constant. The transmitter sends electromagnetic waves of a defined frequency into the ground at regular intervals. The waves are reflected and absorbed at the interface of subsurface features with different material properties. The intensity and characteristics of the reflected signal are continuously recorded by the receiver. (Annan 2009; Hubbard & Glasser 2005) The recorded traces are stacked horizontally to create a 2D image. The result of a GPR survey is a radargram of the subsurface (Figure 21). .

The x-axis shows the time passed or, in case a GPS is connected to the unit, the distance of the antenna from the starting point. The y-axis shows the travel time of the wave which can be transformed into a depth value when the propagation velocity is known. Each vertical line represents a single pulse sent out by the radar. A colour pattern is created by the contrast in electrical properties of different materials and allows the determination of material interfaces. The signal shows either a + - + deflection from the y-axis, when reflection occurs at an interface where the material located at greater depth has a higher dielectric constant (for example at an ice-sediment or ice-water interface), or a - + - signal, when, for instance, reflected from air with a lower dielectric constant than ice (Hubbard & Glasser 2005). The first and strongest recorded signal is the arrival of the air wave or direct wave (Figure 1). The air wave is the electromagnetic wave that travels between the transmitter and receiver through the air at the speed of light. The second signal represents the arrival of the ground wave reflected at the air-ground interface (Figure 1). The ground wave travels slower than the air wave due to the higher relative permittivity in the ground ($\varepsilon_r > 1$) compared to air ($\varepsilon_r = 1$). Therefore, the ground wave is located at a lower position in the radargram. All other reflections recorded after the air and ground wave can be related to features in the subsurface (Hubbard & Glasser 2005).

Signal variations are due to the variability of electrical permittivity and electrical conductivity of the materials present in the subsurface. These two material properties allow to differentiate between various materials and to locate them in the ground. The electrical permittivity (ε) (or dielectric constant κ) is the capacity of a material to store an electrical charge (Hubbard & Glasser 2005). Since the permittivity of a material is

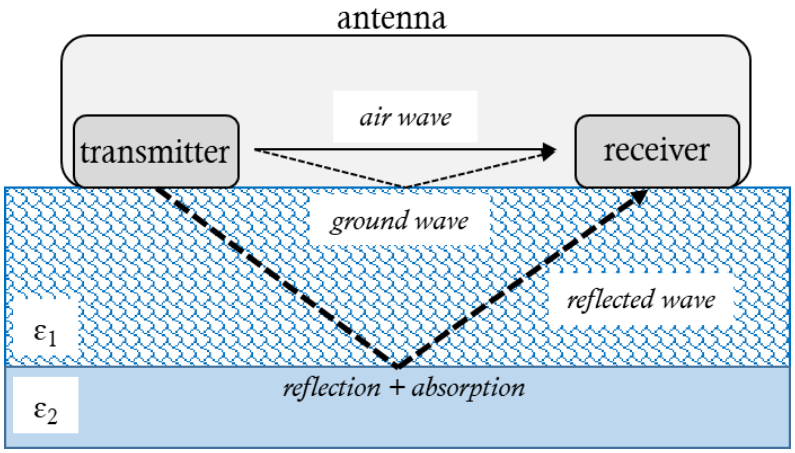

Figure 1: The common-offset reflection survey design. The transmitted electromagnetic wave is reflected and absorbed at the interface of materials with different electrical properties (ε_1 and ε_2).

commonly described relative to the permittivity in free space or vacuum, it is termed relative permittivity (ε_r):

Eq. 1

$$\varepsilon_r = \frac{\varepsilon}{\varepsilon_0}$$

where ε is the permittivity of the material and ε_0 the permittivity of free space or vacuum. Table 1 lists the relative permittivity of different materials. The notable differences in relative permittivity of ice and other materials present in a glacial system make GPR an especially favourable method in the study of glaciers. The electrical conductivity (EC or σ) is the ability of a material to conduct an electrical current (Hubbard & Glasser 2005). In fluids, the electrical conductivity is increased by the abundance of dissolved ions (Cassidy 2009a). This can be seen in Table 1 by comparing the values of distilled water and the more conductive salt water.

These different electrical properties of materials govern the travel velocity (V) of the electromagnetic wave in the subsurface. Since the EC of ice is low, the velocity equation can be simplified to:

Eq. 2

$$V = \frac{c}{\sqrt{\varepsilon_r}}$$

where c is the speed of the radar wave in free space (same as the speed of light = 3.0*108 m s^{-1}) and ε_r the relative permittivity.

The varying propagation velocities of the radar wave through a medium can be assessed through common-midpoint (CMP) or wide-angle reflection and refraction (WARR) surveys. These surveys are used to investigate changes in the radar signal velocity with depth. The measured travel velocity can subsequently be used to

Table 1: Electrical properties of different materials (Hubbard & Glasser 2005).

Material	Relative electrical permittivity (ε_r)	Electrical conductivity (σ) (mS m^{-1})	Velocity (V) ($\times 10^8$ m s^{-1})	Attenuation (α) (dB m^{-1})
Air	1	0	3.0	0
Distilled water	80	0.01	0.33	0.002
Fresh water	80	0.5	0.33	0.1
Salt water	80	3000	0.1	1000
Dry sand	3–5	0.01	1.5	0.01
Saturated sand	20–30	0.1–1.0	0.6	0.03–0.3
Silt	5–30	1–100	0.7	1–100
Clay	5–40	2–1000	0.6	1–300
Granite	4–6	0.01–1	1.3	0.01–1
Ice	3–4	0.01	1.67	0.01

calculate the depth of a reflector seen on the radargram. In a CMP survey, both the transmitter and receiver are moved across the surface. The distance between these two is increased stepwise above a common mid-point. In a WARR survey either the transmitter or receiver is moved over a mid-point while the other remains stationary. (Annan 2009) Since the offset between the antenna and the transmitter is known, variations in the two-way travel time for each separation step can be used to calculate the travel velocity of the wave through the given medium. Studies have shown that the WARR method only gives usable results when the reflector in the subsurface is horizontally oriented. Therefore, CMP surveys are preferred due to their wider applicability. (Hubbard & Glasser 2005) The two-way travel time of the wave is given as:

Eq. 3

$$t^2 = \frac{x^2}{V^2} + t_0^2$$

where x is the antenna separation, V the propagation velocity and t_0 the one-way travel time at zero offset. By rearranging the upper equation and inserting the measured values, the propagation velocity of the wave can be calculated as:

Eq. 4

$$V = \sqrt{\frac{x^2}{t^2 - t_0^2}}$$

Attenuation (α) (Table 1) describes the loss of energy of the radar wave when it passes through a certain material. The loss of energy is governed by the materials permittivity, electrical conductivity and the frequency of the radar. The higher the permittivity, the EC and the radar frequency, the higher the attenuation. (Cassidy 2009a; Hubbard & Glasser 2005) Therefore, the penetration depth of the radar wave decreases with increasing frequency but also with the presence of sediment and water.

2.3.2 GPR in Cryosphere Sciences and the Study of Icings

GPR is a frequently used method in the study of ice sheets, ice streams, ice shelves, valley glaciers and permafrost. Systems with frequencies ranging from 2 to 1500 MHz are used (Arcone 2009), whereas the applied frequency depends on the research question, desired penetration depth and resolution. A trade-off between penetration depth and resolution always applies. Low frequencies penetrate far into the subsurface but result in a low resolution and vice versa (Sjöberg et al. 2015). Hence, high

frequencies are used where small features close to the surface are of interest whereas low frequencies help to image large features at greater depths. In recent studies ground-penetrating radar was employed to answer various questions regarding accumulation rates and mass balance (Dunse et al. 2008; Kruetzmann et al. 2011; Marchenko et al. 2017; Munneke et al. 2017), basal ice stratigraphy (Arcone et al. 1995), the thickness of ice masses (Bohleber et al. 2017; Capt et al. 2016; Lapazaran et al. 2016), internal drainage system (Bælum & Benn. 2011), bed topography (Bohleber et al. 2017), thermal regime (Moore et al. 1999), debris cover (McCarthy et al. 2017), and permafrost (Monnier et al. 2011; Sjöberg et al. 2015; Watanabe et al. 2013; Westermann et al. 2010).

Although GPR is an often-applied method in the research of glaciers and periglacial environments, only two published studies currently exist where GPR was employed on proglacial icings. The internal structure of icings, however, can be imaged well with GPR due to their composition of different ice layers with varying air and water content as shown by Moorman & Michel (2000) and Stachnik et al. (2016). Moorman & Michel (2000) studied the proglacial icing forming in front of Fountain Glacier (unofficial name) on Bylot Island, Canada. An antenna with a frequency of 200 MHz was employed to image the stratigraphy and the base of the icing with a resolution of <0,5 m. Through common-midpoint surveys and point-source reflection analysis, the travel velocity of the radar wave through the icing was calculated. Velocities ranged between 0,12 to 0,17 m ns^{-1} in the seasonal icing and 0,15 to 0,17 m ns^{-1} in the perennial icing. The range owes to the varying content of air and water within the ice body. Stachnik et al. (2016) applied a high frequency antenna with a centre frequency of 800 MHz to quantify the depth of the Werenskioldbreen icing, but also to describe the stratification within the ice body and to locate water reservoirs.

2.4 Glacial Hydrochemistry

2.4.1 Ionic Chemistry

The ionic composition is one of the most frequently studied properties of glacial meltwaters (Hubbard & Glasser 2005). It varies on a diurnal and seasonal basis and also between glaciers due to the geology of the catchment, the chemical signature of the source water, the thermal regime of the glacier and the configuration of the drainage system (Brown 2002). Analyses of the chemical composition of glacial

meltwaters provide information about the origin of the water and weathering processes. It has been used, for example, to infer the source of water, by differentiating between different water provenances, flow paths and their efficiency (Brown 2002; Brown et al. 1996b; Hodson et al. 2002a; Hodson et al. 2002b; Hodgkins 1998; Hubbard & Nienow 1997; Tranter et al. 1996; Wadham et al. 2000; Yde et al. 2008).

The presence of dissolved solutes in glacial meltwaters is ascribed two main sources: the atmosphere and geologic material. Atmospherically derived solutes are dominated by Cl^-, Na^+ and SO_4^{2-} from sea salt and, to a smaller extent, SO_4^{2-} and NO_3^- from acidic sulphate and nitrate aerosols (Hodgkins & Tranter 1998; Wadham et al. 2000). The chemical composition of precipitation depends on the moisture source and the trajectory of the clouds. Glacierized catchments located close to the sea receive a higher input of sea salts through precipitation than those located in a more continental location. The proximity to populated areas, on the other hand, can increase the concentration of anthropogenic aerosols. (Brown 2002; Hubbard & Glasser 2005; Tranter et al. 1996; Raben & Theakstone 1994) Compared to initial precipitation, containing atmospherically derived solutes, glacial meltwater can further be enriched in crustally derived solutes such as HCO_3^-, SO_4^{2-}, Ca^{2+}, Mg^{2+}, Na^+ and K^+ from chemical weathering of geologic material. This includes rocks, glacial flour and dust in the snowpack. (Tranter et al. 1996)

As explained, SO_4^{2-} can be derived from both main solute sources. In order to separate the amount of SO_4^{2-} in a sample which is not snowpack-derived and hence indicates chemical weathering, $*SO_4^{2-}$, denoting the portion of SO_4^{2-} in a sample dissolved from crustal material through weathering, can be calculated. Since all Cl^- is assumed derived from the atmosphere, Hodgkins et al. (1998) define $*SO_4^{2-}$ as:

Eq. 5

$$^{*}SO_4^{2-} = SO_4^{2-} - (0{,}126 * Cl^-)$$

where SO_4^{2-} and Cl^- are the total concentrations measured in the sample in equivalent units and 0,126 the elution ratio of SO_4^{2-}: Cl^- in dry snow. The same calculation can be performed for other solutes present in the snowpack and derived from weathering, however, with different ratios to Cl^-.

When water is in contact with reactive debris, chemical weathering enriches the meltwater with solutes whereas the solute species depend on the geology of the

catchment. The rate of chemical weathering is controlled by several factors such as: the geology of the catchment influencing the availability of freshly eroded and highly reactive sediment, the particle size (the smaller, the larger the surface area), the availability of protons and oxygen for weathering reactions and the duration of rock-water contact. (Brown 2002; Hubbard & Glasser; Tranter et al. 1996; Raiswell 1984) Main minerals contributing to the solute content of meltwater have a reactivity in the order evaporites (Halite, Gypsum) > carbonates (Calcite, Dolomite) > sulphides (Pyrite) > aluminosilicates (Feldspar) (Tranter et al. 1996). Acid hydrolysis is the most important chemical weathering reaction (Raiswell 1984). Acidic water reacts with the geologic material dissolving minerals into their compounds. Carbonate, silicate and aluminosilicate minerals are weathered through hydrolysis, whereas the fastest reaction is the hydrolysis of carbonate minerals which are dissolved by free protons in the water *(aq* denotes the aqueous and *s* the solid form) (Brown 2002; Hubbard & Glasser 2005):

Eq. 6

$$CaCO_3\,(s) + H^+\,(aq) = Ca^{2+}\,(aq) + HCO_3^-\,(aq)$$

Protons are mainly supplied through two processes (Tranter et al. 1993; Brown et al. 1996a). Firstly, the contact of meltwater with the atmosphere and the dissolution and dissociation of atmospheric CO_2 (Eq. 7 shows the dissociation):

Eq. 7

$$CO_2\,(aq) + H_2O\,(aq) = H^+\,(aq) + HCO_3^-\,(aq)$$

and secondly, the oxidation of sulphide minerals such as pyrite (FeS_2):

Eq. 8

$$4FeS_2\,(s) + 15O_2\,(aq) + 14H_2O\,(aq) = 16H^+\,(aq) + 4Fe(OH)_3\,(s) + 8SO_4^{2-}\,(aq)$$

Since these reactions, sulphide oxidation providing free protons, and carbonate hydrolysis, are coupled and occur at the same time, the equations can be combined to:

Eq. 9

$$4FeS_2\,(s) + 15O_2\,(aq) + 14H_2O\,(aq) + 16CaCO_3\,(s) = 4Fe(OH)_3\,(s) + 8SO_4^{2-}\,(aq) + 16Ca^{2+}\,(aq) + 16HCO_3^{-}\,(aq)$$

The relative proportion of HCO_3^- and SO_4^{2-} in glacial meltwater indicates the predominate weathering reaction that provides protons to the solution (Raiswell 1984, Brown 2002) and is assessed through the S-ratio calculated as (Brown et al. 1996a):

Eq. 10

$$\frac{SO_4^{2-}}{SO_4^{2-} + HCO_3^-}$$

where a ratio of 1 reports protons supplied exclusively by sulphide oxidation (Eq. 8), 0 a supply of protons only through the dissolution and dissociation of atmospheric CO_2 (Eq. 7) and 0,5 through coupled sulphide oxidation and carbonate dissolution (Eq. 9).

2.4.2 Geochemical Calculations and Physical Properties

With the results of major ion analyses, geochemical calculations can be performed. Here, a background is provided for the partial pressure of CO_2, charge balance, charge balance error and saturation indices. Further, physical properties of meltwater measured in-situ, such as electrical conductivity, pH, oxidation-reduction potential and dissolved oxygen are presented below.

The partial pressure of carbon dioxide (pCO_2) of a solution helps to study the relation between proton supply and consumption through weathering reactions in meltwaters (Brown 2002; Hubbard & Glasser 2005). PCO_2 of a solution is calculated as (Brown 2002):

Eq. 11

$$logPCO_2 = log(HCO_3^-) - pH + pKCO_2 + pK_1$$

where $pKCO_2$ = 1,12 and pK_1 = *6,58* for a water temperature of 0°C. It can further be assessed by calculating the saturation index of CO_2 in a solution. A $log_{10}pCO_2$ of -3,5 is equal to that of the atmosphere ($10^{-3,5}$ bar) and indicates a solution in equilibrium with the atmosphere where: proton supply = removal, as is the case for an open system. A $pCO_2 \neq$ -3,5 denotes a closed system. When the pCO_2 of a solution is less than the atmospheric level (<-3,5), more protons are consumed than resupplied. This signifies either a closed system without drawdown of CO_2 from the atmosphere but also the contact of relatively pure water with highly reactive rock material, where the depletion through chemical weathering exceeds CO_2 diffusion in the water. A pCO_2 > -3,5 indicates the opposite process where protons are supplied faster than depleted through weathering. This occurs for example through the coupled carbonate dissolution and sulphide oxidation (Eq. 9), proton supply through snowmelt or the freezing of meltwater. (Brown 2002; Hodgkins et al. 1998; Raiswell 1984; Yde et al. 2012) These relationships are used in a glacial setting to distinguish between water

flowing through open or closed systems. PCO_2 values indicating a closed system could denote a closed channel without the exchange of CO_2, but also the slower dissolution of CO_2 between the gas and water phase than usage during fast acid hydrolysis (Brown 2002).

Aqueous solutions are electrically neutral. Hence, the sum of dissolved anions and cations must be equal when calculated as equivalent concentrations:

Eq. 12

$$Charge\ Balance: \sum^{+} = \sum^{-}$$

where $\sum^{+}$ is the sum of cations and $\sum^{-}$ the sum anions of a solution. Balancing the charge of a solution is commonly used for quality assessments of water analyses through the charge balance error (CBE) reported as:

Eq. 13

$$CBE\ (\%) = \frac{(\sum^{+} - \sum^{-})}{(\sum^{+} + \sum^{-})} * 100$$

CBE can be a negative and positive value indicating a higher concentration of anions or cations, respectively. A solution in balance has a CBE of 0 %. The CBE, however, often deviates from 0 % when not all major solutes in samples are quantified. A high CBE indicates errors occurred either during sampling, sample preservation or laboratory analyses. (Knödel et al. 2007; Zhu & Anderson 2002). A CBE of <±5 % is regarded as acceptable (Freeze & Cherry 1979). For dilute solutions, the errors are, however, reported to be greater due to a higher sensitivity to imbalances (Zhu & Anderson 2002).

The Saturation Index (SI) indicates the thermodynamic state of a solution and helps to assess whether it is under-saturated, super-saturated or in equilibrium in regard to a solid phase (mineral). It is calculated as:

Eq. 14

$$SI = log_{10} \frac{IAP}{K_{SP}}$$

where *IAP* is the ion-activity product and K_{SP} the solubility product, the maximum possible solubility of a mineral at a defined water temperature and pH. SI values can be positive and negative. Negative values show under-saturation of the solution with a given mineral and a positive value super-saturation. A value of 0 indicates thermodynamic equilibrium, whereas a range between -0,05 – +0,05 is commonly

defined as equilibrium. The higher under-saturated a mineral in solution is, the higher its dissolution rate. With a positive SI, precipitation of the given mineral occurs, unless precipitation kinetics are slow in which case the supersaturated mineral phase remains in solution. (Merkel & Planer-Friedrich 2008; Deutsch 1997)

The electrical conductivity (EC) is the ability of a material or solution to conduct an electric current. In solutions, the EC depends on the abundance of dissolved ions and the temperature of the sample. EC rises with temperature due to increasing mobility of dissolved ions. Hence, values need to be corrected for temperature when comparing EC values measured from solutions with different temperature as:

Eq. 15

$$C_{25} = \frac{C_t}{1 + \alpha\,(t - 25)}$$

where *Ct* is the measured conductivity at a temperature other than 25°C (*t*) and *α* a linear temperature coefficient defined as 2% per degree Celsius for fresh water (Hayashi 2004).

The pH is a measure of the concentration of dissolved hydronium ions (H_3O^+) in a solution. It is defined as the negative logarithm of the concentration and can be calculated with the following equation (Hubbard & Glasser 2005):

Eq. 16

$$pH = -log_{10}\,(H_3O^+)$$

With increasing concentration of H_3O^+ ions, the pH decreases and vice versa. The pH is measured in mol dm^{-3} on a scale from 0 - 14 whereas values below 7 show an acidic and values above 7 an alkaline solution. A solution with a pH of 7 is neutral, as is the case for pure water.

Oxidation-reduction potential (ORP), also redox potential or reduction potential, denotes the tendency of a solution to either acquire or release electrons in a redox reaction. The more negative charged a solution, the higher its capacity to release electrons and to be oxidized. Contrary, the more positive charged a solution, the higher its capacity to gain electrons and to be reduced. A negative charged solution therefore acts as a reducing agent and a positive charged solution as an oxidizing agent. Oxidizing conditions are indicative for surface water. A negative potential can be found

in places where the supply of air is limited, as is the case, for instance, for groundwater. (DeBolster 1997; VanLoon & Duffy 2000)

Dissolved oxygen (DO), indicates the amount of free oxygen (O_2) dissolved in a solution. Oxygen enters the solution either from the atmosphere or is a result of photosynthesis. Three factors influence the solubility of oxygen in water: the water temperature, the content of dissolved solids and the atmospheric pressure. Cold water with a low conductivity can hold more DO than warm water with a high abundance of dissolved solids. The higher the atmospheric pressure, the more oxygen is dissolved. The amount of dissolved oxygen drives chemical and biological reactions in water bodies and can therefore change quickly due to reactions but also due to degassing and mineral precipitation. This applies especially for groundwater which is in a disequilibrium with the atmosphere. (Rounds et al. 2013)

2.4.3 Stable Water Isotope Chemistry

Both elements forming water molecules, hydrogen (^{1}H) and oxygen (^{18}O), have several stable isotopes. While isotopes of an element have the same number of electrons and protons, their number of neutrons is unequal. Hydrogen has three isotopes of which two, ^{1}H (protium) and ^{2}H (deuterium (D)), are stable whereas ^{3}H (tritium) is radioactive. The number of neutrons varies from 0 to 3. Oxygen, on the other hand, has 11 isotopes of which three, ^{16}O, ^{17}O and ^{18}O, are stable and contain 8 to 10 neutrons in the core, respectively. ^{16}O is the most abundant oxygen isotope and accounts for 99,7% of the oxygen in natural waters (Yao et al. 2011). Hence, the heaviest stable oxygen isotope is rare with a natural abundance of only 0,204% relative to ^{16}O (Clark & Fritz 1997; Kumar 2011c). Since water molecules are made up of two hydrogens and one oxygen atom, 18 possible combinations between these elements and their isotopes exist. The most frequent one is H_2O^{16} (997.680 ppm), followed by H_2O^{18} and HDO^{18} with only 2000 ppm and 320 ppm due to the low abundance of heavy isotopes (Dansgaard 1964; Kumar 2011a+d; Tranter 2011).

In the analyses of water isotopes, the ratio of isotopes in a sample is of interest rather than their absolute abundance. Ratios of stable water isotopes such as $^{18}O/^{16}O$ and $^{1}H/^{2}H$ are expressed as δ values ($\delta^{18}O$ and $\delta^{2}H$ or δD) and reported in ‰ relative to a standard. δ values are calculated as:

Eq. 17

$$\delta = \frac{R_s - R_r}{R_r} \times 1000$$

where *R* is the isotope ratio in the sample (*s*) and in the reference standard (*r*), respectively. To calculate the ratio of oxygen isotopes, the following equation is applied:

Eq. 18

$$\delta^{18}O = \frac{\left(\frac{^{18}O}{^{16}O}\right)_s - \left(\frac{^{18}O}{^{16}O}\right)_r}{\left(\frac{^{18}O}{^{16}O}\right)_r} \times 1000$$

The same equation is used to calculate δ^2H from the ratio of the hydrogen isotopes ^{1}H/^{2}H. For stable water isotope analyses, the VSMOW (Vienna Standard Mean Ocean Water) standard is used as reference. The δ value of the standard is defined as 0 ‰. Hence, a positive δ value indicates that the ratio of the analysed isotope in the sample is higher than in the standard and a negative δ value that the ratio of heavy to light isotopes in the sample is lower than in the standard (Kendall & Caldwell 1998).

When both, δ^{18}O and δ^2H, values are known, the second-order isotope parameter deuterium excess (d-excess) can be calculated as:

Eq. 19

$$d\ excess = \delta D - 8 * \delta^{18}O$$

The value for deuterium excess of a sample contains information about kinetic fractionation of the water isotopes during phase changes such as evaporation and freezing (Bertler 2011; Ritter & Kuells 2010; Yde et al. 2012).

2.4.4 Water Isotopes in Precipitation

The mass of isotopes varies due to the unequal number of neutrons which results in different chemical and physical properties. Due to a smaller mass and weaker bonds, $H_2{}^{16}O$ is more volatile compared to $H_2{}^{18}O$, resulting in fractionation during phase changes such as evaporation and freezing. (Kendall & Caldwell 1998) When water evaporates from the ocean, fractionation changes the ratio of heavy to light isotopes in the vapor phase compared to the parental source since the lighter isotopes evaporate preferentially. When water vapor condenses to form clouds, the phase change results in anew fractionation. Now the heavy molecules condense faster while

the light molecules preferentially remain in the vapour state. As water vapor moves further inland, it becomes increasingly depleted in heavy water molecules during every condensation. Precipitation close to the coast might have a very similar isotopic fingerprint as ocean water and therefore as the reference standard (Dansgaard 1964), but the farther away from the original water source precipitation falls, the lower its isotope ratio and the more negative the δ values. (Kumar 2011b) Different $\delta^{18}O$ and $\delta^{2}H$ values have been measured in precipitation which are usually aligned close to the Global Meteoric Water Line (GMWL) defined as (Craig 1961):

Eq. 20

$$\delta D = 8 * \delta^{18}O + 10$$

$\delta^{18}O$ and $\delta^{2}H$ values in precipitation depend on two main factors: the isotopic composition of the ocean surface from which water is evaporated and the air temperature during condensation (Ingraham 1998). With decreasing temperatures, precipitation is depleted of heavy isotopes. Therefore, snow has lower δ values than rain, especially at high latitudes (Dansgaard 1964; Tranter 2011). Less depleted precipitation on the other hand results from higher temperatures. Since increased fractionation occurs at lower temperatures, $\delta^{18}O$ and $\delta^{2}H$ values further decrease with increasing elevation. For $\delta^{18}O$ a decrease of -0,36 ‰ per 100 m is applied for adiabatic cooling (Ritter & Kuells 2010). In relation to the air temperature, the isotopic composition of precipitation can be altered due to evaporation as it falls to the ground (Ingraham 1998). Further effects have been observed to influence the isotopic ratio of precipitation, such as continentality, latitude and amount effects (Dansgaard 1964; Ingraham 1998; Ritter & Kuells 2010).

2.4.5 Water Isotopes in Meltwater

The isotopic composition of meltwater can provide important information about the origin of the water. Since isotopes constitute water molecules, they are used as natural tracers to distinguish between different water sources contributing to runoff such as snow, firn, ice and rain, exhibiting different isotopic signatures (Brown 2002; Kendall & Caldwell 1998; Theakstone 2003; Yde et al. 2008; Yde et al. 2012). The reason for varying isotopic signatures of snow, firn, ice and rain is fractionation. Fractionation occurs during the formation of snowflakes since heavier molecules preferentially enter the solid state. This leads to a different isotopic fingerprint of snow compared to rain

characterised by d-excess values of >10 ‰ (Cooper 1998). In the stratigraphy of the winter snowpack the specific isotopic signature of precipitation events is preserved. Prior to snowmelt, the isotopic signal of single precipitation events in the snowpack is diluted through water vapour exchange with the atmosphere and melting and refreezing processes (Cooper 1998; Raben & Theakstone 1994). At the onset of melting, fractionation occurs when lighter isotopes leach preferentially from the snowpack. During this time, meltwater from snow is depleted in heavy isotopes while the snowpack becomes increasingly enriched (Cooper 1998; Jouzel & Souchez 1982; Raben & Theakstone 1994; Theakstone 2003). Enriched meltwater percolating into the underlying firn results in relatively enriched firn and later glacier ice compared to the mean value of the snowpack (Theakstone & Knudsen 1996). The isotopic composition of meltwater varies over the melt season. While low values are measured in the beginning due to the retention of heavy isotopes in the snowpack, values increase when the remaining, enriched, snow cover, firn and glacier ice contribute to river discharge. Short-term variations in the isotopic ratio of the meltwater can often be attributed to rainfall events (Yde et al. 2008).

No fractionation occurs during the melting of ice. Water from ice melt therefore exhibits the same isotopic ratios as glacier ice. However, the isotopic composition can be altered due to refreezing (Theakstone 2003). During freezing, heavy molecules enter the solid state faster than lighter ones (Tranter 2011). This fractionation process during freezing leads to a depletion of heavy isotopes in the remaining water. Once the water is frozen, the isotopic ratio remains unchanged. When plotting $\delta^{18}O$ and $\delta^{2}H$ values of samples from liquid precipitation that have undergone freezing or of solid precipitation that have undergone melting and refreezing, the slope of the line connecting these data points deviates from the slope of precipitation values. This different slope is used to detect phase changes after precipitation (Jouzel & Souchez 1982; Souchez & Jouzel 1984).

2.4.6 Water Isotopes on Svalbard

On Svalbard, water isotopes have been used for example to reconstruct annual accumulation rates through an ice core sampled from Lomonosovfonna (Pohjola et al. 2002) and to study the provenances of glacial meltwater (Yde et al. 2008). Regarding proglacial icings, one study by Yde et al. (2012) exists, which compares $\delta^{18}O$ and δD

values from ice sampled in front of Austre Grønfjordbreen with other water sources in the catchment to determine the origin of water forming the icing.

$\delta^{18}O$ values of precipitation from Longyearbyen were analysed by Humlum (unpublished data). 291 samples of liquid and solid precipitation were collected during all seasons between November 1999 to Mai 2003 together with meteorological data at the time of precipitation. Figure 2 (left) shows a large spread of values between precipitation events and a poor correlation between air temperature and $\delta^{18}O$ values ($R^2 = 0,35$). For liquid precipitation, the maximum value of -3,54 ‰ was measured on September 21st, 2000 at +3°C air temperature and the minimum value of -18,48‰ on August 2nd, 2000 also at +3°C. The maximum value of solid precipitation was measured in the sample from February 2nd, 2001 (-5,03 ‰ at +1,2°C) and the minimum value of -35,21 ‰ at -18,4°C on April 2nd, 2003. Seasonal differences in the isotopic signature at one location are attributed to varying atmospheric temperatures during condensation, a seasonally different source area of water vapor and varying influence of evaporation during precipitation (Dansgaard 1964). From Figure 2 (right) it is evident, that $\delta^{18}O$ values in precipitation do not show a seasonal trend in Longyearbyen. Values vary greatly between precipitation events, but high and low values occur in winter as well as summer. Different $\delta^{18}O$ values on Svalbard and a distinct signature of each precipitation event are therefore rather attributed to different source areas of water vapor than the air temperature. However, Ritter & Kuells (2010) show that a seasonal pattern is present in precipitation samples from Ny Ålesund when calculating deuterium excess. Compared to the d-excess of the Global Meteoric Water Line (=10), values of winter precipitation in Ny Ålesund are higher and values of

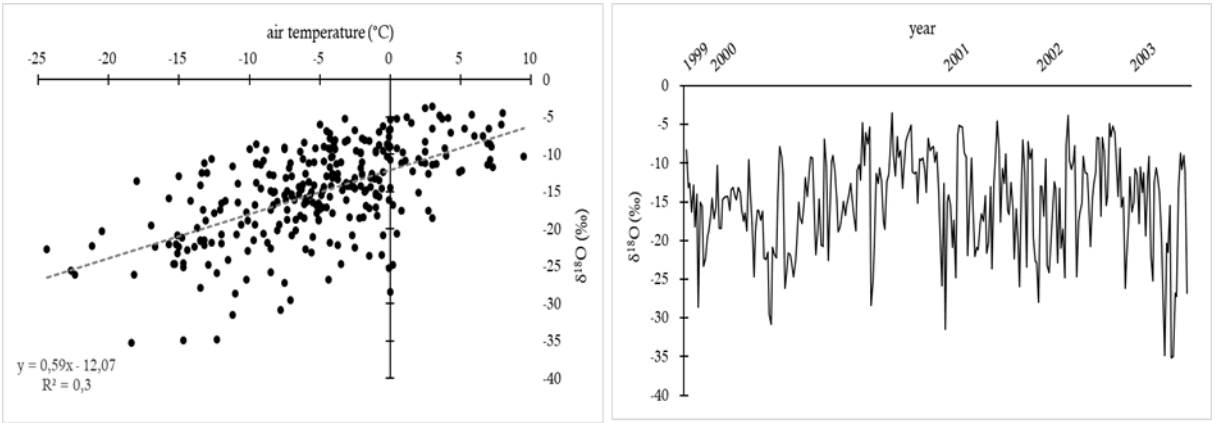

Figure 2: (left) $\delta^{18}O$ values of precipitation sampled in Longyearbyen from 1999-2003 plotted against measured air temperature during the precipitation event (data: Humlum (unpub.)); (right) $\delta^{18}O$ values of precipitation in Longyearbyen from November 1999 to Mai 2003 (data: Humlum (unpub.)).

summer precipitation lower. Mean d-excess values for the months November-March are >10‰, values for June-September range around 5‰ and the months April, Mai and October are considered as transition period with d-excess values ~10‰. The seasonal variability of d-excess is attributed to different origins of the moisture source. Compared to the seasonality of d-excess, no seasonal pattern was observed for the ratios of $\delta^{18}O$ or $\delta^{2}H$ in this location either.

2.5 Dye Tracing

For over a century salt and dye have been used as tracer to study the drainage system of glaciers (Hubbard & Glasser 2005; Nienow 2011). Openings in the glacier surface such as moulins, crevasses or, as on Rieperbreen, the upper endpoints of cut-and-closure channels, act as injection points for the tracer. When leaving the hydrologic system of the studied glacier, the emergence of the tracer is recorded by a detection device set up close to the terminus of the glacier in the proglacial stream (Benn & Evans 2010; Hubbard & Nienow 1997). A suitable tracer is non-toxic, detectable at low concentrations, soluble in cold water, physically and chemically stable, does not adsorb onto minerals and has a low background concentration (Hubbard & Glasser 2005). In case quantitative parameters are of interest, the hydraulic behaviour of the tracer further must be similar to that of water (Nienow 2011). Fluorescent dyes such as Rhodamine and Fluorescein are the preferred tracers for glaciological studies. Due to their detectability at a concentration of < 1ppb, smaller quantities have to be carried into the field and injected into the glacier compared to experiments with salt (Hubbard & Nienow 1997). Rhodamine, also called Rhodamine WT (water tracer) in its liquid form, is a fluorescent dye that emits red light while absorbing green light and therefore appears bright red/pink. Fluorescein is a green fluorescent dye which is seldom used exclusively, but rather simultaneously with Rhodamine (Hubbard & Glasser 2005). The emergence of dye in the proglacial river is detected by fluorimeters measuring light in the wavelengths as emitted by the dye (for example the wavelength of red light for Rhodamine). The higher the concentration of dye passing by the sensor, the more emitted light is detected and the stronger the measured fluorescence (Hubbard et al. 1982; Hubbard & Nienow 1997). Fluorimeters are often wired to data loggers that record the measurements at predefined regular intervals.

2.5.1 Dye Tracing in the Study of Glaciers

Large parts of the hydrologic system of glaciers, such as the en- and subglacial drainage networks, are often inaccessible. Even though several englacial channels have recently been explored in the winter months through glacio-speleological investigations (Gulley & Benn 2007; Gulley et al. 2009; Naegeli et al. 2014), this approach is not possible during the ablation season when meltwater is routed along subsurface flow paths. To remotely study these channels, several methods were developed, with tracer studies among them (Hubbard & Nienow 1997; Nienow 2011).

In glaciology, dye tracing experiments are an often-applied method. They have been performed to study the drainage systems of glaciers spread over a wide geographical scale with different thermal regimes. Studies were conducted for example on glaciers situated in the European Alps (Nienow et al. 1996; Nienow 1998; Krainer & Mostler 2002), Scandinavia (Clason et al. 2015; Seaberg et al. 1988; Theakstone & Knudsen 1981; Willis et al. 2012), High Arctic (Bingham et al. 2005; Gulley et al. 2009; Irvine-Fynn et al. 2005) and the Greenland Ice Sheet (Chandler et al. 2013). In these studies, dye tracing was used to map drainage basins, to characterise the morphology and connection of existing water flow paths, to monitor temporal and spatial changes in the routing of meltwater over a whole ablation season and, as in this study, to determine whether a connection between an injection and detection point exists (Hock & Hooke 1993; Nienow et al. 1998; Theakstone & Knudsen 1981; Willis et al. 1990).

2.5.2 Dye Breakthrough Curve Analyses

Since fluorescent dyes behave like water, the movement of water through the hydrologic system can be deduced from the observed behaviour of the dye (Hubbard et al. 1982). Dye breakthrough curves (BTCs) yield information about the connection of an input and detection site and the character and efficiency of the drainage system between these two known points. The type of drainage system within a glacier can be assessed through visual BTC analyses. Nienow (1993) distinguishes six shapes of return curves representing different types of drainage configurations, given equal experimental settings regarding straight line distance, amount of injected dye and discharge volume. Due to the subjectivity of visual interpretations of BTCs, additional numerical analyses are often performed in tracer studies. Quantitative parameters such as throughflow velocity, dispersion coefficient and dispersivity can be calculated

from dye returns by measuring the time passed between injection and detection of a slug of dye and analyses of the pattern, shape and concentration of dye returns at the hydrologic station (Clason et al. 2015; Nienow 2011).

Throughflow velocity or transit speed (v) (in ms^{-1}) indicates the mean flow velocity of water between the injection and detection point during one tracer experiment. It is calculated as:

Eq. 21

$$v = \frac{x}{t_m}$$

where x (in m) is the transit distance between the injection and detection point and t_m (in s) the time passed between dye injection and peak concentration registered by the fluorimeter. Since the transit distance is approximated by a straight line, v is the minimum estimate of the flow velocity. The throughflow velocity has been applied to characterise the efficiency of flow paths of the en- and subglacial drainage system (Clason et al. 2015; Hubbard & Nienow 1997; Seaberg et al. 1988). Different threshold values are presented in the literature to distinguish between fast and slow flow. Theakstone & Knudsen (1981), Hubbard & Nienow (1997) and Nienow (2011) propose a threshold of 0,2 ms^{-1} whereas throughflow velocities of >0,2 ms^{-1} are interpreted as fast and velocities <0,2 ms^{-1} as slow while Willis et al. (2009) consider values <0,05 ms^{-1} as slow, 0,1 ms^{-1} as moderate and >0,15 ms^{-1} as fast. Fast flow is indicative for water routing through a channelized, efficient drainage system and slow flow for water routed through a system of linked cavities, as water film at the base of the glacier or through permeable basal sediment (Nienow 2011).

Spreading of the dye cloud, as it travels through the drainage system of a glacier is caused by the process of dispersion. The longitudinal dispersion of dye depends on variations in flow velocities along the flow path and temporal storage of dye (Seaberg et al. 1988). The rate of spreading influences the shape of the dye return curve and can be quantified by calculating the dispersion coefficient (D) (in m^2s^{-1}) as:

Eq. 22

$$D = \frac{(x^2(t_m - t_i)^2)}{\left(4\, t_m^2\, t_i \ln(2(\frac{t_m}{t_i})^{\,0,5}\right)}$$

where x (in m) is the transit distance, t_m (in s) the duration between dye injection and peak concentration and t_i (in s) the time passed until half the peak concentration is

reached on the rising (t_i1) and the falling limb (t_i2) of the dye return curve. Equation 22 represents two equations which are calculated separately for t_i1 and t_i2. Seaberg et al. (1988) and Hubbard & Nienow (1997) interpret values of >10 m^2s^{-1} to reflect inefficient drainage systems whereas efficient pathways are characterised through values of <10 m^2s^{-1}. Since only three points on the curve are taken into account when calculating D, a variety of shapes of curves can yield the same values. The dispersion coefficient can further be used to calculate the dispersivity (*d*) (in m) which relates the rate of spreading to the transit velocity:

Eq. 23

$$d = \frac{D}{v}$$

Dispersivity is regarded as low when <5 m and high when >20 m (Hubbard & Nienow 1997; Seaberg et al. 1988). Nienow et al. (1998) associate low d values with efficient and high values with inefficient drainage. High dispersivity results from an elongation of the falling limb of the BTC showing that dye is stored temporarily in the channel (Clason et al. 2015). However, Gulley et al. (2012) propose that small d values might be attributed to a decrease of roughness of the conduit bed during high discharge. Therefore, rough beds can exhibit the same dye return signature at low flow as distributed drainage systems.

3 Study Area

This chapter gives an introduction into the geography of the study area, its past and present climate and its geologic settings. Further, characteristics of the Rieperbreen glacier are outlined followed by the development of the glacier and the proglacial area since the Little Ice Age and the occurence of the proglacial icing in the recent past as seen on aerial photographs.

3.1 Geographical Setting

Svalbard is an archipelago situated 1000 km north of the coast of mainland Norway and 1300 km south of the North Pole (Figure 3a). It consists of five main islands located between 74° and 81°N and 10° and 35° E (Figure 3b) with a total area of 62,250 km² whereas the biggest island, Spitsbergen, accounts for almost half of the land area (Liestøl 1988). The icing studied in this thesis forms in front of the Rieperbreen glacier situated in Nordenskiöld Land in the central part of the island of Spitsbergen (Figure 3c). Nordenskiöld Land extends southward of Spitsbergen's main fjord, Isfjorden. Four big valleys (Adventdalen, Sassendalen, Colesdalen and Reindalen) cut through the landscape and have, as well as their tributary valleys, the characteristic U-shape of former glaciated valleys. Bolterdalen, which is the valley closest to the study area, harbours the Bolterelva, a braided river system flowing in a north-westward direction into Adventdalen. Water from the Foxfonna catchment drains north into Adventelva

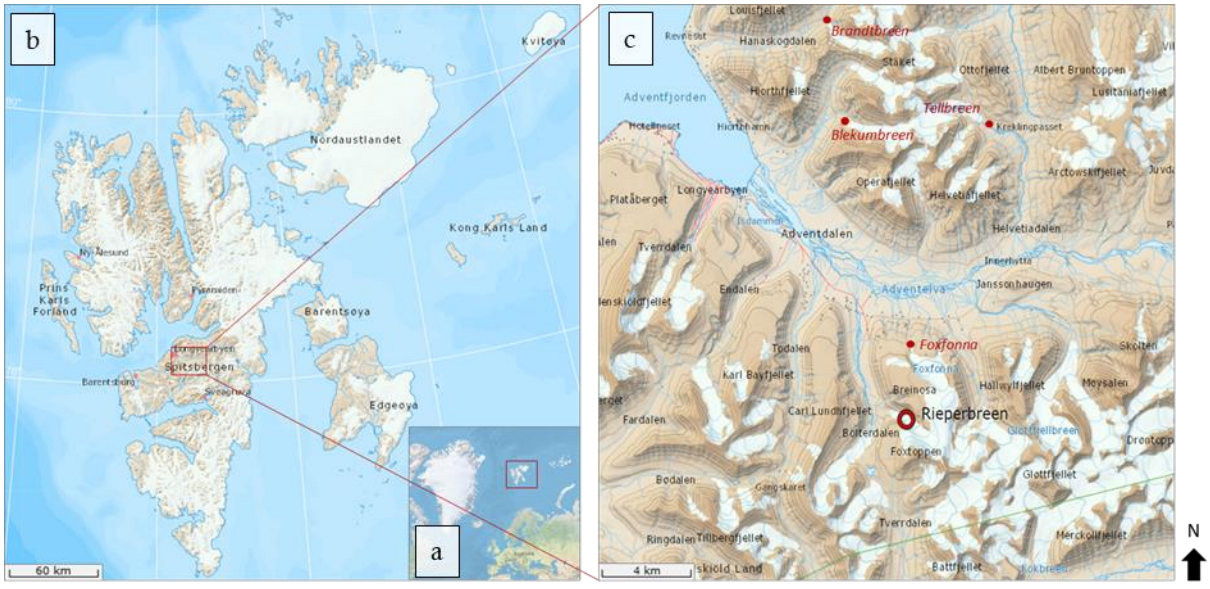

Figure 3: (a) Location of Svalbard 1000 km north of mainland Norway (Esri 2011); (b) the archipelago of Svalbard with the location of the study area in central Spitsbergen (Norwegian Polar Institute, n.d.); (c) Location of Rieperbreen south-east of Longyearbyen. Names in red indicate glaciers in the neighbourhood with the formation of proglacial icings (Norwegian Polar Institute, n.d).

which later discharges into the Adventfjord alongside Longyearbyen, the administrative centre. The plateau-type mountains in Nordenskiöld Land reach maximum heights of around 1000 m a.s.l and are characterised by steep slopes and flat summits. Most mountains, especially to the east towards Isfjorden, are unglaciated. Since the central part of Spitsbergen has the mildest climate on Svalbard, only 18% of the Adventdalen area are covered by glaciers. As a comparison, the average glacier coverage of the whole archipelago is 60%. (Dallmann et al. 2001; Major & Nagy 1972)

3.2 Glaciers, Permafrost and Proglacial Icings on Svalbard

More than 1000 glaciers cover about 60% of the land area of the Svalbard archipelago (Dallmann 2015; Hagen et al. 1993; Hagen et al. 2003a; Liestøl 1988). The biggest ice coverage can be found on the east coast due to lower air temperatures and higher precipitation compared to the central and western parts. Many different glacier types exist on Svalbard such as land- and tidewater terminating glaciers whereas the second is the most abundant glacier type accounting for two-thirds of Svalbard's glaciers (Dallmann 2015). Large ice caps are present in the east of the archipelago on the islands Noraustlandet, Edgeøya and Barentsøya and constitute 40% of the glaciated area of Svalbard (Dallmann 2015). The southeast, northeast and northwest of Svalbard are dominated by ice fields, large ice bodies consisting of several ice streams divided by mountain ridges and Nunataks. These continuously glaciated areas are separated by the less glaciated Nordenskiöld Land (Dallmann 2015). On Spitsbergen the most common glacier types are valley and cirque glaciers. The only glacier type absent on Svalbard are ice shelves, since all glacier fronts of tidewater glaciers are grounded (Liestøl 1988; Hagen et al. 2003a).

Even though only about 1% of the glaciers worldwide are classified as surge type (Jiskoot et al. 1998), an exceptionably high abundance is suggested for Svalbard. Estimates of surge type glaciers on Svalbard range between 13% (Jiskoot et al. 1998) and 90% (Hagen & Liestøl 1990; Jiskoot et al. 2000; Lefauconnier & Hagen 1991) of the total number of glacier. Most of the glaciers on Svalbard belong to the polythermal type consisting of warm and cold ice. Warm ice, often present in the accumulation area, is created in spring when meltwater percolates into the snow and firn and releases latent heat when refreezing. Warm ice further often exists at the base of glaciers providing sufficient ice thickness to raise the ice temperature to the pressure melting

point due to strain heating (Benn & Evans 2010; Dallmann 2015; Liestøl 1988). Basal ice layers at the pressure melting point preserve taliks underneath the glacier in the otherwise continuously frozen ground. Meltwater routed to the bed can, under these conditions, percolate into the ground and feed groundwater streams (Åkerman 1980; Hagen et al. 1993; Hagen et al. 2003a). Liestøl (1977) suggests that these groundwater streams flow underneath the permafrost layer towards the sea or emerge in front of the glacier terminus. Smaller glaciers are often <100 m in thickness, hence below the pressure melting point and frozen to their beds.

Svalbard lies within the boundary of continuous permafrost. Permafrost is a thermal phenomenon defined as: *"ground (i.e. soil and/or rock) that remains at or below 0°C for at least two consecutive years"* (French 2007, p.83). The classification *continuous* indicates, that at least 90% of the land area is frozen. The thickness of permafrost on Svalbard varies from less than 100 m close to the sea to 400 m (Dallmann 2015) or 500 m (Humlum et al. 2003) in the mountains. Active layer thickness ranges from 0,5 to 3 m whereas the thickest active layers are found in rock and the thinnest in unconsolidated sediments (Dallmann 2015). Dallmann & Elvevold (2015) describe the presence of permafrost everywhere on Svalbard except underneath glaciers. Humlum et al. (2005; 2007) however suggest, permafrost extending below some glaciers, such as small, cold-based glaciers in Central Spitzbergen.

Even though proglacial icings have been reported from several parts of the Arctic, they are especially abundant on the Svalbard archipelago. Early descriptions of the occurrence and some characteristics of Svalbard's proglacial icings are found in Liestøl (1977), Åkerman (1980, 1982) and Baranowski (1982). These authors relate icings to polythermal glaciers with winter drainage of sub-glacial meltwater and ground water from taliks beneath the glacier. Åkerman (1980, 1982), provides an inventory of several icing types for the western part of the island of Spitsbergen and notes that proglacial icings are the most common type in this area. He further describes different shapes of icings, depending on the topography of the glacier forefield, differentiating between two appearances: elongated ice bodies due to formation in meltriver channels and icings located on the outwash plain with a large extent but without specific shape. These early studies, however, only deal with specific icings or investigations of a small land area. The first inventory (in English) of proglacial icings for the whole Svalbard archipelago is provided by Bukowska-Jania & Szafraniec (2005). Aerial photographs taken

between July 19th to August 25th, 1990 were investigated for the occurrence, size and shape of proglacial icings. Proglacial icings were present in front of 217 glaciers covering an area of 12,3 km². It must be noted, however, that these numbers likely present minimum values due to the analyses of images from the late ablation season when smaller icings, such as the one in front of Rieperbreen, may already have vanished.

3.3 Climatic Setting

Even though the archipelago of Svalbard lies in the High Arctic, the climate is relatively mild and dry when compared with other landmasses at the same latitude (Bælum & Benn 2011). This is due to the West Spitsbergen Current, a branch of the Gulf Stream, that transports warm water northward along the west coast of Svalbard and keeps the sea and fjords in this area mostly ice free during winter. The warmth transported by the current results in relatively high temperatures on the whole archipelago and in a spatial temperature gradient from west to east, especially during winter (Hagen et al. 1993; Humlum et al. 2007; Liestøl 1988). Temperatures during winter average around -10°C on the west coast and -20°C in the north-east (Førland et al. 2009). The inner parts of the archipelago show a more continental climate with higher summer and lower winter temperatures compared to the coastal areas (Liestøl 1988). Air temperatures do not only vary spatially, but fluctuate greatly on a day to day basis. Temperature differences of +/- 20°C within 24 hours are not uncommon during winter (Humlum et al. 2003). Further, plus degrees can occur during warm spells even in the coldest months leading to snowmelt and liquid precipitation.

The cause of the large temperature fluctuations, especially during winter, is the location of the polar front. Since the polar front is constantly changing its position, large temperature and weather fluctuations occur over a short period on the Svalbard archipelago (Førland et al. 2009). The climate is further influenced by the presence and distribution of sea ice that leads to significant inter-annual temperature differences. Sea ice reflects most of the incoming solar radiation and forms a barrier for the latent and sensible heat flows from warmer water. In years when the sea around the coast is ice free, a relatively mild and humid maritime climate is recorded. With the presence of sea ice, the climate shows continental characteristics with lower temperatures and less precipitation. (Førland et al. 2009) During the last century an increase in air

temperatures and a decline in sea ice cover is recorded. Since the 1970s a significant decrease in sea-ice cover during winter and even more in the summer months can be observed not only for the Barents Sea, but for the whole Arctic. (Førland et al. 2009)

In general, Svalbard is a very dry region due to stable air masses carrying small amounts of water vapour. Most precipitation falls during the months February, March and August whereas precipitation in the form of snow and rain is possible all through the year (Førland et al. 2009). A spatial gradient in precipitation can be observed. The highest amounts are measured in the south-east with more than 1000 mm per year on exposed mountain sides. Towards the northeast, the west coast and the inner parts of Spitsbergen, precipitation amounts decrease gradually. The west coast registers on average 400 mm precipitation per year, the inner parts even less. (Liestøl 1988)

3.3.1 Climate of Longyearbyen

In Longyearbyen, meteorological measurements have been conducted since 1912 (Førland et al. 2009). Over the observed period, the mean annual air temperature (MAAT) averaged at -5°C and the mean annual precipitation (MAP) at 180 mm (Humlum et al. 2007). Four months of the year (June-September) have average temperatures above freezing. The coldest and warmest months of the year are February and July with average temperatures of -13,4°C and +6,5°C measured at Longyearbyen airport in the period 1975-2015 (Figure 43 (appendix)). Between 1975-2015 most precipitation was recorded for the month August (24,3 mm) (Figure 42 (appendix)). Since the beginning of measurements in Longyearbyen, the MAAT increased by 2°C, however not gradually (Figure 41 in the appendix). From 1912 until the 1930s, a warming trend is observed during which the MAAT at the Longyearbyen airport increased by 4°C until the 1920s from -9 (-9,5) °C to -5,5°C and further to -4,5°C in the 1930s (Humlum et al. 2003, 2005, 2007). This period of increasing MAAT was followed by a period of cooling from 1957-1968 by 4°C - 5°C (Førland et al. 2009; Humlum et al. 2003, 2005, 2007). Since 1970, a constant increase of MAAT is registered. In the early 21st century the MAAT of -5°C is close to the warmest years in the 1930s. The MAP increased by 2% per decade since 1912. (Førland et al. 2009)

3.3.2 Precipitation and Temperature Longyearbyen 2016-2017

For the formation of last year's proglacial icing in front of Rieperbreen the precipitation and temperature values of the last accumulation season, from October 2016 until June 2017, are of interest. Precipitation and temperature data from the Longyearbyen airport meteorological station is available since August 1975. Figure 42, Figure 43 and Figure 44 (in the appendix) show a comparison of monthly precipitation and air temperatures for the period August 1975 to December 2015 and for the past year from July 2016 to June 2017. Air temperatures and precipitation during the past year show a notable difference when compared to the long-term average values.

For the first five months of the accumulation season 2016/2017 (October-February), more precipitation was documented than during the reference period. In 2016 the months October and November were the wettest since 1975. Mean monthly precipitation in October 2016 was 57 mm compared to 15,3 mm during the period 1975-2015. This is a deviation of 41,7 mm or +273% from the long-term average. Precipitation in November 2016 deviated by 40,4 mm or +232% from the long-term average. The amounts of precipitation during the months December (+23%), January (+51%) and February (+167%) were also significantly higher compared to the period 1975-2015. The month of February 2017 was the second wettest since 1975.

Not only the amount of precipitation shows increased values during the last accumulation season, but also the average monthly temperature. In the months October-April of the 2016/2017 accumulation season the average monthly temperature was higher compared to 1975-2015. The highest temperature deviation from the reference period occurred in October (+7,9°C) resulting in an average monthly value with plus degrees compared to a negative long-term average. In 2016, the average monthly values of October (+3,2°C) and November (-0,7°C) were the highest recorded at Longyearbyen airport since 1975. Of special interest in regard of the proglacial icing are positive degree days resulting in snowmelt and precipitation in the form of rain (Figure 44). Most days during October and the beginning of November had average daily temperatures above 0°C. Frost days did not occur continuously until late November and warm spells resulted in periods with positive degrees. also during December and February. Highest precipitation values in the first months of the accumulation season were recorded during warm spells whereby parts of precipitation are likely to have fallen as rain.

3.4 Geologic Setting

The plateau-type mountains in the Adventdalen area with steep slopes and flat or rounded summits consist of flat-lying clastic sedimentary rocks with interbedded biochemical sedimentary rocks (Dallmann et al. 2001; Dallmann & Elvevold 2015). Three types of sedimentary rocks are present in the study area which can be subdivided into sandstones, siltstones and shale by their grain size. (Bælum & Benn 2011) The age of the five different formations assembling Breinosa range from the Lower Cretaceous (145 Ma) to the Eocene (33,9 Ma) (Figure 4). The oldest formation in the study area is the Carolinefjellet Formation, marine sequence of sandstones, siltstones and shales surfaceing in between 75 m to 375 m a.s.l. The Formations overlying the Carolinefjellet Formation belong to the tertiary system showing marine, estuarine and terrestrial facies. The Tertiary formations lie directly on top of the Lower Cretaceous since the Upper Cretaceous beds have been eroded during the Cretaceous when Spitsbergen was uplifted (Hjelle 1993). The first formation of the tertiary system is the Firkanten Formation from the Paleocene composed of shales, siltstones and sandstones with five interbedded coal seams. Because of the occurrence of coal, Gruve 7 and its mine shaft are located within this unit on the northern side of Breinosa. The Firkanten Formation ranges from about 375 m to 475 m a.s.l. near Rieperbreen and can be divided into two parts. The rocks of the lower

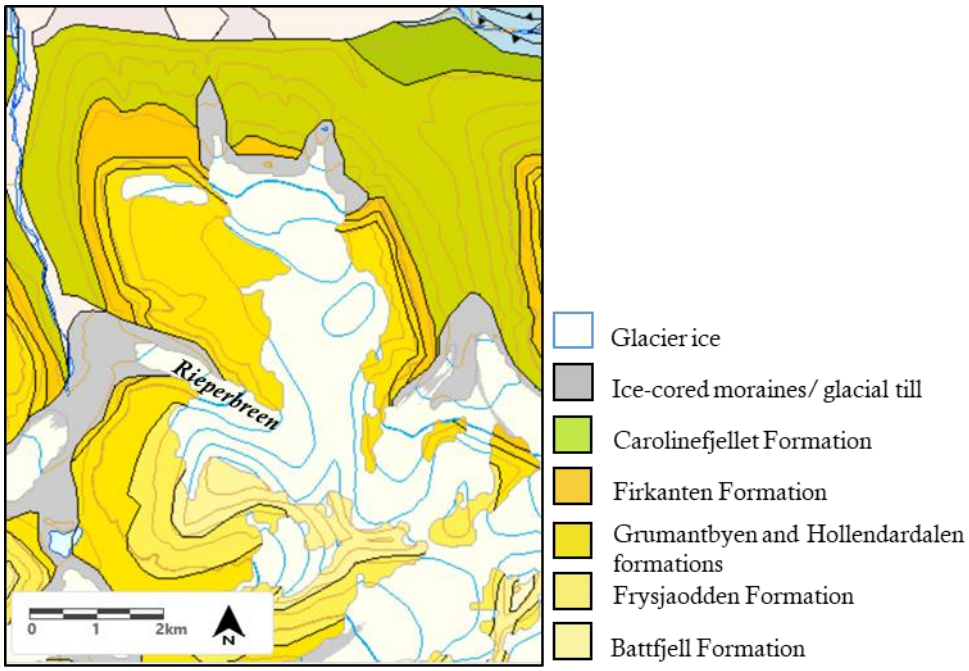

Figure 4: Geological map of the study area (Norwegian Polar Institute 2016, adapted).

part are easily erodible whereby the lowest layers are often scree covered. Reddish-grey and light brown weathered sandstones with conglomeratic beds are indicative for the upper part of this formation. Figure 4 shows that the lowest lying parts of the Rieperbreen glacier are located within the Firkanten Formation. The sandstones from the late Paleocene to the early Eocene, Grumantbyen and Hollendardalen formation, form a layer with a width of 50 m. The shale- and sandstones from the Frysjaodden Formation (late Paleocene to early Eocene) surface on the Breinosa plateau. In the southernmost part of the ice cap, the Battfjell Formation is present on the surface of the plateau. This lithographic unit from the early Eocene is assembled by polymict sandstones that are interbedded with shales and siltstones. (Major & Nagy 1972; Norwegian Polar Institute 2016)

3.5 Rieperbreen

Rieperbreen (breen = norw. glacier) is a small and narrow land terminating valley glacier. Its name originates from the word Ryper, Norwegian for ptarmigan. The glacier is located 15 km south-east of Longyearbyen on the Breinosa massif at 78°7'N, 16°5'E (Figure 5). Rieperbreen is presently ~2 km long and covers an altitudinal range from 300 to 500 m after Lysså & Lønne (2001) or up to 955 m a.s.l after Rutter et al. (2011). The confusion about the upper elevation originates from Rieperbreen being an outlet glacier of Foxfonna (fonna = norw. ice cap) and different interpretations of the margin between Foxfonna and Rieperbreen. An elevation of 955m, however, clearly is an overestimate since the maximum hight of the Breinosa massif is 809 m a.s.l. Rieperbreen drains Foxfonna in westward direction into Bolterdalen. The plateau of Breinosa is partly covered by Foxfonna. and is bound by three valleys: Adventdalen (north), Foxdalen (east) and Bolterdalen (west). Two more outlet glaciers drain the ice cap. The Foxfonna glacier in the north, flowing towards Adventdalen, and Foxbreen in the east flowing into Foxdalen.

Previous research conducted on Rieperbreen encompasses the study of the ice-cored lateral and frontal moraine complexes (Lysså & Lønne 2001), the englacial conduit (Gulley et al. 2009, 2012, 2014), the mass balance, runoff hydrology and hydrochemistry (Rutter et al. 2011) and the cryconite communities (Cameron et al. 2012). Lysså & Lønne (2001) describe the glacier as presently being composed of three

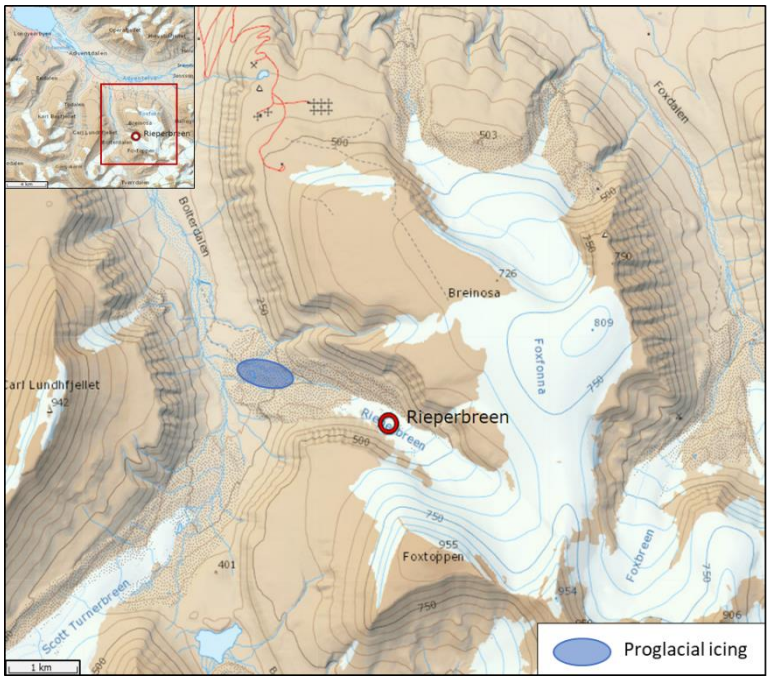

Figure 5: Topographic map of the study area (Norwegian Polar Institute, n.d.) indicating the location of the studied proglacial icing in front of Rieperbreen.

ice lobes indicating different origins (letters A, B, C in Figure 45b and Figure 46 in the appendix). The northernmost ice lobe originates from the Foxfonna ice cap; the middle and southern lobes are fed by snow transported onto the glacier by avalanches from Foxtoppen which confines the glacier in the south. Transversal profiles show that the glacier is tilted to the north at an angle of 7° (Lysså & Lønne 2001; Rutter et al. 2011). This has implications for the drainage system of the glacier. Three supraglacial channels flow towards the northern margin of the glacier where they drain into an englacial and later subglacial conduit formed through the process of cut-and closure (Gulley et al. 2012). The conduit has been thoroughly studied and mapped by Gulley et al. (2012) who describe the subglacial channel as incised into frozen till and with little variation of its morphology from one year to the next. This channel drains most of the meltwater from Rieperbreen at the north-westerly point of the glacier snout. Other sources of meltwater in the proglacial area originate from an ice patch located in the valley north of Rieperbreen, from ice-cored lateral and frontal moraines and from springs in the forefield forming the icing during winter.

3.5.1 Development of Rieperbreen since LIA

At the end of the Little Ice Age (LIA) Rieperbreen was more extensive and thicker than today. Ice-cored frontal and lateral moraines, several kilometres away from the present glacier front and several tens of meters higher in elevation, are remaining evidence of

the former glacier extent. Since its LIA maximum extent Rieperbreen has receded and down wasted significantly, a general trend observed on valley glaciers in Svalbard that reached their Neoglacial maximum extent at around 1900. Since then, valley glaciers down wasted continuously by 0,3 m water equivalent per year since 1936 (Rutter et al. 2011) and hence retreated. This is due to a negative mass balance caused by a step-like increase of air temperatures that terminated the LIA at around 1920 (Hagen et al. 2003b; Humlum et al. 2003). The only exception are glaciers that experienced a surge after the termination of the LIA (Lovell et al. 2015). Aerial photographs of Rieperbreen from 1936, 1961, 1990, 2009 and 2016 help to quantify the retreat and down wasting (Figure 45). Lysså & Lønne (2001) identifed a retreat of the glacier front of 900 m and a surface lowering of 50-60 m in the period 1936-1990. However, the total retreat of Rieperbreen since the maximum extent is even greater because the glacier front was already located behind its maximum position in 1936 and since 1990 the glacier has further receded significantly. This can be seen by comparing the aerial photograph from 1990 with the composite drone image from 2016 (Figure 45 c and e). The present-day position of the glacier front is located about 2 km behind its maximum extent during the LIA (Figure 45 e). Some of the former glacier ice remains in the proglacial area as buried dead ice, which can still be connected to en- and subglacial drainage systems as suggested by Hambrey (1984).

3.5.2 Past and Present Thermal Regime

Rieperbreen is believed to have been polythermal at the termination of the LIA. Lysså & Lønne (2001) explain the existence of debris-rich foliation in the moraine complex with a former polythermal regime of the glacier. They conclude that during this state, subglacial debris was incorporated into the basal ice forming debris bands. However, other features are discernible on aerial photographs that indicate with higher certainty the existence of a more dynamic glacier under polythermal conditions in the past. These are crevasse traces on the glacier surface of the lower snout and flutes on the surface of the southern ice-cored lateral moraine (Figure 45 e). Crevasse traces are relict features that indicate a heavily crevassed glacier. Crevasses form during a time when the glacier experiences a more dynamic ice flow, as is associated with a warm base, inducing longitudinal stretching which leads to the opening of transverse crevasses (Hambrey et al. 2005; Lovell et al. 2015). All crevasses have closed now and no crevasses are newly forming. This shows that the glacier was warm-based

before but is currently frozen to its bed and therefore a cold glacier. Flutes are narrow linear sediment ridges that can be found in the foreland of glaciers. Other than traces of transverse crevasses, flutes are aligned parallel to the ice flow. They form when the glacier slides over boulders located at the bed which leads to the formation of cavities at the lee side of the boulders. These cavities are then filled with basal sediment squeezed upwards. Flutes become visible in the forefield as the glacier recedes. Since the formation of cavities at the bed requires a downslope movement of the ice mass, these features are associated with warm-based glaciers rather than with a glacier that is frozen to its bed. Flutes are seldomly preserved in the forefield of small valley glaciers due to thermo-erosion. (Roberson et al. 2011; Lovell 2014) They can, nevertheless, still be found on the lateral ice-cored moraine of Rieperbreen. Probably because of the fast retreat of the glacier in the last decades which left little time for degradation.

No ice temperature data exists currently for Rieperbreen, but existing publications assume that the glacier is entirely cold-based and frozen to its bed (Gulley et al. 2012; Lyså & Lønne 2001; Rutter et al. 2011) as is the case for most of the small land-terminating valley glaciers on Svalbard less than 5 km in length (Lovell et al. 2015). This argument is supported by an average ice thickness of 40 m estimated by Lyså & Lønne (2001). Rutter et al. (2011) confirm that the ice is less than 80 m thick and entirely cold based as seen in data from an unpublished GPR survey. Further, the Foxfonna glacier was shown to be cold based by Liestøl (1974), and therefore it is unlikely that Rieperbreen should be of a different thermal regime (Rutter et al. 2011). Hodgkins et al. (2004) name a minimum ice thickness of 95 m for pressure-melting. This implies that Rieperbreen has undergone the thermal transition from a polythermal to a cold-based regime due to significant mass loss since the termination of the LIA. No information exists on when Rieperbreen underwent the transition. The timing, however, contains interesting implications for the thermal state of the ground and possible sources and flow paths of water in the proglacial area feeding the icing.

3.5.3 Morphology and Formation of the Frontal Moraine Complex

The morphology of the Rieperbreen forefield is dominated by a 700 m long and up to 850 m wide moraine complex consisting of a series of three moraine ridges. Thermo-erosional processes leading to debris flows and topographic inversions have altered the morphology. These processes are induced by the action of meltwater and by the

decay of the ice-core (Lovell 2014). Traces of inactive and active meltwater channels and meltwater pools are present in the area. The most distal moraine ridge is located about 2 km in front of the present glacier front. It outdates the oldest available aerial photograph from 1936, is believed to represent the maximum extent of Rieperbreen during the LIA maximum in the early 20th century (Figure 45 a). Since a vegetation cover developed on the moraine distal side where the activity of present day meltwater channels or sediment transport of former meltwater channels is absent (visible on Figure 45 e), the maximum extent of the glacier has not reached further behind this line into the Bolterdalen valley in the recent past. During the formation of the LIA moraine ridge, a connection between the Foxfonna ice cap and the Rieperbreen basin is believed to have existed north of Rieperbreen (Lysså & Lønne 2001). A small ice patch connected to Foxfonna remains in the valley north of Rieperbreen. The formation of the next moraine ridge behind the LIA moraine must have taken place between 1936 and 1961 since the ridge is not visible on the aerial photograph from 1936, but discernible on the image taken in 1961. The third moraine ridge can first be seen on the 1990 aerial photograph and correlates well with the location of the glacier front in the 1961 image.

The morphology of the LIA and the younger moraines is rather different in regard of their height and stability. The height decreases with increasing distance from the glacier front. The LIA moraine is about 20 m high, the second and third one 25 m and 35 m, respectively (Lysså & Lønne 2001). The height difference might be attributed to the age of the moraines. Since the LIA maximum occured several decades before the younger moraine ridges were formed, the disintegration of the ice core in the corresponding moraine is more advanced or completed compared to the younger ridges. The height difference might also be attributed to less abundant sediment in the proglacial area during the formation of the LIA moraine compared to the time of the formation of ridge 2 and 3 (Lovell 2014). Mud flows and slide scars visible during the ablation season on ridges 2 and 3 indicate the presence of an ice core whereas traces of active thermo-erosional processes are absent on the LIA moraine. A series of meltwater channels are present within the moraine complex (Figure 46). The main meltwater channel cuts through all three ridges. A valley south of the active meltwater channel indicates a relict channel that cut through moraine ridges 1 and 2 but not through 3. This channel is assumed to have been the main meltwater channel during the LIA maximum extent of the glacier and in 1936. An indentation in the LIA ridge and

a depression in the glacier front on the 1936 aerial photograph can be observed that coincides with the location of this channel. Several traces of smaller inactive meltwater channels can be identified. Good examples start at the distal side of moraine ridge 2 and cut through ridge 1. The ponds present between moraine ride 2 and 3 can first be seen on the image from 1990 and are therefore younger than 1961. The topographic inversion in which meltwater accumulates, was most likely formed by the disintegration of the moraine's ice core.

3.5.4 Rieperbreen Proglacial Icing

A proglacial icing is mentioned to be present in the forefield of Rieperbreen in three publications: Åkerman (1982), Lysså & Lønne (2001) and Rutter et al. (2011). Little details are provided about its formation, morphology or chemical composition. The only information reported on its formation and possible source of water is found in Lysså & Lønne (2001), who refer to the study of Scott Turnerbreen by Hodgkins (1994) and therefore assume that the icing is formed by *"slow winter drainage of water that has been stored in ice-marginal drainage channels"* (p. 522). No records exist showing the onset of icing formations in front of Rieperbreen. Aerial photographs help to reconstruct the existence and location of a proglacial icing discontinuously from 1936 onwards (Figure 45) On the aerial photographs from 1990 the icing can be clearly identified for the first time (Figure 45 c). The image from 1961 shows white patches in front of the glacier snout. Given the location they are, however, interpreted as late season snow rather than a proglacial icing (Figure 45 b). Since all aerial photographs in Figure 45 were taken in the months August or October and therefore towards the end of the ablation season, the visible icing presents the minimum extent of the icing after melting and erosion by meltwater. Hence, an icing could also have been present in earlier years but might not have been recorded on the aerial photographs taken at the end of summer. In 1990, the icing was in close proximity to the glacier front. The ice survived most of the accumulation season on the outwash plain in front moraine ridge 3. In 2009, an icing was present on the same outwash plain as in 1990 and in the valley occupied by the main meltwater channel between ridge 2 and 3.

4 Data Collection and Processing

This chapter comprises a step-by-step description of data collection during fieldwork from March to September 2017, subsequent post processing and laboratory analyses. The applied methods are listed in chronological order of application and encompass GPR surveys, the sampling of ice cores, spring and lake water, in-situ measurements of hydrochemical parameters and dye tracing experiments.

4.1 GPR

During the accumulation season, two ground-penetrating radar surveys were conducted on the Rieperbreen icing. This method was employed to (i) map the extent of the icing and to (ii) evaluate whether the two visible icings, separated by snow covered areas, are connected. Further, radar data was collected to (iii) estimate the thickness of the icing and to (iV) study the internal morphology. The crucial goal, however, was to (V) locate spring(s) forming the icing. This can be challenging during the ablation season when apart from the spring water, meltwater from the glacier, snow and ice-cored moraines is present. Hence, it was attempted during the accumulation season to allow sampling water directly from the source in a next step.

4.1.1 Survey Design

Radar data was collected on March 26th and April 9th, 2017. The GPR system consisted of a MALÅ ProEx control unit, a MALÅ XV monitor and a MALÅ shielded 800 MHz antenna (Figure 6a). This frequency was chosen since a high resolution was desired and the depth of the icing was expected to be relatively shallow (~2 m). The used antenna combines both, the transmitting and receiving antenna in the housing with a spacing of 14 cm. At the beginning of each field campaign the settings and acquisition parameters were adjusted to be in accordance with the system setup and planned investigations. The time window length, defining the recorded depth, set to 10 m is by far deeper than the expected depth of the icing, but ensured that crucial information was collected. The wave velocity in the subsurface was set to 0,15 m ns^{-1} to provide more accurate depth information of reflections seen on the monitor during the survey. This value was adjusted during post processing. The acquisition mode time triggering was chosen from the menu since the antenna was pulled on foot and ski and the sampling frequency was set to the lowest possible option of 0,025 s. During the survey,

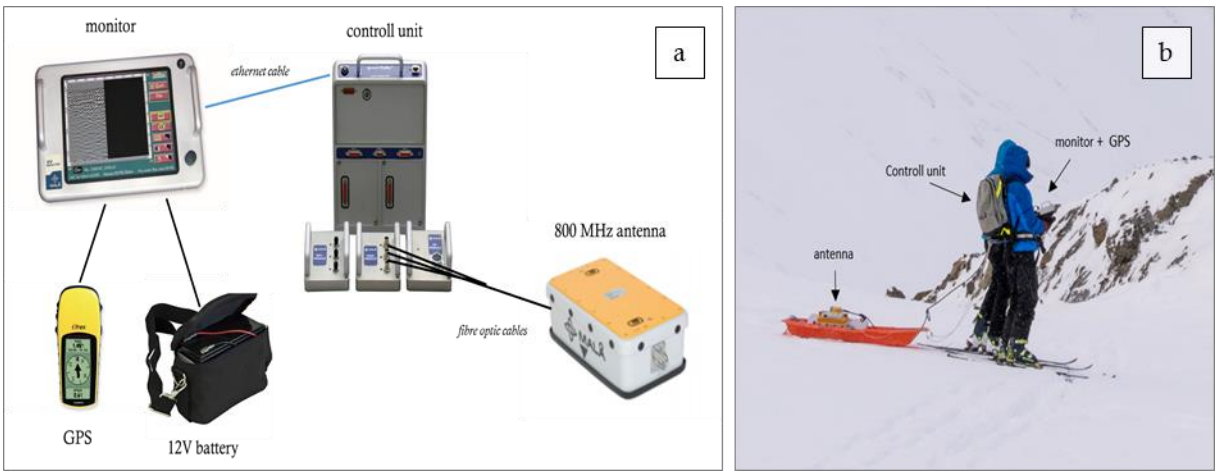

Figure 6: (a) Individual parts of the GPR system (images from: malagpr.com); (b) setup of the GPR equipment during the surveys in this study conducted by two people (Kuschel 2017).

the control unit was carried in a backpack and monitor, battery and handheld GPS receiver in hand. The antenna was fastened with tape to a plastic pulk which was pulled with a rope attached to a harness by the person carrying the backpack (Figure 6 b).

During the first field campaign on March 26th, 2017, the snow covered plain in front moraine ridge 3 was investigated thoroughly even though a visible icing was absent. Aerial photographs from 2007 show an icing occupying this part of the glacier forefield and a spring was communicated present here in former years. Hence, GPR was applied to detect an icing underneath the snow layer as well as water indicating the location of an active spring. During the repeated survey on April 9th, 2017, several longitudinal profiles were recorded from the visible icing. The focus, however, lay on collecting data from the snow-covered area between the two icings. The intention was to detect if the ice bodies are connected or if several springs are present feeding separate icings. Thereafter, the surroundings of the ice core 1 sampling site (refer to chapter 4.2.1) were surveyed as to locate a spring. Further, the ~900 m long valley leading to the glacier was investigated for the existence of more icing areas closer to Rieperbreen. Since visible ice was absent on the surface, no radar data was collected.

4.1.2 Data Post Processing

Editing and processing of the recorded GPR data is necessary before subsurface structures can be interpreted. The aim of post processing is to enhance data interpretation by improving the quality of the raw data while still showing subsurface reflectors accurately. After data editing, the same processing routine was applied to all profiles in ReflexW ver.8.5.3 (Sandmeier Software). The processing flow mainly

consisted of applying filters and gain to increase the signal to noise ratio and to correct system induced irregularities. Since it is easy to over-process GPR data and introduce user bias, the processing was kept as simple as possible.

The first step of post processing was data editing which consisted of deleting files, assessing the quality of GPS data and the length and orientation of profiles. Data recorded during the setup of the system and short profiles resulting from the disconnection of the ethernet cable were discarded from further processing. The length of the profiles was assessed through three approaches (Figure 7 a-c). Since automatic collection of GPS data failed during the first survey, the length of the profiles was deduced from the position information of the start and end points noted down separately for each profile. The minimum length was approximated by a straight line connecting these two points (Figure 7 a). The trace increment and hence the position of traces along the profile was calculated from the end coordinate in X direction, given by the profile's length, and the number of traces assuming equidistance.

During the second survey, GPS coordinates were simultaneously acquired with GPR data and recorded in a separate file containing the trace number and GPS coordinates. By plotting the coordinates recorded with roughly every 20th trace, the accuracy of the position information was evaluated. This showed that the quality of the data varied greatly. For profiles with a good spatial accuracy, the distances were calculated from the coordinates during data import into ReflexW (Figure 7 b). The location of traces without position information in these profiles was interpolated from the existing coordinates. The length of profiles with poor accuracy was measured from the end point of the previous and the start point of the following profile. This was possible since profiles were recorded consecutively, especially when walking along the icing (Figure

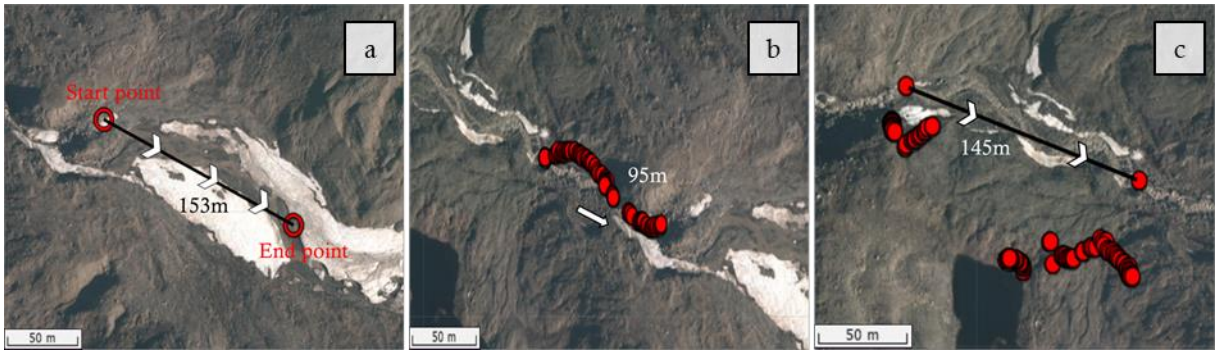

Figure 7: Assessing the length and orientation (black errors) of GPR profiles: (a) by measuring the distance between separately recorded start and end points; (b) from automatically recorded coordinates with a good accuracy and (c) from the end point of the previous and the start point of the following profile due to poor quality of GPS data (aerial photograph: Norwegian Polar Institute 2009).

7 c). The position of traces along the x axis was calculated according to the data from survey 1. Profiles recorded towards the end of the second survey miss information in the coordinate files. Where possible, the position and length of these profiles was approximated afterwards or, otherwise, omitted. Further, the orientation of the profiles was noted down. Profiles surveyed from E-W or N-S were flipped along the x axis after updating the position information. All profiles are presented from west to east and south to north.

Processing in ReflexW was performed to facilitate interpretation by improving the visualization of the data and to correct errors during data acquisition. Through iterative processing of several profiles, a processing routine was compiled. The processing flow was kept as simple as possible to avoid over processing and the introduction of user bias, for example by creating artefacts. The same order of processing steps and parameters were applied to all icing profiles from area 2 and 3 and a slightly different routine to profiles from area 1 due to the absence of ice on the surface. The processing consisted of applying filter to remove background noise, correcting time zero, time gain and topographic correction as suggested by Annan (1999), Cassidy (2009b), Robinson et al. (2013) and Sandmeier (2017).

GPR raw data contains low frequency signals caused by electromagnetic induction (Møller 2006), artificial instrument noise (Hubbard & Glasser 2005) or signal saturation due to the proximity of transmitting and receiving antenna (Cassidy 2009b). As first processing step these low frequency components of the signal were removed through temporal filtering by applying a one-dimensional subtract-mean (de-wow) filter (Figure 8). The filter acts independently on each trace. A running mean value within a specified time window is calculated for each value of all traces. This mean value is subsequently subtracted from the data value of the central point in the time window (Sandmeier 2017). The time window was set to 1,25 ns representing one principal period as suggested by Sandmeier (2017).

Since the timing of the arrival of the first wave can vary along a profile due to damaged cables and temperature differences between the instrument and air (Møller 2006), the next processing step was a correction of the zero time. Resampling the time zero for

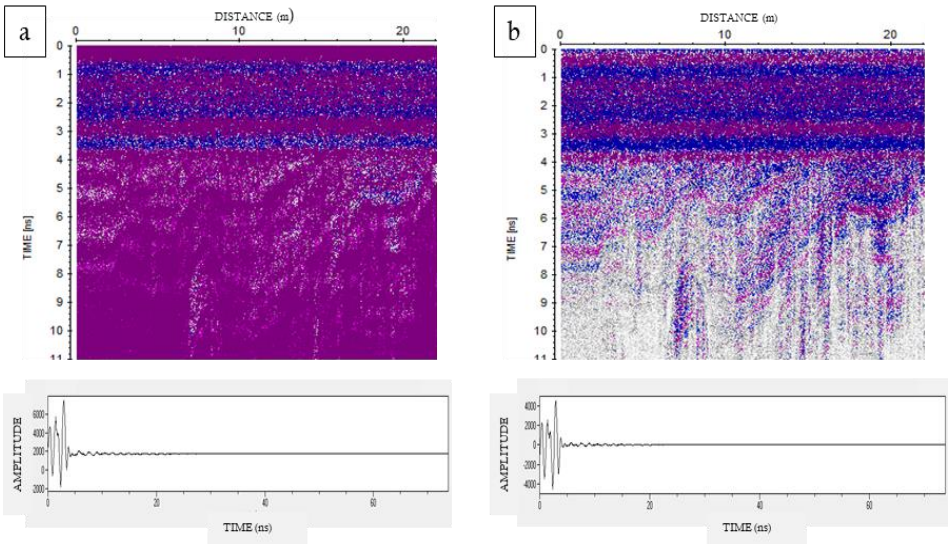

Figure 8: A section of a profile (a) before and (b) after applying a de-wow filter with a time window of 1,25 ns. Notice the shift to an amplitude of 0 in the bottom box of image b with increasing time due to the removal of low frequency components of the signal.

all traces ensures aligning reflections along the profile at correct depths. The approach suggested by Cassidy (2009b) defining time zero as first break point was not operational due to varying polarity of the first peak in some profiles. Hence, another definition for time zero was chosen to ensure consistency along all traces and comparability between profiles. The time-zero position was defined as the peak with maximum positive amplitude within the first 10 ns of each trace, corresponding to the positive peak of the ground wave. These returns were selected and aligned at time 0 resulting in the correct alignment of traces in y-direction (Robinson et al. 2013). As a subsequent step, all data in front of time zero was removed (Figure 9). For the profiles from area 1, a manual adjustment of the start time was evaluated to work best keeping surface parallel reflections in alignment.

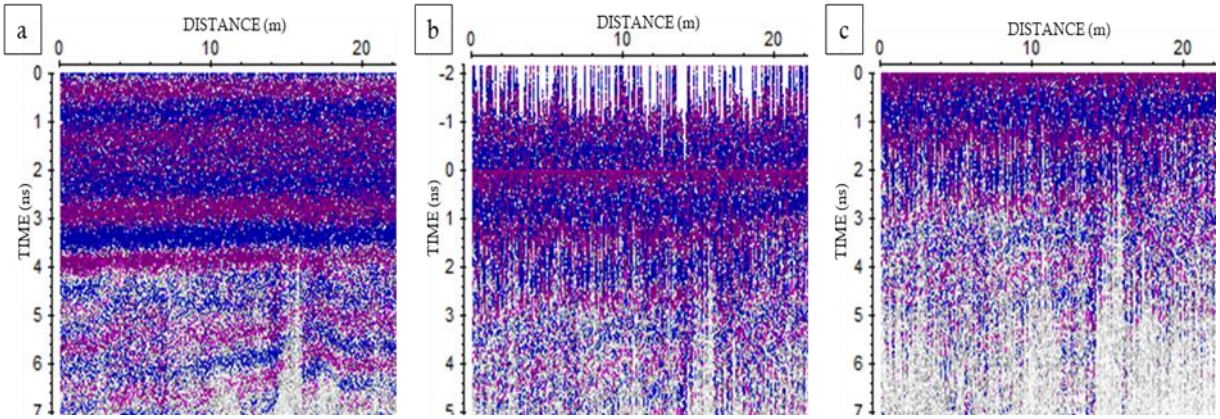

Figure 9: A section of a profile (a) before adjusting time zero; (b) after selecting positive peaks and alignment at time zero and (c) after removing data in front of time zero.

The recorded signal strength decreases with increasing distance from the antenna due to signal attenuation and geometrical spreading losses (Cassidy 2009b). Hence, the signal from a reflector close to the surface shows a higher amplitude than it would from the same reflector at a greater depth. Due to this effect, the GPR data needs to be time gained to compensate for the energy losses. A manual gain filter was found to work best for all profiles of the obtained data. This filter allows the user to apply spatially variable gain in y direction. By applying this gain function, the region of interest between 10 and 40 ns could be emphasized while no gain was applied to the first 5 ns already showing a high amplitude. Further, the noise level at greater depth could be kept at a minimum compared to other gain filter options (Figure 10).

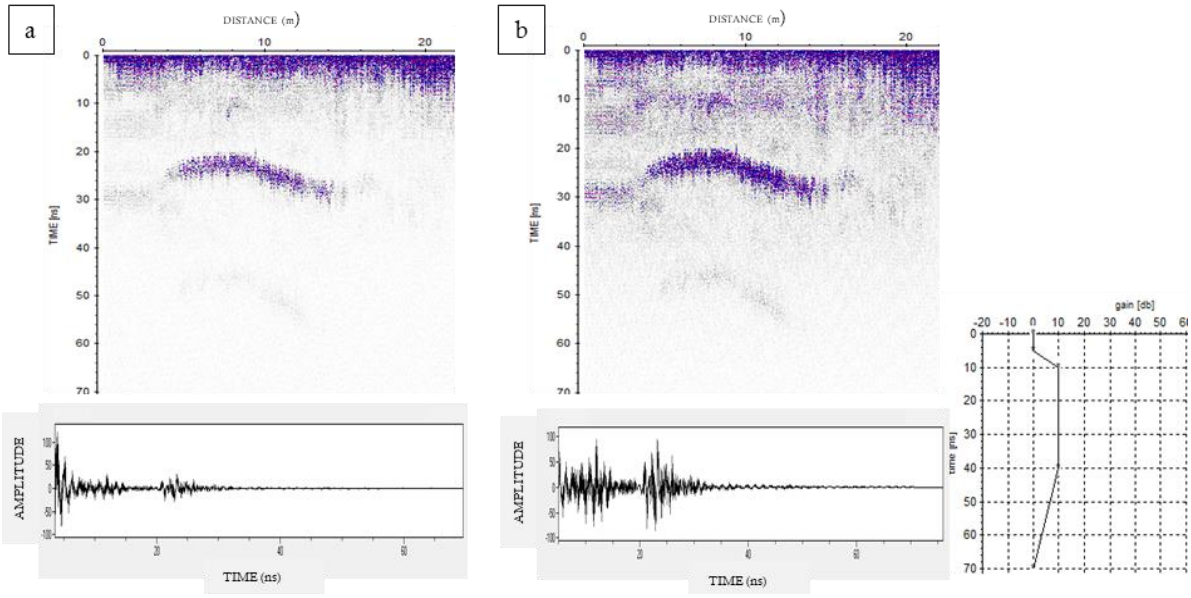

Figure 10: A section of a profile (a) before and (b) after applying a manual gain function. The graph on the right side of (b) shows the applied gain that varied with time. The areas of most interest between 10 to 40 ns were modified with the largest gain.

Due to the high noise level of the data set, a bandpass filter acting in the frequency range was applied to improve reflections at the bed. A butterworth filter with an upper cut off frequency at 800, corresponding to the centre frequency, yielded the best result.

The time range during data acquisition was deliberately set to a much higher value than the expected depth of the icing. To remove parts of each trace without data, a maximum time of 40 ns was defined for all icing profiles and 30 ns for those recorded in area 1. Repeated traces at the front and end of profiles, produced by standing pauses during data acquisition, were deleted. To further increase the visual quality, a mean filter in time direction was applied (Figure 11) to profiles from the icing. This filter

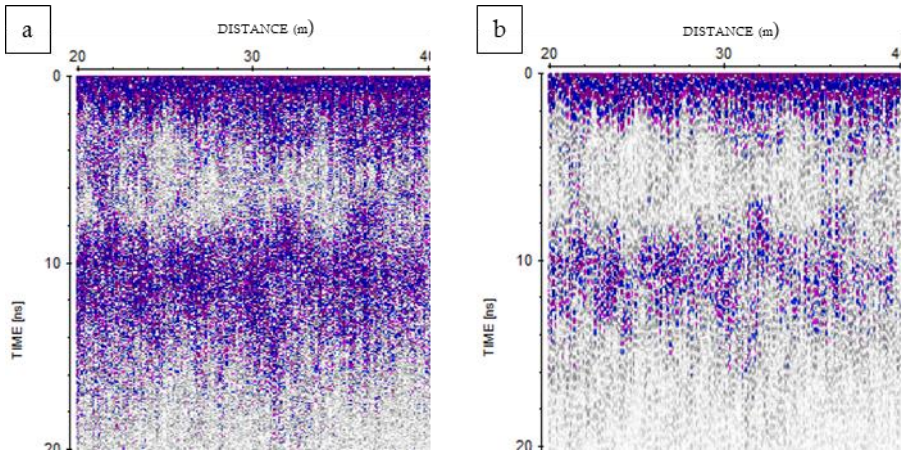

Figure 11: (b) Shows the smoothing effect of the mean filter compared to (a) an unfiltered section.

calculates the mean value over a defined time window and hence smooths the data (Cassidy 2009b). A range of 5 ns was chosen.

As a last step, a topographic correction was performed for those profiles where besides x and y coordinates also robust z coordinates were available. This step is especially helpful for the interpretation of profiles collected in longitudinal direction along the icing were significant variations in relief occurred. By correcting the topography, the subsurface reflections are shown in relation to the surface topography (Figure 62 b in the appendix). The correction was performed with the correct 3D topography function based on the altitudes saved as z trace coordinates.

4.2 Hydrochemical Sampling

4.2.1 Ice Core Samples

Five ice cores were drilled from the Rieperbreen icing on March 26th, 2017. The aim for sampling ice from the icing was to (i) investigate spatial changes of the icing stratigraphy and hydrochemistry and to (ii) validate reflections seen in radargrams by sampling along the ground-penetrating radar transects.

The sampling sites were located in three different areas of the moraine complex (Figure 12). Ice core 1 was sampled most proximate to the glacier in front moraine ridge 3. Here, the GPR survey revealed the presence of an ice layer underneath 60 cm of snow (Figure 13 b). The snow was removed before the ice was sampled. Ice cores 2 and 3 were taken down valley from sampling site 1 from the top and bottom of an inclined icing. Cores 4 and 5 were sampled between moraine ridge 2 from the top of another

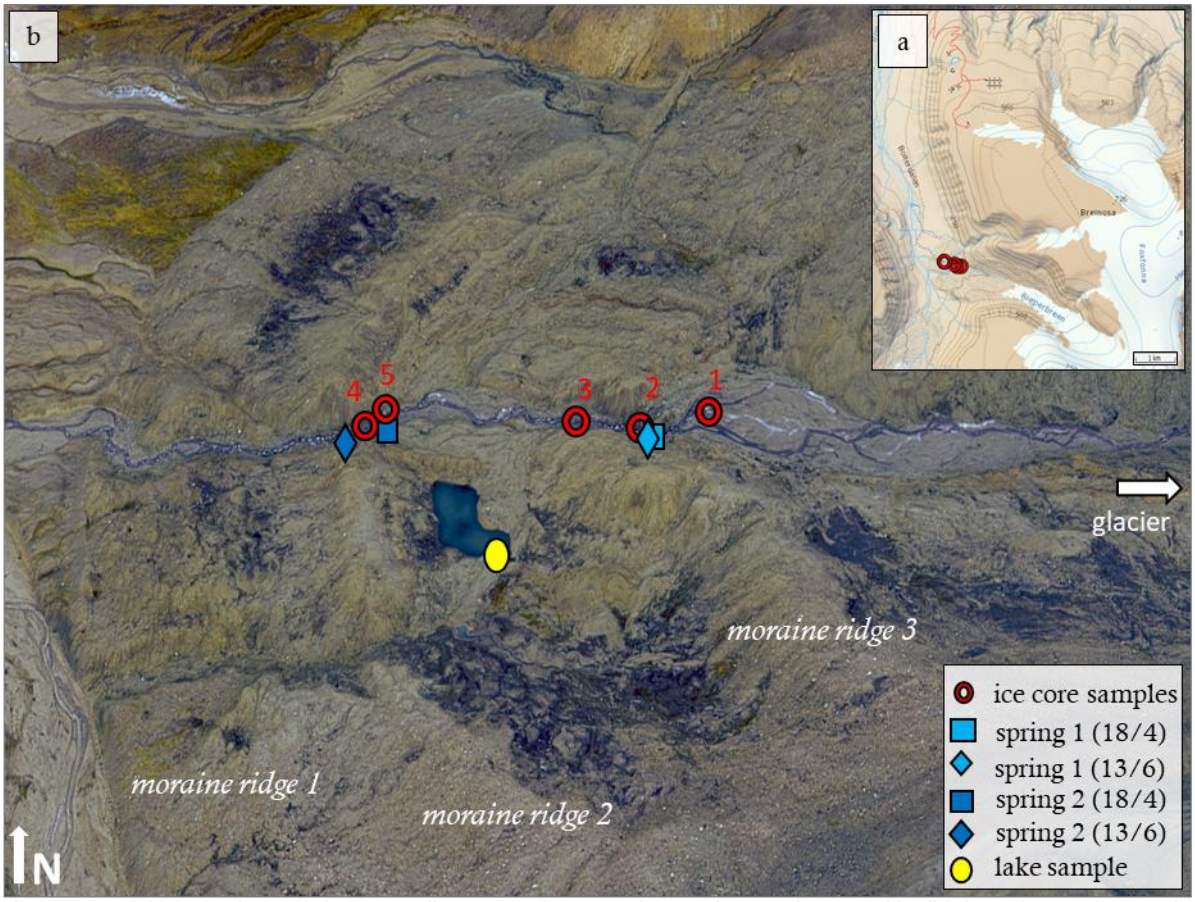

Figure 12: (a) Overview of the sampling area (Norwegian Polar Institute n.d.); (b) locations of samples for hydrochemical analyses from ice cores, springs and lake (background image: Holmlund 2016).

icing. Ice cores were obtained using a 70 cm long and 12 cm wide metal core barrel attached to a two-stroke Stihl BT 121 engine (Figure 13 a). Since the barrel did not have core dogs (teeth in the inside of the core barrel to hold the core in place) some ice cores had to be pulled out with the aid of an ice screw and a rope, others could be retrieved by hand. The top of the core pieces was marked through indents made with an ice screw before packaging for transportation (Figure 13 d+e).

4.2.2 Water Samples

The Rieperbreen icing was visited several times during the accumulation and ablation season to sample water from the springs found to feed the icing. The aim was to (i) identify the origin of water feeding the icing and link it to a water source in the catchment as well as (ii) assess the possibility of water from the lake, located within the ice-cored moraine complex close to spring 2, forming the lower icing.

On April 18th, 2017, water was sampled from two locations (Figure 12 b) where subsurface water was present below a thin layer of ice. A set of samples from the upper

spring, spring 1, was collected on top of the upper icing close to the sample site of ice core 2. Upon reaching the location, flowing water was audible and its source easily detectable. Water was exiting from the side of moraine ridge 3. A low ice dome had formed around the spring (Figure 13 a). Water flowed underneath a thin layer of ice which was punctured with the end of a core barrel. The sample location of the lower spring, spring 2, was located close to ice core 4 and 5 sample locations. Here, water was absent on the surface, however, flowing water was audible underneath a thin layer of ice. Below an injection mound the ice was punctured with the end of a core barrel (Figure 14 b). The hole quickly filled up with a water-ice melange of which the water was extracted with a syringe. On June 13th, 2017, water samples were collected from two locations (Figure 12 b). Replicates were sampled from spring 1 after removing a layer of snow (Figure 14 d). The location of spring 2 from April was then occupied by the main meltwater channel. Water was sampled a couple of meters down valley from the original sampling location after removing about 10 cm of snow (Figure 14 b+e). After June 13th, 2017, no more samples could be retrieved from the springs. During every field visit throughout the ablation season, the locations of the springs were surveyed for the presence of water other than the meltwater stream. However, the springs could not be located anymore. They have either stopped flowing during the ablation season, become undetectable due to large amounts of debris on the slopes and meltwater in the channel or, most likely, moved their location due to increased discharge through water from snow- and ice melt and cessation of pressure exerted by the icing. Upon visiting the study area on July 10th, 2017, most of the snow in the area had melted and a lake had become visible in the moraine complex (Figure 14 c+f). The lake was located south of the meltwater channel in close proximity to spring 2 and the top of the lower icing. Even though no outflow of the lake towards the icing area occurred during the ablation season, water from the lake was sampled to examine the possibility of a connection between the lake and the formation of the lower icing (lake sample in Figure 12 b).

The same sampling routine was applied during all field visits for the spring and lake samples. Water was extracted with a syringe from the source, filtered immediately through Whatman cellulose acetate syringe filters with a 0,45 µm retention into three 15 ml and one 50 ml polypropylene tubes rinsed three times with sample water for ICP-OES, ICP-MS, DOC/DIC and major ion analyses, respectively. Tubes for DOC and DIC analyses were filled to the top (17 ml) to avoid reactions with entrapped air during

Figure 13: Sampling ice cores from the Rieperbreen icing on March 26th, 2017: (a) drilling ice core 2 using a Stihl BT 121 engine and a 70cm long metal drill barrel operated by two people (Kuschel 2017); (b) location 1: sampling ice present underneath 60 cm of snow (Kuschel 2017); (c) intra icing water in drill hole from ice core 4 (Enzenhofer 2017); (d) marking the top of ice core subsample with an indent and wrapping in aluminium foil for transport (Enzenhofer 2017); (e) packed ice cores for transport from field site with pulk (Enzenhofer 2017).

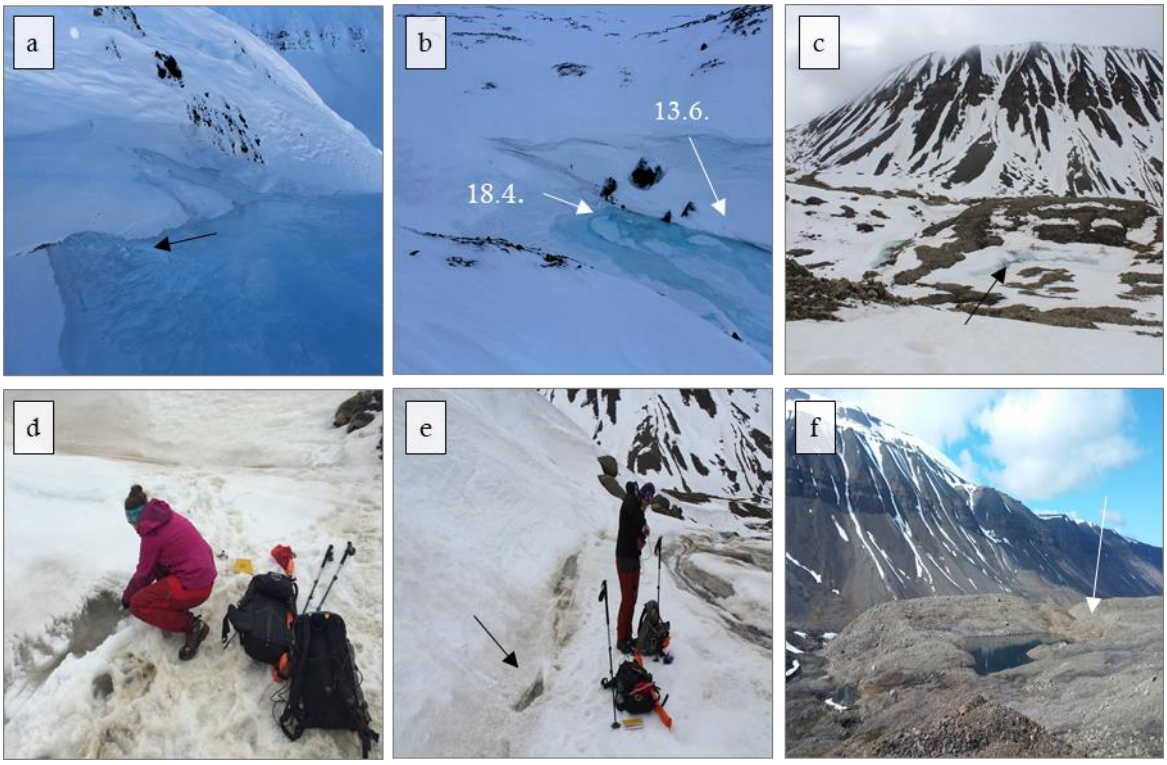

Figure 14: (a) The ice dome formed by spring 1 and the hole made in the ice for sampling on April 18th, 2017; (b) location of spring 2 as seen on April 9th, 2017. Arrows and dates indicate sample locations in April and June; (c) the arrow points at the lake first seen to be present in the moraine complex on June 13th, 2017; (d) sampling water from spring 1 on June 13th, 2017 (Peek 2017); (e) sampling locations of spring 2 on June 13th, 2017 (Peek 2017); (f) lake as seen on July 10th, 2017, when samples were collected. The arrow indicates the location of the lower icing.

storage. On April 18th, 0,1 ml of concentrated Nitric acid (HNO_3) was added to tubes for ICP-MS analyses of dissolved iron and manganese containing precisely 10 ml sample water since OPR measurements of the springs were negative. The acidification of the sample with HNO_3 prevents oxidation and precipitation in the tube during storage. Finally, a small whirl-pak bag was filled with 100 ml unfiltered water for water isotope analyses. A duplicate set of samples was taken for quality conformance tests. Collected water samples are listed in Table 2. During the remaining fieldwork and the transport back to the laboratory, the polypropylene tubes were carried in the inside of jackets to keep the samples from freezing. Since freezing does not affect the ratio of stable isotopes in the water, whirl-pak bags were transported in the backpack. All samples were stored in the fridge at UNIS until they were sent to laboratories in Leeds and Norwich for analyses.

Table 2: Summary of water samples collected from springs and lake.

location	name (date)	samples filtered (mL)				samples unfiltered (mL)
Spring 1	S 1.1 (18/4)	10 (acidified)	15	17	50	-
	S 1.2 (18/4)	10 (acidified)	15	17	50	100 ml whirl-pak
Spring 2	S 2.1 (18/4)	10 (acidified)	15	17	50	-
	S 2.2 (18/4)	10 (acidified)	15	17	50	100 ml whirl-pak
Spring 1	S 1.1 (13/6)	10	15	17	50	100 ml whirl-pak
	S 1.2 (13/6)	10	15	17	50	100 ml whirl-pak
Spring 2	S 2.1 (13/6)	10	15	17	50	100 ml whirl-pak
	S 2.2 (13/6)	10	15	17	50	100 ml whirl-pak
Lake	LA 1 (10/7)	10	15	17	50	100 ml whirl-pak

After sampling water from the springs and lake, pH, oxidation-reduction potential (ORP) and dissolved oxygen (DO) were recorded at the sampling site with a Hach multimeter of the model HQ 40D. The pH and ORP electrodes were placed directly into the surfacing water. For the measurement of DO, the hand warmed oxygen electrode was placed in a clean 50 ml tube, rinsed three times with spring water and subsequently filled up. Since this is an optical measurement, the tube was wrapped with tape and the top shielded from light by hand. During the measurement, the tube was warmed by hand to keep the water from freezing. Measurements were repeated three times for statistical quality control unless stabilization of readings took several minutes due to air temperatures far below freezing.

4.2.3 Sample Preparation and Laboratory Analyses

Ice cores were stored in a freezer of the UNIS laboratory before processing started on March 31st, 2017. 30 minutes after taking the ice cores out of the freezer, snow and

loose ice frozen to the outside was removed. Subsequently, the length of the cores and the width of layers composed of different ice types, was recorded. Each core was divided into ~10 cm wide subsamples using a metal saw, unless smaller pieces broken from the core were used as subsamples or subsamples were shortened or lengthened according to different ice types. 26 subsamples were obtained and melted at room temperature in individual glass beakers covered with plastic foil. Once all ice had melted and the temperature of the water adjusted to room temperature, EC and pH was measured using a VWR pHenomenal multi parameter instrument of the Model MU 6100H with previously calibrated EC (CO 11) and pH electrodes (phenomenal 11).

Figure 15: Filter papers of subsamples from ice cores 1 (upper left) to 5 (lower right) before drying.

Subsequently, 26 Whatman glass fibre microfilters of the type GF/D and a 2,7µm retention were weighted on an analytical balance with a 0,0001g readability and placed into prelabelled plastic bags. The water of each subsample was filtered through the correspondent filter paper (Figure 15) into a clean beaker to avoid chemical reactions during storage. For the analyses of the suspended sediment concentration (SSC) in the subsamples, the filter papers were dried in the oven at 105°C for one hour, set aside for two hours to cool and absorb atmospheric moisture before they were weighted on the same balance as the unused papers before. Since the measurements yielded unreasonable values (presumably due to a too large volume filtered through the papers), the results of SSC were excluded from further analyses and interpretation. For hydrochemical analyses, four 15 ml polypropylene tubes and one 30 ml glass vial were filled from each subsample. The glass vial was filled to the top with sample water and closed without entrapping air to avoid reactions during storage. All samples were stored in the fridge at +5°C until half of the samples were transported to Sheffield for analyses. The other half of the samples was kept in storage at the UNIS laboratory as backup.

Samples of ice core water were analysed by the laboratory of the Geography Department at the University of Sheffield. First, the concentration of NH_4 and Si were determined colourmetrically using an unopened sample vial and a Skalar Autoanalyser. Then, the concentrations of key ionic species (Na, K, Mg, Ca, F, Cl, NO_3

and SO_4) were measured with a Dionex ICS-90 Ion Chromatography System (Thermo Scientific). The abundance of dissolved organic carbon (DOC) and dissolved inorganic carbon species (HCO_3^- and CO_3^{2-}, whereas ratio is pH dependent, hereafter referred to as DIC) was quantified using the Membrane Conductometric Detection method on a Sievers 5310 C TOC Analyser. The detection limit for this analysis was 0,01 mg l^{-1} and the precision error < 5%.

The concentration of trace elements and metals in spring and lake samples were analysed by the Laboratory of the School of Earth and Environment at the University of Leeds. Inductively Coupled Plasma Optical Emission Spectrometry (ICP-OES: iCAP 7400 ICP-OES, Thermo Fisher Scientific) was used to measure the abundance of K, Ca, Na, Mg, S, P and Inductively Coupled Plasma Mass Spectrometry (ICP-MS: iCAP Qc ICP-MS, Thermo Fisher Scientific) for Al, Ti, V, Cr, Mn, Fe, Co, Ni, Cu, Zn, As, Sr, Cd, Pb and U. Before analyses, all pre-acidified samples from April (1 ml concentrated, reagent-grade HNO_3 into 10 ml syringe-filtered sample) were diluted 1:5 with deionised water. Internal reference standards were run throughout all analyses (1ppm Y for ICP-OES and 1ppb Rh for ICP-MS). Where the concentration of certain elements was above the range of calibration, the samples were further diluted 1:100 and the analyses repeated. The concentration of anions in water samples was analysed in the same way as for ice core samples. The concentrations of NH_4 and Si colourmetrically using an unopened sample and a Skalar Autoanalyser and F, Cl, SO_4, NO_3 and PO_4 with a Dionex ICS-90 Ion Chromatography System (Thermo Scientific).

Unfiltered water samples from springs and the lake were analysed for the abundance of stable water isotopes (δ^2H and $\delta^{18}O$) by the Stable Isotope Laboratory of the University of East Anglia. Repeated analyses were performed with a Finnigan DELTAplus XP Isotope Ratio Mass Spectrometer (Thermo Fisher Scientific).

4.2.4 Quality Assessment and Geochemical Calculations

The limit of quantification (LOQ), the minimum concentration of an element that can be quantified, was calculated as:

Eq. 24

$$LOQ = 10 * stdev$$

where the standard deviation (*stdev)* was calculated from 6 replicate blank solutions. The percentage of uncertainty of the analyses was determined by calculating the 95% confidence interval of 6 certified quality control standards measured throughout the analyses. LOQ and uncertainty varied for all measured ions and are listed in Table 3 for ICP-OES and ICP-MS analyses.

Besides measuring the concentration of DIC in ice core samples with the Sievers conductometric analyser, DIC was also calculated from charge balance as sum of cations (Ca^{2+}, Mg^{2+}, Na^{+}, K^{+}, NH_4^{+}) less the sum of F^{-}, Cl^{-}, NO_3^{-} and SO_4^{2-} after converting to equivalent units of concentration. Figure 16 (a) indicates a robust, statistically significant linearity between the calculated and measured DIC values (R^2 = 0,979). The slope of >1, however, indicates an accuracy problem either with the measured or calculated value. Measured DIC may be biased due to analyses conducted from previously opened samples which had sufficient time to adapt to the atmospheric equilibrium. Inaccuracy in calculated values arise from the sensitivity of the charge balance method to the charge of ions. In a solution with a pH > 8, as measured in ice core meltwater, DIC is present as HCO_3^{-} and CO_3^{2-} with a charge of one and two, respectively. DIC was, however, calculated as HCO_3^{-} only. Quantifications of DOC and DIC in water samples through the Membrane Conductometric Detection method on a Sievers 5310 C TOC Analyser yielded unrealistic values due to a much higher concentration of DIC compared to DOC. Hence, no DOC values are available for the water samples and DIC was calculated from charge balance as the sum of the concentrations of Na^{+}, K^{+}, Mg^{2+}, Ca^{2+}, NH_4^{+} and Sr^{2+} less the sum of Cl^{-}, SO_4^{2-}, F^{-} and NO_3^{-}, in equivalent units of concentration, whereby NO_3^{-} and Sr^{2+} was only included in the calculation for June spring and lake samples since concentrations in April samples were < LOQ.

The Charge Balance Error (CBE %), a measure of data quality, was calculated for ice core samples from the sum of cations (Ca^{2+}, Mg^{2+}, K^{+}, Na^{+} and NH_4^{+}) and anions (Cl^{-}, NO_3^{-}, F^{-}, SO_4^{2-}, and measured DIC) as in Eq. 13. CBE for ice cores ranges between 7,5% to 21,7% (Table 13). The values are significant in some cases due to the importance of carbonate and bicarbonate anions, but uncertainty exists over their relative importance. CBE (%) for water samples was calculated from the sum of anions F^{-}, Cl^{-}, SO_4^{2-}, DIC and NO_3^{-} and cations NH_4^{+}, Mg^{2+}, K^{+}, Na^{+}, Ca^{2+} and Sr^{2+}. Values range between -2,65% to 11,68% (Table 15). Standard deviations of replicate samples are low for April samples with 0,17 and 1,07 for spring 1 and spring 2, respectively and

Table 3: Limit of quantification (LOQ) and uncertainty (%) for quantified ions through ICP-OES and ICP-MS.

	all mg L^{-1}						all µg L^{-1}															
	K	Ca	Mg	S	P	Ti	Al	V	Cr	Mn	Fe	Co	Ni	Cu	Zn	As	Sr	Cd	Pb	U
LOQ	2,1E+0	1,7E+0	1,7E+0	4,1E+0	1,1E-01	1,5E-01	1,7E-01	7,2E+0	4,4E-01	3,4E-01	2,3E+0	8,8E-02	1,8E+0	4,2E-01	2,2E+0	3,6E-01	1,4E+0	8,8E-02	5,3E-02	4,1E-02
% Uncertainty	0,90	0,81	1,00	1,55	0,93	1,06	2,00	4,04	1,55	1,81	3,19	2,92	1,64	1,26	2,22	2,54	2,10	0,70	1,74	1,31

higher for the June sample from spring 1 (7,03). CBE was not calculated for the June sample of spring 2 due to erroneous concentrations of Na^+, K^+, Mg^{2+} and Ca^{2+} which were excluded from further analyses. CBE is within the acceptable error range of <±5% (Freeze & Cherry 1979) for April samples but above in June sample with 11,68% and 7,32% for spring 1 and 2, respectively. This likely indicates a higher sensitivity to imbalances of these solutions due to lower concentrations of solutes (Zhu & Anderson 2002).

Total dissolved solid (TDS) content was calculated for ice cores as the sum of NH_4^+, Si, Na^+, K^+, Mg^{2+}, Ca^{2+}, F^-, Cl^-, NO_3^-, SO_4^{2-}, and HCO_3^- (from charge balance) and estimated to indicate minimum values due to missing concentrations of metals. TDS controls the electrical conductivity (EC), hence, these parameters were compared for quality assessment. Since the EC of melted ice core samples was measured at varying water temperatures, the value was first corrected to 25°C (Eq. 15) assuming a linear temperature coefficient of 2% per degree Celsius (Hayashi 2004). Calculated EC (25°C) and TDS values were highly correlated (R^2 = 0,9957) (Figure 16 b). TDS for spring samples was calculated as the sum of all ion species listed in Table 3 plus NH_4^+, Si, Na^+, F^-, Cl^-, SO_4^{2-}, $NO_3^-$and DIC.

Saturation indices (SI) for minerals and CO_2 were calculated using WEB-PHREEQ (Saini-Eidukat & Yahin 1999), the web application of PHREEQC for aqueous geochemical modelling, with the phreeqc database. Input parameters were the observed pH values, measured with a VWR pHenomenal, and concentrations (4 decimal places) of Ca^{2+}, Cl^-, F^-, Mg^{2+}, K^+, Na^+, Si, N (as NO_3^-), S (as SO_4^{2-}) and C in mmol l^{-1} for ice core samples and additionally Al, Cd, Cu, Fe, Pb, Mn, P, Sr^{2+} and Zn for water samples. DIC was calculated from charge balance and defined as C. A constant temperature of 0,0°C was assumed.

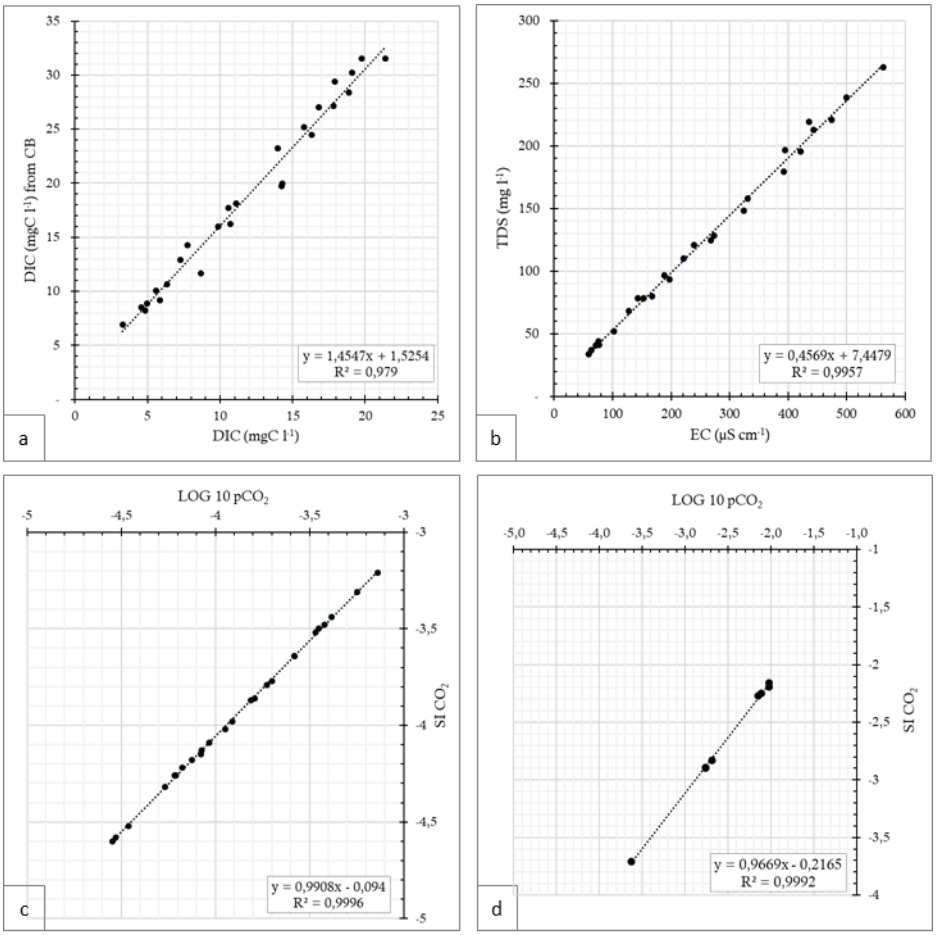

Figure 16: (a) Correlation between measured dissolved inorganic carbon (DIC) and DIC calculated from charge balance for ice core sub-samples; (b) correlation between total dissolved solids (TDS) and electrical conductivity (EC) at 25°C of ice core sub-samples; (c) correlation between calculated partial pressure of CO_2 (LOG 10 pCO_2) and saturation index (SI) of CO_2 for ice core sub-samples; (d) correlation between calculated partial pressure of CO_2 (LOG 10 pCO_2) and saturation index (SI) of CO_2 for water samples. All R^2 values indicate a high correlation and further good data quality of ice core and water samples.

Partial pressures of CO_2 (pCO_2) at 0°C was calculated for ice core sub-samples and water samples using Eq. 11, where HCO_3^- , in mmol l^{-1}, was assessed from charge balance. Since gases were included in the SI calculations, calculated pCO_2 was also compared to the more comprehensive pCO_2 through WEB-PHREEQ. Comparison of values from both methods shows a high correlation for ice cores (R^2 = 0,9996) (Figure 16 c) and water samples (R^2 = 0,9992) (Figure 16 d).

4.3 Dye Tracing

Dye tracing experiments were performed on Rieperbreen from August 20th to August 23rd, 2017. This method was used primarily to (i) detect whether the hydrologic system of Rieperbreen and the upper spring are connected through a flow path other than the

main meltwater river, to (ii) study the connection between supraglacial channels and the proglacial river and (iii) to characterise the englacial drainage system.

4.3.1 Experimental Setup

Due to the primary objective, two gauging stations were set up in the proglacial river. Station 1, the upper station, was located close to the glacier terminus and station 2, the lower station, downstream from the sample location of spring 1 during the previous months (Figure 17). The straight-line distance between these two stations was about 1 km. By comparing the dye return curves recorded from the two stations, it was expected to detect if all injected dye leaves the glacier through the portal or if a flow path exists routing dye into the meltwater channel downstream of station 1. A period in late summer was chosen for the experiments since the drainage system is best developed towards the end of the ablation season.

For automatic measurements of the dye emergence, gauging stations were set up on August 20th consisting of a fluorimeter (Cyclops 7; Turner Designs), with the sensor placed in a shake cap, wired to a Campbell Scientific CR1000 data logger and a 12V battery powering the instruments (Figure 18 a). The instruments were transported into the field separately and wired after choosing an appropriate site. Requirements for the locations of the stations were an area with constrained flow in one stable channel and water deep enough to ensure continuous submergence of the sensor even during low discharge. Additionally, the data logger had to be placed far enough from the slopes of the valley to prevent destruction through small mass movements. Once such location was found, the fluorimeter was wired to the data logger and submerged in the middle of the channel with the sensor facing upstream. To remove air bubbles entrapped inside the shake cap and potentially impairing measurements, the sensor was shaken strongly several times under water. Rocks were placed at the end of the fluorimeter to secure the sensor in the water. Few drops of dye were poured into the stream above the sensor to test if the instruments worked properly. When the gauging station was operational, the data logger was placed in a plastic box and a heavy-duty bag which was taped tight around the wires to protect the sensitive electronics against water. To avert animals (arctic foxes) from chewing on the cable of the fluorimeter, it was covered with rocks. The lower station started measuring the fluorescence on August 20th at 12:56 and the upper station at 14:16. Every 30 seconds the data logger

stored the average value calculated from measurements taken every 10 seconds. The stations were operational until August 28th.

4.3.2 Dye Tracing Experiments

Six dye tracing experiments were carried out between August 20th and 23rd to study the connections between three injection points on the glacier and one in the proglacial river with the stations. The input sites were chosen to understand changes of the drainage system with increasing distance and altitude from the terminus. The straight-line distances from station 1 ranged between 128 to 1830 m and elevation differed ~200 m between injection points (Table 4). A known quantity of Rhodamine WT dye with 20% active ingredient was used as tracer for all experiments. The dye was ordered ready-made as a liquid from Town End (Leeds) plc. The amounts injected into flowing water ranged between 20 – 150 ml. Relatively large amounts of dye were used in this study compared to the only other published dye tracing experiment on Rieperbreen by Gulley et al. (2012) where 10-25 ml Rhodamine WT of the same concentration were injected. Since station 2 was located about 1 km further downstream than the fluorimeter in the Gulley et al. (2012) study, larger amounts were used to detect a signal at station 2 after hydrologic dispersion of dye in the proglacial river. Further, in case dye was transported through a flow path connected to spring 1, the discharge was

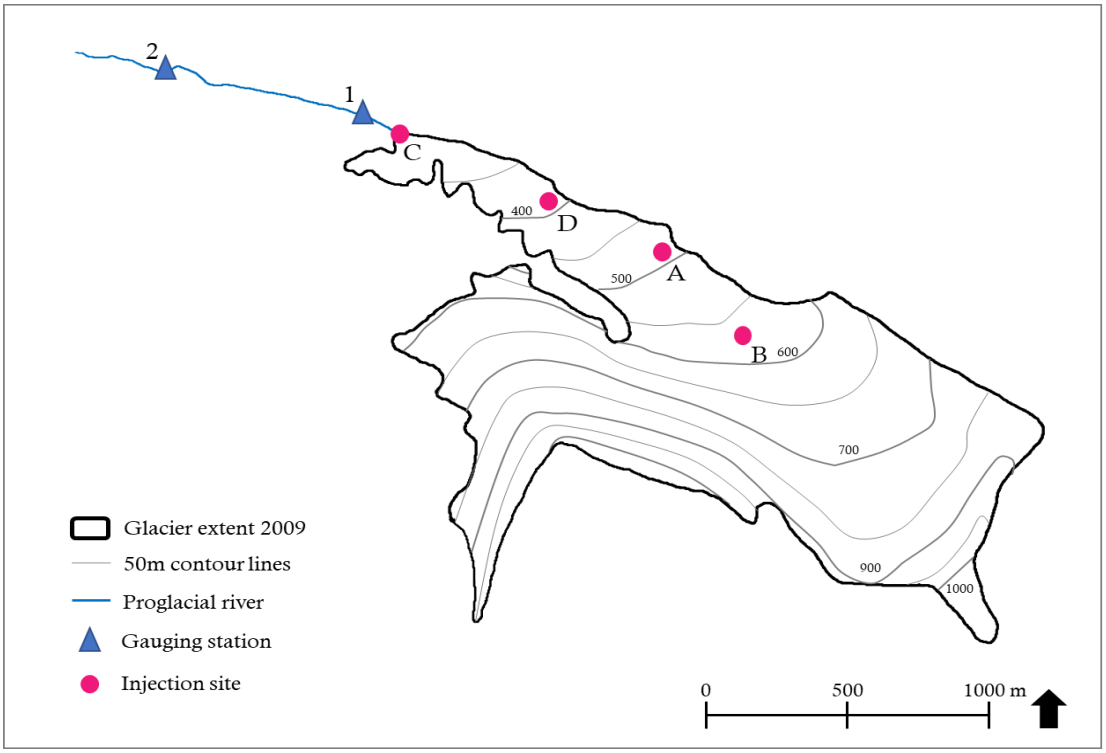

Figure 17: Location of gauging stations (1 = upper station; 2 = lower station) and injection sites. Three injections were performed in point A and one in points B-D (glacier extent: topographic map from TopoSvalbard, Norwegian Polar institute).

expected to be very small and therefore, large amounts of dye were used. After setting up the gauging stations on August 20th, the surface of Rieperbreen was investigated for appropriate injection sites where supraglacial meltwater streams disappear into the interior of the glacier through a moulin. Gulley et al. (2012) described the existence of several moulins along the northern margin of the glacier snout in 2010. These moulins were not formed by hydrofracturing of crevasses but are the upstream openings of cut-and-closure channels.

The procedure of the dye injections was the same in all tests. A known quantity of Rhodamine WT dye with 20% active ingredient was poured into a supraglacial stream disappearing through an opening in the glacier a short distance away. The containing the dye were rinsed until all dye had been transferred to the stream. Ice on the sides of the channels, which had absorbed some of the dye, was loosened with crampons and added to the stream. A supraglacial stream on the northern side, disappearing into the glacier through a hole in the roof of a cut-and-closure channel at 488 m a.s.l., was chosen as first injection site (letter A in Figure 17). At 16:26 100 ml Rhodamine WT were poured into the supraglacial stream at a safe distance from the hole (Figure 18 b). The englacial channel was seen to already carry a significant amount of water to which the dye was added by the supraglacial stream. Another cut-and-closure channel was discovered further up glacier. The closest accessible point upstream of the englacial channel at 568 m a.s.l. was chosen as second injection site (letter B in Figure 17). Water was flowing underneath a thin layer of ice which was removed with crampons. To avoid an overlap of this experiment with the previous one, an hour was waited before the next dye injection. At 18:02, 100 ml Rhodamine WT were poured into the stream underneath a water pool to prevent temporary dye storage at the injection site (Figure 18 c). The third dye injection took place on August 22nd at 16:45.

Table 4: Summary of dye tracing experiments.

Code	Injection Site	Location	Elevation (m)	Julian Day, Injection Time	Amount (ml)
1	A: Supraglacial stream	N78°07.139'; E16°07.377'	488	232, 16:26	100
2	B: Supraglacial stream	N78°06.945'; E16°08.302'	568	232, 18:02	100
3	A: Supraglacial stream	N78°07.139'; E16°07.377'	488	234, 16:45	100
4	C: Proglacial stream	N78°07.458'; E16°04.621'	293	235, 13:57	20
5	D: Moulin	N78°07.295'; E16°06.065'	364	235, 14:47	130
6	A: Supraglacial stream	N78°07.139'; E16°07.377'	488	235, 15:30	150
Station 1 (up)	-	N78°07.485'; E16°04.327'	286	-	-
Station 2 (down)	-	N78°07.631'; E16°01.849'	225	-	-

100 ml dye were injected by students from the UNIS AG-340 course in the same location (A) as the first dye injection two days before. During the next field visit on August 23rd, the two stations along the proglacial stream were checked for operativeness. The fluorimeters were still submerged and the recording of the measurements continuous. A first set of data was downloaded onto a field laptop. At the lower station, a quick analysis showed that dye return curves were recorded. Nothing was changed at this station. At the upper station, a first analysis indicated that the recorded signal seemed to be very faint. Therefore, the sensitivity of the fluorimeter was increased tenfold from 13:35 onwards. Further, three dye tracing experiments were performed that day.

An interesting feature was found while walking from the upper station towards the glacier along the proglacial stream. The meltwater stream disappeared behind the station for about 120 m underneath a former part of the glacier snout that is now disconnected to the present glacier and covered with debris. Behind this feature the

Figure 18: Dye tracing experiments at Rieperbreen: (a) wiring fluorimeter and data logger and setting up the gauging station (Bergsman 2017); (b) injection site A for experiments 1, 3 and 6 (Enzenhofer 2017); (c) dye injection for experiment 2 into a channel that had already started to freeze; (d) adding Rhodamine WT to the proglacial stream before it disappears underneath a former, now disconnected, part of the glacier snout for experiment 4 (Coumou 2017); (e) 5th dye injection into a supraglacial stream flowing into a moulin (Moran 2017).

stream was visible all the way to the glacier portal. At 13:57 20 ml dye were added to the proglacial stream (location C) before it disappears underneath the ice (Figure 18 d) to detect if a direct connection to the stream at the upper station exists or if a part of the water is also routed towards the southern ice-cored moraine. Upon walking on the glacier, a big moulin was found on the northern side at 364 m a.s.l. (location D). Even though the surface of the biggest channel leading into the moulin was already frozen, water was still flowing underneath an ice layer. The ice was broken with crampons and 130 ml dye were injected into the channel at 14:47 (Figure 18 e). The 6th and last dye injection took place at 15:30. 150 ml dye were poured into the supraglacial channel at location A as for the injections 1 and 3. The amounts of injected dye were increased for the last two measurements since discharge had decreased due to colder air temperatures and the recorded signal at the upper station was believed to be faint. In order to record the dye return of the last experiments, the stations remained in the field for a couple of days until removal on August 28th at 14:45 (upper station) and 15:31 (lower station).

4.3.3 Data Processing

First investigations of the data showed that the stations worked continuously from August 23rd – August 28th. A total of 23.094 measurements of the fluorescence in the proglacial river were recorded at the upper and 23.354 at the lower station. Some adjustments were performed before visual and numerical analyses. Measurements taken while the stations were set up on August 20th, readjusted on August 23rd and dismantled on August 28th were deleted from the files. Since the sensitivity of the fluorimeter at station 1 was increased tenfold on August 23rd at 13:35, a comparison of dye returns recorded before and after this point was problematic. By calculating the average of the last 5 values recorded before the increase (35,94 mV) and after the increase (189,08 mV), the difference was found to be 5,3 mV on average rather than tenfold. Therefore, all values of fluorescence recorded at station 1 after 13:35 were divided by the factor 5,3 and could hence be compared to the previous values.

To compare values from the two used fluorimeters, a calibration curve was calculated from three measurements performed with both sensors. For additional evaluation of the influence of natural background fluorescence, turbid water from Bolterelva, the river located in Bolterdalen which is among other sources fed by Rieperbreen, was collected on August 31st. First, the fluorescence of 500 ml sediment rich river water was

measured. After adding 500 ml tap water, a second value was noted down. For the third measurement, few drops of Rhodamine dye and 2 L tap water were added to the sample. By plotting the three values measured by the fluorimeter used at station 1 against the values of the fluorimeter from station 2, a simple linear regression of y = 1,1492x + 6,2629 was calculated (Figure 19). The formula was applied to correct the measured fluorescence values at station 1 (y = 1,149 * Station 1 + 6,2629).

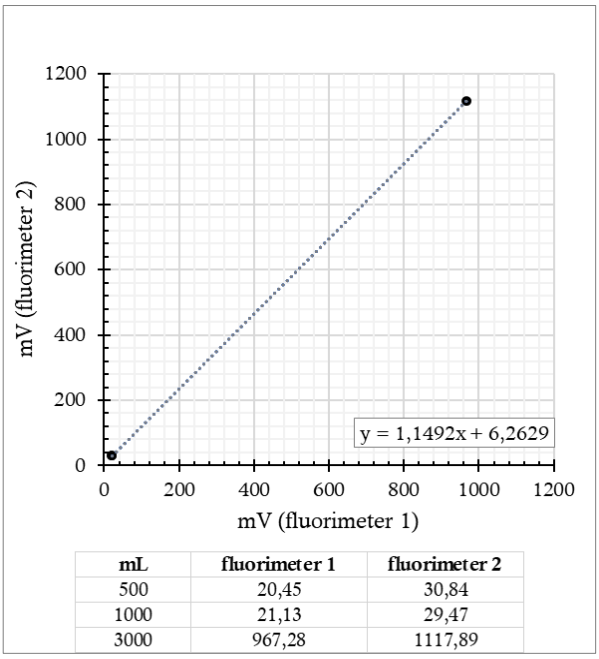

mL	fluorimeter 1	fluorimeter 2
500	20,45	30,84
1000	21,13	29,47
3000	967,28	1117,89

Figure 19: Calibration line for the two fluorimeters used in the dye tracing experiments. Fluorimeter 1 was located at station 1 and fluorimeter 2 at station 2.

5 Results

5.1 Location and Morphology

During the accumulation season of 2016/17, the Rieperbreen icing formed in the main meltwater channel cutting through the frontal moraine complex whereas the glacier proximal icing was located about 1 km from the terminus of Rieperbreen. By comparing the location and extent of the icing seen on older aerial photographs (Figure 45 c+d) with the field observations during the winter of 2017, a location change of the icing is discernible. In 2017, the icing did not form on the outwash plain located in front of moraine ridge 3 and with, as to date, not recorded impressive volume down valley of moraine 2. The icing covers large areas of the ~500 m long narrow valley cutting through moraine ridge 2 and 3 (Figure 12). The first visible icing area extended ~70 m from the distal side of ridge 3 down to an area with flat topography between ridge 2 and 3. The top part of the icing had a gentle slope which increased with distance down valley. A second icing was visible with its uppermost end between ridge 2, occupying the entire valley down to the LIA moraine. No ice could be found to have formed in the valley leading towards the glacier between moraine ridge 3 and the present glacier front.

Significant changes of the icing morphology occurred during the accumulation season and between winter and summer. During the accumulation season, the icing surface was light-blue in colour and underwent fast morphological changes (Figure 49) in March and April when the icing area increased markedly in longitudinal and lateral direction. In late March, the icings had a flat surface with areas of deep snow slush surrounding the edges. Upon the next visit in the beginning of April, the snow slush was already incorporated into the icing through growth in all directions. Snow on the valley slopes above the visible icings was observed to slide off (as seen in Figure 49, picture 5), attributed to a destabilizing effect conditioned by icing growth underneath. Along the valley slopes, the icing grew to a slightly higher elevation than in the centre. This process is explained through pressure induced by the icing (van Everdingen 1982a) and the restricted area given by the morphology of the location. Sub-icing water is pushed to the valley sides where it freezes at steadily increasing elevation upon surfacing. Movement of the spring feeding the upper icing to a higher elevation between March and mid-April is also explained by pressure exerted onto the ground

through the ice mass. While only one injection mound was present at the end of March on top of the lower icing, number and size of mounds increased with advancing accumulation season, as did cracks in the icing surface adjacent to the mounds (Figure 49 picture 4+7). The fast growth during April was accompanied by a notable presence of water at the top parts of the two icings. Water was not only audible underneath the ice, but also flowed across the icing as sheet flow. Through cracks in injections mounds, water reached the surface and froze within short distance from the exit point due to air temperatures far below 0°C.

With the onset of the ablation season in the beginning of June, the colour of the icing changed from light-blue to a dirty-white, thereby complicating the differentiation from the surrounding snow. As the icing ablated, needle ice with a length of up to 5 cm became visible on the surface (Figure 47 a). Since the icing is located in the valley occupied by the main meltwater river of the catchment, it was eroded quickly through incision, undercutting and bank erosion of the river. At the end of the ablation season, the icing was not visible anymore. Hence, the Rieperbreen icing is a periodic feature. Only marginal areas could persist throughout the melt-season through a debris layer transported onto the icing by mass wasting from the valley sides, burying and preserving the ice underneath. After the icing had ablated, white precipitates remained on the valley slopes indicating the former presence of an icing and provided an estimate of its extent (Figure 47 b).

5.2 GPR

GPR surveys were performed to investigate the overall extent of the Rieperbreen icing, sub-surface connections between icing areas visible during winter, its internal morphology and thickness and to locate the spring(s) feeding the icing.

5.2.1 GPR Surveys

A total of 1500 m of GPR profiles from the icing itself and adjacent areas are presented in this study: 10 radargrams obtained on March 26th and 13 from April 9th, 2017 (in the appendix from Figure 51 onwards). Locations of ice cores taken along GPR profiles are indicated with red arrows in the corresponding radargrams. The maps of Figure 20 illustrate the location of GPR transects and the division of the study site into area 1, 2 and 3, as further referred to in the analyses. Area 1 was investigated thoroughly during both surveys (GPR profiles 1-6 and 14-18) because the top of the icing and the spring

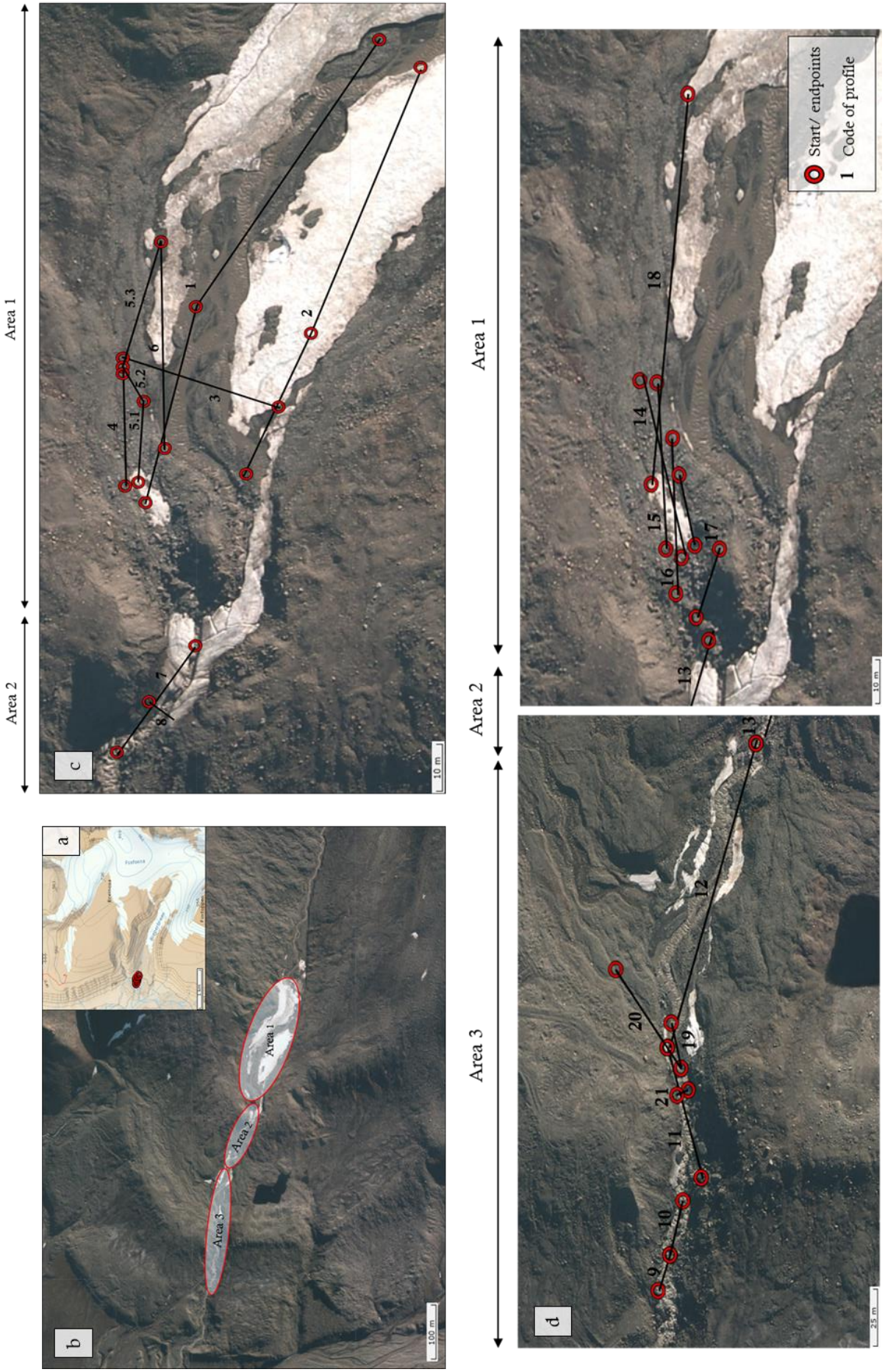

Figure 20: Location maps of GPR surveys: (a) survey area in the forefield of Rieperbreen; (b) breakdown of the study site into area 1-3; icings were visible in area 2 and 3; (c) Overview of collected GPR profiles on March 26th, 2017. Nine profiles were recorded in area 1 and two in area 2. (d) Radar profiles collected on April 9th, 2017. Five profiles were recorded in area 1, one in area 2 and seven in area 3.

forming the icing were assumed to be located in this part of the forefield, although the surface was covered with snow and no icing visible. Area 2 was surveyed in March and April and is represented by GPR profiles 7, 8 and 13. GPR profiles from area 3 were recorded on April 9th (profiles 9-12 and 19-21).

Figure 21 is an example of the obtained radargrams. While the first x-axis (left) shows the two-way travel time (TWTT) of the radar wave (in ns), the second axis indicates the depth (in m). In this study, the travel velocity of the radar wave was neither calculated through a CMP survey nor through another method. Further, due to several materials present in the subsurface, a structural velocity routine was not feasible in the given setting. To determine the depth from the TWTT, a wave propagation velocity of 0,145 m ns^{-1} was applied for icing profiles from area 2 and 3, the mean value measured in a seasonal icing by Moorman & Michel (2000). Stachnik et al. (2016) used a similar travel velocity of 0,15 m ns^{-1} through an icing. Due to a thick snow cover and the questionable presence of ice in area 1, the depth of profiles was calculated with a higher wave propagation velocity of 0,21 m ns^{-1} obtained for snow in Clair & Holbrook (2017). The depth of the basal reflector (ice or debris) in the radargrams corresponds with snow depths measured from snow profiles and probing. Further, the stratigraphy of ice cores sampled along the profiles aligns with low frequency reflections recorded in radargrams collected from the icing. Therefore, despite present uncertainty regarding the travel velocity, the depth and thickness of features is evaluated to yield a good estimate.

Reflection and scattering of the radar waves at the interfaces of materials with different electrical properties (Table 1) results in a divergence of the wave amplitude. The polarity of the divergence of the returning wave can be visualized through different colours depending on the chosen colour scheme. In this study, two different schemes were used ranging from blue, indicating negative divergence, over yellow (for example Figure 21) or white (Figure 51) to pink for a positive divergence. The strength of the returned signal (amplitude) is dependent on the electrical permittivity and electrical conductivity of the materials present in the subsurface. The higher the contrast of these electrical properties at the interface of different materials, the higher the amplitude of the reflection and vice versa. Further, the amplitude is subsequently decreased with increasing depth of the reflectors through scattering, absorption, attenuation and geometrical spreading (Hubbard & Glasser 2005). The polarity of reflections helps to differentiate between materials present in the subsurface (Figure 21). Given the used

orientation of the antenna, with the receiver located behind the transceiver, a red-blue-red pattern is created by reflections composed of three half cycle wavelets with a + - + polarity which indicate the interface of a material with a lower permittivity overlying a material with a higher permittivity, such as air-ice, ice-sediment, ice-water, snow-ice or snow-water interfaces. A blue-red-blue colour pattern or reflection with a - + - polarity is created when the upper layer at an interface exhibits a higher permittivity than the underlying one as is the case at the boundary between ice-air, sediment-air or water-ice. However, from the polarity alone, the type of material located at both sides of the interface cannot be determined. Therefore, the nature of the reflection must be interpreted in context with the location. Multiple wavelet reflections within the icing can be caused by the presence of channels. The first 3-wavelet signal is produced when the wave enters and the second when it leaves the channel. From the polarity of these two reflections, the nature of the channel can be deduced. A channel filled with water

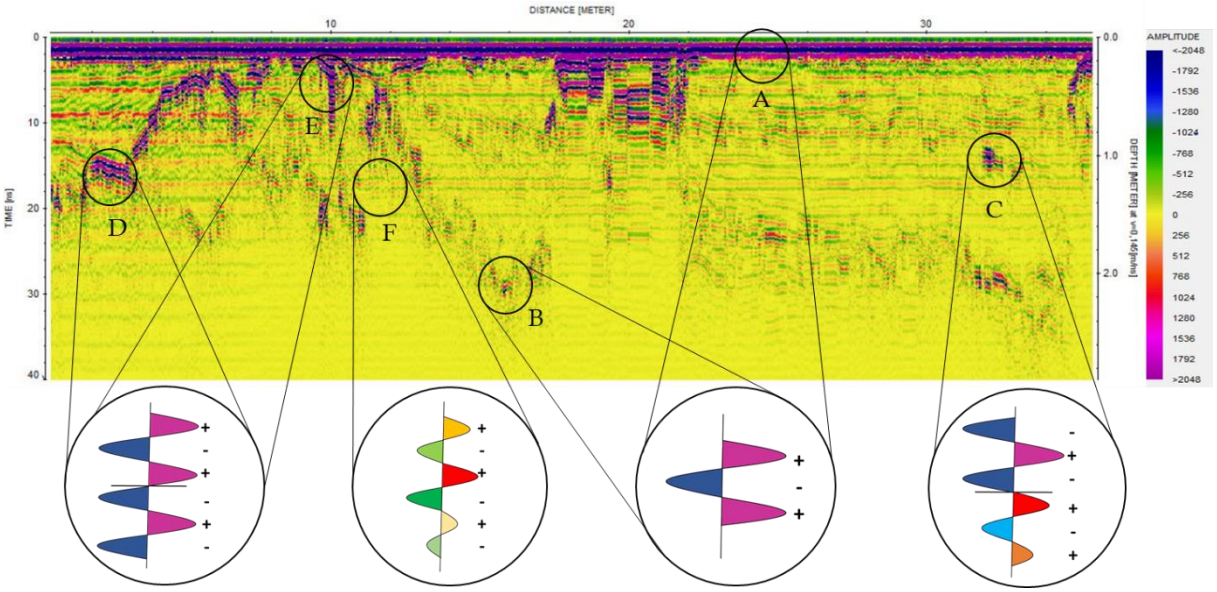

Figure 21: GPR profile 7, recorded from the icing in area 2, aids as example of collected radargrams found in the appendix. This colour scheme facilitates the interpretation of the polarity of reflections by containing more subdivisions for amplitude values than radargrams in the appendix. A) Wavelet with a + - + polarity present at the top of all radargrams shows the air-ice interface in radargrams from the icing or the air-snow interface in area 1. B) + - + reflection at the bed found as quasi-continuous linear reflections in profiles recorded in area 1 and discontinuously from icings in area 2 and 3. These three-wavelet signals show the interface between the ice or snow body and the geologic materials of the bed. C) Strong internal reflectors are absent in area 1 but often present within radargrams from the icing, here with a - + -/+ - + polarity interpreted as air-filled void. D) Multiple reflection at a dipping interface. The initial wavelet shows a + - + polarity which is immediately followed by a - + - reflection. Such signals may be caused by a water film at the base of the icing or snow pack but also by a water- or sediment-filled void. E) Strong reflections at the top after the arrival of the ground wave are frequently present in radargrams from the icing and interpreted as water film on the surface. The water further causes a ringing and a penetration of the signal to greater depths as multiple reflections. F) Example of low amplitude reflections composing most areas of the radargrams. Reflections are caused by different air/water content of layers within the snow pack and interfaces of bubble-rich and clear ice sections composing the icing.

produces a + - + (icing - water filled channel) - + - (water filled channel - icing) signal. An air-filled internal void is identified through a - + - (ice-air) + - + (air-ice) reflection. On the actively forming icing, water was frequently present on the surface. Since the wave first travels through the air before entering the icing, surface water is indicated by a + - + (air-water) - + - (water-ice) reflection. All highlighted reflections were checked in the original data since processing included applying a de-wow filter. De-wow filtering can lead to the creation of a precursor in front of a reflection (Figure 22).

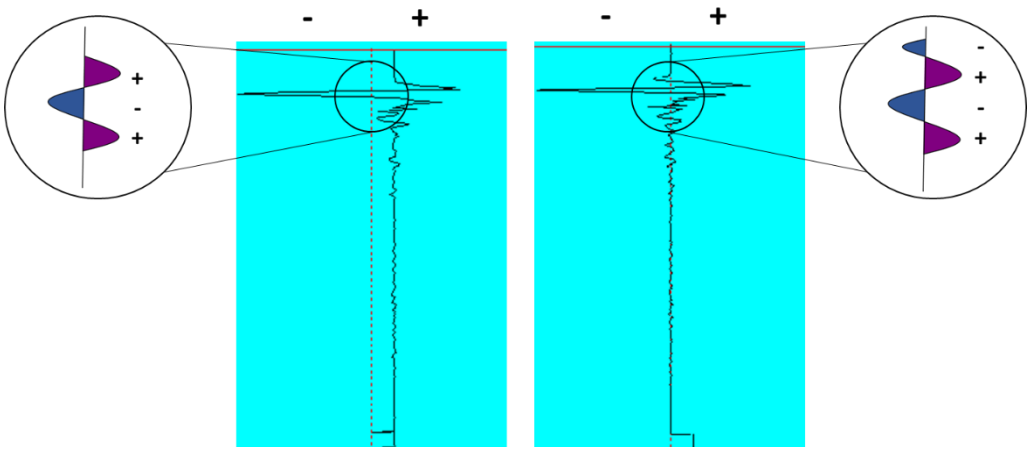

Figure 22: shows the same radar wave before (left) and after (right) applying a de-wow filter. Magnified is the arrival of the ground wave. The subtraction of the calculated mean value can lead to the creation of a precursor with a different polarity absent in the unprocessed data.

Radargrams from area 1 differ significantly from the ones recorded in area 2 and 3. In area 1 internal reflectors often extend over several metres and are aligned parallel to reflections from the base of the snow pack that can easily be identified through a strong + - + signal. Due to the nature of bottom reflections, two materials are assumed present causing different signals. A single 3-wavelet is interpreted indicative of the interface between snow and debris whereas multiple strong reflections show the presence of ice between the snow pack and the bottom sediments. Radargrams from the surveys in April show similar bottom reflectors to those from March leading to the assumption that no significant icing growth took place in area 1 between the surveys. Radargrams collected from the visible icings in area 2 and 3 are characterised by a less homogeneous picture and more high amplitude reflections. Strong reflections are present throughout the profile: close to the surface, at the presumed bottom and in elongated or localized form within the profile at varying depths. Other than in radargrams from area 1, many reflectors within the icing are not parallel to the surface but inclined. Bottom reflectors are less continuous than in area 1, complicating the identification of the base of the icing.

In area 1, snow was present on the surface and no icing visible. Hence, strong subsurface reflections with a + - + polarity were of interest when interpreting radargrams from this part which would indicate the presence of a material with a higher dielectric constant than snow such as ice (but also water or sediment) below the snowpack. Snow profiles and probing along transect 4 indicated a snow depth of >1m on the northern river bank which corresponds with the area of low amplitude reflections in the radargram (Figure 52 b). Lateral, bed parallel, low amplitude reflections present in the upper parts of all profiles collected in area 1 are caused by the stratigraphy of the snowpack and related to warm spells (Kohler et al. 1997). Stronger reflections within the upper 1 m are referred to as ice lenses with a higher density as encountered when digging profiles (Figure 23 F). Two types of strong reflections were recorded at the bottom of the profiles. The first is composed of a 3-wavelet + - + signal marking the interface of snow to sediment in almost all profiles (Figure 23 E). Multiple reflections (Figure 23 B+C) are mainly found in the western part of area 1 (Figure 24) but also locally within other profiles (Figure 25) and interpreted as ice. In the western part of area 1, the occurrence of ice could indicate the presence of an actively forming icing underneath the snow pack. The 40-cm long ice core 1 was sampled from this area after removing 60 cm of snow (location indicated in Figure 24) and validates the thickness of ice seen in the radargram. Strong reflections within other profiles were recorded over short distances. Figure 25 shows that strong bottom reflectors in profile 17 are focused in small depressions of the river bed. Hence, the present ice could be refrozen meltwater in the channels of the braided river, rather than an actively forming icing. Another possible explanation would be a wet base of the snow pack. However, since strong bottom reflectors are absent in the profiles further up on the river bank (for example profile 4), and very localized in other profiles, this explanation is disregarded.

Radargrams from the icing provide a noisier image of the subsurface. Due to the absence of continuous bottom reflectors, the base of the icing is only discernible in few sections (Figure 26). The reason might be the low penetration depth of the used high-frequency antenna, additional dampening of the signal due to the presence of liquid water or the base consisting of a mixed ice-debris layer resulting in a less precise interface between ice and debris. Strong reflections were recorded frequently within the icing. Most of these reflections are interpreted as liquid water present either localized in channels (Figure 26, distance 12 m and 17 m) or as a water film in the icing (Figure 57 a). This ~10 m long reflection in profile 10 could, given the polarity, also be

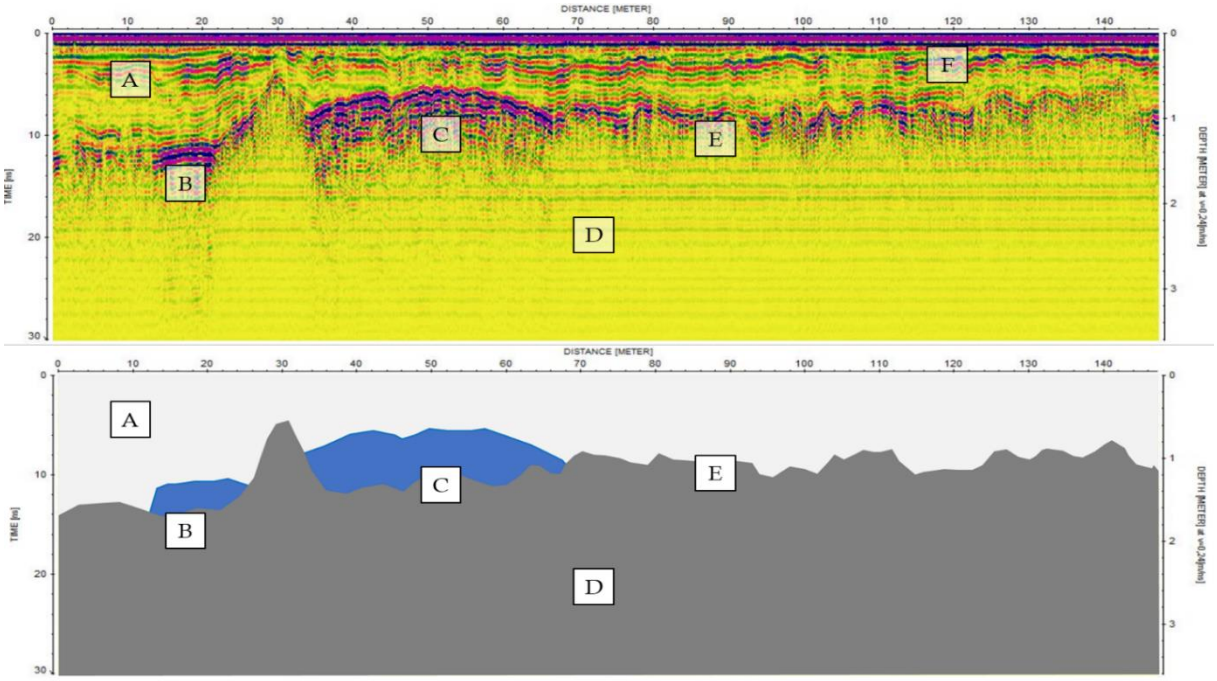

Figure 23: Radargram 1 collected in area 1. The upper part of the profile is composed of snow (letter A). Reflections within the snowpack (F) are assigned snow layers with varying density and ice lenses. Multiple strong reflections at distances 15-25 m and 34-68 m are interpreted as ice (letter B and C) overlying the sediment and debris mix composing the braided river bed (D). When ice is absent, the interface between snow and sediment is indicated by a single + - + reflection (E) of varying amplitude, possibly influenced by the material of the bed. The bottom image illustrates the interpretation of the radargram (white = snow, blue = ice, grey = sediment).

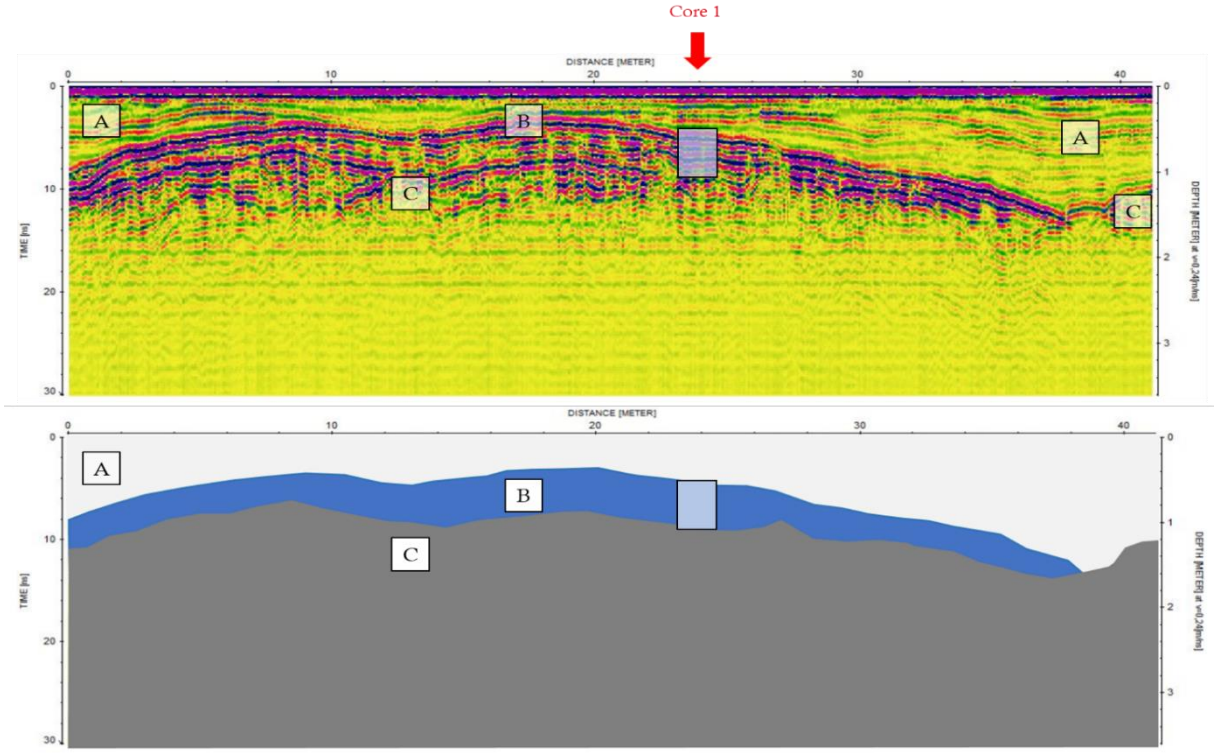

Figure 24: Radargram 3 collected in area 1. Toward the west of area 1, an ice layer (B) was found underneath the snow cover (A) from which core 1 was drilled (light blue rectangle, location indicated with red arrow). The presence of ice causes a + - + reflection at the snow-ice interface (B). Another strong + - + reflection below the ice (C) is interpreted as the ice-sediment interface with sediment exhibiting a higher dielectric constant. The bottom image illustrates the interpretation of the radargram (white = snow, blue = ice, grey = sediment).

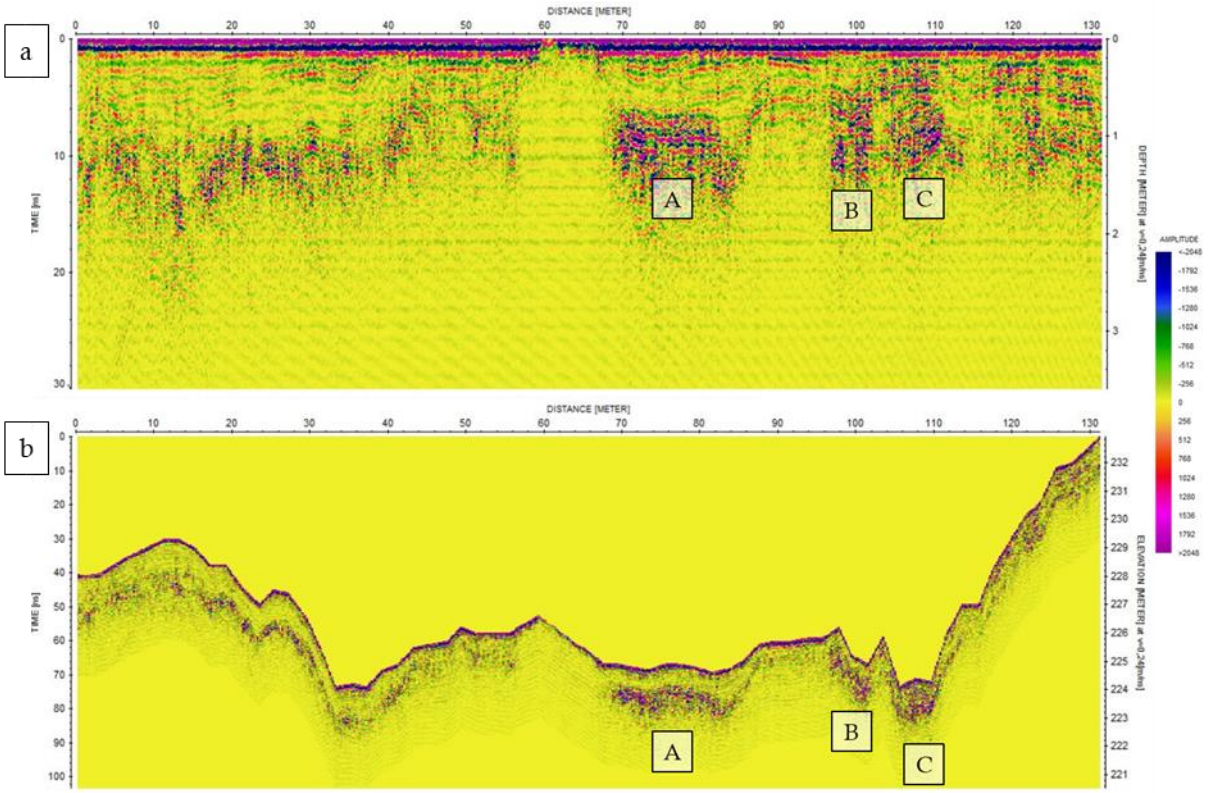

Figure 25: (a) GPR profile 17 shows three localized strong reflections at the bed, which are interpreted as ice (A-C) whereas basal reflections towards the left of the profile are interpreted as the base of the snowpack. (b) The topographically corrected profile reveals the location of these reflections (A-C) in small depressions of the relief likely indicating channels of the braided river.

caused by a sediment or debris inclusion. A similar reflection is present in profile 11 (Figure 58) at 125-150 m distance from the starting point but closer to the surface. Small mass movements from the slopes bordering the meltwater channel potentially transport material onto the growing icing. However, no signs indicated recent mass movements from the slopes and sediment or debris was absent on the icing during the field surveys and since the icing forms during winter when the surrounding ground is frozen, this process is deemed unlikely. Hence, reflections within the icing are interpreted as internal water film/ water reservoir or, depending on the depth, water saturated sediment at the base of the icing. Another potential cause for strong reflections within the icing are air-filled voids identifiable through a - + - polarity in the beginning of the reflection (Figure 26, distance 32 m). They are likely to be former intra-icing water-filled channels. Since this example appears as point reflector, this suggests orientation perpendicular to the survey direction whereas features causing elongated reflection run parallel. Different ice types within the icing can also cause reflections (Figure 26, distance 25 m) because varying liquid water content and grain size influence the scattering and velocity of the radar wave (Hubbard & Glasser 2005). Two

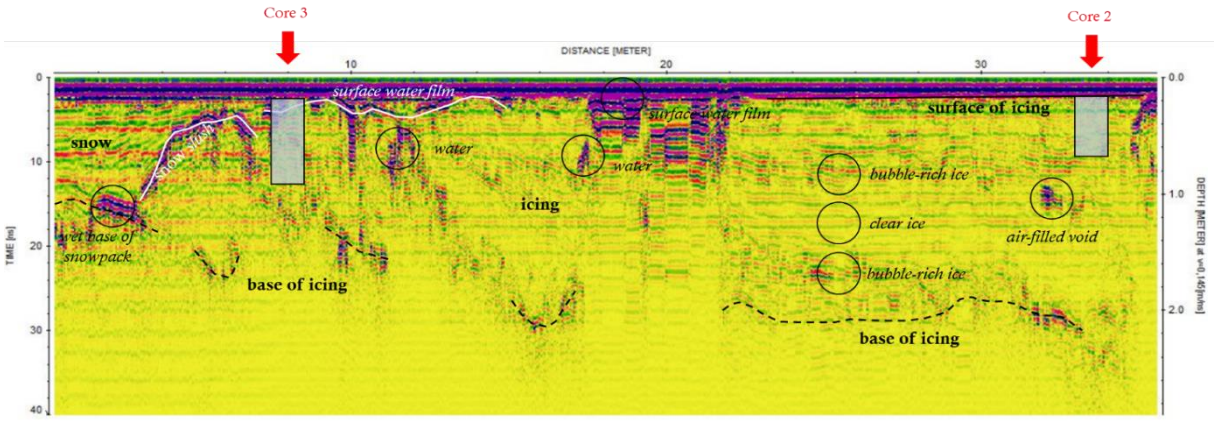

Figure 26: Interpretation of profile 7 recorded from the surface of the icing in area 2. The base of the icing cannot be identified continuously and attempts of defining the base were drawn with caution. Two ice cores were sampled along this profile: core 2 at the top of the icing and core 3 at the bottom. The cores showed a sequence of bubble-rich and clear ice layers which are believed to cause the low amplitude reflections within the ice body. Strong internal reflections are interpreted as air-filled voids (at distance 32 m) but more commonly as water. A water film on the surface caused a strong + - + reflection after the arrival of the ground wave. The downward propagation of the strong reflections (for example at distance 10 m) is believed to result from multiple reflections causing a ringing. The surface water film towards the left of the profile seems to disappear into the subsurface. This area is interpreted as the downslope end of the icing. The dipping reflector represents snow slush present at the margin of the icing. Stronger low amplitude reflections in the adjacent snowpack on the left side of the radargram might be due to a higher abundance of liquid water in this area of icing expansion.

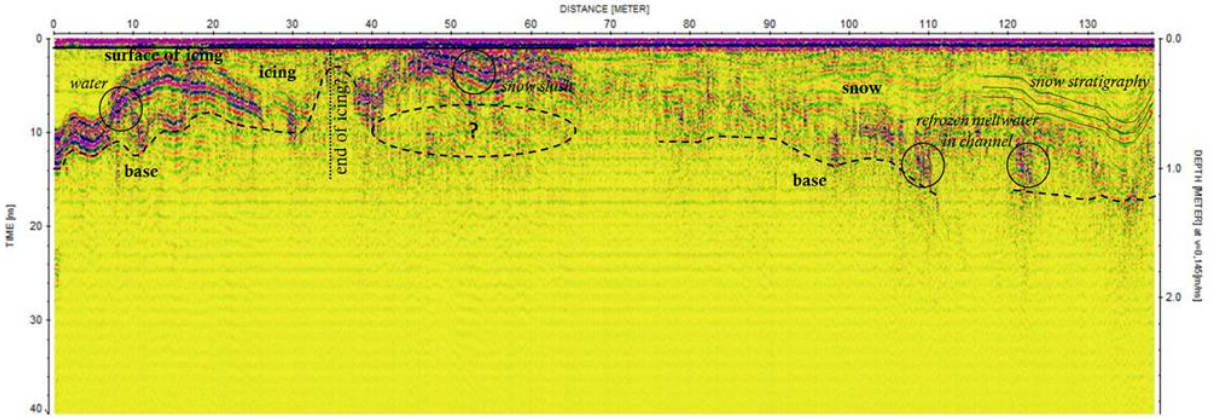

Figure 27: Interpretation of profile 12 recorded from the flat plain between the upper and lower visible icings. GPR data from this location aids to investigate whether the two ice bodies exhibit a subsurface connection, although they appear separated seen from the surface. The base should be interpreted with care since a continuous bottom reflector is absent. Strong reflections on the left of the profile are interpreted as the presence of liquid water. The sudden termination of the strong reflector at a distance of 25 m might indicate the margin of the icing followed by snow slush present close to the surface between a distance of 40-65 m. The wet surface may dampen the high frequency wave sufficiently to prevent the recording of an identifiable reflection from the bed (indicated with a question mark). Areas towards the right of the image were covered with snow. Bed-parallel low amplitude reflections were recorded in this region comparable to those from the snow pack in area 1 and interpreted as differences within the snowpack stratigraphy. No continuous bottom reflector is discernible which would indicate the presence of an icing in the subsurface. Localized strong reflections towards the assumed base are interpreted as refrozen meltwater in the channels of the braided river as in area 1.

different ice types were distinguished in the analyses of sampled ice cores: clear ice and bubble-rich ice (chapter 5.3). Due to the higher air content of bubble-rich ice compared to the bubble-free clear ice layers, the dielectric constant is lower in the first ice type.

5.2.2 Source of Error GPR and Future Adaptations

On account of disturbances, the two GPR surveys were more time consuming than anticipated. This resulted in recording less profiles than planned and conducting the survey with only one frequency (800 MHz) rather than additionally with a 500 MHz antenna. Sources of error in the GPR data are primarily attributed to the malfunction of the GPS device resulting in the recording of profiles without position data or with a poor accuracy of the data. This further led to limitations during the processing stage, when migration of the data had to be omitted.

The GPR equipment, especially the cable connections, turned out to be very fragile. Establishing a communication between all components was challenging and interrupted repeatedly during data acquisition. The main reasons were unstable cable connections linking different parts of the radar system. Communication between the hand-held GPS and radar could not be established on March 26th leading to the collection of radar data with missing coordinates. In order to locate the obtained data from this day and to calculate an accurate length for the profiles during the post processing stage, the coordinates of the start and end points of each profile were noted down separately. For fieldwork on April 9th a different GPS device and several cables were brought into the field as back up. Communication with the radar could be established and traces with position information were recorded. Assessing the quality of the position information during the post processing stage however showed, that the accuracy changed rapidly during data acquisition resulting in some profiles with illogical position data. This applies to the horizontal as well as vertical accuracy of the GPR position. Additionally, the ethernet cable, linking the monitor to the control unit, disconnected easily. The recording of data stopped immediately, thus leading to several very short profiles. This problem mainly arose due to the cold and when pulling the radar upwards on the inclined and slippery icing. The situation could be improved during the second survey by holding the monitor inverted and constantly pressing the cable into the socket.

Due to the vertical movement of the radar across the surface and the conical transmission of waves, point reflectors in the underground appear as upward pointing hyperbolas (Hubbard & Glasser 2005) since reflections are not only recorded when the antenna is located directly above the reflector, but also when in front or behind it. This additionally causes dipping reflectors to be shifted from their true geometrical position (Møller 2006). To correct geometrical irregularities in the data, migration is an often-applied processing step. Migration collapses the legs of hyperbolas into a single point located at the apex, corrects the position of dipping reflectors and focuses scattered signals (Cassidy 2009b; Møller 2006). During the processing phase of this study, an Fk migration after Stolt with a scaling factor of 1 was applied on the data. In order to migrate the data, the wave velocity in the ground has to be known. No CMP survey was conducted in this survey to calculate the velocity due to the used 800 MHZ shielded antenna with a fixed offset of transmitter and receiver. Figure 28 shows the effects of migration on a sample trace and clearly illustrates the problems related to this processing step by inducing bias in the given data. Inaccurate GPS data and velocity values result in the creation of artefacts and downward pointing hyperbolas impairing the data quality and subsequent interpretation. Even though migration is a common processing step when surveying glaciers, the necessity of this analysis depends on the data set and questions aimed to be answered by this method (Hubbard

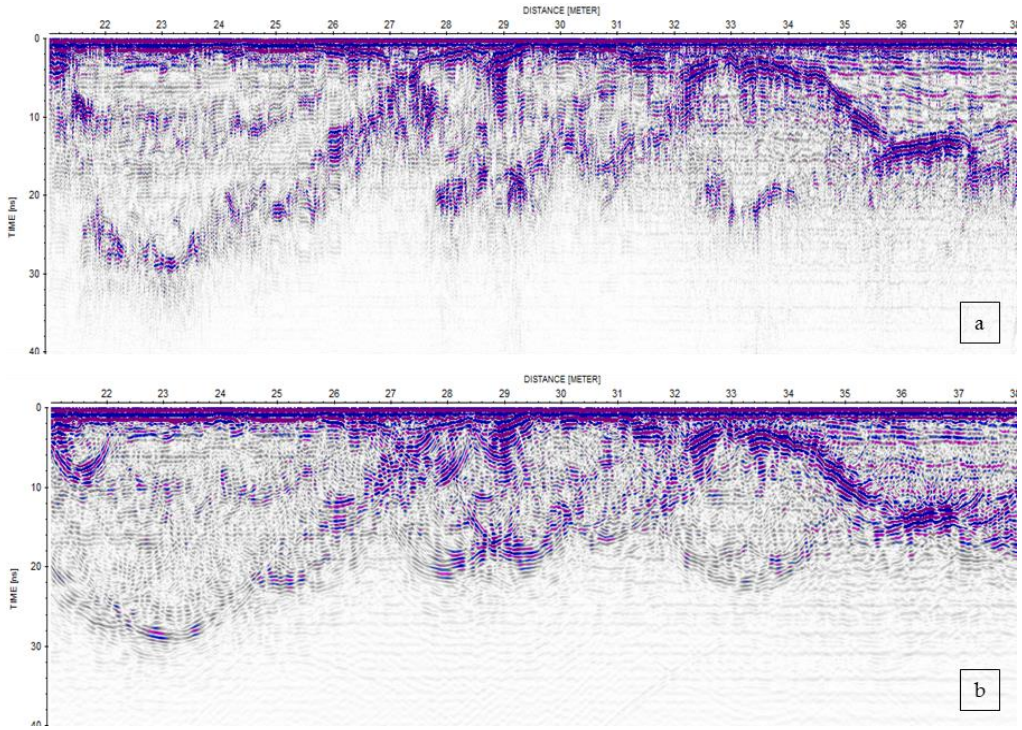

Figure 28: A section of profile 7 (a) before and (b) after migration.

& Glasser 2005). In this study, migration of the GPR data was omitted and all GPR images show unmigrated radargrams. As a result, hyperbolas created by point reflectors remain in the processed profiles and the slope of reflectors appears less steep in the radargrams as is the case in the icing. In the given study, position errors of reflectors in unmigrated profiles are considered as minor since only few hyperbolas exist in the data set and an incorrect slope of reflectors does not hinder to answer the formulated research questions. Therefore, errors remaining in the data by omitting migration were evaluated as less severe than the bias introduced by migration.

In future studies, several adaptations would be implemented to the experimental setup of GRP surveys. Even though GPR surveys provided insight into the structure of the icings, some features, such as the reflection from the ice-debris interface indicating the base of the ice body, are believed to have been missed because of the high frequency of the employed antenna and hence low penetration depth. Therefore, an additional survey of the icing with a lower frequency antenna, for example 500 MHz, as initially planned for this study, would be beneficial. Comparison of the obtained radargrams, given the same survey grid for both frequencies, hold promise to record reflections at greater depth from the lower frequency antenna besides the high resolution of reflectors close to the survey from the high frequency antenna. A closely spaced survey grid of longitudinal and transverse transects would allow to create an ice thickness map of the icing and to subsequently calculate the volume of the icing. Since the approximate location of the springs is known now, it is advised to pin point their exact position with GPR early in the season, before location changes occur due to pressure exerted by the overlying ice, to facilitate localizing the spring during the ablation season. The use of another frequency antenna and the collection of a greater number of profiles may facilitate locating the water sources. Additionally, the use of a second GPS would be useful in future GPR surveys as backup and to further allow topographical correction of all profiles during the post processing stage.

5.3 Hydrochemistry

5.3.1 Stratigraphy of Ice Cores

Five ice cores, ranging in length between 26 to 70 cm, were sampled from different areas of the Rieperbreen icing (locations indicated in Figure 12b) at the end of March. All ice cores show a distinct stratigraphy with several surface parallel layers as seen

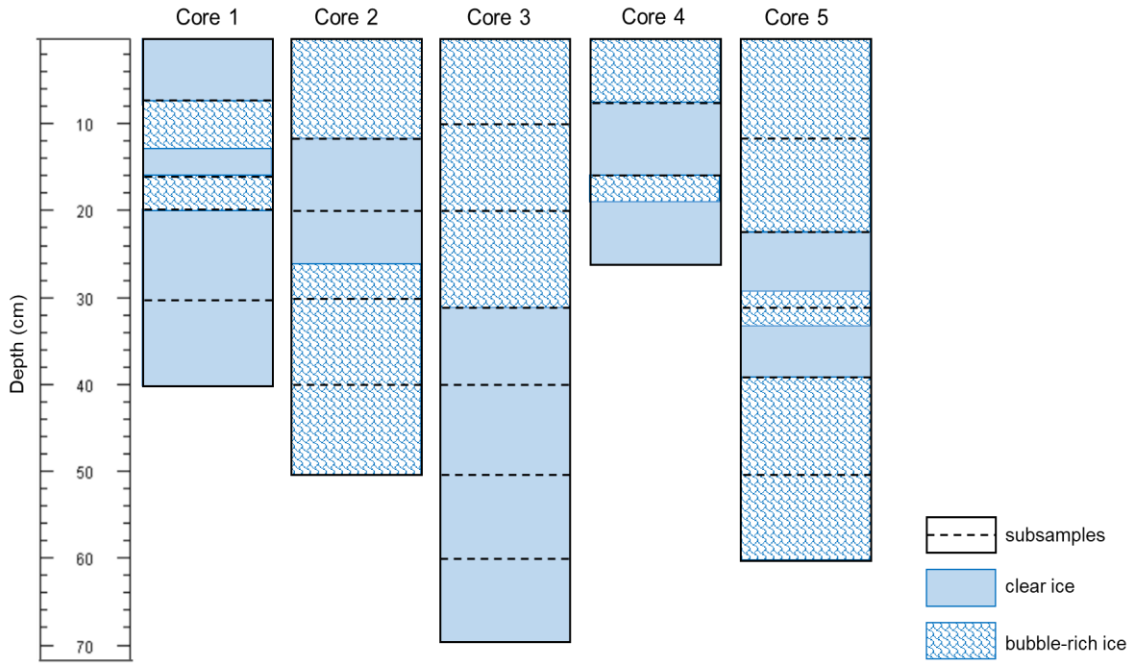

Figure 29: Length, stratification and main ice types of ice cores 1 to 5 from the Rieperbreen icing. The dotted lines indicate the boundary of the subsamples cut from the cores (layout after Stachnik et al. 2016).

on the photographs in Figure 64 (appendix). Through visual analysis, two ice facies were distinguished in all cores: clear ice and bubble-rich ice. Due to the lack of air bubbles, the clear ice sections of the cores are transparent and light blue in colour whereas the bubble-rich ice layers are opaque and white in colour. The ratio of clear and bubble-rich ice layers, the width of the layers and their depths are only partly comparable in the five ice cores (Figure 29). Core 1 is mainly composed of clear ice. This core is the only one of the sampled with a top layer consisting of transparent ice. Core 2 and 3 are composed mainly of bubble-rich ice with clear ice layers in the middle of the cores. The stratigraphy of core 3 deviates from the others. Only two layers can be distinguished in this core; bubble-rich ice composing the top 30 cm and transparent ice the bottom 40 cm. For further analyses of the correlation of the abundance of solutes and ice type in the next chapter, each subsample was ascribed one ice type. The class *mixed ice* was introduced for subsamples composed of both, clear and bubble-rich ice.

5.3.2 Ionic Chemistry of Ice Cores

The mean composition of melted ice cores shows an abundance of solutes in the order $SO_4^{2-} > Na^+ > Ca^{2+} > HCO_3^- > Cl^- > Mg^+$. The ranking of solutes varies slightly between the five ice cores with $Ca^{2+} > Na^+$ in core 1 and 3 and $Mg^+ > Cl^-$ in core 2, 3 and 5.

Other analysed solutes are very low in concentration compared to the most abundant species. Absolute abundances of measured ion species in ice core subsamples are visualized summarized in Figure 30 and separated in Figure 65. Absolute values of all subsamples are listed in Table 13 (appendix) and relative concentrations in Table 14 (appendix). Ion concentrations from subsamples were used to calculated averages for ice cores 1 – 5 (absolute and relative abundance listed in Table 12).

The most abundant ion species in the ice cores is SO_4^{2-} which accounts for 18 – 45 % of TDS. The lowest concentrations are found in cores 1 and 4 (32,47 mg l^{-1} and 31,26 mg l^{-1}) and highest in core 2 (86,76 mg l^{-1}). Absolute concentrations in subsamples range between 7,97 – 122,7 mg l^{-1} (avg. = 49,89 mg l^{-1}; std. = 33,47 mg l^{-1}). However, SO_4^{2-} is not the most abundant ion in all subsamples. At the bottom of core 1 (sample 1.5) and in core 3 (samples 3.3, 3.5 and 3.6), Ca^{2+} is the most abundant ion species although Ca^{2+} concentrations in these subsamples are among the lowest in cores 1 and 3. The second most abundant solutes are cations but the species varies between cores. Ca^{2+} ranges second in cores 1 and 3 with 19,49 mg l^{-1} (22,29 %) and 21,06 mg l^{-1} (24,08 %) and third in cores 2, 4 and 5 with 31,67 mg l^{-1} (16,45 %), 15,35 mg l^{-1} (17,05 %) and 24,31 mg l^{-1} (17,75 %), respectively. Na^+ is the second most abundant ion in cores 2, 4 and 5 accounting for 19,31 %, 21,34 % and 20,83 % of TDS, but ranks third in cores 1 and 3 with 16,57 % and 15,18 %. Concentrations of Na^+ vary greatly between subsamples (3,9 – 59,91 mg l^{-1}; avg. = 26,31 mg l^{-1}; std. = 17,98 mg l^{-1}). The range of Ca^{2+} values, although also apparent, is less pronounced than of Na^+. Here, values range between 7,52 – 43,7 mg l^{-1} (avg. = 22,89 mg l^{-1}; std. = 8,99 mg l^{-1}). Measured DIC, here as HCO_3^-, places 4th in all ice cores with average abundance between 9,26 – 15,57 mgC l^{-1} and between 3,27 – 21,40 mCg l^{-1} in subsamples. Magnesium is the 5th most abundant ion species in cores 1, 3 and 5 followed by Cl^- but vice versa in cores 1 and 4. Si, K^+ and DOC account for >1 mg l^{-1} in at least one core, concentrations of NH_4^+, F^- and NO_3^- are < 1 mg l^{-1} and <1 % of TDS in all cores or even below the detection limit in some subsamples, as the case for F^-.

TDS, calculated with DIC from charge balance, ranges between 37 – 275 mg l^{-1} in subsamples (avg. = 133 mg l^{-1}; std. = 73 mg l^{-1}) (Table 13). On average, the highest abundance of dissolved solids was measured in core 2 (206 mg l^{-1}) followed by core 5 (148 mg l^{-1}) and core 3 (110 mg l^{-1}). TDS is lower in cores 1 and 4 with 94 mg l^{-1} and 98 mg l^{-1}, respectively (Table 12). Within the ice cores, no trend is apparent regarding

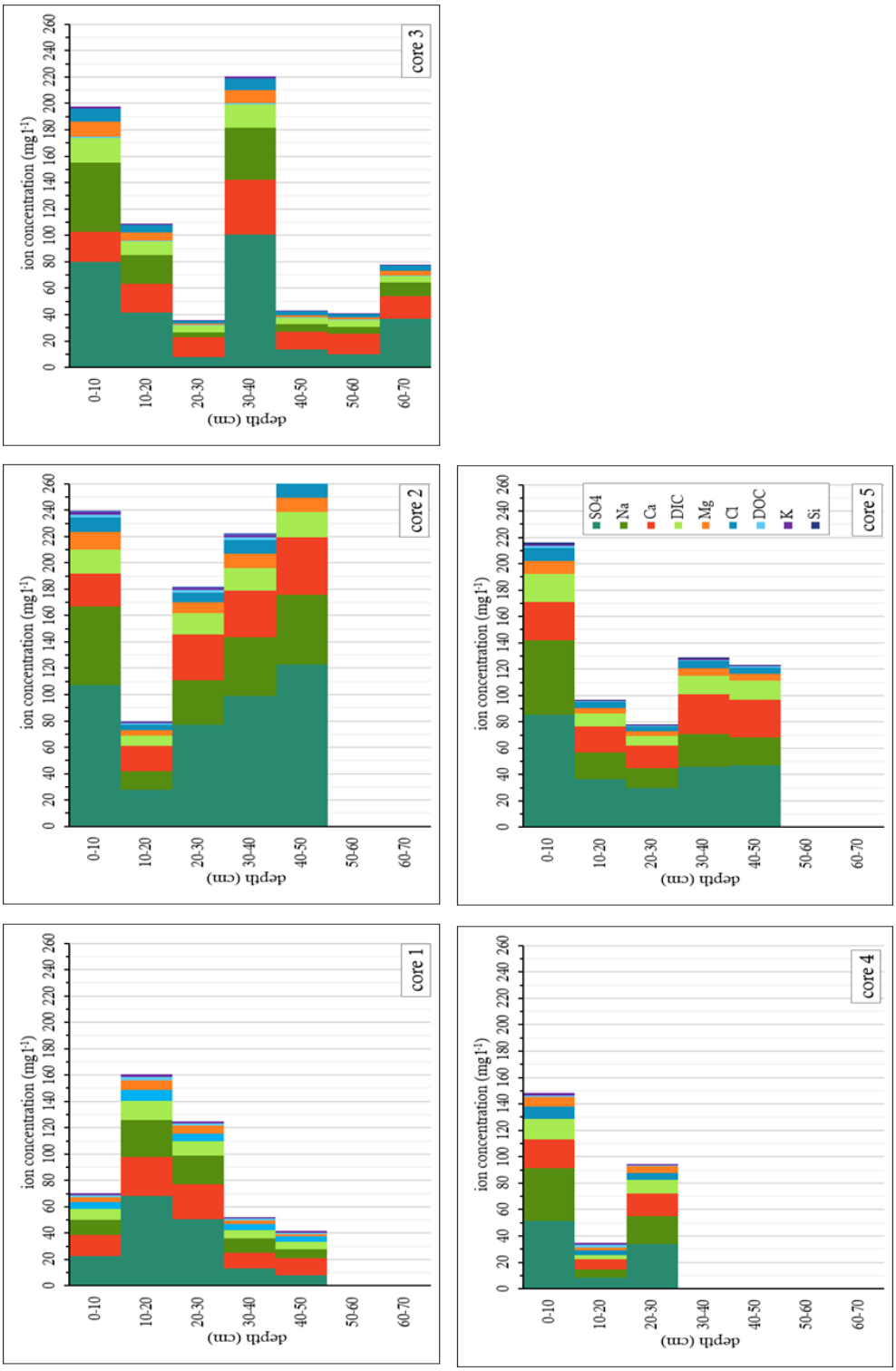

Figure 30: Concentration of ions ice core subsamples. DIC (measured value) in mgC l^{-1} as HCO_3^-. Displayed are only those ions with an abundance of >1 mgL^{-1} in at least one subsample. Quantities of NH_4^+, F^-, and NO_3^- were below this limit in all cores and Si in cores 1, 3 and 4. The order of ions in the cores mirrors the abundance averaged for the ice core.

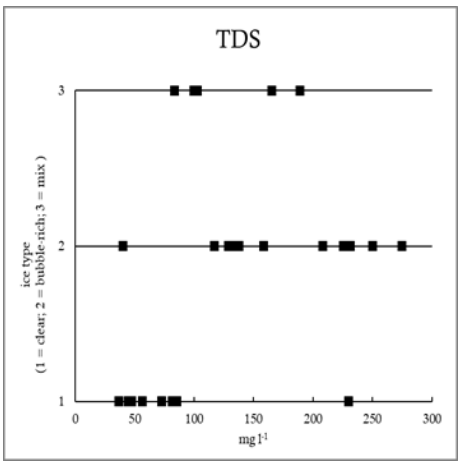

Figure 31: Relationship between TDS and ice type of subsamples. Lowest TDS was calculated for clear ice and highest values for bubble-rich ice (except subsamples 3.3 and 3.4). Layers defined as mixed ice range in the middle.

depth and TDS. While all cores, except core 1, exhibit either the highest or seconds highest TDS in the first subsample, high solute abundance was also measured in the middle part of cores 1 and 3 and in bottom samples of core 2. TDS, however, correlates well with the ice type assigned to each subsample (Figure 31). The lowest values (<100 mg l^{-1}) were measured in subsamples defined as ice type 1 (clear ice) with the exception of sub-sample 3.3 and highest values for bubble-rich ice (ice type 2) with sub sample 3.4 as outlier.

EC (25°C) varies greatly between subsamples (59 – 562 µS cm^{-1}; avg. = 257,93; std. = 152,01) and consequently ice core averages (180 – 419 µS cm^{-1}). The water of ice cores is slightly alkaline with pH values predominantly ranging between 8,3 – 9,1 in subsamples (exception: subsample 4.2 with 7,6) and 8,3 – 8,9 in ice cores. To assess the origin of solutes, Pearson correlation coefficients (r) were calculated for all measured ions (Table 5). A strong positive correlation of r > 0,9 exists between Na^+, Mg^{2+}, Cl^-, SO_4^{2-} and DIC. Si showed significant correlation with Na^+, Mg^{2+}, Cl^-, DIC and

Table 5: Pearson correlation coefficient (r) for ion concentrations in ice core subsamples (DIC from charge balance). Values can range between ±1 whereas r < 0 indicates inverse correlation.

	NH_4^+	Si	Na^+	K^+	Mg^{2+}	Ca^{2+}	F^-	Cl^-	NO_3^-	SO_4^{2-}	DOC
NH_4^+	1										
Si	-0,24	1									
Na^+	-0,23	0,87	1								
K^+	0,32	0,48	0,69	1							
Mg^{2+}	-0,26	0,83	0,97	0,73	1						
Ca^{2+}	-0,31	0,77	0,67	0,48	0,73	1					
F^-	0,11	0,40	0,44	0,37	0,39	0,27	1				
Cl^-	-0,08	0,83	0,97	0,80	0,96	0,68	0,47	1			
NO_3^-	0,26	-0,17	0,04	0,57	0,17	0,22	0,23	0,19	1		
SO_4^{2-}	-0,27	0,85	0,91	0,69	0,95	0,87	0,37	0,91	0,20	1	
DOC	0,50	0,35	0,47	0,86	0,50	0,39	0,49	0,58	0,55	0,52	1
DIC	-0,29	0,90	0,97	0,63	0,95	0,78	0,44	0,94	0,04	0,91	0,42

SO_4^{2-} (r > 0,83). Ca^{2+}, the second or third most abundant ion in the cores, only correlates with SO_4^{2-} with r > 0,8.

The relation between the abundance of ion species and the ice type, defined for each subsample during ice core processing, was assessed. Figure 66 shows a similar pattern for SO_4^{2-}, Na^+, Ca^{2+}, DIC, Mg^{2+} Cl^- and Si. Lowest values were measured in subsamples defined as clear ice, intermediate values in mixed ice and highest concentrations in bubble-rich ice. Two exceptions exist throughout the data. Ion concentrations in subsample 3.3, defined as bubble-rich ice, ranges consistently with clear ice values and concentrations in subsample 3.4, defined as clear ice, with subsamples composed of bubble-rich layers. For DOC, K^+, NO_3^-, F^- and NH_4^+ values are distributed between all ice types and no pattern is apparent.

Table 6 lists SI for all oversaturated minerals in ice cores. Positive SI were calculated for five minerals: Aragonite, Calcite, Dolomite, Quartz and Talc. Hence, saturation only occurred for carbonate and silicate minerals but not for sulphate minerals, although

Table 6: Saturation indices (SI) ice core averages and subsamples. SI > -0,05 was calculated for the minerals: Aragonite ($CaCO_3$), Calcite ($CaCO_3$), Dolomite ($CaMg(CO_3)_2$), Quartz (SiO_2) and Talc ($Mg_3Si_4O_{10}(OH)_2$). SI of CO_2 is compared to pCO_2 calculated with Eq. 11.

sample	Aragonite	Calcite	Dolomite	Quartz	Talc	CO_2	pCO_2
core 1	-	-	-	-	-	-3,78	-3,76
1-1	-	0,1	-	-	-	-4,26	-4,21
1-2	-	0,14	-	-	-	-3,64	-3,58
1-3	-	-	-	-		-3,48	-3,42
1-4	-	-	-	-	-	-3,5	-3,45
1-5	-	-	-	-	-	-4,26	-4,22
core 2	0,47	0,64	0,68	-	0,33	-3,95	-3,88
2-1	0,51	0,68	1,02	-	1,42	-3,98	-3,91
2-2	0,09	0,25	-	-	-	-4,18	-4,12
2-3	0,42	0,58	0,46	-0,05	-	-3,86	-3,79
2-4	0,63	0,8	1,01	0,09	1,74	-4,02	-3,95
2-5	0,57	0,73	0,79	0,04	0,33	-3,77	-3,70
core 3	0,15	0,31	-	-	-	-4,14	-4,04
3-1	0,28	0,45	0,52	-	-	-3,79	-3,73
3-2	0,21	0,37	0,11	-	-	-4,09	-4,03
3-3	0	0,16	-	-	-	-4,58	-4,53
3-4	0,03	0,2	-	-	-	-3,31	-3,25
3-5	-0,05	0,11	-	-	-	-4,6	-4,55
3-6	-	-	-	-	-	-4,22	-4,18
3-7	-0,1	0,07	-	-	-	-4,52	-4,46
core 4	-	-	-	-	-	-3,52	-3,50
4-1	0,52	0,68	0,84	-	1,11	-4,15	-4,08
4-2	-	-	-	-	-	-3,21	-3,14
4-3	-	-	-	-	-	-3,52	-3,47
core 5	0,15	0,31	-0,01	-	-	-3,78	-3,76
5-1	0,22	0,38	0,4	-	-	-3,64	-3,58
5-2	0,34	0,5	0,44	0,03	-	-3,64	-3,58
5-3	0,13	0,29	0,14	-	-	-4,13	-4,07
5-4	0,08	0,25	-	-0,6	-	-4,32	-4,27
5-5	0,36	0,52	0,25	-	-	-3,87	-3,81
5-6	-	-0,05	-	-	-	-3,44	-3,38

SO_4^- abundance is high. Ochre precipitates are visible in the area of icing formation in summer, indicating saturation of $Fe(OH)_3$, but the SI of ferrihydrites was not calculated for icing subsamples due to there being no available data on Fe concentration. The mean SI of ice cores shows $SI_{Calcite}$ > $SI_{Aragonite}$ > $SI_{Dolomite}$ for carbonate minerals, except in core 2 where $SI_{Dolomite}$ is the highest. The high SI of carbonate minerals suggests the formation of layers of precipitates within the icing. SI_{Quartz} and SI_{Talc} show saturation in four subsamples and SI_{Talc} for core 2. Ice core 1 varies notably in its SI from the others since only Calcite reached saturation in two subsamples. SI_{CO2} ranges between -4,60 to -3,21. The calculated pCO_2 is slightly less negative for all subsamples and ranges between -4,55 to -3,14. Values are below atmospheric equilibrium (pCO_2 = -3,5) in all samples except five for SI_{CO2} (subsamples 1.3, 1.4, 3.4, 4.2 and 5.6) and six for calculated pCO_2 (subsamples 1.3, 1.4, 3.4, 4.2, 4.3 and 5.6).

5.3.3 Ionic Chemistry of Spring and Lake Water

The order of the most abundant ions in water samples is quite variable. Ion species with a concentration > 1mg l^{-1} are plotted in Figure 32, absolute abundances of all measured species listed in Table 15 and relative abundances compared to TDS in Table 16 (both in appendix).

The most abundant ion species in all water samples is SO_4^{2-} followed by Na^+ and DIC in all April and the June S2 sample. SO_4^{2-} concentrations range between 195 – 226 mg l^{-1} (26 - 29% of TDS), 12-32 mg l^{-1} (27 - 33% of TDS) and 258 mg l^{-1} (57% of TDS) in samples from the springs in April, June and the lake, respectively. Na^+ is the second most abundant solute in all April samples with 119 - 145 mg l^{-1} (15 - 17% of TDS) and in the June sample from spring 2 (10 mg l^{-1} accounting for 23% of TDS). in June and lake samples with 10 – 12 mg l^{-1} (10 - 22% of TDS) and 9 mg l^{-1} (22% of TDS) but only 4th in June samples from S1 with ~ 11 mg l^{-1} and therefore 11% of TDS. DIC accounts for 9% of TDS in April samples (62 – 76 mg l^{-1}) and 6-12% in June samples. Most pronounced differences between the average ion concentrations of April and June samples are given by Fe, (977-times higher in April), Cu (518-times higher), Al (89-times higher), PO_4^{3-} (58-times higher) and Mn (53-times higher) (Figure 33). The composition of the lake water is markedly different compared to the April spring water. Besides similar values of SO_4^{2-}, Ca^{2+}, S and Mg^{2+}, concentrations of Na^+, DIC, Fe and

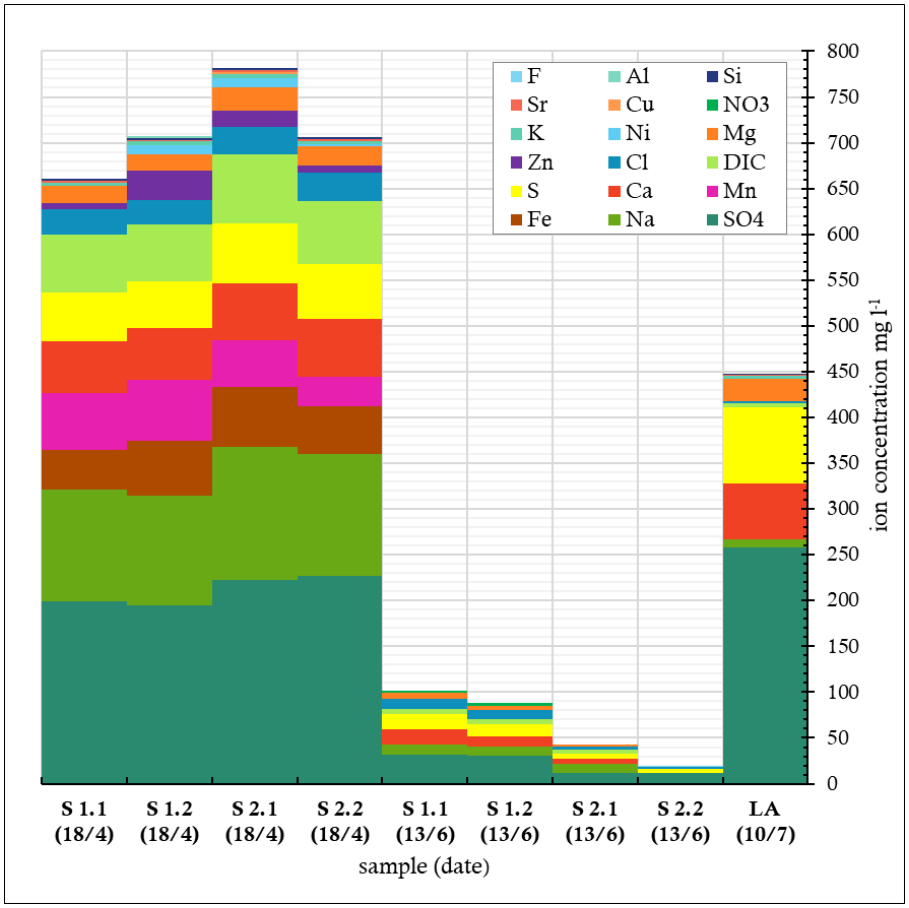

Figure 32: Ion concentration of water samples from spring 1 (S1), spring 2 (S2) and lake (LA). Duplicates were sampled and analysed for springs (e.g. S 1.2). DIC (as HCO_3^- in mgC l^{-1}) was calculated from charge balance. Only ions with a concentration > 1mg l^{-1} are plotted.

Mn are 120, 62, 55 and 53 mg l^{-1} lower, respectively, in the lake water compared to the average of April spring samples.

From the concentration of the most abundant ion species it becomes apparent, that a pronounced difference in TDS exists between the April, June and lake samples but also, although to a lesser degree, between the June samples from spring 1 and 2 (length of bars in Figure 32 and Table 15). April samples have the highest TDS with 850 mg l^{-1} and 768 mg l^{-1} in sample 1 and 2 from spring 2 and 715 mg l^{-1} and 760 mg l^{-1} in S1.1 and S1.2, respectively. TDS of S2.1 is therefore 11% higher than S2 and 19% compared to S1.1. TDS of June samples is significantly lower than of April samples. Concentrations range between 90 – 105 mg l^{-1} in S1.1 and S1.2 and 20 – 44 mg l^{-1} for S2. TDS of S 2.2 (20 mg l^{-1}), however, is an underestimate due to erroneous concentrations of Na^+, K^+, $Mg^{2+}$and Ca^{2+} which were excluded from further analyses. Ion abundance in June S1 are more than twice the concentration of S2.1. The lake places between the April and June samples in TDS concentration with 449 mg l^{-1}.

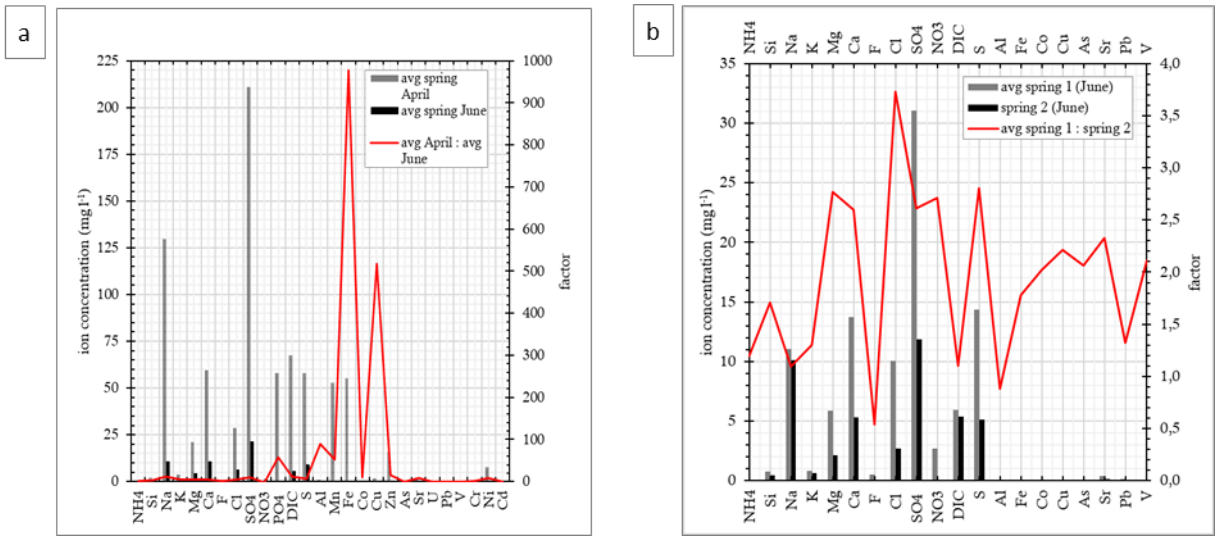

Figure 33: (a) shows the difference in solute abundance between the April and June spring samples. Grey bars display the average of ion concentration in April samples and black bars in June samples. The red line gives the factor with which the concentration of a certain ion species deviates between the samples. Positive values indicate a higher abundance in April. (b) Illustrates the difference of solute abundance in June spring samples. Grey bars display the average of spring 1 calculated from samples 1.1 and 1.2 (13/6), and black bars the ion concentrations of sample 2.1 (13/6). The red line gives the factor with which the concentration of a certain ion species in higher in spring 1 than spring 2.

To assess the correlation between water samples, Pearson correlation coefficients were calculated for all spring samples except June S2.2 and the lake samples (Table 7a). Spring samples collected in April show a high correlation (r = 0,98 – 0,99) as expected from ion abundance visualized in Figure 32. The correlation between April and June S1 is lower with r = 0,86 – 0,91. April samples correlate less with June S1 (r = 0,89) than with June 2.1 (r = 0,93 – 0,95). The lowest correlation was calculated for the lake in regard to all spring samples except June samples from spring 1. Even though Pearson r might indicate a good correlation between samples, the absolute abundance of certain ions can be significantly different as shown by Figure 33 a+b. To further help determine sources of dissolved solutes, Pearson correlation coefficients were also calculated for major ions (Table 7 b). When correlating the abundance of

Table 7: Pearson correlation coefficient (r) matrix for ion concentrations in water samples. Values can range between ±1 whereas r < 0 indicates inverse correlation. (a) Correlation calculated for spring (April and June) and lake samples. (b) Correlation for solute concentrations of April spring samples.

a

	S 1.1 (18/4)	S 1.2 (18/4)	S 2.1 (18/4)	S 2.2 (18/4)	S 1.1 (13/6)	S 1.2 (13/6)	S 2.1 (13/6)
S 1.1 (18/4)	1						
S 1.2 (18/4)	0,99	1					
S 2.1 (18/4)	0,99	0,99	1				
S 2.2 (18/4)	0,99	0,98	0,99	1			
S 1.1 (13/6)	0,88	0,86	0,86	0,88	1		
S 1.2 (13/6)	0,90	0,88	0,88	0,91	0,98	1	
S 2.1 (13/6)	0,95	0,93	0,94	0,94	0,89	0,89	1
LA (10/7)	0,82	0,80	0,79	0,82	0,90	0,92	0,72

b

	Si	Na^+	K^+	Mg^{2+}	Ca^{2+}	F^-	Cl^-	SO_4^{2-}	PO_4^{3-}
Si	1								
Na^+	-0,58	1							
K^+	-0,35	0,96	1						
Mg^{2+}	-0,49	0,98	0,98	1					
Ca^{2+}	-0,63	0,85	0,73	0,72	1				
F^-	-0,19	-0,19	-0,18	-0,05	-0,56	1			
Cl^-	-0,72	0,64	0,45	0,48	0,94	-0,54	1		
SO_4^{2-}	-0,66	0,87	0,75	0,75	1,00	-0,50	0,93	1	
PO_4^{3-}	-0,60	1,00	0,96	0,97	0,86	-0,20	0,67	0,89	1
DIC	-0,57	1,00	0,97	0,98	0,83	-0,17	0,62	0,86	1,00

major solutes in April samples, very strong correlations were found between Na^+, K^+, Mg^{2+}, PO_4^{3-} and DIC ($r > 0,97$) and further between Ca^{2+}, SO_4^{2-}, and Cl^- ($r > 0,93$).

As for ice cores, Saturation indices were calculated for water samples using WEB-PHREEQ (Saini-Eidukat & Yahin 1999). Oversaturation occurred in regard to 21 minerals mainly from the groups of silicates (Albite, Anorthite, Ca-Montmorillonite, K-feldspar, K-mica, Kaolinite, Illite, Quartz and Willemite) and oxides ($Al(OH)_3$, $Fe(OH)_3$, Gibbsite, Goethite, Hematite and Manganite) but also sulphates (Alunite and Jarosite-K), phosphates (Hydroxyapatite and Vivianite) and carbonates (Rhodochrosite and Smithsonite). All 21 minerals exhibit SI > 1 in April samples. The highest saturation values are in the order $SI_{Hematite} > SI_{K\text{-}mica} > SI_{Goethite}$ with a maximum SI in all four samples of 23,84, 15,59 and 11,08, respectively. Spring water sampled in June is only saturated in regard to 8 minerals which are silicates and oxides but not sulphates, phosphates and carbonates. June samples show highest SI in the order $SI_{Hematite} > SI_{Goethite} > SI_{K\text{-}mica}$ with SI of 17,55, 7,84 and 7,25, respectively. For those minerals, where saturation occurred in April and June samples, SI is higher in all April samples. Comparisons of spring and lake water show slightly higher SI in the lake than the June samples, but significantly lower than in April samples. SI calculations further affirm that, given the pH values of the samples, it was correct to assume the presence of DIC primarily as HCO_3^- for charge balance calculations. For S2.1 (18.4), with a DIC concentration of 75,7 mg l^{-1} and a pH of 7,61, the HCO_3^- : CO_3^{2-} ratio is 1,137E-03: 1,177E-06. Bicarbonate is therefore present in a concentration of mmol and carbonate in µmol. With lower pH, as in June samples, the presence of HCO_3^- becomes even more dominant compared to CO_3^{2-}.

Calculated pCO_2 (Table 15) is above atmospheric equilibrium for all spring samples. April samples show higher values for both springs (-2,15 to -2,02) than June samples (-2,76 to -2,69). The lake sample exhibits the lowest pCO_2 value of water samples with -3,63 and hence below the atmospheric equilibrium. SI_{CO2} (Table 8) are slightly lower than calculated pCO_2 ranging between -2,89 to -2,16 for the springs and give a value of -3,71 for the lake sample. The relation, however, is the same as for calculated pCO_2 with the lake sample showing lower values than the atmosphere and the springs higher values which decrease between April and June samples.

Table 8: Saturation index (SI) for water samples. Not calculated for S 2.2 from June 6 due to missing ion concentrations. Saturation occurred in regard to the following minerals: Albite ($NaAlSi_3O_8$), Alunite ($KAl_3(SO_4)_2(OH)_6$), Anorthite ($CaAl_2Si_2O_8$), Ca-Montmorillonite ($Ca_{0,165}Al_{2,33}Si_{3,67}O_{10}(OH)_2$), Gibbsite ($Al(OH)_3$), Goethite ($FeO(OH)$), Hematite ($Fe_2O_3$), Hydroxyapatite ($Ca_5(PO_4)_3OH$), Illite ($K_{0,6}Mg_{0,25}Al_{2,3}Si_{3,5}O_{10}(OH)_2$), Jarosite-K ($KFe_3(SO_4)_2(OH)_6$), K-feldspar ($KAlSi_3O_8$), K-mica ($KAl_3Si_3O_{10}(OH)_2$), Kaolinite ($Al_2Si_2O_5(OH)_4$), Manganite ($MnO(OH)$), Quartz ($SiO_2$), Rhodochrosite ($MnCO_3$), Smithsonite ($ZnCO_3$), Vivianite ($Fe_3(PO_4)_2{:}8H_2O$) and Willemite ($Zn_2SiO_4$).

	S 1.1 (18.4)	S 1.2 (18/4)	S 2.1 (18/4)	S 2.2 (18/4)	S 1.1 (13/6)	S 1.2 (13/6)	S 2.1 (13/6)	LA (10/7)
Al(OH)3	0,73	1,17	0,8	0,61	-	-	-	-
Albite	0,26	0,7	0,58	0,35	-	-	-	-
Alunite	5,7	6,79	5,53	4,94	-	-	-	-
Anorthite	-	0,45	0,07	-	-	-	-	-
Ca- Montmorillonite	7,3	8,31	7,52	7,06	1,46	-	1,5	3,13
$Fe(OH)_3$	5,91	6,04	6,16	6,06	2,92	2,85	2,65	3,74
Gibbsite	3,67	4,11	3,74	3,55	1,93	1,03	2,35	2,08
Goethite	10,83	10,96	11,08	10,98	7,84	7,77	7,57	8,66
Hematite	23,54	23,8	24,05	23,84	17,55	17,41	17,01	19,2
Hydroxyapatite	4,01	4	5,14	5,13	-	-	-	-
Illite	6,31	7,33	6,74	6,24	0,05	-	-	2,58
Jarosite-K	7,24	7,42	7,64	7,32	-	-	-	-
K-feldspar	1,43	1,89	1,76	1,52	-	-	-	-
K-mica	14,26	15,59	14,72	14,09	6,88	4,02	7,25	9,38
Kaolinite	8,58	9,45	8,72	8,33	4,21	2,42	4,59	5,05
Manganite	1,1	1,15	1,65	1,47	-	-	-	-
Quartz	0,26	0,26	0,26	0,26	-	-	-	0,09
Rhodochrosite	2,12	2,15	2,25	2,03	-	-	-	-
Smithsonite	-	0,31	0,24	-	-	-	-	-
Vivianite	2,45	2,82	1,71	1,34	-	-	-	-
Willemite	-	0,52	0,49	-	-	-	-	-
SI CO_2	-2,16	-2,19	-2,25	-2,27	-2,83	-2,9	-2,89	-3,71

In-situ measurements of the spring and lake water were performed for pH, ORP and DO (Table 9). The pH of the springs shows slightly alkaline water with values ranging between 7,11 – 7,61. Both, for spring 1 and 2, the pH was higher in April than in June. The highest pH was measured in the lake water (7,91). ORP was clearly negative in April for spring 1 and 2, showing reducing conditions, but positive in June. ORP of the lake water reveals oxidizing conditions, as indicative for surface water. While DO was low in spring water in April, concentrations were higher in June.

Table 9: In-situ measurements of spring and lake water. Values show the average calculated from three measurements except for spring 2 (18/4) DO and lake water where only one measurement was performed. DO was not recorded for lake water since it is a surface water body. Standard deviation in parentheses.

Location (date)	pH	ORP (mV)	DO (mg l^{-1})
Spring 1 (18/4)	7,44 (0,01)	-79,87 (0,17)	5,36 (0,42)
Spring 1 (13/6)	7,12 (0,00)	67,10 (10,39)	12,38 (0,32)
Spring 2 (18/4)	7,61 (0,05)	-67,70 (1,13)	4,50
Spring 2 (13/6)	7,11 (0,00)	121,77 (1,87)	12,73 (0,03)
Lake (10/7)	7,91	134,00	-

5.3.4 Comparison of Ice Core and Spring Hydrochemistry

Comparisons between the chemical composition of ice cores and waters samples are carried out on the basis of those solutes that were quantified in both sets of samples: NH_4^+, Si, Na^+, K^+, Mg^{2+}, Ca^{2+}, F^-, Cl^-, NO_3^-, SO_4^{2-} and DIC. The same order of ion abundance was measured in ice cores and April samples whereas $SO_4^{2-} > Na^+ >$ DIC $> Ca^{2+}$. When comparing TDS of ice cores with water samples, ice cores show a significantly lower abundance of dissolved solutes compared to the springs sampled in April and the lake. Average TDS in ice cores is a factor 4,1 lower than in the average of April spring samples and 2,9 than TDS of lake water. The dilute composition of the ice cores compares best to TDS measured in spring samples from June whereas TDS is 0,5 times higher in ice core averages compared to June spring samples (Figure 34). A high correlation exists between all ice cores and spring samples with Pearson correlation coefficient (r) > 0,9. Lowest correlation was calculated between lake sample and ice cores, especially core 4 and 5 with r = 0,78 and 0,83, respectively, sampled from the part of the icing located beneath the lake.

Figure 35 displays ternary plots to illustrate the relative proportion of the cation (a) and anion (b) composition in ice cores and water samples calculated in % mEq. Ice core

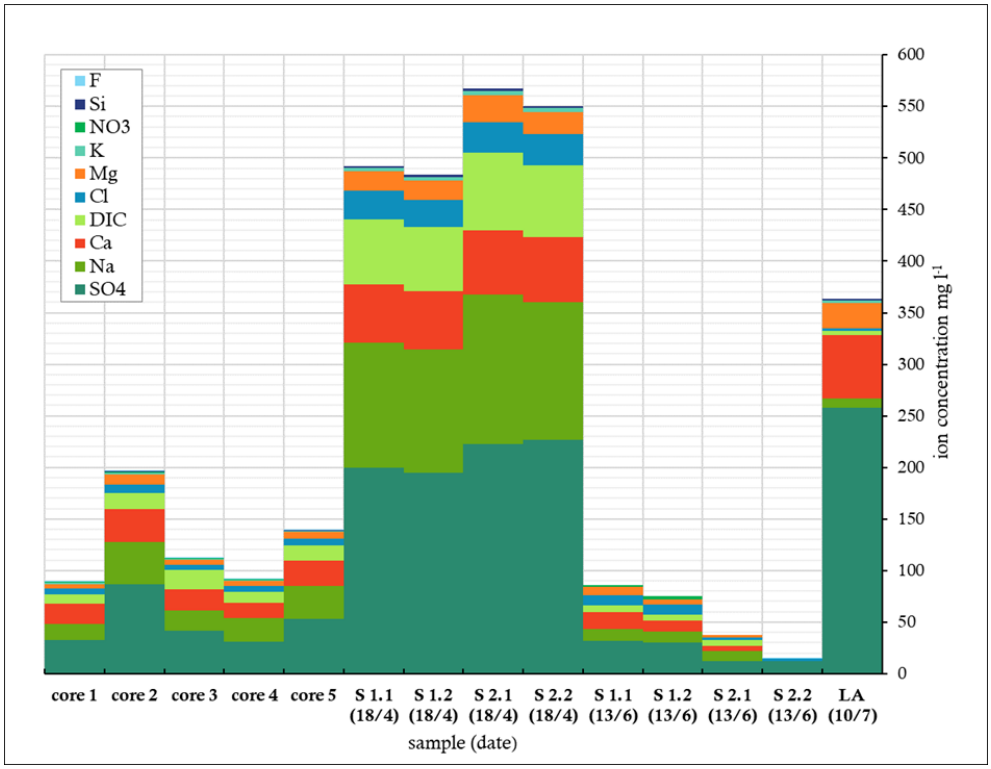

Figure 34: Comparison of solute species quantified in both, ice core and water samples. Concentrations in ice core subsamples are averaged for the whole core. S1 denotes spring 1, S2 spring 2 with duplicate samples and LA lake. Only ions with a concentration > 1mg l^{-1} are plotted.

samples show a heterogeneous signature in regard to Cl^-. The stretch in the anion plot is caused by the range of SO_4^{2-} and HCO_3^- whereas HCO_3^- is the dominating anion in most subsamples. SO_4^{2-} is more abundant than Cl^- in all samples. In the cation plot it becomes obvious, that the cluster of ice core subsamples is less coherent than for anions with Ca^{2+} as dominant cation in most, but not all subsamples. Ca^{2+} ranges between 24 – 72 % and $Na^+ + K^+$ between 17 – 55 %. Samples with a high Ca^{2+} concentration are low in $Na^+ + K^+$ and vice versa, whereas Na^+ dominates the $Na^+ + K^+$ abundance.

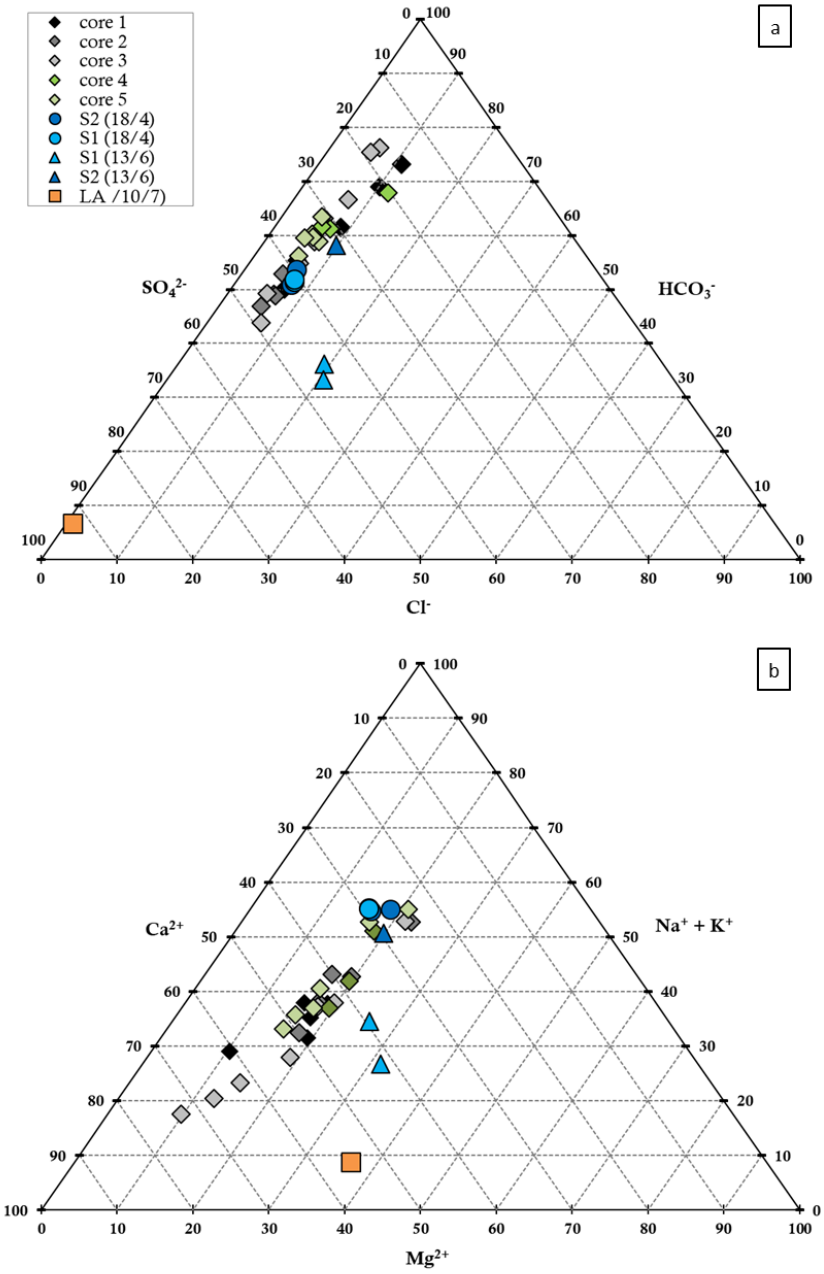

Figure 35: Ternary plots for comparison of (a) cations and (b) anions (in % mEq) in ice core and water samples.

April spring samples and June sample of spring 2 align well with those ice core sub-samples with Na^++K^+ as dominant cation and with average HCO_3^- and SO_4^{2-} ratios. June samples of spring 1 deviate more due to the higher portion of Cl^- and lower HCO_3^- as well as Ca^{2+} as dominating cation, higher Mg^{2+} and hence lower Na^++K^+. The lake sample deviates most from all other samples through the dominance of Ca^{2+} as cation compared to Na^+ in ice cores, April spring and spring 1 in June. SO_4^{2-} is clearly the dominant cation in the lake sample with 92% locating the sample in the SO_4^{2-} corner of the plot.

To assess the predominate weathering reactions that provides protons to the solution, the S-ratio was calculated as in (Eq. 10) with * SO_4^{2-} (non-snowpack derived portion of SO_4^{2-}). All ice core and spring water samples range around 0,5 with ice core averages between 0,36 – 0,58 and April spring samples at 0,4. June samples from S1 are slightly higher (0,54 and 0,57) than April and June S2 samples (0,35). S-ratio of lake water distinctly deviates from ice core and spring samples with an S-ratio of 0,93. Values around 0,5 indicate proton supply through coupled sulphide oxidation and carbonate dissolution with a slightly higher influence of sulphide oxidation in those samples >0,5 and of carbonate dissolution in samples <0,5. S-ratio of lake water shows the clear domination of sulphide oxidation. (Brown 2002)

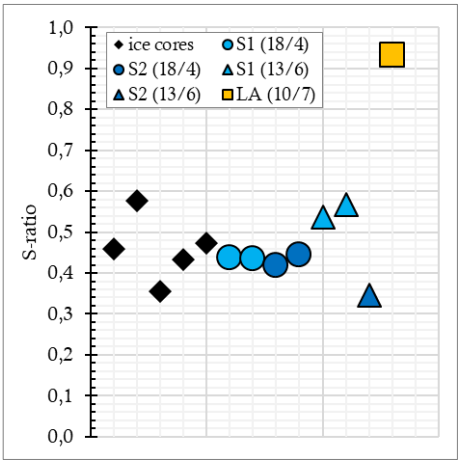

Figure 36: S-ratio calculated for ice core averages and water samples with *SO_4^{2-} as in Eq. 10 in equivalent units of concertation. The ratio ranges between 0 (carbonation) – 1 (sulphide oxidation).

5.3.5 Stable Water Isotopes

The ratio of stable water isotopes, $^{18}O/^{16}O$ and $^{1}H/^{2}H$, was quantified in four samples from the springs and lake collected between April to July 2017 in the forefield of Rieperbreen. The abundance of light isotopes in both measured stable isotopic ratios (δD and $\delta^{18}O$) is higher than in the reference standard resulting in negative values

(listed in Table 10). δD and $\delta^{18}O$ values range between -108,89‰ to -84,72‰ and -15,95‰ to -11,44‰, respectively. Lake water is the sample most enriched in heavy isotopes shown by highest values. Spring samples are considerably depleted in heavy isotopes compared to lake water. Values of repeated measurements for the spring samples (1.2, 1.4 and 2.2, 2.4) are in good agreement with the first values (1.1, 1.3 and 2.1, 2.3). However, isotopic ratios vary significantly between the April and June samples. While June samples from spring 1 are more depleted compared to April samples, water from spring 2 shows enrichment of heavy isotopes later in the season. $\delta^{18}O$ values in April samples from spring 1 and spring 2 are comparable but water from spring 2 is more depleted in δD. Differences in the isotopic ratios of the springs are even more prominent in June samples. Especially when comparing δD with values averaging around -108‰ for spring 1 and significantly higher values in the water of spring 2 (-92‰). D-excess was calculated in accordance to Eq. 19 and ranges between 6,8‰ to 18,82‰. The lake sample (6,8‰) exhibits a markedly lower d-excess than spring samples ranging between 13-15‰. Only S1.3 and 1.4 deviate with a d-excess of almost 19‰.

Table 10: *Isotopic ratios of water samples collected from springs and. Deuterium excess was calculated as* $d = \delta D - 8*\delta^{18}O$.

Location (date)	δ^2H	$\delta 18O$	D excess
Spring 1.1 (18/4/17)	-105,57	-15,11	15,29
Spring 1.2 (18/4/17)	-106,10	-15,11	14,79
Spring 1.3 (13/6/17)	-108,53	-15,92	18,82
Spring 1.4 (13/6/17)	-108,89	-15,95	18,69
Spring 2.1 (18/4/17)	-108,34	-15,46	15,34
Spring 2.2 (18/4/17)	-108,18	-15,38	14,90
Spring 2.3 (13/6/17)	-92,43	-13,22	13,32
Spring 2.4 (13/6/17)	-92,27	-13,23	13,56
Lake 1 (10/7/17)	-84,72	-11,44	6,8

In Figure 37a, data from the springs and lake at Rieperbreen are plotted in a co-isotope δD - $\delta^{18}O$ diagram together with data from the Rieperbreen springs sampled in 2014/15 and the spring feeding the Foxfonna icing (2017) provided by Hodson (2017, unpublished data) and springs feeding an icing in front of Brandtbreen. The values are plotted together with the Global Meteoric Water Line (GMWL) and a Local Meteoric Water Line (LMWL), indicating the isotopic ratio of precipitation in a certain region, to assess a relationship between isotopic values of samples and precipitation. The GMWL is defined as $\delta D = 8 * \delta^{18}O + 10$ (Craig 1961). The LMWL was constructed from data provided by the International Atomic Energy Agency (IAEA 2017). It deviates

from the GMWL and is defined by a slope of $\delta D = 6{,}46 * \delta^{18}O - 5{,}98$. Data used for the LMWL consists of 75 monthly averages of δD and $\delta^{18}O$ values measured in precipitation samples collected between 1961-1965 and 1972-1975 at Isfjord Radio. Even though the study area is located 57 km east of Isfjord Radio, all spring samples fit relatively well with the LMWL. While the June samples from Rieperbreen align perfectly with the LMWL, the other spring samples are located slightly below. The lake sample shows significantly higher values and deviates most from the LMWL. Values of samples from the Rieperbreen springs obtained in Mai 2014 and April 2015 show a good correlation with April samples from 2017.

The relationship between δD and d-excess is examined in Figure 37b, to assess whether the deviation from the LMWL is caused by fractionation. While δD and d-excess show a linear correlation in precipitation ($R^2 = 0{,}91$ in the used LMWL), fractionation during evaporation and freezing after precipitation changes the values compared to the LMWL. During evaporation, lighter isotopes evaporate preferentially leaving the remaining water enriched in heavy isotopes; during freezing heavy isotopes enter the solid state sooner leaving the remaining water depleted in heavy isotopes (Kendall & Caldwell 1998; Tranter 2011). All samples from the Rieperbreen spring are located above the LMWL, samples from Brandtbreen and Foxfonna align with the LMWL and the lake sample is located below the LMWL.

The increase in d-excess in the Rieperbreen spring samples can be explained by fractionation during freezing. The effect is most prominent in the June samples from spring 1 showing the highest d-excess values. The deviation from the LMWL is comparable for both samples from spring 2 and the April sample from spring 1. Samples from the Rieperbreen springs collected in 2014 and 2015 lie within the range of the 2017 samples. Samples from the springs at Brandtbreen and Foxfonna are aligned close to the LMWL. Hardly any fractionation occurred in these samples leaving the isotopic ratio similar to that of the parental water. The lake sample deviates most from the LMWL and shows a large decrease of d-excess compared to meteoric water.

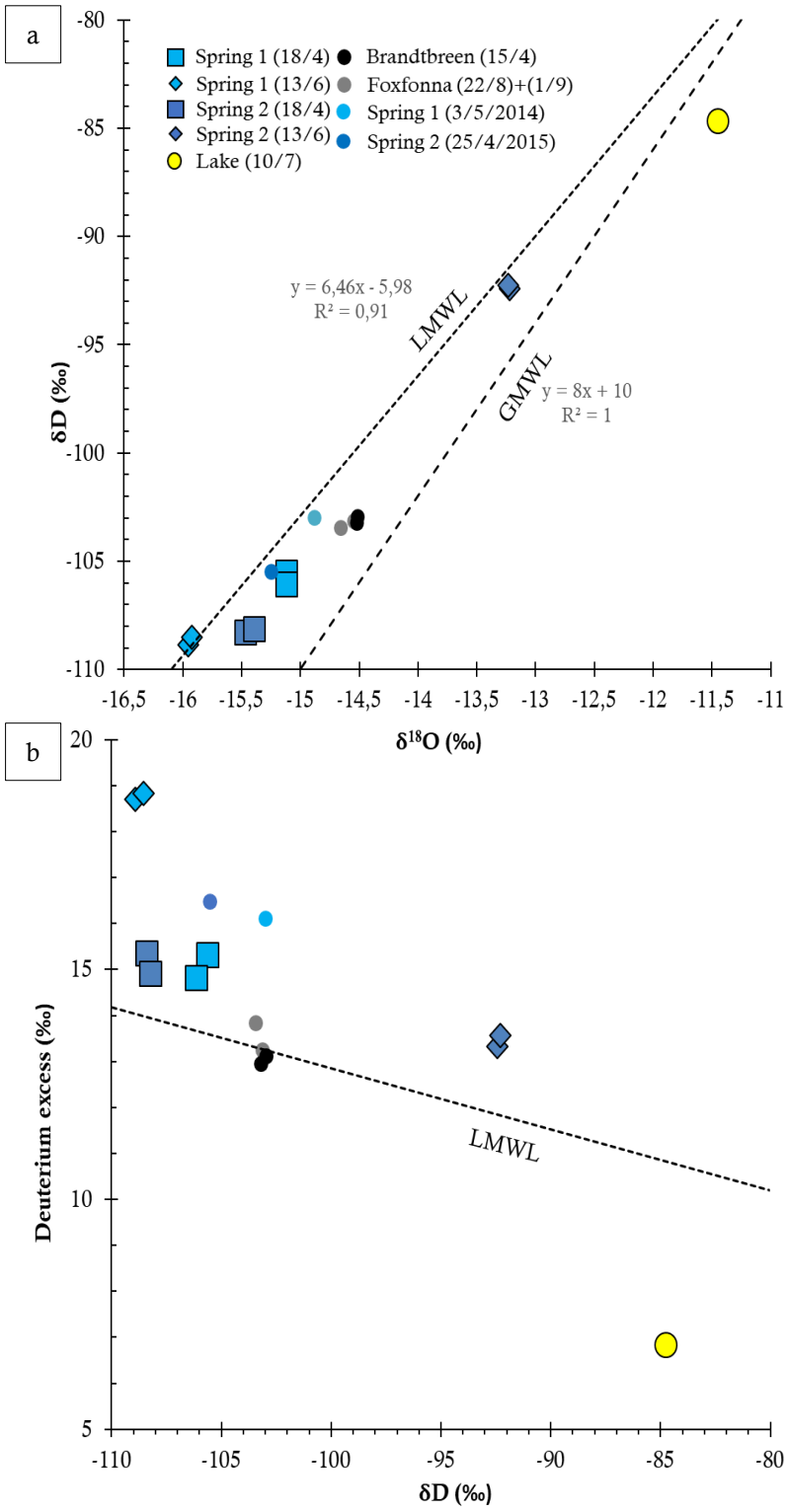

Figure 37: (a) δD - $\delta^{18}O$ diagram for spring samples from Rieperbreen, Brandtbreen, Foxfonna and the lake in the Rieperbreen moraine complex. The lines indicate the Global Meteoric Water Line (GMWL) defined as $\delta D = 8 * \delta^{18}O + 10$ (Craig 1961) and the Local Meteoric Water Line (LMWL) of $\delta D = 6,46 * \delta^{18}O - 5,98$ ($R^2 = 0,91$) (after IAEA 2017); (b) δD - d relationships of samples. Deuterium excess is defined as $d = \delta D - 8*\delta^{18}O$. The dashed line indicates the LMWL. Isotopic data from spring 1 (2014) and spring 2 (2015) at Rieperbeen and from the spring at Foxfonna (2017) is provided by Hodson (2017, unpublished data).

5.3.6 Source of Error Hydrochemistry and Future Adaptations

Sources of error in hydrochemical results may arise from technical difficulties during the sampling process, unavailable quantities of solutes as well as contamination during sampling and processing.

Difficulties arose during ice core sampling due to technical reasons. The maximum possible sampling depth of ice cores, given the used core barrel, were 70 cm. This depth was only reached for core 3 whereas the length of the others varied between 26 to 60 cm. When sampling core 1, the bed was reached after 40 cm when a sediment-ice mix started to accumulate around the barrel. Ice core 2 was 60 cm long since the bottom 10 cm could not be retrieved from the drill hole, neither by hand nor with the help of an ice screw. While drilling ice core 4, a reservoir of intra icing water was punctured at a depth of 26 cm. As soon as the core was pulled out, the drill hole filled up with water (Figure 13 c). Due to the intrusion of water into the core barrel, the upper ~10 cm of core 4 froze to the inside of the barrel immediately and could only be removed later in the laboratory. Therefore, the maximum possible depth for core 5 were 60 cm.

Stable water isotopes and certain solutes such as Fe, Mn, S, Zn and Ni quantified in water samples and showing considerable abundance, remained unanalysed in ice core samples due to cost limitations and missing acidification of ice core water. This resulted in a high charge balance error (up to 22%) in those ice core subsamples were unanalysed ions were abundant, a dilute composition of ice cores compared to spring samples and further saturation indices calculated for less minerals than for spring samples. Whether the analyses of stable water isotopes in melted ice cores from the icing would have yielded valuable information is questionable due to bias introduced by freezing. Further, HCO_3^- concentrations for water samples were calculated with the charge balance method only due to unrealistic values obtained for DOC. The values therefore might be biased since they also include concentration uncertainties of those solutes used in the calculation.

Several adaptations are recommended regarding sampling for hydrochemical analyses. In case the composition of the icing is of interest, it is advised to drill ice cores to the bottom of the icing, as intended in this study, but not accomplished given the equipment. Full-depth ice cores allow to better assess the average composition of

the icing and process of icing formation. More ice core samples would further allow a better assessment of changes in the icing chemistry due to preferential freezing. In general, the collection of more spring water samples with less time between sample collection is recommended since water samples yield more realistic results of the water provenance than ice cores due to smaller freezing bias. With the exact location of the springs feeding the icing, spring samples could be collected sooner during the accumulation season and might be located again once the icing has ablated providing a longer sample record to deduce changes in the chemistry of the surfacing water during the season.

5.4 Dye Tracing

5.4.1 Dye Breakthrough Curves

By plotting the measured fluorescence in the proglacial river against the time, dye passing by stations 1 and 2 was visualized as breakthrough curves (BTCs). Figure 38 displays such graphs for both stations combined (a) and station 1 (b) and station 2 (c) separately. Soon after all dye injections (vertical red lines), a distinct increase in fluorescence can be seen at both stations. BTCs from station 1 and 2 exhibit similar shapes. The strength of the recorded signal however, varies significantly between stations (a). All BTCs exhibit a stronger signal at station 1 compared to station 2. The intensity of the signal further varies between experiments. Dye returns attributed to experiments 4, 5 and 6 emerge with a markedly higher concentration at both stations than the previous ones. It is evident from Figure 38 b, that the returns of the last three injections overlapped. Hence, the fluorescence in the river did not drop to its base level before the next dye cloud arrived. As a result, the BTCs start and/or end at an increased level of fluorescence. Additionally, a notable time lag between the arrivals of dye clouds at station 1 and 2 can be seen from Figure 38 a. As expected, due to the location of the stations, the dye cloud is first registered at the upper station before arriving at the lower station.

A striking difference of the breakthrough curves is, that apparently more dye returns were recorded at station 1 than at station 2. Especially noticeable are four curves, recorded on Julian Day (JD) 233, 234, 235 and 236 at station 1, which exhibit a significantly different shape to all other BTCs. These curves are not characterised by a gradual increase of fluorescence in the river followed by a slow decrease resulting in

a smooth curve with a single peak, as is the case for most other breakthrough curves, but instead through a sudden increase from the base level, multiple higher values of similar magnitude followed by a sudden drop of the fluorescence back to base level values resulting in an edgy shape of the curve. Figure 40 shows these curves in detail which were all recorded in the morning hours lasting from about 8 - 11am. Figure 38 c reveals that these signals were not recorded at station 2.

The shape of BTCs is best examined in Figure 39 a+d. BTCs attributed to dye injections 1, 2 and 3 exhibit a single-peaked shape. While the curves recorded on JD 232 and 234 indicate a fast increase and a slower decrease in fluorescence, BTC recorded on JD 233 is flat-angled due to a slower in- and decrease. At station 1, dye BTCs from experiments 4, 5 and 6 consist of two distinguishable peaks following in quick succession. The curve produced by experiment 6, however, was regarded as single-peaked in further analyses since the decline after the first peak is rather small before fluorescence values increased again. At station 2, the two peaks of BTC from injections 4,5 and 6 merged to produce a single-peaked curve whereas the first peak only remains as a faint signal. Further, the BTCs at station 2 are wider than at station 1. This can be seen especially by comparing the BTC from injection 3. While the dye cloud produced a noticeable curve at station 1, the signal at station 2 is practically lost. Towards the end of the experimental period (JD 236 onwards), increased levels of fluorescence were recorded at both stations.

The duration between injection and recorded peak concentrations (= return time) were calculated for each experiment and are listed in Table 11. At station 1, peak concentrations were recorded between 14 to 1389 minutes after injection, with most curves peaking after < 4h. In all experiments, the return time compares well with the transit distance. As expected, the fastest return was recorded from experiment 4 with the most proximate injection point located 128 m from the station. At station 2, the dye concentration peaked on average 89 minutes after station 1. For comparison of return times, the BTCs of all experiments were plotted against the time since injection (Figure 39). Calculated throughflow velocities for dye passing station 1 ranged between 0,02 to 0,25 ms^{-1}. The lowest velocities were calculated for experiment 2 and the highest for the first peak of the curve attributed injection 5. Throughflow velocities calculated for BTC at station 2 ranged between 0,03 to 0,20 ms^{-1}. Further, the flow velocity between the two stations was calculated (see Table 11).

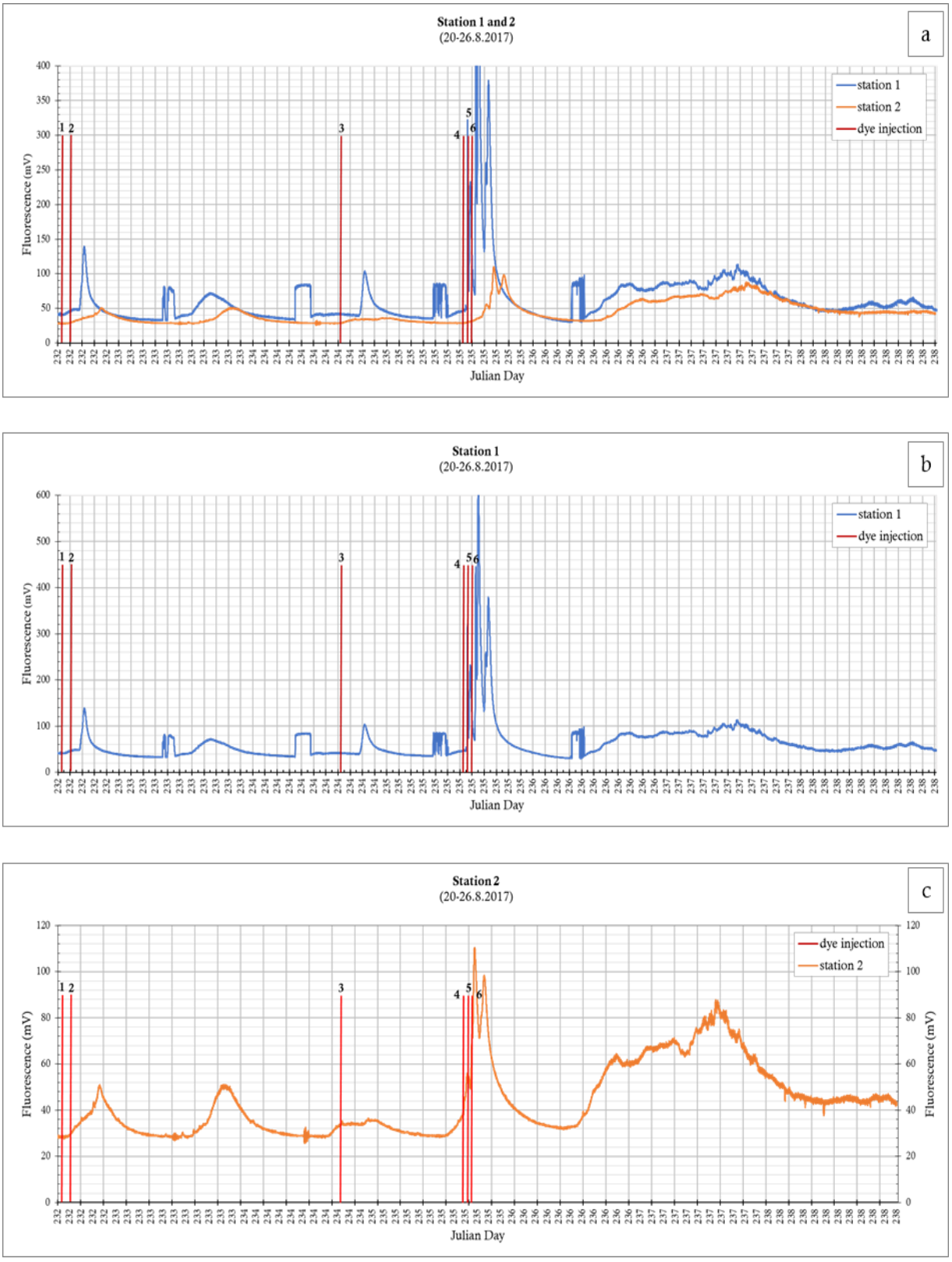

Figure 38: (a) Dye BTCs recorded at station 1 and 2; (b) at station 1 only and (c) at station 2 only. The vertical red lines mark the times of dye injection. Notice the different scaling of the y-axis in (c) for better visualisation. While experiments were conducted between Julian Days 232 to 235, the whole record until day 238 is plotted.

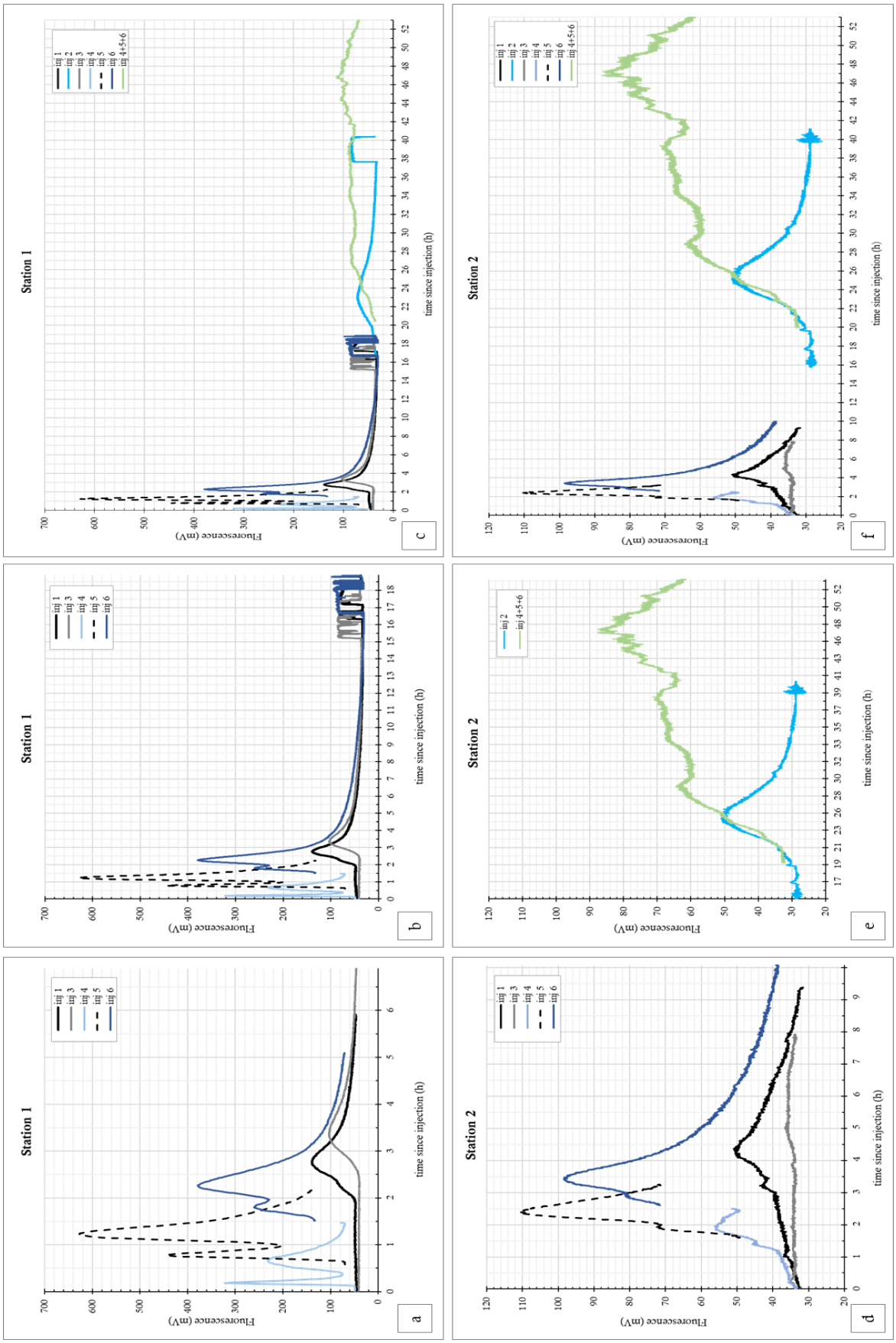

Figure 39: (a-c) BTCs at station 1 and (d-f) at station 2 plotted as time since injection. BTCs attributed to injections 5 and 6 do not start at time 0 since another dye return was registered after injection. Note the diferent scaling of the x axis between graphs of station 1 and 2.

Table 11: Results of dye BTC analyses for station 1 and station 2. The transit distance was approximated by a straight-line between injection and detection point measured from TopoSvalbard (toposvalbard.npolar.no). As *time of peak*, the moment of the highest fluorescence value of a BTC was selected. The difference of return times at station 1 and 2 was calculated with the return time of peak 1 at station 1 unless otherwise indicated by an asterisk.

		Station 1						Station 2					
Code	**Julian Day, injection time**	**transit distance (m) station 1**	**time of peak(s)**	**return time (min) peak 1**	**return time (min) peak 2**	**throughflow velocity (ms^{-1}) peak 1**	**throughflow velocity (ms^{-1}) peak 2**	**transit distance (m) station 2**	**time of peak**	**return time (min) peak 1**	**diff (min) return time station 1**	**throughflow velocity (ms^{-1})[1]**	**velocity from station 1 (ms^{-1})[2]**
1	232, 16:26	1340	19:16	170	-	0,13	-	2328	20:50	264	94	0,15	0,18
2	232, 18:02	1830	17:11 (JD 233)	1389	-	0,02	-	2818	19:12	1500	111	0,03	0,15
3	234, 16:45	1340	20:09	204	-	0,11	-	2328	21:41	296	92	0,13	0,18
4	235, 13:57	128	14:11; 14:39	14	42	0,15	0,05	1116	15:56	119	91*	0,16	0,18*
5	235, 14:47	749	15:37; 16:03	50	76	0,25	0,16	1737	17:13	146	83*	0,20	0,20*
6	235, 15:30	1340	17:49	139	-	0,16	-	2328	18:57	207	68	0,19	0,24

* calculated with the average of return times from peak 1 and 2 at station 1

[1] The distance between injection and detection point was approximated by a channel with a sinuosity of 0.

[2] Flow velocity of the proglacial river between station 1 and 2. The value represents the minimum velocity since the distance was approximated by a 988 m long straight line measured in TopoSvalbard (toposvalbard.npolar.no).

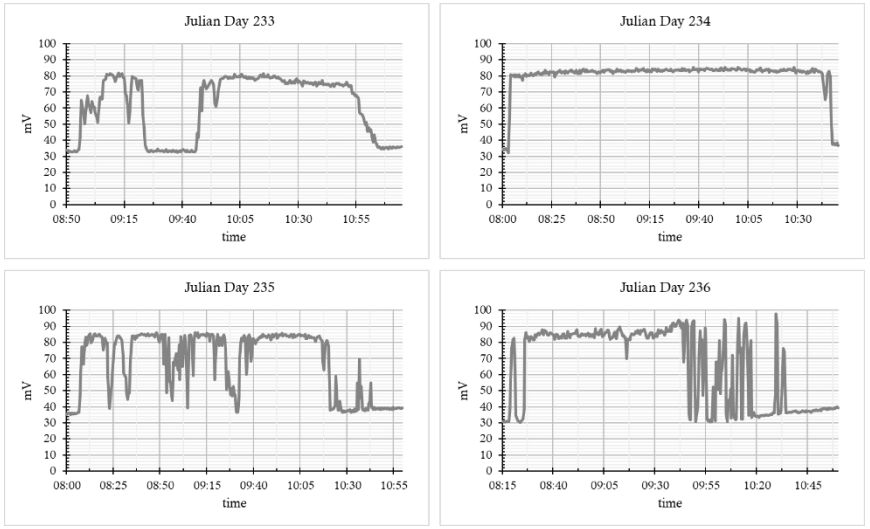

Figure 40: shows the four edgy curves recorded in the mornings of on JD 233-236 at station 1 as seen in Figure 38.

5.4.2 Source of Error Dye Tracing and Future Adaptations

Sources of error regarding the results of dye tracing experiments mainly arise from the interpretation of breakthrough curves. The overlap of BTCs in the given study complicates the ascription of a measured dye emergence to one of the experiments. The calculation of the dispersion coefficient and dispersivity was omitted whereas the rationale for this decision was threefold. Firstly, due to the overlap of several return curves, mathematical interpolations would need to be performed to recreate overwritten values. Since discharge was not measured together with the fluorescence, missing values cannot be approximated from a simple regression of a constant discharge-fluorescence relationship but would rather involve assumptions about the geometry of the curve and further the channel geometry. Secondly, parameters obtained through numerical BTC analyses would presumably yield similar values due to the comparable shape of the return curves and would not provide information on the connection between the spring and the glacier. And thirdly, the principal aim for this method was to investigate water provenance, rather than the configuration of the meltwater channels, for which visual analyses of BTCs suffice.

To ensure the recording of emerging dye from spring 1, future work should include a relocation of station 2, in case of downstream movement of the spring compared to the sample location in June, and the measurement of discharge of the proglacial river at both stations. With a known discharge, the weight of dye (*W*) (in g) passing the station can be calculated by multiplying the discharge of the river with the area underneath the BTCs (Hubbard & Glasser 2005; Clason et al. 2015):

Eq. 25

$$W = \sum_{t=1}^{n} c * Q * dt$$

where *c* is the concentration of dye, *Q* the average discharge during the experiment and *dt* the interval between recorded values. From this value, the percentage of tracer recovery (*W%*) is derived through:

Eq. 26

$$W\,\% = 100 * \frac{W}{W_0}$$

where W_0 is the mass of dye that was injected (Clason et al. 2015). Results from these calculations would, in this study, provide information about the amount of dye that did not pass by the stations but was stored in the glacier or routed into another flow path besides the one emerging through the portal and therefore assess a connection between the current drainage system with a channel not discharging through the glacier portal.

Discharge data would further aid in separating overlapping BTCs for the calculation of numerical parameters such as dispersion and dispersivity, and turbidity measurements in quantifying the influence of natural background fluorescence. For future dye tracing experiments, it is advised to perform only one dye tracing experiment per day to allow sufficient time between experiments to allocate return curves to the corresponding dye injections and to allow fluorescence levels in the river to drop to base concentration before the arrival of next dye cloud. This would permit to calculate dispersivity without having to model missing limbs of the BTC due to overlaps. Further, in order to trace a very slow flow path connecting the en- and subglacial drainage system with the springs, the experimental period is needed to be extended.

6 Discussion and Interpretation

6.1 Interpretation of Radargrams

GPR surveys of the icing and adjacent areas were performed to map the extent of the icing, evaluate the connection of visible icing areas during winter, study the internal morphology, estimate the icing thickness, and locate the spring(s) forming the icing.

Results from GPR surveys help to map the overall extent of the icing. An extensive icing on the flat outwash plain in front of moraine ridge 3, as seen on older aerial photographs, is deemed absent during the 2016/17 accumulation season. Indications are the absence of ice on the surface and the lack of strong reflections displaying the presence of ice between snow and the debris-sediment mix covering the floor of the braided river channel. Later visits during the ablation season confirmed this assumption, when the meltwater river was seen to quickly erode through the snow pack, but no stratified ice bordered the channel as observed farther down within the visible icing bodies. The ice at the bottom of the snow pack in the western part of area 1, from which ice core 1 was sampled, could be the top part of the icing fed through spring 1 but also refrozen meltwater in a channel of the braided river. The origin of this ice is further discussed in chapter 6.2.5.

Radargrams recorded from the flat outwash plain between the two visible icings further downstream indicate the absence of a subsurface connection. The top of the lower icing; eastern margin of area 3; and the bottom of the upper icing; western margin of area 2; (Figure 26 and Figure 27) show inclined reflections which are interpreted as soaked snow found at the edge of icings. The two icing areas are therefore interpreted separated which further leads to the assumption of the presence of at least two springs in the Rieperbreen forefield.

Radargrams obtained from the icing reveal a complex internal morphology. The icing is composed of different ice types and water is abundant throughout the icing, on the surface as well as at the base. Internal reflections further reveal the existence of former water filled channels which are now abandoned and filled with air. The thickness of the icing is difficult to describe since no continuous bottom reflector can be identified in radargrams from the icing. However, strong basal reflections found in several locations of the icings are likely to indicate the presence of water at the base of the icing. These

reflections are found at depths of 2m (Figure 26) which is expected to yield a good estimate for the maximum thickness of the icing. The springs feeding the icing could not be discerned in the radargrams collected here.

6.2 Interpretation of Hydrochemistry

6.2.1 Stratigraphy of Ice Cores

The parallel layering of ice cores shows the formation of the icing through freezing of successive sheet flow. Different ice facies within the icing have been described to either develop from the incorporation of snow deposited onto the icing surface by sheet flow (Åkerman 1980, Hodgkins et al. 2004) or to indicate the speed of freezing (Moorman & Michel 2000). Åkerman (1980) proposes, that snow deposited onto the icing surface during precipitation or through wind drift is soaked by sheet flow and subsequently incorporated into the icing as snow slush. This is suggested to lead to the formation of an ice layer characterised by a higher air bubble content and a different crystal structure than the freezing of sheet flow, when snow is absent, which results in clear ice layers. Moorman & Michel (2000), however, describe that clear ice layers are formed when water freezes slowly allowing air bubbles to be pushed out of the forming ice layer. This process may take place on the icing surface during relatively warm air temperatures and slow freezing of sheet flow but also within and below the icing when sub- or intra-icing water freezes slowly onto the existing ice layer. Contrary, bubble-rich ice layers indicate a fast-freezing process during which existing air bubbles are trapped within the ice (Moorman & Michel 2000) as would be the case when water surfaces under low atmospheric temperatures.

The chemical composition of ice core sub-samples defined as clear and bubble-rich ice varies significantly. The larger portion of snow in bubble-rich ice layers compared to clear ice layers, as suggested by Åkerman (1980), cannot be validated by the chemical composition of ice cores sampled in this study. Concentration of Cl^-, indicative for snow, is higher in subsamples defined as bubble-rich ice. Most other solutes follow this trend leading to a significantly higher solute abundance in bubble-rich ice compared to clear ice subsamples. The suggestion by Moorman & Michel (2000), that the speed of freezing explains the ice type whereas air bubbles are expelled to the freezing front, also applies to solutes rejected from the forming ice crystal lattice during freezing. Therefore, the ice types and stratigraphy of the icing are

assumed to be governed by the speed of freezing rather than by the presence or absence of surface snow and further to hold information about the process of formation of the ice layers rather than the source of water. However, ice cores could have been divided into too few and hence too wide subsamples to detect layers primarily composed of snow.

6.2.2 Process of Icing Formation

The hydrochemical composition of ice cores shows a high variability regarding the concentration of dissolved solutes whereas intra-ice core differences are more pronounced than inter-ice core differences. TDS varies with a factor of up to 6 between subsamples of the same ice core (core 3) but only with a factor of 2 between the most concentrated and most dilute cores. The high intra-ice core variability, however, results in solute concentrations up to 7,6 times higher in the subsample with the highest compared to the lowest TDS in all cores.

These pronounced differences within a vertical icing profile could be interpreted as layers formed from water of different composition and, further, origin. The periodic presence of snow on the icing surface may offer a possible explanation: snow incorporated by sheet flow is expected to result in the formation of an ice layer with low TDS and higher abundance of atmospherically derived solutes (Cl^- and Na^+) compared to a layer formed exclusively from concentrated spring water under the absence of snow. However, the concentrations of snowpack-derived Cl^- and Na^+ show a positive linear correlation with TDS and hence increase with increasing solute concentration in sub-samples. For this reason, low TDS does not indicate a subsample composed mainly of incorporated surface snow diluting concentrated spring water and further, that the composition of different water sources fails to explain the highly variable TDS of subsamples. Incorporated snow, rain and, potentially, surficially routed snowmelt from the adjacent slopes, are nevertheless regarded to contribute to the volume of the icing. Major crustally derived ion species (SO_4^{2-}, HCO_3^- and Mg^{2+}) follow the trend of correlation with TDS ($R^2 > 0,9$) in subsamples. Further, a strong exponential correlation ($R^2 > 0,93$) prevails between increasing solute concentrations and SI_{Halite}, $SI_{Anhydrite}$ and SI_{Gypsum}. Against expectations, minerals reaching SI > 1 in sub-samples do not correlate with TDS. Precipitates, remaining in the glass beakers used for ice core melting and not transferred into sample bottles for analyses, may account for the missing correlation. SI values in (Table 6) are therefore interpreted as underestimates.

The high variability of solute concentrations is explained by cryochemical effects during icing formation as before by Wadham et al. (2000). When water first freezes, most dissolved solutes (up to 99%) are rejected from the growing ice lattice. The first ice layer forming either on the icing surface when sheet flow freezes or onto the sides of a water-filled intra-icing void, is denoted by a low concentration of dissolved solutes. The remaining water is relatively enriched in solutes compared to the initial water with progressively increasing concentrations as freezing continues. (Wadham et al. 2000) Once the residual water freezes, it results in the formation of the ice layer with the highest TDS formed from the same initial water. Consequently, the variable TDS holds information about the process of freezing rather than different water sources, as was also shown for different ice types, and the relative timing of formation of an ice layer compared to the neighbouring ones. This process further indicates, that the chemical composition of the icing is altered compared to the initial water and that the ion abundance of sub-samples is biased through freezing.

Due to the high variability of the ionic composition within subsamples, averages were calculated for ice cores presumed to decrease the freezing bias and hence yield better estimates of the water that formed the icing (Wadham et al. 2000). From average concentrations, the relative proximity of the sampled ice core to the spring can be assessed. Certain minerals such as calcium carbonate and calcium sulphate precipitate out of solution soon after surfacing due to low solubility in low temperatures. Enrichment of ions composing these minerals (Ca^{2+}, SO_4^{2-} and HCO_3^-) in an ice core therefore indicate the proximity of the sample location to the outlet whereas depletion of these ions is expected in samples collected at greater distance. (Wadham et al. 2000) This implies, that the concentration of Ca^{2+}, SO_4^{2-} and HCO_3^- are supposed to be higher in the ice cores sampled closer to a spring, hence core 2 and 5, compared to core 3 and 4 sampled farther from spring 1 and 2, respectively. Concentrations of Na^+, Mg^{2+} and Cl^- are expected to behave conversely. This implication is verifiable for Ca^{2+}, SO_4^{2-} and HCO_3^-, however not for Na^+, Mg^{2+} and Cl^-. HCO_3^- is more abundant in core 2 than core 3 (ratio of 1,61) and in core 5 than core 4 (ratio of 1,39). The same applies for the concentration of SO_4^{2-} with a ratio of 2,1 for core 2: core 3 and 1,7 for core 5: core 4 as well as for Ca^{2+} with a ratio of 1,5 and 1,6. Further, SI for saturated minerals (Aragonite, Calcite, Dolomite, Quartz and Talc) follow the same pattern. However, opposite to the study of Wadham et al. (2000), Na^+, Mg^{2+} and Cl^- as well as

all other solutes are more concentrated in cores 2 and 5 compared to cores 3 and 4. This is presumed to yield additional information regarding the formation process.

Owing the higher TDS in proximity to the outflow compared to more distal icing areas, the icing is assumed to form mainly through surface sheet flow where most of the water freezes fast onto the surface and only small amounts are transported greater distances protected from sub-zero atmospheric temperatures in intra-icing voids. It is further suggested, that the surfacing water is saturated with more minerals than calculated with the available data (as is the case for April spring water) resulting in precipitation upon surfacing and the depletion of the remaining water of most solutes. Dolomite precipitation, for example, calculated to occur predominantly in subsamples of cores 2 and 5, additionally removes Mg^{2+} from the surfacing water together with other ions composing carbonate minerals. Since ice cores were not sampled directly at the source, initial surfacing water is assumed to have even higher TDS than core 2. Higher solute concentration in core 5, compared to core 3, despite sampling from a location farther downslope, attests the presence of another outflow below spring 1.

Due to additional water input through the incorporation of snow and rain from the ice surface and, potentially, surficially routed snowmelt, adding to the overall icing volume as well as the described bias introduced by freezing, ice cores and their hydrochemical composition are considered unreliable indicators of the origin of the water and its flow paths. These can better be established through information contained within the water samples collected from the springs assumed responsible for the formation of the icing.

6.2.3 Solute Composition of Icing and Springs and Provenance of Water

Solutes quantified in ice core and water samples can derive from two sources: atmospheric aerosols and geologic material. Atmospherically derived solutes are dominated by Cl^-, Na^+ and small amounts of SO_4^{2-} from sea salt and, to a lesser degree, NO_3^- and SO_4^{2-} from acidic nitrate and sulphate aerosols (Hodgkins & Tranter 1998; Wadham et al. 2000). The species of crustally derived solutes depends on the local geology which is dominated by shales, sandstones and siltstones in the Rieperbreen catchment whereby SO_4^{2-}, Mg^{2+}, HCO_3^- and Ca^{2+} prevail from the weathering of carbonate and sulphate minerals and Na^+ and K^+ from feldspar (Rutter at al. 2011). All ice cores, April spring and June spring 2 samples show a dominance of crustally derived solutes with abundances in the order $SO_4^{2-} > Na^+ > HCO_3^- > Ca^{2+}$.

The presence of SO_4^{2-} does not necessarily indicate chemical weathering, since SO_4^{2-} also derives from the atmosphere as sea salt or acidic sulphate aerosols. To quantify the influence of snowpack derived sulphate in the ice core and water samples, the ratio of SO_4^{2-} from the snowpack and non-snowpack sources ($*SO_4^{2-}$) was calculated given the SO_4^{2-}: Cl^- ratio of 0,13 as in Eq. 5 (Hodgkins & Tranter 1998; Hodgkins et al. 1998). $*SO_4^{2-}$ accounts for 97-99% of total SO_4^{2-} in ice cores, whereas the lowest percentage in a subsample was 93,56% (Table 12 and Table 13 in appendix). No correlation exists between ice types and $*SO_4^{2-}$, showing, as previously discussed, that ice types fail to reveal the source of water but are attributed to the speed of freezing. Comparable ratios were calculated for water samples where 94-99,9% of total SO_4^{2-} is derived from weathering. Here, crustal sulphate was lowest for June samples from spring 1 (~94,5%) leading to the assumption that fresh snowmelt influenced the composition of these samples as is discussed in more detail below. When compared to values in Hodgkins et al. (1998), SO_4^{2-}: $*SO_4^{2-}$ ratios correlate well with icing interstitial water, whereas average April spring concentration is 1,4 times higher. Values obtained in this study, however, deviate clearly from the meltwater composition in Hodgkins et al. (1998) since the concentration of $*SO_4^{2-}$ in April samples is 15 times higher. The high $*SO_4^{2-}$ abundance and further elevated Ca^{2+} and Mg^{2+} concentrations are most likely attributed to the oxidation of sulphide minerals present in siltstones and shales (Hodgkins et al. 1998; Rutter et al. 2011; Yde et al. 2008). Positive SI for Alunite and Jarosite in April spring water indicate high enough concentrations for the precipitation of sulphate minerals under the given pH. S-ratios calculated for ice core and spring samples arrange around 0,5 (Figure 36) and hence show the additional importance of carbonate dissolution, coupled to the oxidation of sulphides, in the allocation of protons for chemical weathering and further explains the abundance of HCO_3^-. The range of S-ratio values in ice core samples is explained by precipitation of carbonate minerals leaving cores 3 and 4 depleted in HCO_3^- relative to cores 2 and 5 sampled closer to the springs.

Concentrations of Cl^- are interpreted as exclusively derived from sea salt, and hence the atmosphere, since other sources of Cl^- are reported absent in the Rieperbreen catchment (Hodgkins & Tranter 1998; Rutter et al. 2011). High chloride values in samples therefore indicate the presence of snowmelt and, possibly, rain. The composition of snowmelt regarding atmospherically derived solutes varies significantly during the melt season. At the onset of melting, meltwater percolates through the

snowpack and leaches present solutes such as Cl^-, Na^+ and SO_4^{2-}. The first meltwater leaving the snowpack is therefore enriched in these solutes compared to the remaining, eluted, snowpack. Melting of the residual snowpack results in increasingly dilute bulk meltwater which is further diluted once runoff from ice melt starts to contribute (Raben & Theakstone 1994; Tranter et al. 1996). Several hydrochemical studies of the Rieperbreen and nearby proglacial rivers describe decreasing levels of Cl^- in bulk meltwaters as the ablation season wears on (Hodgkins et al. 1998; Rutter et al. 2011; Yde et al. 2008). Increases in Cl^- content during the melt season can often be attributed to snowfall events and the subsequent elution of the snowpack (Rutter et al. 2011).

Cl^- concentrations reach up to 30 mg l^{-1} in collected samples. These values are compared to published concentrations in snow and bulk meltwater for Longyearbreen (Yde et al.2008), Scott Turnerbreen (Hodgkins & Tranter 1998) and Rieperbreen (Rutter et al. 2011). In the Longyearbreen study, Cl^- concentrations in snow average at 2,6 mg l^{-1} with a standard deviation of the same magnitude. Concentration in bulk meltwater, with data available for the entire melt season from the end of May until mid-September, ranged between 1-18 mg l^{-1}. The maximum concentration was measured at the onset of the ablation season in late May. Values decreased to <3,5 mg l^{-1} in early July and remained at low levels until the end of the ablation season. (Yde et al. 2008) Similar values are reported from Hodgkins & Tranter (1998) for meltwater at the nearby Scott Turnerbreen where Cl^- concentrations started at <7 mg l^{-1}, reached the maximum of 30 mg l^{-1} nine days after the onset of melting and then declined to 2 mg l^{-1} for the remaining ablation season. Cl^- values in snow samples averaged at 7 mg l^{-1} but with concentrations up to 85 mg l^{-1} in snow layers. No data is available on snow in the Rieperbreen catchment, but due to the proximity of Scott Turnerbreen and Longyearbreen, values from these studies are evaluated comparable. Compared to snow, glacier ice is poor in Cl^-. Riger-Kusk (2006) and Wadham et al. (1998) report values of 0,4 mg l^{-1} for clear ice from Longyearbreen and Finsterwalderbreen. Further, values for early season runoff are not presented in the Rutter et al. (2011) study, where the time series starts at the beginning of July, when highly concentrated snowmelt has already left the system and the river is mainly fed by meltwater from a leached snowpack and, possibly, already diluted ice melt. Between the end of June and the middle of August, Cl^- in the meltwater river is similarly abundant to Longyearbreen and

Scott Turnerbreen with <5 mg l^{-1}, before concentrations rise to 10 mg l^{-1} at the end of August after a snowfall event.

Given the high Cl^- levels of spring samples, with up to 30 mg l^{-1} in April, snow meltwater is assumed to account for a considerable proportion of spring water. June samples deviate significantly. Values are 3 times higher in April than in June spring 1 (avg. 10 mg l^{-1}) and 6 times higher than in June spring 2 (avg. 5 mg l^{-1}). Values of April samples are comparable to highest values in meltwater from Scott Turnerbreen (Hodgkins & Tranter 1998) while June values correspond to concentrations in meltwater later in the season after highly concentrated snowmelt has left the system. The high Cl^- values in April samples reveal snowmelt as source water derived from an unleached snowpack and further, that the spring is not fed by late season ice melt which would exhibit significantly lower concentrations. Lower levels of Cl^- in June samples suggest dilution of the spring water by snowmelt from an already partially leached snowpack.

The most abundant cations are Ca^{2+} and Na^+ whereas $Ca^{2+} > Na^+$ only in June spring 1 samples (ratios of 1,03 and 1,44) and ice cores 1 and 3. Ratio of Ca^{2+}: Na^+ in April samples are between 0,43 – 0,47 and 0,52 in June spring 2. Hodgkins & Tranter (1998) show, that Na^+ from sea salt is the second most abundant ion in snow with a Na^+: Cl^- ratio of 0,85. Therefore, the non-snowpack derived amount of Na^+, $*Na^+$ was calculated as before described for $*SO_4^{2-}$, to quantify the portion of Na^+ derived from chemical weathering. Results show that most of Na^+ comes from weathering because $*Na^+$ accounts for 81-89% of total Na^+ in ice cores and for 85-89% is spring samples from April and June spring 2. As is the case with $*SO_4^{2-}$, $*Na^+$ is lowest in June spring 1 accounting for only half of total Na^+ ($*Na^+$ = 48 and 51%) and hence indicating the importance of fresh snowmelt in this sample.

In bulk meltwater from Rieperbreen and Longyearbreen, the concentration of Na^+ was shown to be higher than Ca^{2+} over the melt season (Rutter et al. 2011; Yde et al. 1998). Rutter et al. (2011) describe higher Na^+ than Ca^{2+} concentrations in highly concentrated springs sampled close to the glacier terminus and explain the reverse correlation through ion exchange, which has been described before to decrease the Ca^{2+}: Na^+ ratios (Hodson et al. 2002b; Wadham et al. 1998). Another reason might be calcite reaching saturation and hence terminating the dissolution of Ca^{2+} while acquisition of Na^+ from feldspar weathering wears on. Rutter et al. (2011) further describe, that both processes may be indicative for the transit of this water through a

flow path in reactive debris that *"operates separately to the Rieperbreen drainage system"* (p.48).

Si concentration in snow is low (max. 1,5 µmol in Hodgkins & Tranter (1998)) and can therefore be regarded as derived exclusively from the weathering of silicate minerals. High concentrations of Si in meltwater have previously been interpreted as indicative of a long residence time of the water, since dissolution of silicate minerals is slow (Hodgkins et al. 1998; Raiswell 1984). Si concentrations in ice cores are lower than in springs. The discrepancy may be explained by precipitation of silicate minerals, removing Si from the surfacing water and reducing the concentration in ice cores at greater distances. SI_{Quarz} and SI_{Talc} in core 2 show that the surfacing water was initially saturated in Si under the given pH. Si concentration is therefore assumed higher in source water than that quantified in ice cores. When comparing Si content to the mean value calculated for meltwater of the Rieperbreen proglacial river in Rutter et al. (2011, Table 3), Si concentrations in April samples are 4 times higher. The values in springs best compare to quantities in Rutter et al. (2011) samples RP5 and RP6 which could, from their location, be connected to the same hydrological pathways as the springs sampled in this study.

Another solute, that has been used before as tracer of snowmelt, is NO_3^-. NO_3^- together with NH_4^+ and SO_4^{2-} are deposited in snow derived from anthropogenic aerosols (Hodson et al. 2010). NO_3^- levels in samples are higher in ice cores (between 0,32 to 0,59 mgN l^{-1}) than in April spring samples (<LOQ) but up to 3,4 mgN l^{-1} in June samples. NH_4^+ concentrations are constant and range between 0,03-0,08 mg l^{-1}. A ratio of 0,09 for NO_3^-: Cl^- and 0,04 for NH_4^+: Cl^-, in equivalent units, was calculated by Hodson et al. (2009) for snow. When applying these ratio to the quantities of NO_3^- and NH_4^+ in the samples, a shortage of NO_3^- is not only revealed in April samples, as expected with concentrations below the limit of quantification, but also for ice cores. The present NO_3^- only accounts for 67%, 30%, 48%, 35% and 32% of expected NO_3^- in cores 1-5, respectively. Measured concentrations in June spring samples, on the other hand, reveal a surplus with up to 217% of the expected concentration. Quantified concentrations of NH_4^+ are also below the expected abundance, accounting for 28-74% of expected NH_4^+ in ice cores, only 5% in April samples and up to 75% in June samples.

Concentrations below the limit of quantification in April samples are interpreted as sign of denitrification, a microbial-mediated process where nitrate is reduced. This process occurs preferentially in anoxic environments, when NO_3^- is used as electron acceptor once oxygen, for example dissolved O_2 in meltwater, is depleted. Subglacial environments have been described to promote denitrification. (Hodson et al. 2005) Same levels of NO_3^- would be expected in ice core samples in case the icing is fed by the springs. NO_3^- values in ice cores, however, are notably higher. This is attributed to the incorporation of snow whereas values below the expected snow ratio are explained by the mixing with denitrified spring water. Higher levels of NO_3^- in June and overall lower ratios of NH_4^+: Cl^- suggest microbial-mediated nitrification of NH_4^+ to NO_3^- under aerobic conditions described by the following equation (Hodson et al. 2005; Yde et al. 2008):

Eq. 27

$$NH_{4\,(aq)}^{+} + 2O_{2\,(aq)} \rightarrow NO_{3\,(aq)}^{-} + 2H_{(aq)}^{+} + H_2O$$

In-situ measurements of hydrochemical parameters support the interpretation of denitrification under anaerobic conditions in April samples. The negative ORP of April samples reveals reduced water and the demand of oxygen in the system as is characteristic for subsurface water where the supply of air is limited. The oxygen demand is ascribed sulphide oxidation (Eq. 8) but also denitrification. Mn, Fe and SO_4^{2-} concentrations are high in April samples and reveal that these ions were not yet used as electron acceptors. Therefore, Mn, Fe and SO_4^{2-} reduction did not yet take place indicating that the water has not moved far down the redox ladder. Low DO concentrations measured in April are assumed to show that oxygen only has dissolved in the water upon surfacing and hence shortly before measurement. This also explains the iron staining around the outflow by precipitation of iron oxyhydroxides upon contact with oxygen. Therefore, negative ORP is estimated as a better indicator of water that was initially sub-oxic. The pronounced difference in ORP, but also DO, measured in June, is ascribed an additional source of water diluting the spring. Fresh snow meltwater may have entered the system and changed the anaerobic conditions to aerobic in the channel by supplying oxygen and hence raising the ORP and DO values. This resulted in higher concentrations of NO_3^- in June samples indicating the absence of denitrification due to the availability of oxygen as electron acceptor additional to nitrification of NH_4^+.

Besides the solute composition, the pCO_2 yields information regarding the flow path of the water. Most pCO_2 values of ice core sub-samples are below atmospheric equilibrium (< -3,5). In theory, this displays water flow through a closed system where no CO_2 is drawn down from the atmosphere. But also, the contact of relatively pure water with highly reactive debris and a faster depletion of CO_2 through chemical weathering than diffusion in the water. While both processes are plausible in the given setting, care should be taken when interpreting the pCO_2 values of ice samples due to bias introduced by freezing. In the ice cores, the low pCO_2 values are very likely caused by the rejection of dissolved gases during ice formation. Hence, pCO_2 of spring samples are assumed to yield a more accurate estimate for the source water. PCO_2 > -3,5 in all spring samples indicates a faster supply of protons than depletion through weathering. This could either be due to coupled carbonate dissolution and sulphide oxidation and/or the mixing with snowmelt. Further, the possibility of bias through partial freezing and the rejection of CO_2 from the water resulting in pCO_2 higher than the atmospheric equilibrium also exists in spring samples. Higher values in April than in June could indicate partial freezing but also the presence of CO_2 from microbial respiration.

6.2.4 Solute Composition and Provenance of Lake Water

The chemical composition of lake water is significantly different to that of the springs and icing. Given the topography, the lake is assumed to be fed by surficially routed snowmelt and rain during the summer.

Differences in solute composition between the springs and lake reveal, that the lake was neither feeding the springs in June nor in April. Lowest correlations between ice cores and water samples was calculated for lake water. Especially between the lake and ice cores 4+5 which, given their sampling location, were the samples most likely to show the influence of lake water. The highest correlations for the lake water exists with June samples from spring 1 (r = 0,90; 0,92). This is explained by the presence of snowmelt in the spring samples and snowmelt recharging the lake. The high SO_4^{2-} concentration in lake water derive from the lake being surrounded by an active layer in shale and subsequent sulphide oxidation throughout summer.

6.2.5 Icing Formed by Spring Water?

If the icing were formed by the water sampled from the springs, a similar chemical composition of ice core and water sample is expected. However, the solute composition and abundance in ice cores, April and June spring samples deviate notably.

The chemical composition of the five ice cores indicates, that at least cores 2-5 are composed of ice formed from the same source water. The chemistry of core 1 varies significantly from the others regarding lower concentration of Si, Mg^{2+}, Ca^{2+}, HCO_3^-, Na^+ and Cl^-, resulting in the lowest TDS of ice cores. NO_3^- on the other hand, has the highest concentration in core 1. This leads to the assumption, that ice core 1, initially thought to represent an ice sample from the uppermost area of the icing, was sampled from refrozen meltwater in a channel of the braided river occupying this area during summer. Localized strong reflections in topographic depressions seen in GPR profiles from this area underline the assumption of the presence of ice in the river channels. This would imply, that the upper icing margin is located roughly were spring 1 was sampled and further, that no icing formed on the broad outwash plain during the 2016/17 accumulation season, as previously recorded on aerial photographs.

Ice cores are depleted in solutes compared to April spring water. The different composition of the icing may be sufficiently explained through the incorporation of snow and rain, surficially routed snowmelt from the adjacent slopes and the sampling of ice cores some distance from the outlet where several minerals could already have dropped out of solution. These additional sources of water as well as freezing effects result in a dilute composition of the ice cores compared to the springs.

The April samples are evaluated to yield a good estimate for the composition of the water that is forming the icing during the accumulation season. High correlation exists between April samples and cores 2-5, certainly sampled from the icing, whereas spring 1 correlates with $r > 0,98$ with cores 2 and 3 and spring 2 with $r > 0,98$ with cores 4 and 5. Ternary plots (Figure 35) show a good alignment of ice cores and springs and hence water coming from the same source. The range present within ice core samples is explained through cryochemical processes during freezing.

Not only ice cores and April spring samples have a significantly different composition, April samples vary greatly from spring samples obtained in June. June samples are even lower in dissolved solutes than the icing and seem to be composed mainly of fresh snowmelt with a short contact time with reactive debris and fast flow. Although strong correlation exists between April springs and June spring 2 ($r > 0,93$), hinting that parts of the sample may still contain spring water, the signal from this source was altered beyond recognition by the dilution through fresh snowmelt. June samples are therefore disregarded to obtain information about the source of water and the flow paths of the water.

6.2.6 Interpretation of Stable Water Isotopes

Tracing the origin of water sampled at the springs with the available data from stable water isotope analyses is difficult due to the small data set. Some assumption can however be made. The good alignment of all spring samples along the LMWL (Figure 37 a) show a small deviation of the isotopic composition of the sampled water from that of local precipitation. This suggests parental water derived from precipitation. D-excess values in all spring samples are >10‰ and located above the LMWL. Ritter & Kuells (2010) propose d-excess values >10‰ indicating precipitation fallen during winter (November-March) or during a transition period (April-Mai, October) but not in summer (June-September) for NyÅlesund. Spring water is therefore most likely derived from precipitation fallen during the accumulation season and therefore mainly consists of snowmelt, strengthened by light values. June samples of spring 1 and 2 align with the LMWL likely indicating water derived exclusively from snowmelt. Snowmelt is also expected to be the main source of water in the April samples. The slight deviation from the LMWL and higher d-excess in April denote an alteration of the isotopic ratio attributed either freezing effects, fractionation in the snow pack or a combination of both.

The good agreement between April samples suggests water derived from the same flow path at both locations. The low $\delta^{18}O$ values are comparable to values measured in the bulk meltwater from Longyearbreen in the early ablation season (Yde et al. 2008), when snowmelt is the dominant contributor to runoff. Since snowmelt had not started at the time of sampling, the water is believed to be derived from warm spells during the winter resulting in a partial melt of the snowpack with meltwater depleted in

heavy isotopes leaving the pack. The values might be altered by mixing with stored water from late summer snow- and ice melt. The good correlation between April samples and spring samples obtained at Rieperbreen in 2014/15 validate the 2017 values and suggest water from the same origin feeding the icing in the previous years.

Significantly deviating values between spring 1 and 2 in the June samples may be explained by an altitude effect influencing the onset of snowmelt. The higher δD and $\delta^{18}O$ values from spring 2 could indicate water derived from an eluted snowpack with a higher proportion of heavy isotopes already leached out due to a location at lower altitude. Lower values in the sample from spring 1 may be linked to water derived from snowmelt at a higher altitude where heavy isotopes are enriched in the snowpack and snowmelt shows a higher proportion of lighter isotopes. However, it is questionable if an altitude effect would be as pronounced in the study area which exhibits a relatively small altitudinal range. This explanation would further imply a very fast flow path between higher altitudes and spring 1. Results from dye tracing experiments however indicate the absence of an efficient flow path. Hence, it is more likely that meltwater from the local snow pack was sampled in June. The varying values are related to meltwater derived from different precipitation events exhibiting a different isotopic signature which are preserved as layers in the local snowpack. Figure 2 shows the great variability in isotopic composition between precipitation events. Meltwater derived from the snowpack early in the melt season also explains the high d-excess caused by fractionation in the snowpack and further the difference between June and April samples of spring 1. The high δD and $\delta^{18}O$ values and low d-excess of the lake fed by snowmelt is most likely linked to evaporation leaving the remaining waterbody enriched in heavy isotopes with the possibility of a contribution of summer precipitation with higher values.

6.3 Interpretation of Dye BTCs

Through visual BTC analyses it is assumed, that the emergence of dye was recorded for all experiments and, further, that dye injected into all openings on the glacier emerged through the glacier portal. Each curve was attributed to one dye injection (as seen in Figure 39). Due to the short time between some dye injections, it is difficult to assess the corresponding signal. The flat-angled curve from JD 233, for example, was attributed to experiment 2 and interpreted as long residence time due to a larger

distance of the injection point and low discharge. This curve, however, could also be interpreted as stored dye from injection 1, which emerged from the glacier portal a day after dye injection due to increased discharge starting in the afternoon of JD 233.

The increased level of fluorescence towards the end of the record (JD 236 onwards), is allocated a partial storage of dye from injections 5 and/or 6 and slow release over the following days. Since dye injection for these experiments was performed with little time in-between, it cannot be explicitly distinguished from which experiment produced the long signal of increased fluorescence. Another explanation for this long-lasting signal of raised fluorescence could be a raised concentration of suspended sediment in the proglacial river emitting natural fluorescence in the wavelength of red light due to increased discharge. The effect of natural fluorescence by sediments transported by the main river leaving the catchment, Bolterelva, however, was evaluated through measurements performed for the construction of a calibration curve between the two fluorimeters (Figure 19). The fluorescence of highly turbid sample water did not differ from the base level recorded in the Rieperbreen proglacial river. Hence, natural background fluorescence is not believed to be recorded throughout the experiment biasing the measured signals.

The difference in signal strength between experiments and stations (Figure 38) can be explained by varying amounts of injected dye and transit distances. Increased fluorescence values of BTCs from the last three experiments are attributed to the short travel distance of the dye in experiment 4 and to the larger amounts of dye injected in experiments 5 and 6. The overall weaker signal at station 2 is attributed to the greater distances to the injection points.

Given their position on the record of station 1, the angled BTCs could be interpreted as the emergence of a second part of the dye cloud from experiments 1, 2, 3 and 6, strengthened by the fact that these curves were only recorded after injections into the injection points located farthest up glacier (points 1 and 2). Further, all angled returns were recorded at equal intervals after the first single-peaked dye return from the experiments. Several convincing indicators, however, suggest, that these curves are not caused by the passage of a dye cloud. Firstly, the four deviating curves were only recorded at station 1. Although longitudinal dispersion in the proglacial river between the two stations has shown to alter the signal recorded at station 2 compared to station 1, a sign of these curves would be expected to be transported downriver to station 2 in

case they are not a systematic error. Secondly, similarly shaped BTCs, produced by a sudden increase, several values at a higher level followed by a sudden decrease, have not been described in the literature. The lack of data points in the vertical lines itself, marking the sudden increase and decrease of fluorescence (especially pronounced in the curve from JD 234 in Figure 40), is a sign for a different cause than the passage of a dye cloud which would raise the fluorescence steadily but not as abruptly. Further, all curves were recorded at the same time during the day between 8 am to 11 am, very likely to represent a time span with low discharge. Hence, it is assumed that the edgy curves were recorded due to the interference of short wave radiation (sunlight) with the sensor upon partial exposure during low discharge. Another explanation of an artificial signal could be the entrapment of a rock inside the shake cap impairing the recorded value. The repeated occurrence of these curves, and the timing, nevertheless, support the first explanation. The absence of similar curves in the morning hours of JD 237 and 238 are believed to be due to rain inducing increased discharge and hence water level in the proglacial river.

As visible in Figure 38 and Figure 39, some BTCs are single-peaked while others exhibit two peaks. A possible explanation is offered by an observation made after experiment 4. Here, the dye cloud was discovered to disappear into two separate openings underneath the former part of the glacier snout (Figure 18 d). Hence, it is assumed that the injected dye is separated into two flow paths underneath the dead ice body before re-joining shortly before station 1. The two peaked-returns indicate different throughflow velocities of the two flow paths. This theory would explain the two-peaked returns of experiments 4, 5 and 6, however, not the single-peak of BTCs from experiments 1, 2 and 3. These may be explained by water routed along another flow path leaving the glacier at another location than the portal. However, it is more likely that all water is routed through the glacier portal since Gulley et al. (2012) describe the presence of only one subglacial channel on Rieperbreen. The different number of peaks of the BTCs may be the consequence of varying transit distances between injection and detection site and injected amounts of dye exerting influence on the degree of longitudinal dispersion of the dye cloud. Due to the larger transit distance, the dye clouds from experiments performed at points 1 and 2 arrive at the separation point with a higher degree of dispersion than dye injected for experiments 4 and 5. Hence, the separation of the dye cloud, shortly before arriving at station 1, did not produce a noticeable signal. This would explain the two peaks of experiment 6, when

more dye was injected than during experiments 1 and 3, which are not as pronounced as in 4 and 5, but still noticeable. In experiment 4, the dye cloud was observed to have arrived at the separation point without significant longitudinal dispersion due to the short distance travelled from the injection point. The same process is assumed for injected dye in experiment 5 which had the second most proximate injection site.

The absence of distinct second peaks from injection 4, 5 and 6 as well as flatter BTCs are evident in Figure 39. Since no additional inflow of water to the proglacial river between the stations was visible, the discharge of the proglacial river was consistent at both gauging stations. Hence, differences of BTCs at station 2 are interpreted as consequence of hydrodynamic dispersion of the dye cloud during the transit in the proglacial river. Due to the increased transit distance to station 2, the dye cloud experienced a higher degree of longitudinal dispersion causing flatter BTCs and the merging of peaks.

Applying thresholds of throughflow velocities as defined by Theakstone & Knudsen (1981), Hubbard & Nienow (1997) and Nienow (2011) to the calculated values on Rieperbreen, all dye clouds, except the one responsible for the first peak of experiment 5, travelled with a slow velocity (<0,2 ms^{-1}) through the drainage system. Values, however, only show a minimum estimate since a flow path with a sinuosity of 1 was assumed. The values are comparable to those measured by Gulley et al. (2012) on Rieperbreen in the beginning of the ablation season when discharge is comparably low as during the experimental period at the end of the ablation season. The throughflow velocities for BTCs at station 2 are raised compared to station 1. This is explained by higher flow velocities in the proglacial river between the stations. The velocity of the dye cloud in the proglacial river was calculated from the peaks in concentration recorded at station 1 and 2 and is listed in Table 11. As expected, due to the higher throughflow velocity calculated for BTCs at station 2, the flow velocity in the river is increased compared to water movement in the glacier.

Regarding the characterisation of the en- and subglacial drainage system, the shapes of the return curves, narrow and single-peaked, and the fast return times of dye clouds, hypothesise an efficient drainage system connecting the openings in the glacier with the portal. Throughflow velocities <0,2 ms^{-1}, however, were formerly interpreted as water flowing through an inefficient, distributed drainage system (Nienow 2011). Gulley et al. (2012) showed that these thresholds cannot be applied to Rieperbreen since the

glacier is frozen to its bed and does not exhibit a distributed drainage system. For cold-based glaciers, slow flow velocities and high dispersion do not originate from water routed through an inefficient, distributed drainage system but rather from the bed roughness of the channel. Big boulders are present on the floor of the subglacial channel at Rieperbreen. When the water level in the channel is low, boulders are not fully submerged and the roughness of the channel floor is high. This results in temporal storage of dye which produces breakthrough curves similar to those of a distributed drainage system.

6.3.1 Flow Path Inferred from Dye Tracing

Through the results from BTC analyses, the question regarding the existence of a flow path underneath the southern lateral moraine can be answered. By comparing the strength of dye returns between stations 1 and 2, it appears, that all dye emerged upriver station 1 and thereafter passed both stations. This implies that no additional dye emerged into the river between station 1 and 2 and that all injection points are connected to the glacier portal. It further suggests, that an efficient, channelized flow path, other than the proglacial river, connecting the glacier with the upper spring at the end of the ablation season, is absent. However, the possibility of the presence of such a flow path is not entirely ruled out by the performed experiments. Potentially, the throughflow velocity is too slow for detection within the duration of the study. It is further probable, that spring 1 moved its location due to higher discharge during the ablation season or the disappearance of pressure exhibited by the overlying ice mass, which could result in the emergence of dye below station 2.

6.4 Discussion of Origin of Icing

6.4.1 Discussion of Hypotheses and Potential Sources of Water

The comparability of the hydrochemical composition of April spring water and the icing indicate, that the icing is mainly formed by water discharged from the sampled springs. The origin of the water recharging the springs is discussed below. Four working hypotheses were introduced in Chapter 1 in conjunction with the main research question regarding the origin of the water and the contribution of potential water sources in the formation of the Rieperbreen proglacial icing. These hypotheses and

the corresponding sub-questions (Q) are picked again at this point to be answered and further to verify or falsify the hypotheses with the obtained results.

Hypothesis 1

Hypothesis 1 explores the possibility that the icing is fed by the slow winter discharge of sub-glacially stored summer meltwater as previously suggested as source of water for icings forming adjacent to cold-based glaciers by Bælum & Benn (2011), Hodgkins et al. (1998, 2004) and Lysså & Lønne (2001). If the icing is formed by the slow winter discharge of sub-glacially stored water, it is expected to grow directly adjacent to the glacier terminus since all en- and subglacial channels have been shown to discharge through the portal during the ablation season and also since water can only travel a limited distance in sub-zero temperatures before freezing after emerging from the glacier. Further, ice and spring water are expected to exhibit a high concentration of solutes due to a long residence time in the drainage system and contact with reactive debris at the bed.

Former studies by Gulley et al. (2009, 2012) describe the presence of a channelized drainage system reaching to the bed of Rieperbreen which would allow to store a significant volume of water. However, investigations of the proglacial area during the accumulation season revealed that the proximal icing formed about 1 km from the present glacier terminus (Q1-1). No other icing area was discovered to have formed closer to the glacier or directly adjacent to the portal. Dye tracing results suggest the absence of a connection between the subglacial channel described by Gulley at al. (2009, 2012) and the upper spring feeding the icing. Negative ORP and denitrification removing NO_3^- from April spring water shows water routed through an anoxic environment suggesting an entirely filled and pressurized channel, which further contradicts the hypothesis of source water stored englacially. Therefore, a different location of water storage than in a subglacial channel is highly likely. The chemical composition of April spring water varies greatly from late season meltwater described in Rutter et al. (2011). Although this would be expected to be the case for subglacially stored meltwater due to the long contact time with geologic material at the bed resulting in a high concentration of crustally derived solutes, as present in ice core and water samples (Q1-2), Cl^- levels are too high to indicate water derived from late season ice melt. Consequentially, the theory of icing formation adjacent to cold-based glaciers through the slow release of summer meltwater stored within the glacier, as proposed

by Bælum & Benn (2011), Hodgkins et al. (1998, 2004), and Lysså & Lønne (2001) is, at least for Rieperbreen, disproven.

Hypothesis 2

Hypothesis 2 deals with the kettle lake, present within the frontal moraine complex in close proximity to the lower icing areas, and the possibility of its water forming parts of the icing. Since surface runoff from the lake towards the icing was absent during winter and summer, a possible connection would have to be a sub-lake talik through which water percolates towards the area of icing formation.

Analyses of the ionic and isotopic signature of lake water and comparison with that of ice cores and springs reveals, that the composition of the lake is significantly different to water discharged from the springs. Although the two visible icing areas in winter are not connected, as seen in the GPR data (Q 2-3), the composition of the icing is spatially similar. Hence, the same source of water forms the upper and lower areas of the icing (Q 2-2). The markedly different composition of the lake shows, that the lake is not forming either one of the icings, especially not the more likely lower part since cores 4 and 5 correlate least with lake water ($r < 0,83$). This conclusion based on ionic and isotopic values is further strengthened by the dimension and depth of the lake. Measurements of the lake depth on August 23rd showed a maximum depth of only 1,65 m whereas >2 m water depth and an extent twice the permafrost depth is assumed necessary for taliks to form underneath water bodies (French 2007). Therefore, the lake very likely freezes to the bottom during winter, eliminating the possibility of a talik zone beneath the lake through which water could percolate towards the icing (Q 2-1).

Hypothesis 3

Hypothesis 3 assumes that the icing, forming adjacent to Rieperbreen is not a glacial icing, but rather ascribed to the icing type *spring icing* with long residence sub-permafrost groundwater as source water. Long residence groundwater in the area, for example water discharged through open system pingos, is characterised by a lack of DO and the evidence of redox processes, such as denitrification, sulphide reduction, iron reduction and methanogenesis leading to a negative ORP (Hodson et al. 2018 (in prep.).

The water discharged by the springs in April shows signs of a longer residence time in the ground. The high abundance of crustally derived solutes denotes a prolonged contact with reactive debris. Negative ORP and denitrification are indicative of water discharging from the ground. SO_4^{2-}, Fe and Mn levels, however remain high, demonstrating that no sulphate, iron or manganese reduction has taken place. The slightly anaerobic state of the sampled water in April indicates water with a residence time of several month underground, characteristic for young groundwater, rather than years as would be the case for long residence time groundwater (Q 3-1).

The source of water is therefore not long residence time groundwater and the icing not a spring icing. However, since the water is assumed not to originate directly from the glacier either, the ascription to another icing type cannot be entirely falsified. The accurateness of calling the Rieperbreen icing *glacier icing* is further discussed in Chapter 6.5.1.

Hypothesis 4

Hypothesis 4 assumes, that the icing is formed from surficially routed rain and snowmelt generated during winter warm spells. If the icing is formed by rain and/or snowmelt water routed along the surface, a low concentration of crustally derived solutes would be expected to characterise the icing and spring water due to limited rock-water interaction and further a high abundance of atmospherically derived solutes. The possibility of proglacial icings adjacent to cold-based glacier, forming from surficially routed snowmelt, has been discussed before. Hodgkins et al. (2004) state, that snowmelt generated during short warm periods is unlikely to result in runoff and the formation of an icing because the water would rather refreeze as ice lenses or superimposed ice within the snowpack. Bælum & Benn (2011) evaluate the quantity of winter snowmelt as too small to explain the volume of icings as well as growth occurring continuously during the accumulation season and not just during warm spells. However, surficially routed snowmelt was shown by Wadham et al. (2000) to have contributed significantly to the volume of the Finsterwalderbreen proglacial icing in certain areas.

The hydrochemistry of the icing and spring samples shows, that the water does not originate from surficially routed snowmelt and rain. While these two water sources are acknowledged to contributed to the overall volume of the icing and thereby diluting the

icing signature compared to the springs, it does not account for the largest proportion of the icing. The concentration of crustally derived solutes is too high to indicate meltwater routed along the surface over a short time (Q 4-2). In such waters, the ratio of atmospherically derived solutes compared to crustally derived is significantly higher. Additionally, as previously discussed, negative ORP and denitrification shows water routed in the subsurface. Further, if surficially routed snowmelt and rain would form icings, then they would be expected to be encountered more frequently in topographic depressions in the region. Another source of water or flow path configuration is therefore likely to be present.

Chloride concentrations, on the other hand, shows, that water must be derived from snow since chloride exclusively originates from the atmosphere in the given catchment. The high abundance of Cl^- shows that the water discharged from the springs is meltwater from an unleached snowpack where Cl^- is washed out preferentially. This would be the case when the snowpack melts partially during warm spells. This melting, however, would have to occur early in the season before a considerable height of snow has accumulated, to generate runoff and not ice lenses or superimposed ice within the snowpack as suggested by Hodgkins et al. (2004).

During the accumulation period 2016/17 several warm spells were recorded for Longyearbyen in October, November, December and February, resulting in average daily temperatures above freezing and precipitation fallen as rain (Figure 44) (Q 4-1). Positive degree days often coincided with precipitation, especially in October and during the warm spells in November and February, when highest precipitation amounts of these months were measured during the warm periods. Further indications of these warm spells are ice layers that formed at the bottom of the snowpack which were seen in radargrams and encountered when digging snow profiles.

Even though winter warm spells with positive air temperatures occur on Svalbard during winter, rain or surface runoff of meltwater, generated in these periods, is assumed to not solely explain the localized accumulation of ice, continuous growth during winter and presence of an icing. However, these sources are not disregarded to be responsible in the formation of the icing and to answer Q 4-3, yes, rain and snowmelt can explain the localized accumulation and continuous growth of an icing during winter. Rain and snowmelt is, however, not expected to be routed surficially, but along a flow path in the subsurface where the water is kept from freezing, resulting in

continuous discharge from the springs and icing growth throughout the accumulation season. This hypothesis is therefore not entirely verified or falsified. The source of water is verified, but a flow path on the surface falsified.

6.4.2 Source of Water and Flow Path

The source of water was shown to not be stored summer meltwater, water from the kettle lake or sub-permafrost groundwater. April spring samples are characterised by high concentrations of crustally derived solutes, high Cl^- abundance and negative ORP. The water is believed to originate from snowmelt generated during warm spells in winter. These events are believed to have resulted in partial melt of the snowpack whereas meltwater concentrated in atmospherically derived Cl^-, due to preferential leaching, leaves the snowpack or is washed out by rain. The meltwater is believed to originate from warm spells early in the accumulation season, when the snow cover was thin, resulting in runoff and not in refreezing within the snowpack. This meltwater is routed through a subsurface flow path where it is kept from freezing. This channel is characterised by a high rock-water interaction, slow flow, limited connection to the atmosphere, and is, likely, pressurized. The same signature, as of April spring samples, was found in upwelling water by Wadham et al. (1998, 2000) and further described as indicative of *"the passage of snowmelt through a subglacial chemical weathering environment characterized by high rock : water ratios, prolonged residence times and restricted access to the atmosphere"* (2000, p.1778).

Such a flow path is presumed present underneath or within the southern lateral ice-cored moraine. As suggested by results from dye tracing experiments, it is assumed to be disconnected nowadays from the present en- and subglacial drainage system routing meltwater from the glacier surface to the portal during summer. The channel may be a remnant of the former hydrologic system when Rieperbreen had a larger extent and volume and a polythermal regime. The timing of the thermal transition and the possibility of a surge indicating a polythermal regime in a more recent past, are discussed in Chapter 6.5.2. The location where winter meltwater enters the subsurface and recharges the channel, remains to be identified. Possibilities are water percolating through the lateral moraine or the crevasse at the backwall of the glacier.

6.5 Implications

6.5.1 Terminology

A proglacial icing fed by snowmelt shows, that the formation of proglacial icings is more complex and their occurrence not simply explained by the slow winter discharge of glacial meltwater as is the case for polythermal glaciers. The snowmelt fed Rieperbreen icing fits, given the source of water, better with the classification of spring icings formed from a perennial groundwater spring than a glacier icing. However, since the meltwater likely uses a former channel of the glacier drainage system, its formation is conditioned by the glacier. If the glacial channel were absent, the Rieperbreen icing may likely not form.

A proglacial icing formed by snowmelt does not go along with the common definition of a glacier icing proposed by Åkerman (1980) with water derived from the glacier. Although no consensus exists in the literature regarding the origin of water forming glacier icings, named sources have a glacial provenance in common. To find a remedy regarding the origin of proglacial icings, a new terminology for glacial icings is proposed. This terminology aims to differentiate between (1) proglacial icings formed adjacent to polythermal glaciers and fed by glacial meltwater, and (2) proglacial icings forming adjacent to cold-based glaciers and not fed by glacial meltwater:

- 1) *Glacier-derived icings* = glacier icings formed in front of polythermal glaciers and mainly fed through glacial meltwater,
- 2) *Glacier-conditioned icings* = glacier icings formed in front of cold-based glaciers and fed by a different source of water than glacial meltwater, but dependent on the presence of the glacier.

In this new classification, the Rieperbreen icings falls into the category of glacier icings, however is differentiated from proglacial icings forming adjacent to polythermal glaciers by being ascribed to the sub-group of glacier-conditioned icings.

6.5.2 Rieperbreen – a Glacier with a Surge History?

Proglacial icings being associated with surge-type glaciers is mentioned in Yde & Knudsen (2005). Whether Rieperbreen could have a surge history and possible

implication of a surge behaviour for the formation of a proglacial icing nowadays are discussed below.

Lysså & Lønne (2001) assume, that the moraines behind the LIA moraine have formed due to the melt-out of debris rich foliation during a gradual retreat of the glacier. This assumption is challenged at this point. Several features visible in the moraine complex and in the glacier forefield closer to the present ice margin suggest, that the retreat was interrupted by at least one rapid re-advance after the LIA that formed the moraine ridges behind the LIA moraine. The timing of the advance(s) can be narrowed down temporally through analyses of aerial photographs. The first advance might have taken between 1936 and 1961 when moraine ridge 2 was formed. Moraine ridge 3 could have formed during the same event or shortly after 1961 when the position of the glacier front coincides well with the location of the glacier proximate moraine. No climatically induced anew advance after the LIA is likely to have happened at Rieperbreen since similar sized valley glaciers on Svalbard have continuously retreated during this period (Lovell et al. 2015). Hence, it is possible that the advance of Rieperbreen may have been due to a surge. Several authors, such as Christiansen et al. (2005), Lysså & Lønne (2001) and Sørbel et al. (2001) describe that there are no indications for past surging activities of the glaciers draining the Foxfonna ice cap wherefore they classified Rieperbreen as a non-surge-type glacier. However, features visible in the field and on aerial photographs strengthen the theory of the formation of the moraines behind the LIA moraine through a rapid advance of the glacier rather than through the melting out of debris. These features are: blocked off meltwater channels, crevasse squeeze ridges and flutes. A recent study by Farnsworth et al. (2016) identifies Rieperbreen as surge-type glacier based on the presence of crevasse squeeze ridges.

Relict meltwater channels terminating abruptly at the outer margin of a ridge show, that these channels have been blocked off by the formation of the ridge. These blocked off meltwater channels between moraine ridges are regarded as surge indicative features. By comparing the location of the ridges and the meltwater channels, the number of events forming the ridges, and subsequently glacier advances, can be determined (Lovell 2014). Blocked off meltwater channels are clearly visible in the moraine complex between ridge 1 and 2. The starting points of the channels on the moraine distal side have partly been reworked by the downward movement of sediments from

the top of the ridges. The area between ridge 2 and 3 on the northern side of the present main meltwater channel was heavily altered by the action of younger meltwater channels with meltwater originating from the ice patch in the valley north of Rieperbreen. Therefore, no inactive channels are visible in this part of the moraine complex anymore. On the southern side of the presently active channel, relict meltwater channels are discernible between ridge 2 and 3 on aerial photographs and were also mapped by Lyså & Lønne (2001) in Figure 46. The nowadays inactive meltwater channels between the LIA moraine and the second ridge are believed to have been active during the retreat of the glacier from its LIA maximum position and later blocked off by the sudden advance of the glacier that formed the new moraine ridge. Hence, they were active before 1961. The channels distal of ridge 3 must have formed after 1961 before the formation of ridge 3. If the retreat of the glacier would have been a gradual one, resulting in the formation of ridge 2 and 3 by the melting out of debris as suggested by Lyså & Lønne (2001), the meltwater channels would be expected to have cut through the newly forming moraines. The same applies to a climatically induced slow re-advance of the glacier. Therefore, the advance of Rieperbreen and the formation of the moraine complexes behind the LIA moraine are believed to be linked to a rapid advance, as would be the case during a surge, abruptly cutting off the active meltwater channels. The first surge likely took place before 1961. In case there was a second surge it may have happened shortly after 1961 but before 1990. No further moraines are present in the glacier forefield. Therefore, a gradual retreat without re-advances of the glacier is assumed after the formation of ridge 3.

Other surge-indicative features are crevasse squeeze ridges (CSRs) and flutes. CSRs can be seen on the surface of the southern ice-cored moraine (Figure 45 e). They are oriented perpendicular to the direction of the flowing ice and intersect flutes in the forefield that are aligned parallel to the ice flow. CSRs are evidences for the rapid flow of a glacier during a surge. The high extensional strain rates open surface crevasses behind the surge front until they make connection with the bed (Rea & Evans 2011). High basal water pressure during the surge further leads to the formation of full-depth, bottom-up crevasses by hydrofracturing (Evans et al. 2016). Basal till is squeezed into the crevasses and fills the cavities. As the glacier is downwasting and retreating after a surge, the sediment infills melt out of the ice and are preserved in the forefield as transverse sediment ridges until they are overridden by the next climatically induced glacier advance or surge (Lovell 2014). Flutes are not only indicative of dynamic ice

flow during a polythermal regime, but also regarded as surge-indicative when present in combination with CSRs (Evans & Rea 1999).

A surge of Rieperbreen in the 20th century would imply, that Rieperbreen was not only polythermal during the termination of the LIA as suggested in the existing publications, but also several decades later. A surge in the period 1936-1961 would condition, that Rieperbreen has only been cold-based for maximum 80 years. This possible later thermal transition from polythermal to cold-based may have further implications which could be of interest in regard of the formation of the proglacial icing in front of Rieperbreen. These include the available time for permafrost to aggrade underneath a cold-based glacier and in the ground formerly covered by glacier ice and hence the thermal state of the ground. The thermal state of the ground is believed to influence flow paths in the glacier foreland. A more recent thermal transition could imply, that zones of talik may still be present in the glacier forefield since the period was too short for permafrost to aggrade entirely. And further, that even though the glacier is cold based and frozen to its bed now, former sub-surface flow paths, remnants of the former polythermal regime of the glacier, might still be open.

7 Conclusion

7.1 Summary

Little research has been conducted on icings occurring adjacent to cold-based glaciers, wherefore considerable knowledge gaps exist regarding the source of water forming these extrusive ice bodies, its flow paths and residence time. This thesis aimed to establish the source of water annually forming the icing in front of the Rieperbreen glacier in Central Spitsbergen, Svalbard, and thereby increase the knowledge about hydrological processes at and in front of cold-based glaciers during the accumulation season.

The contribution of different water sources in the formation of the icing such as: sub-glacially stored summer meltwater, water from a kettle lake present within the frontal moraine complex, long residence sub-permafrost groundwater and surficially routed snowmelt and rain was explored with natural tracers. The ionic and isotopic composition of ice cores and water samples were analysed to deduce the origin of the water and to characterise the flow path. Additionally, geophysical investigations of the icing were performed with ground-penetrating radar during the accumulation season to investigate the icing extent and its internal morphology. Experiments with artificial dye tracers at the end of the ablation season aimed to study the hydrological system of Rieperbreen and its connection to the springs in the forefield feeding the icing.

In the 2016/17 accumulation season, the Rieperbreen icing formed about 1 km from the current glacier terminus, covered large areas of the ~500 m narrow valley cut through the frontal moraine complex by the main meltwater river and had a maximum thickness of 2 m. GPR surveys revealed that the two visible icing areas during winter were separated, indicating the presence of at least two springs responsible for the formation of the icing.

Ice cores sampled from the icing had a distinct stratigraphy with several surface-parallel layers and thereby helped to validate reflections recorded in radargrams. They further offered valuable information about the growth of the icing. Vertical intra- and spatial inter-ice core variability reflects the process of icing formation through sheet flow and the alteration of the chemical composition during freezing. The formation of different ice facies, clear ice and bubble-rich ice, is ascribed to the speed of freezing

due to the pronounced difference in the concentration of dissolved solutes. Hydrochemical analyses of ice cores revealed a clear weathering signal through a high abundance of crustally derived solutes. The dilute composition compared to April spring samples denotes the influence of other sources of water, such as incorporated snow, rain and surficially routed snowmelt, adding to the overall volume of the icing. Due to these additional water inputs and bias introduced by freezing, the hydrochemical composition of the icing is considered an unreliable indicator of the origin of the water and its flow paths.

Water sampled from the springs in April is evaluated to yield a better estimate of the water forming the icing during the accumulation season. June samples were highly biased by fresh snowmelt and further disregarded to hold information about the source water. April samples are characterised by a high abundance of crustally and atmospherically derived solutes (TDS up to 850 mg l^{-1}), whereas $SO_4^{2-} > Na^+ > HCO_3^- > Ca^{2+}$, Cl^- concentrations (up to 30 mg l^{-1}) comparable to early season snowmelt, negative ORP (-80 mV), signs of denitrification (NO_3^- < LOQ) and pCO_2 above atmospheric equilibrium (> -3,5). High Cl^- concentrations indicate water originating from an unleached snowpack, high abundance of crustally derived solutes a clear weathering signal and contact of the water with reactive debris whereas the dominant chemical weathering reactions are coupled sulphide oxidation and carbonate dissolution accounting for high SO_4^{2-} and HCO_3^- abundance. Dissolution of silicate minerals indicates a longer residence time allowing slow weathering reactions to take place. Negative ORP denotes water flow through a sub-oxic environment. The oxygen demand is ascribed to sulphide oxidation but also microbial-mediated denitrification. The isotopic composition of spring samples shows low δD and $\delta^{18}O$ values, a good alignment with the LMWL and d-excess values >10‰. This suggests parental water derived from precipitation, most likely fallen as snow during winter or a transition period, but not during summer.

These results from hydrochemical analyses rule out: sub-glacially stored summer meltwater, water from the kettle lake, long residence sub-permafrost groundwater and surficially routed snowmelt and rain as sources of water. The origin of water is most likely snowmelt from an unleached snowpack generated during warm spells in the beginning of the accumulation season. Such warm periods, potentially resulting in precipitation fallen as rain and partial melt of the snowpack producing concentrated

runoff due to preferential leaching, occurred in October, November, December and February of the 2016/17 accumulation season.

The meltwater is routed into the subsurface where it is kept from freezing in a pressurized, anoxic channel with restricted access to the atmosphere, a high rock-water interaction and slow flow. Such flow path is assumed present underneath the southern lateral ice-cored moraine which is likely a remnant of Rieperbreen's former hydrologic system when the glacier had a larger extent and volume and a polythermal regime. Results from dye tracing experiments indicate the absence of an efficient flow path connecting the hydrologic system of Rieperbreen and the upper spring suggesting that the channel is disconnected from the en- and subglacial drainage system of Rieperbreen nowadays. The location where winter meltwater enters the subsurface and recharges this channel remains to be identified. Possibilities are snowmelt percolating through the lateral moraine or backwall crevasse.

The findings of this thesis expand the existing knowledge about proglacial icings forming adjacent to cold-based glaciers. Sub-surficially routed winter snowmelt is proposed as main source of water forming the Rieperbreen icing, which challenges the most common theory explaining icing formation next to cold glaciers through the slow release of summer meltwater stored within the glacier. This study shows that the formation of icings is complex and that water does not need to have a glacial provenance to form a proglacial icing. Therefore, a new terminology is proposed which distinguishes glacier icings into:

1) glacier-derived icings and
2) glacier-conditioned icings

whereas 1) are fed mainly through sub-glacially produced and stored meltwater, as is the case of icings forming adjacent to polythermal glaciers and 2) exist due to the presence of the glacier but are formed from water of another origin than glacial meltwater, as is the case for the Rieperbreen proglacial icing.

7.2 Outlook

Given the results of this study, several questions arise in regard to proglacial icings forming in front of cold-based glaciers that remain to be answered and could fuel future research. More work on Rieperbreen is needed to locate the subsurface channel where

water is kept from freezing and the point of recharge. Additionally, further investigations of proglacial icings forming next to cold-based glaciers should be performed to test obtained results in a larger scale study and to verify the theory of glacier-conditioned icing formation through winter snowmelt.

Regarding the formation of proglacial icings in front of cold-based glaciers, an unanswered question is:

- Why are icings present in front of some, but not all cold-based glaciers?

By addressing this question in future studies, the basic prerequisites for the formation of an icing in front of a cold-based glacier need to be addressed to study the differences between cold-based glaciers with and without the annual formation of proglacial icings. This includes investigations of possible entry points of snowmelt into the subsurface, the location of water storage during winter and the role of ice-cored lateral moraines. Regarding the location of water storage, future studies should assess the position of icings relative to glaciers and whether information about the source and location of water storage can be inferred. This may further offer valuable clues whether the formation of glacier-conditioned icings is only controlled by the existence of an appropriate sub-surface storage or if a former polythermal regime is a prerequisite for the formation of glacier-conditioned icings. Regarding the former thermal regime of the glacier it would be interesting to investigate whether cold-based glaciers with proglacial icings used to have a polythermal regime and thereby if icings are indicative of either a current or former polythermal regime of the glacier. Studying icing formation during a longer time scale would allow to assess whether proglacial icings in front of cold-based glaciers stop to form after a certain period and if the timing of the thermal transition can be estimated from this information.

Results of this study suggest a climatic influence on the formation of glacier-conditioned icings. A study of proglacial icings over a longer time span and analyses of climate data would allow to investigate:

- How does the climate influence the formation of proglacial icings?

and further:

- What influence will the changing climate have on the formation of proglacial icings in the future?

In order to address these question, future research should evaluate the influence of climate variables, such as temperature and precipitation, during the accumulation season on several aspects of glacier-conditioned icings for example: the ice volume, size, area of formation, timing and speed of growth, the number of icings in a region and the presence or absence from one year to the next.

Due to the rapidly warming climate, especially in the High Arctic, glaciers are receding which is ultimately accompanied by a shift of the thermal regime to cold-based in the case of polythermal glaciers. As a result, the number of cold-based glaciers will likely increase with the potential of the formation of new glacier-conditioned icings. This shows the importance of studying hydrological processes at and in front of cold-based glaciers and the configuration of drainage systems in recently deglaciated forefields.

References

Åkerman, J. (1982). Studies on naledi (icings) in West Spitsbergen. *Proceedings of the 4th Canadian Permafrost Conference (1982)*, 189-202.

Åkerman, J. H. (1980). Studies on Periglacial Geomorphology in West Spitsbergen. *PhD thesis. Lund Universitets Geografiska Inst. Ser. Avh. LXXXIX*, 297 pp.

Alekseyev, V. R., & Tolstikhin, O. N. (1973). *Questions of terminology in study of naleds.* (V. R. Alekseyev, Ed.) Hanover, New Hampshire: US Army Cold Reg. Res. Eng. Lab.

Annan, A. P. (1999). *Practical Processing of GPR Data. Proceedings of the Second Government Workshop on Ground Penetrating Radar.* Mississauga, Ontario: Sensors & Software Inc.

Annan, A. P. (2009). Electromagnetic Principles of Ground Penetrating Radar. In H. M. Jol, *Ground Penetrating Radar: Theory and Application. 1st Edition.* (pp. 4-40). Amsterdam: Elsevier Science.

Arcone, S. A. (2009). Glaciers and Ice Sheets. In H. M. Jol, *Ground Penetrating Radar: Theory and Applications* (pp. 361-392). Amsterdam: Elsevier Science.

Arcone, S. A., Lawson, D. E., & Delaney, A. J. (1995). Short-pulse radar wavelet recovery and resolution of dielectric contrasts within englacial and basal ice of Matanuska Glacier, Alaska, U.S.A. *Journal of Glaciology 41(137)*, 68-86.

Bælum, K., & Benn, D. I. (2011). Thermal structure and drainage system of a small valley glacier (Tellbreen, Svalbard), investigated by ground penetrating radar. *The Cryosphere 5*, 139-149.

Ballantyne, C. K. (2018). *Periglacial Geomorphology.* John Wiley & Sons Ltd.

Baranowski, S. (1982). Naled ice in front of some Spitsbergen glaciers. *Journal of Glaciology 28(98)*, 211-214.

Benn, D. I., & Evans, D. J. (2010). *Glaciers and Glaciation. 2nd edition.* London: Hodder Education.

Bertler, N. A. (2011). Ice core. In V. P. Singh, P. Singh, & U. K. Haritashya, *Ecyclopedia of Snow, Ice and Glaciers* (pp. 584-589). Dordrecht, The Netherlands: Springer.

Bingham, R. G., Nienow, P. W., Sharp, M. J., & Boon, S. (2005). Subglacial drainage processes at a High Arctic polythermal valley glacier. *Journal of Glaciology 51(172)*, 15-24.

Bohleber, P., Sold, L., Hardy, D. R., Schwikowski, M., Klenk, P., Fischer, A., & et al. (2017). Ground-penetrating radar reveals ice thickness and undisturbed englacial layers at Kilimanjaro's Northern Ice Field. *The Cryosphere 11*, 469-482.

Bohren, C. F. (1983). Colors of snow, frozen waterfalls, and icebergs. *Journal of the Optical Society of America 73(12)*, 1646-1652.

Brown, G. H. (2002). Glacier meltwater hydrochemistry. *Applied Geochemistry 17*, 855-883.

Brown, G. H., Sharp, M., & Tranter, M. (1996a). Subglacial chemical erosion: seasonal variations in solute provenance, Haut Glacier D'Arolla, Valais, Switzerland. *Annals of Glaciology 22*, 25-31.

Brown, G. H., Tranter, M., & Sharp, M. J. (1996b). Experimental investigations of the weathering of suspended sediment by alpine glacial meltwater. *Hydrological Processes 10*, 579-597.

Bukowska-Jania, E. (2007). The role of glacier system in migration of calcium carbonate on Svalbard. *Polish Polar Research 28(2)*, 137-155.

Bukowska-Jania, E., & Szafraniec, J. (2005). Distribution and morphometric characteristics of icing fields in Svalbard. *Polar Research 24(1-2)*, 41-53.

Cameron, K. A., Hodson, A. J., & Osborn, A. M. (2012). Carbon and nitrogen biogeochemical cycling potentials of supraglacial cryoconite communities. *Polar Biology 35*, 1375-1393.

Capt, M., Bosson, J.-B., Fischer, M., Micheletti, N., & Lambiel, C. (2016). Decadal evolution of a very small heavily debris-covered glacier in an Alpine permafrost environment. *Journal of Glaciology 62(233)*, 535-551.

Carey, K. L. (1973). *Icings developed from surface water and ground water.* Hanover, New Hampshire, USA: Corps of Engineers, U.S. Army. Cold Regions Research and Engeneering Laboratory.

Cassidy, N. J. (2009a). Electrical and Magnetic Properties of Rock, Soils and Fluids. In H. M. Jol, *Ground Penetrating Radar: Theory and Applications* (pp. 41-72). Amsterdam : Elsevier Science.

Cassidy, N. J. (2009b). Ground Penetrating Radar Data Processing, Modelling and Analysis. In H. M. Jol, *Ground Penetrating Radar: Theory and Applications* (pp. 141-176). Amsterdam: Elsevier Science.

Chandler, D. M., Wadham, J. L., Lis, G. P., Cowton, T., Sole, A., Bartholomew, I., & et al. (2013). Evolution of the subglacial drainage system beneath the Greenland Ice Sheet revealed by tracers. *Nature Geoscience 6*, 195-198.

Christiansen, H. H., French, H. M., & Humlum, O. (2005). Permafrost in the Gruve-7 mine, Adventdalen, Svalbard. *Norsk Geografisk Tidsskrift - Norwegian Journal of Geography 59(2)*, 109-115.

Clark, I. D., & Lauriol, B. (1997). Aufeis of the Firth River Basin, Northern Yukon, Canada: Insights into Permafrost Hydrogeology and Karst. *Arctic and Alpine Research 29(2)*, 240-252.

Clark, I., & Fritz, P. (1997). *Environmental Isotopes in Hydrogeology.* Boca Raton and New York: Lewis.

Clason, C. C., Coch, C., Jarsjö, J., Brugger, K., Jansson, P., & Rosqvist, G. (2015). Dye tracing to determine flow properties of hydrocarbon-polluted Rabots glaciär, Kebnekaise, Sweden. *Hydrology and Earth System Sciences 19*, 2701-2715.

Cooper, L. W. (1998). Isotopic Fractionation in Snow Cover. In C. Kendall, & J. J. McDonnell, *Isotope Tracers in Catchment Hydrology* (pp. 119-136). Amsterdam: Elsevier.

Craig, H. (1961). Isotopic variations in meteoric waters. *Science 133(3465)*, 1702-1703.

Dallmann, W. K. (2015). *Geoscience Atlas of Svalbard.* Tromsø: Norwegian Polar Institute, Report 148.

Dallmann, W. K., & Elvevold, S. (2015). Bedrock geology. In W. K. Dallmann, *Geoscience Atlas of Svalbard* (pp. 133-170). Tromsø: Norwegian Polar Institute.

Dallmann, W. K., Kjærnet, T., & Nøttvedt, A. (2001). *Geological Map of Svalbard 1:100,000 Sheet C9G Adventdalen. Temkart No 31/32.* Tromsø: Norwegian Polar Institute.

Dansgaard, W. (1964). Stable isotopes in precipitation. *Tellus 16*, 436-468.

DeBolster, M. W. (1997). Glossary of terms used in bioinorganic chemistry. *Pure and Applied Chemistry 69*, 1251-1303.

Deutsch, W. J. (1997). *Groundwater Geochemistry. Fundamentals and Applications to Contamination.* Boca Raton, Florida: Lewis Publishers.

Dunse, T., Eisen, O., Helm, V., Rack, W., Steinhage, D., & Parry , V. (2008). Characteristics and small-scale variability of GPR signals and their relation to snow accumulation in Greenland's percolation zone. *Journal of Glaciology 54(185)*, 333-342.

Esri. (2011). *ArcGlobe Basemaps*. Retrieved from http://www.arcgis.com/home/item.html?id=dd7341e1e20f4dc49261173cd8e70449 (19.7.2017)

Evans, D. J., & Rea, B. R. (1999). Geomorphology and sedimentology of surging glaciers: a landsystems approach. *Annals of Glaciology 28*, pp. 75-82.

Evans, D. J., Storrar, R. D., & Rea, B. R. (2016). Crevasse-squeeze ridge corridors: Diagnostic features of late-stage paleo-ice stream activity. *Geomorphology 258*, pp. 40-50.

Farnsworth, W. R., Ingólfsson, Ó., Retelle, M., & Schomacker, A. (2016). Over 400 previously undocumented Svalbard surge-type glaciers identified. *Geomorphology 264*, 52-60.

Førland, E. J., Benestad, R. E., Flatøy, F., Hanssen-Bauer, I., Haugen, J. E., Isaksen, K., & et al. (2009). *Climate development in North Norway and the Svalbard region during 1900-2100.* Tromsø: Norsk Polarinstitutt, Report series no. 128.

Fountain, A. G., & Walder, J. S. (1998). Water flow through temperate glaciers. *Reviews of Geophysics, 36*(3), 299-328.

Freeze, R. A., & Cherry, J. A. (1979). *Groundwater.* Upper Saddle River, NJ, USA: Prentice Hall, Inc.

French, H. M. (2007). *The Periglacial Environment. 3rd edition.* Chichester: John Wiley & Sons, Ltd.

Froehlich, W., & Slupik, J. (1982). River icings and fluvial activity in extreme continental climate: Khangai Mountains, Mongolia. *Proceedings of the 4th Canadian Permafrost Conference (1982)*, 203-211.

Gokhman, V. V. (1987). Distribution and conditions of formation of glacial icings on Spitsbergen. *Polar Geography and Geology 11(4)*, 249-260.

Greześ, M. (2005). Naledi of Kaffiøyra (NW Spitsbergen). In M. Greześ, & I. Sobota, *The Outline of Kaffiøyra Geography (NW Spitsbergen)* (pp. 17-26). Toruń: Oficyna Wydawnicza TURPRESS.

Gulley, J. D., Benn, D. I., Screaton, E., & Martin, J. (2009). Mechanisms of englacial conduit formation and their implications for subglacial recharge. *Quaternary Science Reviews 28*, 1984-1999.

Gulley, J. D., Spellman, P. D., Covington, M. D., Martin, J. B., Benn, D. I., & Catania, G. (2014). Large values of hydraulic roughness in subglacial conduits during conduit enlargement: implications for modeling conduit evolution. 296-310.

Gulley, J. D., Wathard, P., Martin, J., Banwell, A. F., Benn, D. I., & Catania, G. (2012). Conduit roughness and dye-trace breakthrough curves: why slow velocity and high dispersivity may not reflect flow in distributed systems. *Journal of Glaciology, 58(211)*, 915-925.

Gulley, J., & Benn, D. I. (2007). Structural control of englacial drainage systems in Himalayan debris-covered glaciers. *Journal of Glaciology 53(182)*, 399-412.

Hagen, J. O., & Liestøl, O. (1990). Long-term glacier mass-balance investigations in Svalbard, 1950-88. *Annals of Glaciology 14*, 102-106.

Hagen, J. O., Kohler, J., Melvold, K., & Winther, J.-G. (2003a). Glaciers in Svalbard: mass balance, runoff and freshwater flux. *Polar Research 22(2)*, 145-159.

Hagen, J. O., Liestøl, O., Roland, E., & Jørgensen, T. (1993). *Glacier Atlas of Svalbard and Jan Mayen.* Oslo: Norsk Polarinstitutt, Meddelelser Nr. 129.

Hagen, J. O., Melvold, K., Pinglot, F., & Dowdeswell, J. A. (2003b). On the net mass balance of the glaciers and ice caps in Svalbard, Norwegian Arctic. *Arctic, Antarctic, and Alpine Research 35(2)*, 264-270.

Hambrey, M. J. (1984). Sedimentary processes and buried ice phenomena in the pro-glacial areas of Spitsbergen glaciers. *Journal of Glaciology 30(104)*, 116-119.

Hambrey, M. J., Murray, T., Glasser, N. F., Hubbard, A., Hubbard, B., Stuart, G., & et al. (2005). Structure and changing dynamics of a polythermal valley glacier on a centennial timescale: Midre Lovénbreen, Svalbard. *Journal of Geophysical Research 110*, F01006.

Hayashi, M. (2004). Temperature-Electrical Conductivity Relation of Water for Environmental Monitoring and Geophysical Data Inversion. *Environmental Monitoring and Assessment 96(1-3)*, 119-128.

Heldmann, J. L., Pollard, W. H., McKay, C. P., Andersen, D. T., & Toon, O. B. (2005). Annual Development Cycle of an Icing Deposit and Associated Perennial Spring Activity on Axel Heiberg Island, Canadian High Arctic. *Arctic, Antarctic, and Alpine Research 37(1)*, 127-135.

Hjelle, A. (1993). *Geology of Svalbard.* Oslo: Norsk Polarinstitutt.

Hock, R., & Hooke, R. L. (1993). Evolution of the internal drainage system in the lower part of the ablation area of Storglaciären, Sweden. *Geological Society of America Bulletin 105(4)*, 537-546.

Hodgkins, R. (1994). The seasonal evolution of meltwater discharge, quality and routing at a High-Arctic glacier. Phd thesis, University of Cambridge. p. 245.

Hodgkins, R., & Tranter, M. (1998). Solute in high arctic glacier snow cover and its impact on runoff chemistry. *Annals of Glaciology 26*, 156-160.

Hodgkins, R., Tranter, M., & Dowdeswell, J. A. (1998). The hydrochemistry of runoff from a 'cold-based' glacier in the High Arctic (Scott Turnerbreen, Svalbard). *Hydroloical Processes 12*, 87-103.

Hodgkins, R., Tranter, M., & Dowdeswell, J. A. (2004). The Characteristics and Formation of a High-Arctic Proglacial Icing. *Geografiska Annaler. Series A, Physical Geography 86(3)*, 265-275.

Hodson, A. J. (2017). Isotope data from Rieperbreen and Foxfonna springs. Unpublished data.

Hodson, A. J., Mumford, P. N., Kohler, J., & Wynn, P. M. (2005). The High Arctic glacial ecosystem: new insights from nutrient budgets. *Biogeochemistry 72*, 233-256.

Hodson, A. J., Porter, P., Lowe, A., & Mumford, P. (2002a). Chemical denudation and silicate weathering in Himalayan glacier basins: Batura Glacier, Pakistan. *Journal of Hydrology 262*, 193-208.

Hodson, A., Nowak, A., Senger, K., Redeker, K., Christiansen, H. H., Jessen, S., & et al. (2018). Direct escape of sub-permafrost methane through open system pingos and its contrubution to atmospheric emissions. *Manuscript in preparation*.

Hodson, A., Roberts, T. J., Engvall, A.-C., Holmen, K., & Mumford, P. (2010). Glacier ecosystem response to episodic nitrogen enrichment in Svalbard, European High Arctic. *Biogeochemistry 98*, 171-184.

Hodson, A., Tranter, M., Gurnell, A., Clark, M., & Hagen, J. O. (2002b). The hydrochemistry of Bayelva, a high Arctic proglacial stream in Svalbard. *Journal of Hydrology 257*, 91-114.

Holmlund, E. S. (2016). *3D drone model of Rieperbreen.* Retrieved from https://sketchfab.com/models/93fe80ba7cd94bbba4d4a190f90bca48 (16.7.2017).

Holmlund, E. S. (2017). *3D drone model of Rieperbreen.* Retrieved from https://sketchfab.com/models/c3e2b83b308e4850a7b32160eacb7f9f (10.1.2018).

Hu, X., & Pollard, W. H. (1998a). The Hydrologic Analysis and Modelling of River Icing Growth, North Fork Pass, Yukon Territory, Canada. *Permafrost and Periglacial Processes 8(3)*, 279-294.

Hu, X., & Pollard, W. H. (1998b). Ground Icing Formation: Experimental and Statistical Analyses of the Overflow Process. *Permafrost and Periglacial Processes 8(2)*, 217-235.

Hubbard, B., & Glasser, N. (2005). *Field Techniques in Glaciology and Glacial Geomorphology.* Chichester: John Wiley & Sons Ltd.

Hubbard, B., & Nienow, P. (1997). Alpine subglacial hydrology. *Quaternary Science Reviews 16*, 939-955.

Hubbard, E. F., Kilpatrick, F. A., Martens, L. A., & Wilson Jr., J. F. (1982). Measurements of time of travel and dispersion in streams by dye tracing. In C. A. USGS-TWRI Book 3, *Techniques of Water-Resources Investigations of the United States Geological Survey.* Washington: United States Government Printing Office.

Humlum, O. (n.y.). *Stable water isotope and temperature data. Longyearbyen. 1999-2003. unpublished data.*

Humlum, O., Christiansen, H. H., & Juliussen, H. (2007). Avalanche-derived Rock Glaciers in Svalabard. *Permafrost and Periglacial Processes 18*, 75-88.

Humlum, O., Elberling, B., Hormes, A., Fjordheim, K., Hansen, O. H., & Heinemeier, J. (2005). Late-Holocene glacier growth in Svalbard, documented by subglacial relict vegetation and living soil microbes. *The Holocene 15(3)*, 396-407.

Humlum, O., Instanes, A., & Sollid, J. L. (2003). Permafrost in Svalbard: a review of research history, climatic background and engineering challenges. *Polar Research 22(2)*, 191-215.

IAEA (International Atomic Energy Agency). (2017). *Global Network of Isotopes in Precipitation (GNIP). WISER (Water Isotope System for Data Analysis, Visualization and Electronic Retrieval) Database*. Retrieved from https://nucleus.iaea.org/wiser/index.aspx (13.12.2017).

Ingraham, N. L. (1998). Isotopic Variations in Precipitation. In C. Kendall, & J. J. McDonnell, *Isotope Tracers in Catchment Hydrology* (pp. 87-118). Amsterdam: Elsevier.

Irvine-Fynn, T. D., Hodson, A. J., Kohler, J., Porter, P. R., & Vatne, G. (2005). Dye tracing experiments at Midre Lovénbreen, Svalbard: Preliminary Results and Interpretations. In B. R. Mavlyudov, *Glacier Caves and Glacial Karst in High Mountains and Polar Regions.* (pp. 36-43). Moscow: Institute of geography of the Russian Academy of Sciences.

Irvine-Fynn, T. D., Hodson, A. J., Moorman, B. J., Vatne, G., & Hubbard, A. L. (2011). Polythermal Glacier Hydrology: A Review. *Reviews of Geophysics, 49(4)*, RG4002.

Jiskoot, H., Boyle, P., & Murray, T. (1998). The incidence of glacier surging in Svalbard: evidence from multivariate statistics. *Computers and Geosciences 24(4)*, 387-399.

Jiskoot, H., Murray, T., & Boyle, P. (2000). Controls on the distribution of surge-type glaciers in Svalbard. *Journal of Glaciology 46(154)*, 412-422.

Jouzel, J., & Souchez, R. A. (1982). Melting-refreezing at the glacier sole and the isotopic composition of the ice. *Journal of Glaciology 28(98)*, 35-42.

Kane, D. L. (1981). Physical mechanics of aufeis growth. *Canadian Journal of Civil Engineering 8(2)*, 186-195.

Kane, D. L., & Slaughter, C. W. (1972). Seasonal regime and hydrological significance of stream icings in central Alaska. In *Role of Snow and Ice in Hydrology: Proceedings of Symposia held at Banff, Septemebr 1972, Publ. 107(1)* (pp. 528-540). Gentbrugge, Belgium: International Association of Hydrological Sciences.

Kendall, C., & Caldwell, E. A. (1998). Fundamentals of Isotope Geochemistry. In C. Kendall, & J. J. McDonnell, *Isotope Tracers in Catchment Hydrology* (pp. 51-86). Amsterdam: Elsevier.

Knödel, K., Lange, G., & Voigt, H.-J. (2007). *Environmental Geology. Handbook of Field Methods and Case Studies.* (Bundesanstalt für Geowissenschaften und Rohstoffe, Ed.) Berlin Heidelberg: Springer.

Kohler, J., Moore, J., Kennett, M., Engeset, R., & Elvehoy, H. (1997). Using ground-prenetrating radar to image previous years' summer surface for mass-balance measurements. *Annals of Glaciology 24*, 355-360.

Krainer, K., & Mostler, W. (2002). Hydrology of Active Rock Glaciers: Examples from the Austrian Alps. *Arctic, Antarctic and Alpine Research 34(2)*, 142-149.

Kruetzmann, N. C., Rack, W., McDonald, A. J., & George, S. E. (2011). Snow accumulation and compaction derived from GPR data near Ross Island, Antarctica. *The Cryosphere 5*, 391-404.

Kumar, B. (2011a). Hydrogen Isotopes. In V. P. Singh, P. Singh, & U. K. Haritashya, *Encyclopedia of Snow, Ice and Glaciers* (pp. 533-534). Dordrecht, The Netherlands: Springer.

Kumar, B. (2011b). Isotopic characteristics of ice, snow, and glaciers. In V. P. Singh, P. Singh, & U. K. Haritashya, *Encyclopedia of Snow, Ice and Glaciers* (pp. 665-668). Dordrecht, The Netherlands: Springer.

Kumar, B. (2011c). Oxygen Isotopes. In V. P. Singh, P. Singh, & U. K. Haritashya, *Encyclopedia of Snow, Ice and Glaciers* (pp. 799-800). Dordrecht, The Netherlands: Springer.

Kumar, B. (2011d). Stable Isotopes. In V. P. Singh, P. Singh, & U. K. Haritashya, *Encyclopedia of Snow, Ice and Glaciers* (pp. 1078-1079). Dordrecht, The Netherlands: Springer.

Kumar, P. P. (2011). Icing. In V. P. Singh, P. Singh, & U. K. Haritashya, *Encyclopedia of Snow, Ice and Glaciers* (p. 640). Dordrecht, The Netherlands: Springer.

Lapazaran, J. J., Otero, J., Martín-Español, A., & Navarro, F. J. (2016). On the errors involved in ice-thickness estimates 1: ground-penetrating radar measurement errors. *Journal of Glaciology 62(236)*, 1008-1020.

Lefauconnier, B., & Hagen, J. O. (1991). *Surging and calving glaciers in Eastern Svalbard.* Oslo: Norsk Polarinstitutt, Meddelelser 16.

Liestøl, O. (1974). Glaciological work in 1972. In T. Gjelsvik, *Årbok 1972* (pp. 125-135). Oslo: Norsk Polarinstitutt.

Liestøl, O. (1977). Pingos, springs and permafrost in Spitsbergen. In K. Z. Lundquist, *Årbok 1975* (pp. 7-29). Oslo: Norsk Polarinstitutt.

Liestøl, O. (1988). Glaciers of Europe - Glaciers of Svalbard, Norway. In R. S. Williams, & J. G. Ferrigno, *Satellite image atlas of glaciers of the world* (pp. 127-151). Denver: U.S. Geological Survey.

Lovell, H. (2014). *On the ice-sediment-landform associations of surging glaciers on Svalbard.* Phd thesis. Queen Mary University of London.

Lovell, H., Fleming, E. J., Benn, D. I., Hubbard, B., Lukas, S., & Naegeli, K. (2015). Former dynamic behaviour of a cold-based valley glacier on Svalbard revealed by basal ice and structural glaciology investigations. *Journal of Glaciology 61(226)*, 309-328.

Lysså, A., & Lønne, I. (2001). Moraine development at a small High-Arctic valley glacier: Rieperbreen, Svalbard. *Journal of Quaternary Science 16(6)*, 519-529.

Major, H., & Nagy, J. (1972). *Geology of the Adventdalen map area.* Oslo: Norsk Polarinstitutt.

Marchenko, S., Pohjola, V. A., Pettersson, R., Van Pelt, W. J., Vega, C. P., Machguth, H., & et al. (2017). A plot-scale study of firn stratigraphy at Lomonosovfonna, Svalbard, using ice cores, borehole video and GPR surveys in 2012-14. *Journal of Glaciology 63(237)*, 67-78.

McCarthy, M., Pritchard, H., Willis, I., & King, E. (2017). Ground-penetrating radar measurements of debris thickness on Lirung Glacier, Nepal. *Journal of Glaciology 63(239)*, 543-555.

Merkel, B. J., & Planer-Friedrich, B. (2008). *Groundwater Geochemistry. A Practical Guide to Modeling of Natural and Contaminated Aquatic Systems. 2nd Edition.* (D. K. Nordstrom, Ed.) Berlin Heidelberg: Springer.

Møller, I. (2006). Ground penetrating radar. In R. Kirsch, H.-M. Rumpel, W. Scheer, & H. Wiederhold, *Groundwater Resources in Buried Valleys. A challenge for Geosciences* (pp. 99-106). Hannover: Leibniz Institute for Applied Geosciences (GGA-Institut).

Monnier, S., Camerlynck, C., Rejiba, F., Kinnard, C., & Galibert , P. Y. (2011). Glacier ice in rock glaciers: a case study in the Vanoise Massif, Northern French Alps. *The Cryosphere Discussions 5*, 3597-3626.

Moore, J. C., Pälli, A., Ludwig, F., Blatter, H., Jania, J., Gadek, B., & et al. (1999). High-resolution hydrothermal structure of Hansbreen, Spitsbergen, mapped by ground-penetrating radar. *Journal of Glaciology 45(151)*, 524-532.

Moorman, B. J. (2003). Glacier-permafrost hydrology interactions, Bylot Island, Canada. *Proceedings of the 8th International Permafrost Conference*, 783-788.

Moorman, B. J., & Michel, F. A. (2000). Glacial hydrological system characterization using ground-penetrating radar. *Hydrological Processes 14*, 2645-2667.

Muller, S. W. (1947). *Permafrost or permanently frozen ground and related engineering problems.* Ann Arbor: J.W. Edwards.

Munneke, P. K., McGrath, D., Medley, B., Luckman, A., Bevan, S., Kulessa, B., & et al. (2017). Observationally constrained surface mass balance of Larsen C Ice Shelf, Antarctica. *The Cryosphere 11*, 2411-2426.

Naegeli, K., Lovell, H., Zemp, M., & Benn, D. (2014). Dendritic subglacial drainage systems in cold glaciers formed by cut-and-closure processes. *Geografiska Annaler: Series A, Physical Geography, 96(4)*, 591-608.

Nienow, P. (2011). Dye Tracer Investigations of glacier Hydrology. In V. P. Singh, P. Singh, & U. K. Haritashya, *Enceclopedia of Snow, Ice and Glaciers.* (pp. 242-244). Dordrecht, The Netherlands: Springer.

Nienow, P. W. (1993). *Dye tracer investigations of glacier hydrological systems. PhD thesis.* Cambridge: University of Cambridge.

Nienow, P. W., Sharp, M., & Willis, I. C. (1996). Sampling-rate effects on the properties of dye breakthrough curves from glaciers. *Journal of Glaciology 42(140)*, 184-189.

Nienow, P., Sharp, M., & Willis, I. (1998). Seasonal changes in the morphology of the subglacial drainage system, Haut Glacier D'Arolla, Switzerland. *Earth Surface Processes and Landforms 23*, 825-843.

Norwegian Meteorological Institute. (2017). *eklima*. Retrieved from http://sharki.oslo.dnmi.no/portal/page?_pageid=73%2C39035%2C73_39049&_dad=portal&_schema=PORTAL (27.7.2017).

Norwegian Polar Institut. (2016). *Svalbardkartet*. Retrieved from http://svalbardkartet.npolar.no/html5/index.html?viewer=svalbardkartet (6.3.2017).

Norwegian Polar Institute (NPI). (2009). *Aerial image Bolterdalen/ Rieperbreen from 27.7.2009*. Retrieved from http://toposvalbard.npolar.no (19.7.2017).

Norwegian Polar Institute (NPI). (n.d.). *Map of Svalbard*. Retrieved from toposvalbard.npolar.no (19.7.2017)

Olszewski, A. (1982). Icings and their geomorphological significance exemplified from Oscar II Land and Prins Karls Forland, Svalbard. *Acta Univer. Nicolai Copernici Geografia 16(51)*, 91-122.

Permafrost Subcommittee. (1988). *Glossary of Permafrost and Related Ground-Ice Terms.* (S. A. Harris, H. M. French, J. A. Heginbottom, G. H. Johnston , B. Ladanyi, D. C. Sego, & R. O. van Everdingen, Eds.) National Research Council of Canada, Technical Memorandum No. 142.

Pohjola, V. A., Martma, T. A., Meijer, H. A., Moore, J. C., Isaksson, E., Vaikmäe, R., & Van De Wal, R. S. (2002). Reconstruction of three centuries of annual accumulation rates based on the record of stable isotopes of water from Lomonosovfonna, Svalbard. *Annals of Glaciology 35*, 57-62.

Pollard, W. (2018). Periglacial Processes in Glacial Environments. In J. Menzies, & J. J. van der Meer, *Past Glacial Environments. Second Edition* (pp. 537-564). Amsterdam: Elsevier.

Pollard, W. H. (2005). Icing Processes Associated with High Arctic Perennial Springs, Axel Heiberg Island, Nunavut, Canada. *Permafrost and Periglacial Processes 16*, 51-68.

Raben, P., & Theakstone, W. H. (1994). Isotopic and ionic changes in a snow cover at different altitudes: observations at Austre Okstindbreen in 1991. *Annals of Glaciology 19*, 85-91.

Raiswell, R. (1984). Chemical models of solute aquisition in glacial melt waters. *Journal of Glaciology 30(104)*, 49-57.

Rea, B. R., & Evans, D. J. (2011). An assessment of surge-induced crevassing and the formation of crevasse squeeze ridges. *Journal of Geophysical Research 116*, F04005.

Riger-Kusk, M. (2006). *Hydrology and hydrochemistry of a High Arctic glacier: Longyearbreen, Svalbard.* Master Thesis. Department of Earth Sciences, University of Aarhus and Department of Geology, University Centre in Svalbard (UNIS).

Ritter, M., & Kuells, C. J. (2010). Deuterium excess anomaly of precipitation in Svalbard. Poster. *AGU Fall Meeting.*

Roberson, S., Hubbard, B., Coulson, H. R., & Boomer, I. (2011). Physical properties and formation of flutes at a polythermal valley glacier: Midre Lovénbreen, Svalbard. *Geografiska Annaler: Series A, Physical Geography 93(2)*, 71-88.

Robinson, M., Bristow, C., McKinley, J., & Ruffell, A. (2013). Ground Penetrating Radar. In *Geomorphological Techniques, Part 1, Sec. 5.5.* British Society for Geomorphology.

Rounds, S. A., Wilde, F. D., & Ritz, G. F. (2013). Dissolved oxygen (ver. 3.0). Chapter A6 Field Measurements. In U.S. Geological Survey, *National Field Manual for the Collection of Water-Quality Data.* Retrieved from https://water.usgs.gov/owq/FieldManual/Chapter6/6.2_ver3.pdf (19.5.2017).

Rutter, N., Hodson, A., Irvine-Fynn, T., & Solås, M. K. (2011). Hydrology and hydrochemistry of a deglaciating high-Arctic catchment, Svalbard. *Journal of Hydrology 410*, 39-50.

Saini-Eidukat, B., & Yahin, A. (1999). Web.phreeq: a WWW instructional tool for modeling the distribution of chemical species in water. *Computers & Geosciences 25(4)*, 347-353. Retrieved from https://www.ndsu.edu/webphreeq/ (20.3.2018).

Sandmeier , K. J. (2017). *ReflexW Version 8.5.* Retrieved from Sandmeier geophysical research: http://www.sandmeier-geo.de/Download/reflexw_manual_a4.pdf (19.11.2017).

Schohl, G. A., & Ettema, R. (1986). Theory and laboratory observations of naled ice growth. *Journal of Glaciology 32(111)*, 168-177.

Seaberg, S. Z., Seaberg, J. Z., Hooke, L. R., & Wiberg, D. W. (1988). Character of the englacial and subglacial drainage system in the lower part of the ablation area of Storglaciären, Sweden, as revealed by dye-trace studies. *Journal of Glaciology 34(117)*, 217-227.

Sjöberg, Y., Marklund, P., Pettersson, R., & Lyon, S. W. (2015). Geophysical mapping of palsa peatland permafrost. *The Cryosphere 9*, 465-478.

Sloan, C. E., Zenone, C., & Mayo, L. R. (1976). *Icings along the Trans-Alaska Pipeline Route. Geological Survey professional paper 979.* Washington DC, USA: U.S. Dept. of Interior, Geological Survey.

Sobota, I. (2016). Icings and their role as an important element of the cryosphere in High Arctic glacier forefields. *Bulletin of Geography. Physical Geography Series 10*, 81-93.

Sørbel, L., Tolgensbakk, J., & Høvgard, K. (2001). *Geomorphological and Quarternary Geological Map, Svalbard 1:100,000, Spitsbergen Sheet C9Q. Temkart No. 31/32.* Tromsø: Norwegian Polar Institute.

Souchez, R. A., & Jouzel, J. (1984). On the isotopic composition in δD and δ18O of water and ice during freezing. *Journal of Glaciology 30(106)*, 369-372.

Souchez, R., Jouzel, J., Lorrain, R., Sleewaegen, S., Stiévenard, M., & Verbeke, V. (2000). A kinetic isotope effect during ice formation by water freezing. *Geophysical Research Letters 27(13)*, 1923-1926.

Stachnik, L., Yde, J. C., Kondracka, M., Ignatiuk, D., & Grzesik, M. (2016). Glacier naled evolution and relation to the subglacial drainage system based on water chemistry and GPR surveys (Werenskioldbreen, SW Svalbard). *Annals of Glaciology 57(72)*, 19-30.

Theakstone, W. H. (2003). Oxygen isotopes in glacier-river water, Austre Okstindbreen, Okstindan, Norway. *Journal of Glaciology 49(165)*, 282-298.

Theakstone, W. H., & Knudsen, N. T. (1981). Dye tracer tests of water movement at the glacier Austre Okstindbreen, Norway. *Norsk Geografisk Tidsskrift - Norwegian Journal of Geography 35(1)*, 21-28.

Theakstone, W. H., & Knudsen, N. T. (1996). Isotopic and ionic variations in glacier river water during three contrasting ablation seasons. *Hydrological Processes 10*, 523-539.

Tranter, M. (2011). Isotopic Fractionation of Freezing Water. In V. P. Singh, P. Singh, & U. K. Haritashya, *Encyclopedia of Snow, Ice and Glaciers* (pp. 668-669). Dordrecht, The Netherlands: Springer.

Tranter, M., Brown, G. H., Hodson, A. J., & Gurnell, A. M. (1996). Hydrochemistry as an indicator of subglacial drainage system structure: a comparison of alpine and sub-polar environments. *Hydrological Processes 10(4)*, 541-556.

Tranter, M., Brown, G., Raiswell, R., Sharp, M., & Gurnell, A. (1993). A conceptual model of solute acquisition by Alpine glacial meltwater. *Journal of Glaciology 39(133)*, 573-581.

van Everdingen, R. O. (1982a). Management of groundwater discharge for the solution of icing problems in the Yukon. *Proceedings of the 4th Canadian Permafrost Conference (1982)*, 212-226.

van Everdingen, R. O. (1982b). Frost Blister of the Bear Rock Spring Area near Fort Norman, N.W.T. *Arctic 35(2)*, 243-265.

VanLoon, G. W., & Duffy, S. J. (2000). *Environmental Chemistry: A Global Perspective. Third edition.* Oxford: Oxford University Press.

von Middendorf, A. T. (1859). *Sibirische Reise. Band 4, Teil 1.* St. Petersburg: Kaiserliche Akademie der Wissenschaften.

Wadham, J. L., Hodson, A. J., Tranter, M., & Dowdeswell, J. A. (1998). The hydrochemistry of meltwaters draining a polythermal-based, high Arctic glacier, south Svalbard: I. The ablation season. *Hydrological Processes 12*, 1825-1849.

Wadham, J. L., Tranter, M., & Dowdeswell, J. A. (2000). Hydrochemistry of meltwaters draining a polythermal-based, high-Actic glacier, south Svalbard: II. Winter and early Spring. *Hydrological Processes 14*, 1767-1786.

Wainstein, P. A., Moorman, B. J., & Whitehead, K. (2008). Importance of Glacier-Permafrost Interactions in the Preservation of a Proglacial Icing: Fountain Glacier, Bylot Island, Canada. In D. L. Kane, & K. M. Hinkel, *Proceedings Ninth International Conference on Permafrost, Fairbanks, Alaska* (pp. 1881-1886).

Wainstein, P., Moorman, B., & Whitehead, K. (2014). Glacial conditions that contribute to the regeneration of Fountain Glacier proglacial icing, Bylot Island, Canada. *Hydrological Processes 28*, 2749-2760.

Wanty, R. B., Wang, B., Vohden, J., Day, W. C., & Gough, L. P. (2007). Aufeis Accumulations in Stream Bottoms in Arctic and Subarctic Environments as a Possible Indicator of Geologic Structure. In L. P. Gough, & W. C. Day, *Recent U.S. Geological Survey Studies in the Tintina Gold Provine, Alaska, United States, and Yukon, Canada - Results of a 5-Year Project* (Vols. Scientific Investigations Report 2007 - 5289 Chapter F). Reston, VA, USA: U.S. Geological Survey.

Watanabe, T., Matsuoka, N., & Christiansen, H. H. (2013). Ice- and Soil-Wedge Dynamics in the Kapp Linné Area, Svalbard, Investigated by Two- and Three-Dimensional GPR and Ground Thermal and Acceleration Regimes. *Permafrost an Periglacial Processes 24*, 39-55.

Westermann, S., Wollschläger, U., & Boike, J. (2010). Monitoring of active layer dynamics at a permafrost site on Svalbard using multi-channel ground-penetrating radar. *The Cryosphere 4*, 475-487.

Whitehead, K., Moorman, B. J., & Hugenholtz, C. H. (2013). Brief Communication: Low-cost, on-demand aerial photogrammetry for glaciological measurement. *The Cryosphere 7*, 1879-1884.

Willis, I. C., Fitzsimmons, C. D., Melvold, K., Andreassen, L. M., & Giesen, R. H. (2012). Structure, morphology and water flux of a subglacial drainage system, Midtdalsbreen, Norway. *Hydrological Processes 26(25)*, 3810-3829.

Willis, I. C., Lawson, W., I., O., Jacobel, B., & Autridge, J. (2009). Subglacial drainage system structure and morphology of Brewster Glacier, New Zealand. *Hydrological Processes, 23(3)*, 384-396.

Willis, I. C., Sharp, M. J., & Richards, K. S. (1990). Configuration of the Drainage System of Midtdalsbreen, Norway, as Indicated by Dye-Tracing Experiments. *Journal of Glaciology 36(122)*, 89-101.

Woo, M. (2012). *Permafrost Hydrology.* Berlin Heidelberg, Germany: Springer.

Yao T., Yu, W., Zhao, H., & Liu, Y. (2011). Isotope Analysis. In V. P. Singh, P. Singh, & U. K. Haritashya, *Encyclopedia of Snow, Ice and Glaciers* (pp. 657-665). Dordrecht, The Netherlands: Springer.

Yde, J. C., & Knudsen, N. T. (2005). Observations of Debris-rich Naled Associated with a Major Glacier Surge Event, Disko Island, West Greenland. *Permafrost and Periglacial Processes 16(4)*, 319-325.

Yde, J. C., Hodson, A. J., Solovjanova, I., Steffensen, J. P., Nørnberg, P., Heinemeier, J., & Olsen, J. (2012). Chemical and isotopic characteristics of a glacier-derived naled in front of Austre Grønfjordbreen, Svalbard. *Polar Research 31, 17628*.

Yde, J. C., Riger-Kusk, M., Christiansen, H. H., Knudsen, N. T., & Humlum, O. (2008). Hydrochemical characterisitcs of bulk meltwater from an entire ablation season, Longyearbyen, Svalbard. *Journal of Glaciology 54(185)*, 259-272.

Yde, J., Knudsen, T. N., Larsen, N. K., Kronborg, C., Nielsen, O. B., Heinemeier, J., & Olsen, J. (2005). The presence of thrust-block naled after a major surge even: Kuannersuit Glacier, West Greenland. *Annals of Glaciology 42*, 145-150.

Yoshikawa, K., Hinzman, L. D., & Kane, D. L. (2007). Spring and aufeis (icing) hydrology in Brooks Range, Alaska. *Journals of Geophysical Research: Biogeosciences 112(G4)*.

Yoshikawa, K., White, D., Hinzman, L., Goering, D., Petrone, K., Bolton, W., & Ishikawa, N. (2003). Water in permafrost: case study of aufeis and pingo hydrology in discontinuous permafrost. In M. Phillips, S. Springman, & L. Arenson, *Proceedings of the 8th International Conference on Permafrost* (pp. 1259-1264). Balkema, Lisse.

Zhu, C., & Anderson, G. (2002). *Environmental Application of Geochemical Modeling.* Cambridge, UK: Cambridge University Press.

Appendix

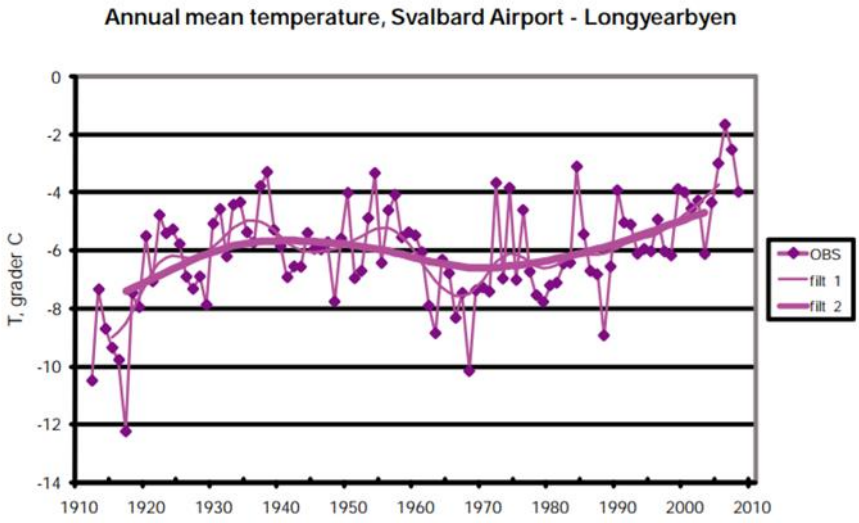

Figure 41: MAAT at the Longyearbyen airport from 1911-2007. OBS – observations, filt 1 – smoothed curve on 10-year scale, filt 2 – smoothed curve on 30-year scale (Førland et al. 2009).

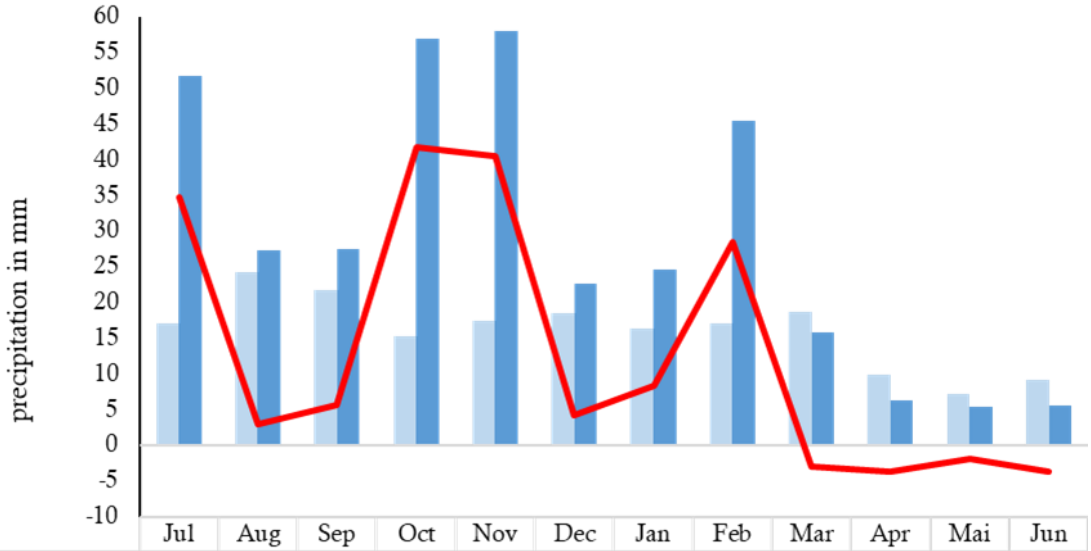

	Jul	Aug	Sep	Oct	Nov	Dec	Jan	Feb	Mar	Apr	Mai	Jun
1975-2015	17,0	24,3	21,7	15,3	17,5	18,4	16,3	17,0	18,7	9,9	7,1	9,2
2016-2017	51,7	27,3	27,4	57,0	58,0	22,7	24,6	45,4	15,8	6,2	5,3	5,6
difference 1975	34,7	3,0	5,7	41,7	40,5	4,3	8,3	28,4	-2,9	-3,7	-1,8	-3,6

Figure 42: Precipitation measured at the Longyearbyen airport. Bars show average monthly precipitation for the periods August 1975 - December 2015 (light blue) and July 2016 - June 2017 (dark blue). The red line indicates the difference between the two periods (data: Norwegian Meteorological Institute 2017).

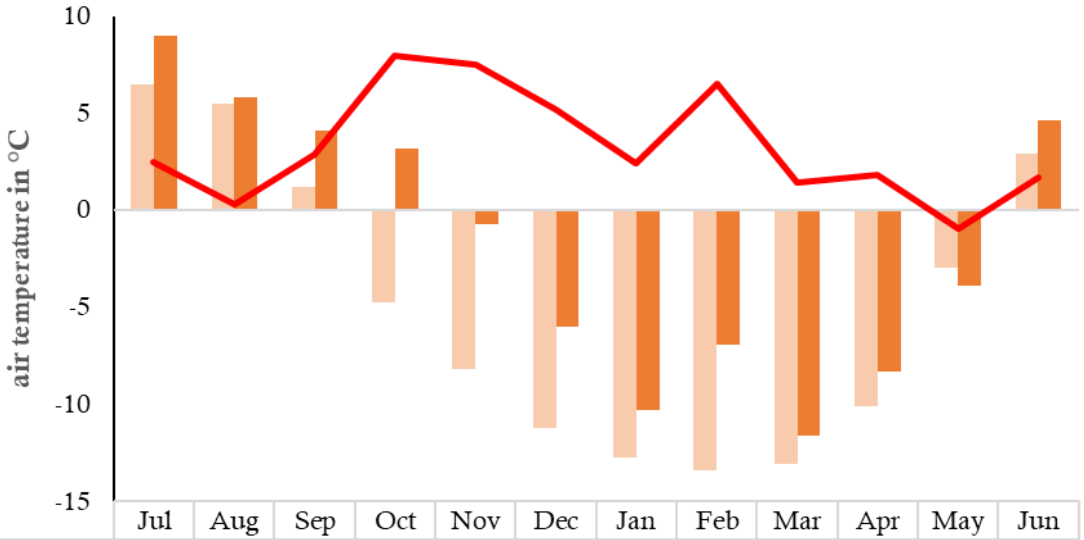

	Jul	Aug	Sep	Oct	Nov	Dec	Jan	Feb	Mar	Apr	May	Jun
1975-2015	6,5	5,5	1,2	-4,7	-8,2	-11,2	-12,7	-13,4	-13,1	-10,1	-3,0	2,9
2016-2017	9	5,8	4,1	3,2	-0,7	-6	-10,3	-6,9	-11,6	-8,3	-3,9	4,6
difference	2,5	0,3	2,9	7,9	7,5	5,2	2,4	6,5	1,5	1,8	-0,9	1,7

Figure 43: Air temperature measured at the Longyearbyen airport. The bars show the average monthly temperatures for the periods August 1975 - December 2015 (light orange) and July 2016 - June 2017 (dark orange). The red line indicates the difference between the two periods (data: Norwegian Meteorological Institute 2017).

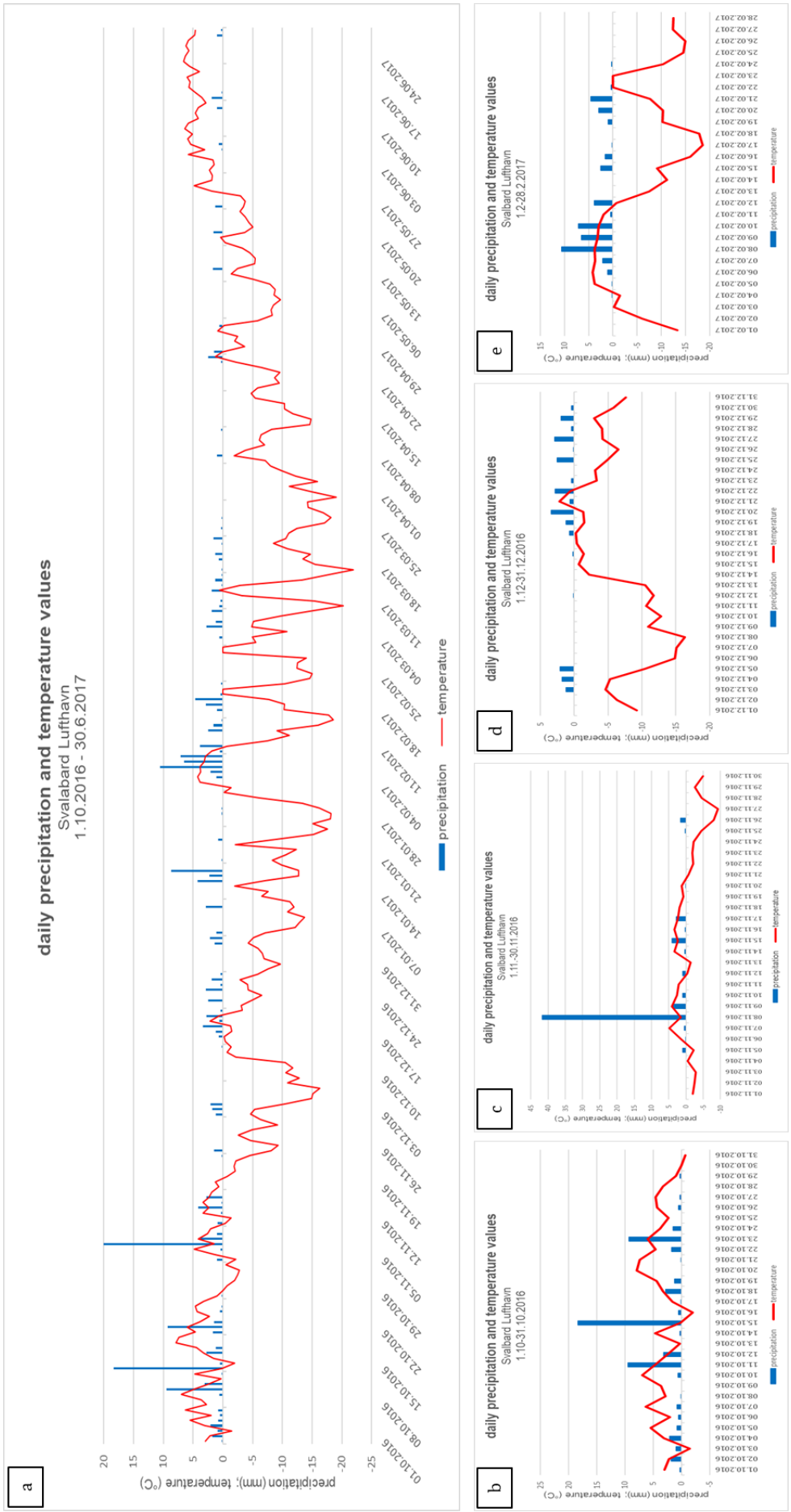

Figure 44: (a) Daily precipitation and temperature values at the Longyearbyen airport for the accumulation season 2016/2017 from 1.10.2016 to 30.6.2017; (b-e) detailed diagrams showing daily precipitation and temperature values for the months October (b), November (c), December (d) and February (e) (data: Norwegian Meteorological Institute 2017).

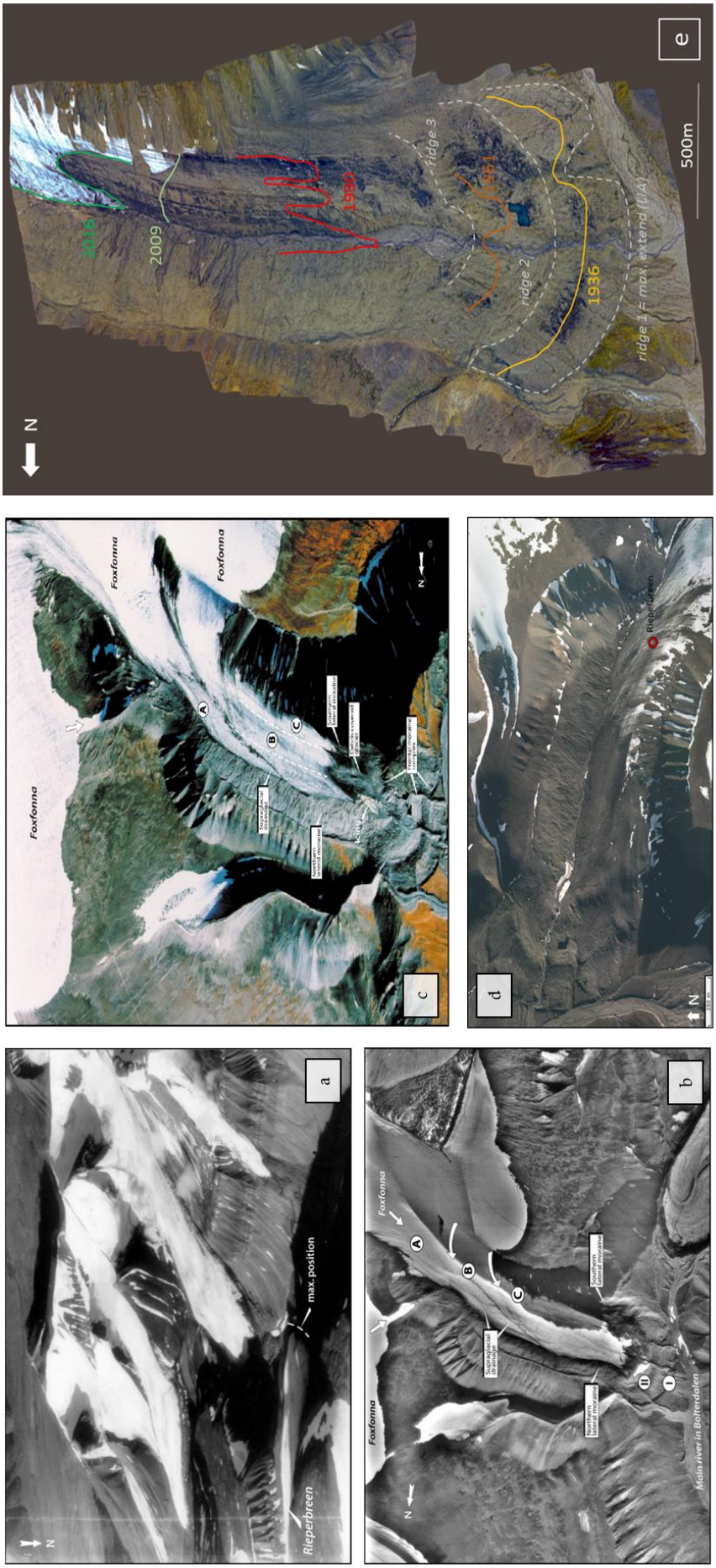

Figure 45: Aerial photographs showing the extent of Rieperbreen between 1936-2016. (a) Aerial photograph from 1936 with maximum position (LIA moraine) (Norwegian Polar Institute 1936; modified by: Lyså & Lønne 2001); (b) Aerial photograph from August 15th, 1961 showing moraine ridge 1 (LIA moraine) and 2. The letters A-C indicate the three ice lobes of the glacier with different origins (Norwegian Polar Institute 1961; modified by: Lyså & Lønne 2001); (c) Aerial photograph from August 14th, 1990. Moraine ridge 3 is visible which formed between 1961-1990. Indication of ice lobes (A-C) (Norwegian Polar Institute 1990; modified by: Lyså & Lønne 2001); (d) Aerial photograph from July 27th, 2009 (Norwegian Polar Institute 2009); (e) Composite 3D drone image from October 8th, 2016 (Holmlund 2016, modified). The lines show the extent of Rieperbreen as visible in the 1936, 1961, 1990 and 2009 aerial photographs and the position of the moraine ridges 1, 2 and 3. Between 1990-2016 the glacier has receded about 1km.

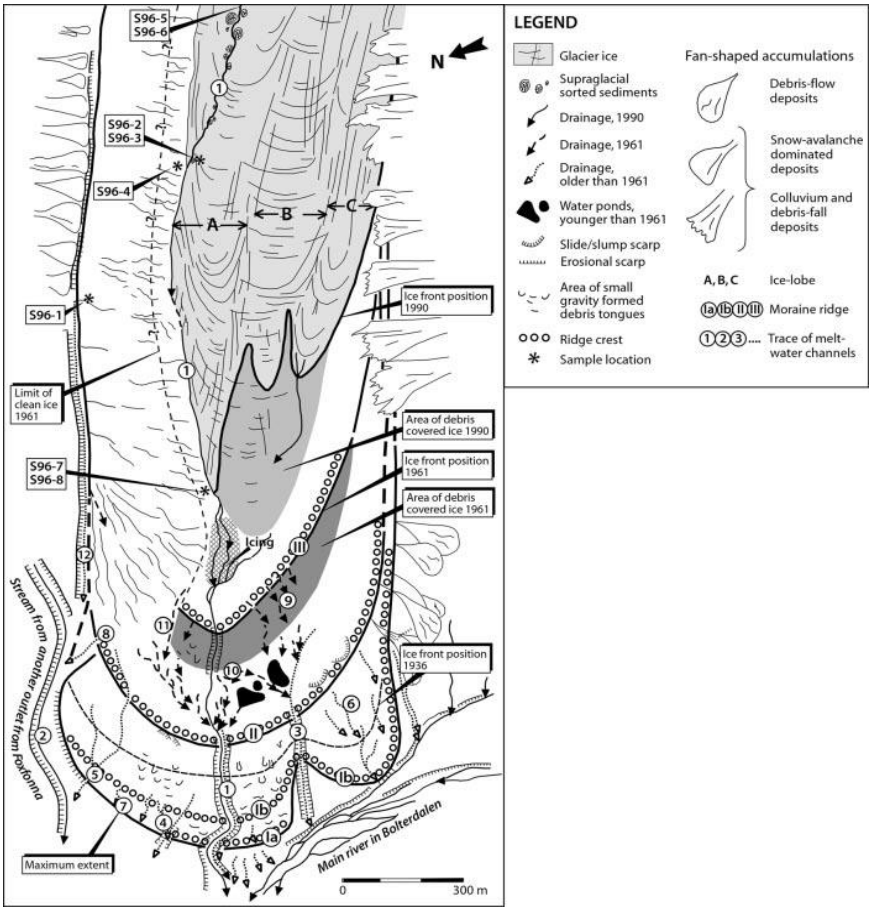

Figure 46: Morphologic map of the Rieperbreen forefield based on the 1936, 1961 and 1990 aerial photographs. Symbols indicate the ice front positions in the given years, the moraine ridges, inactive meltwater channels within the moraine complex and active meltwater channels as present in 1990 (Lyså & Lønne 2001).

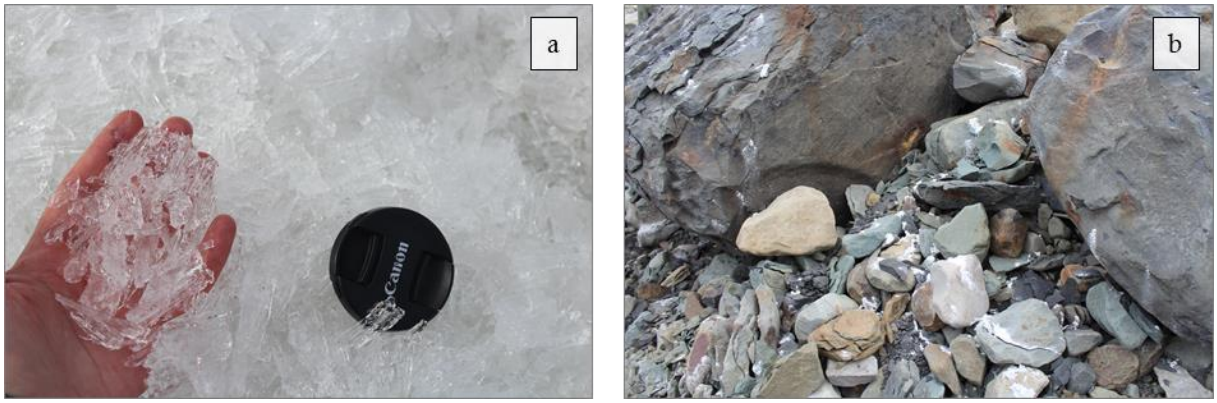

Figure 47: (a) Needle ice from the surface of the ablating icing; (b) white precipitates indicate last winter's icing extent where not washed away from meltwater.

Figure 48: Overview of pictures showing the morphology of the icing and changes between March-June 2017. Numbers from 1-14 indicate the pictures in Figure 49 and Figure 50 and arrows the viewing direction (background image: Holmlund 2017).

Figure 49: Rieperbreen icing during the accumulation season. Refer to location of pictures indicated in Figure 48. (1) lower icing on March 26th; (2) upper icing on March 26th (Kuschel 2017); (3) icing between LIA moraine; (4) injection mound with crack on the top of the lower icing; (5) Stacked images showing the upper area of the lower icing on April 9th. Snow is seen to slide off in the middle of the picture due to lateral icing growth. Wet icing surface underneath an injection mound is indicated by the darker shade of blue towards the left on the picture; (6) view from the top of the upper icing down valley on April 18th. Notice the light-blue, snow-free surface indicating recent sheet flow; (7) water surfacing from spring 1 forming a low mound of rippled ice.

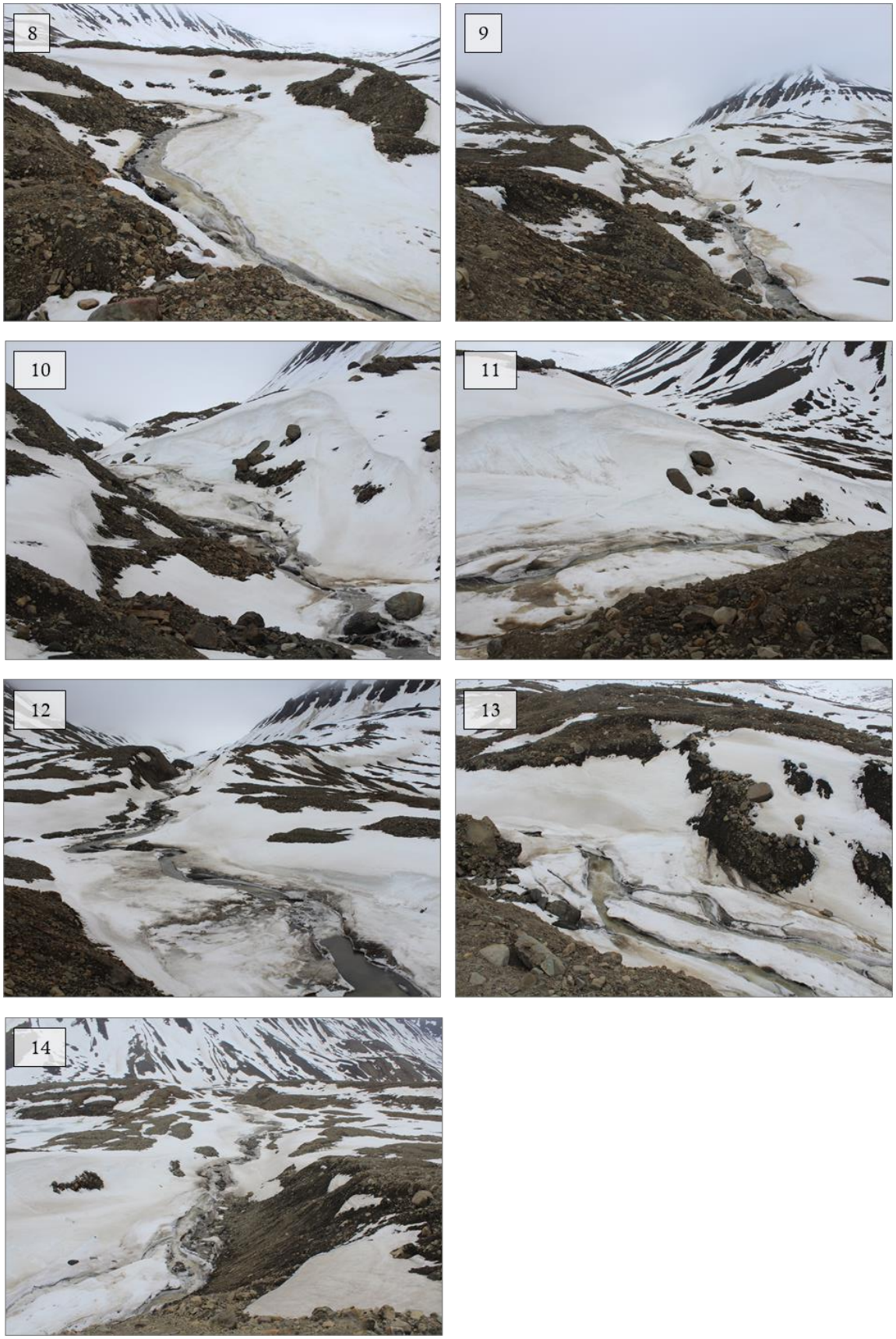

Figure 50: Rieperbreen icing at the onset of the melt-season on June 13th. Refer to location of pictures indicated in Figure 48. (8) Icing between LIA moraine; (9) view up valley towards moraine ridge 2; (10) area of lower icing; (11) lower icing, compare with picture 5 in Figure 49; (12) Area with flat topography between ridge 2 and 3. Notice the debris next to the river in the back of the picture indicating an icing-free stretch. (13) top of upper icing; (14) view down valley from ridge 3.

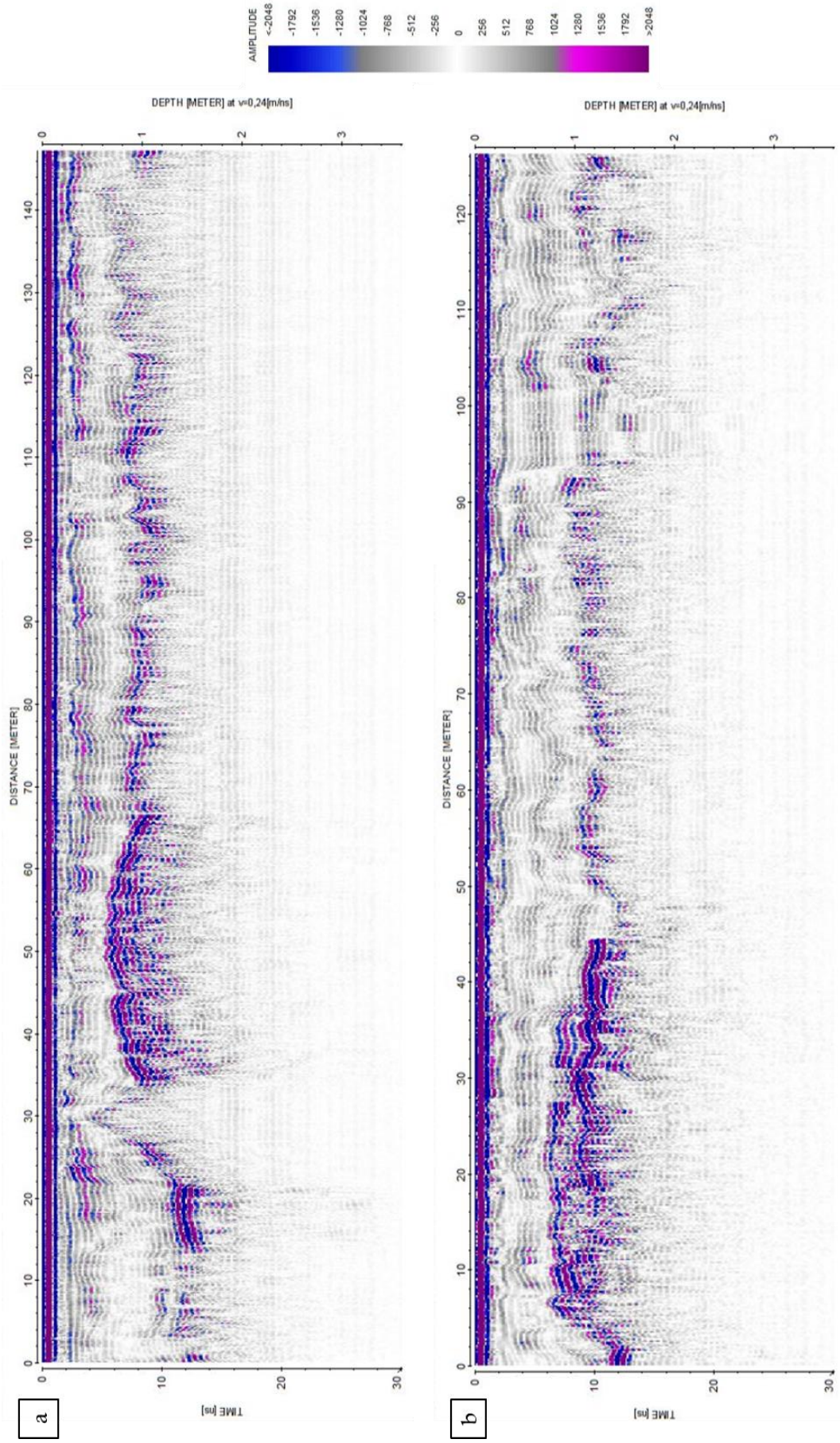

Figure 51: (a) GPR profile 1; (b) GPR profile 2.

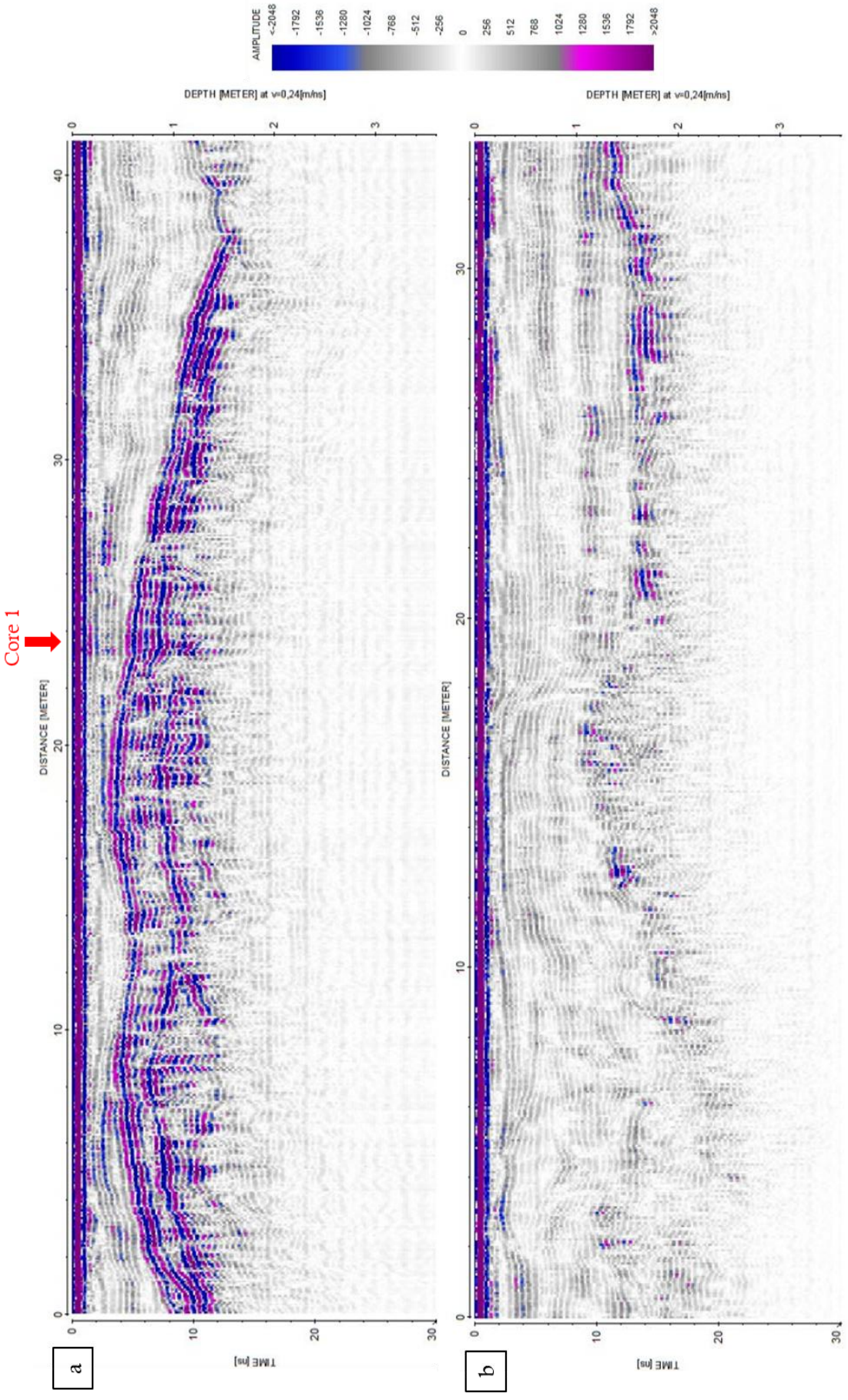

Figure 52: (a) GPR profile 3 with location of ice core sample; (b) GPR profile 4.

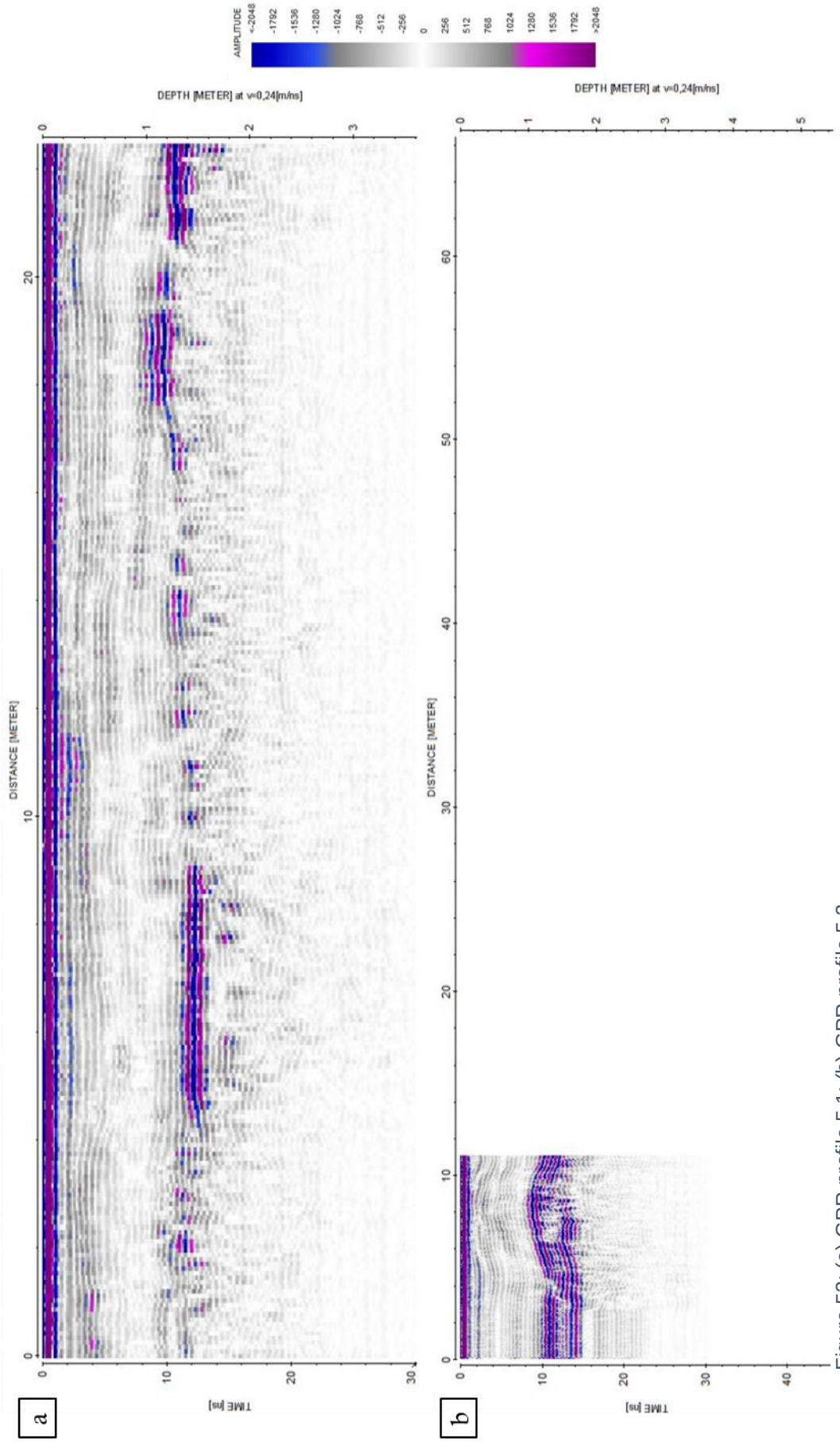

Figure 53: (a) GPR profile 5.1; (b) GPR profile 5.2.

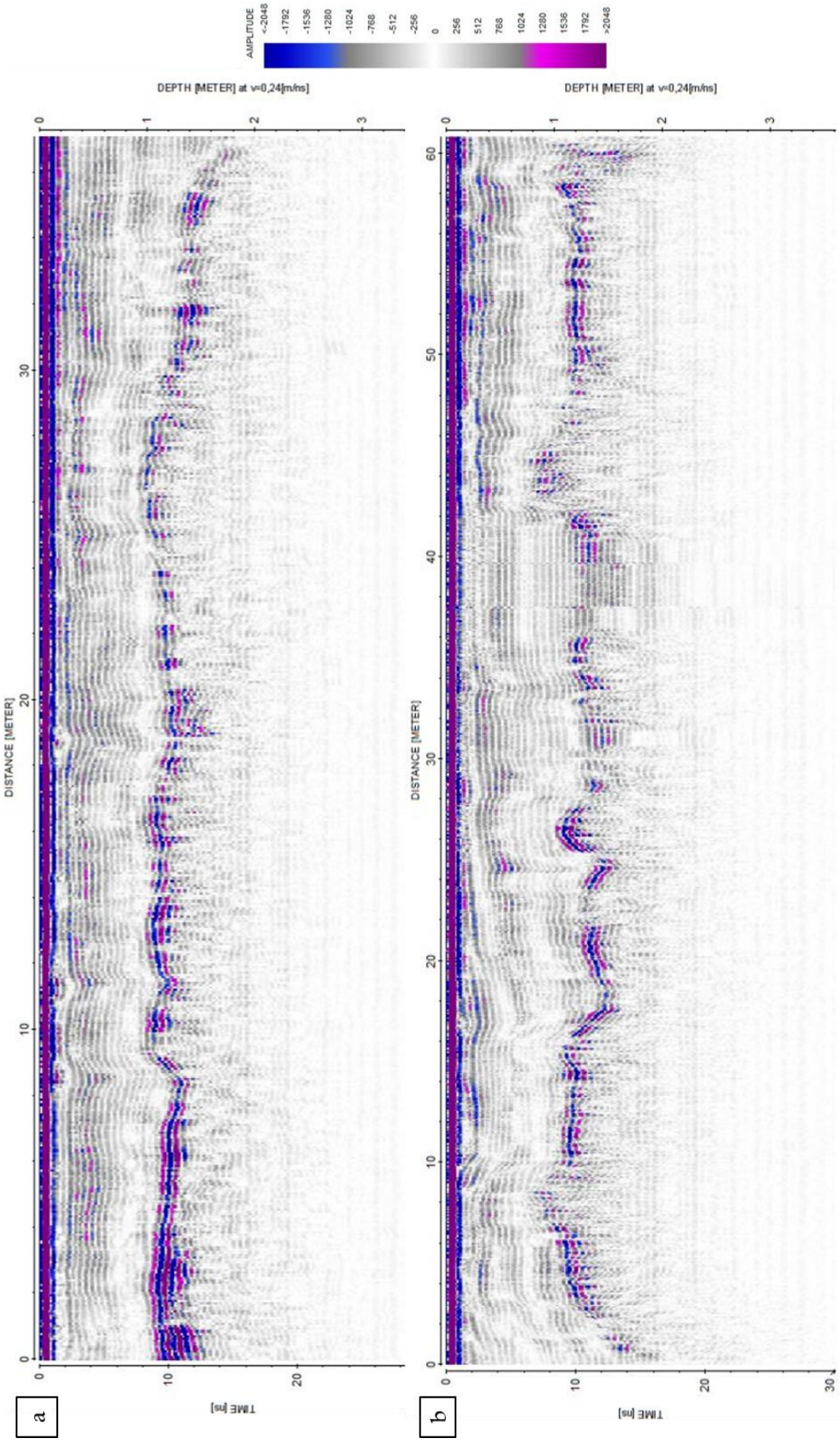

Figure 54: (a) GPR profile 5.3; (b) GPR profile 6.

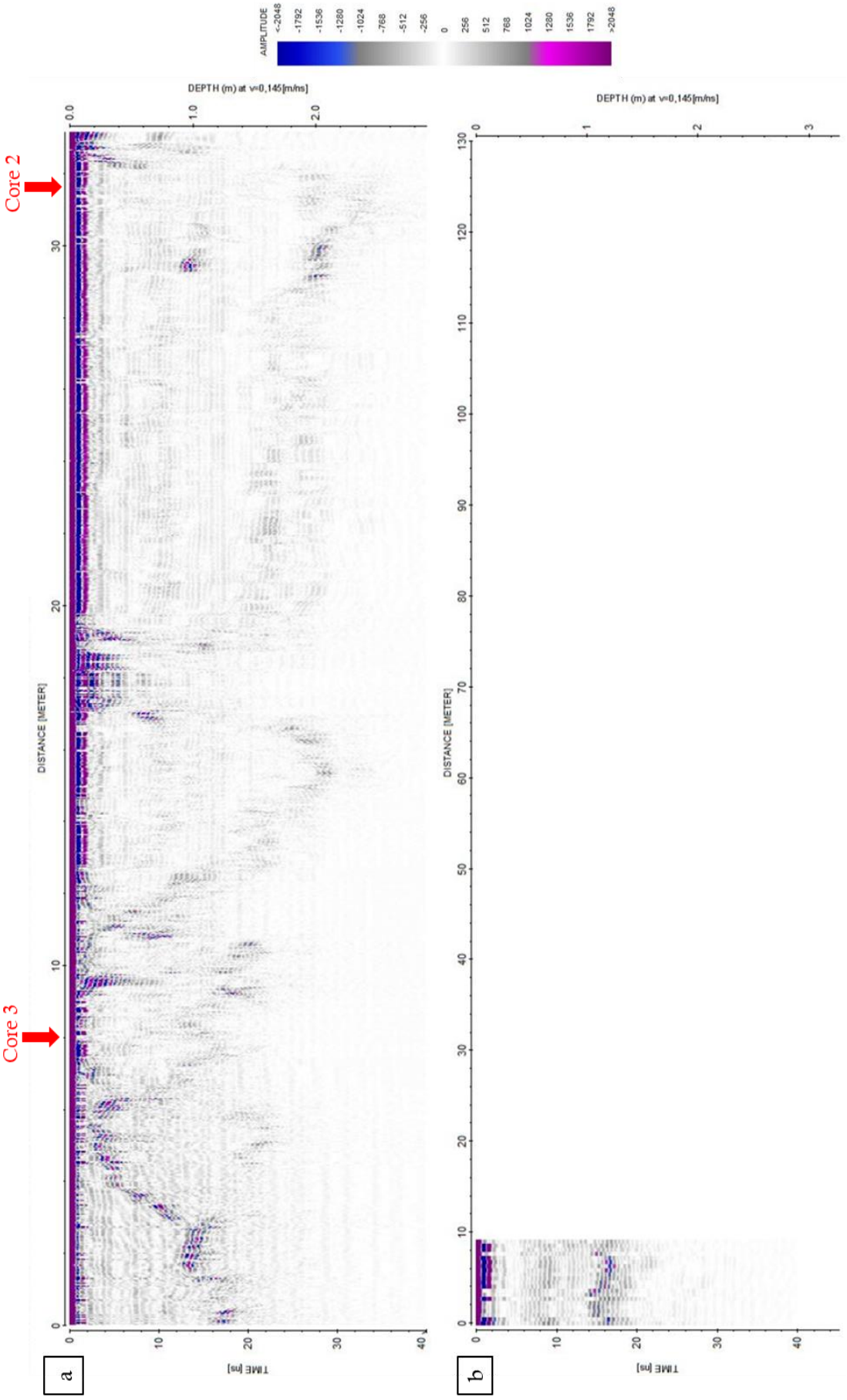

Figure 55: (a) GPR profile 7 with location of ice core samples; (b) GPR profile 8.

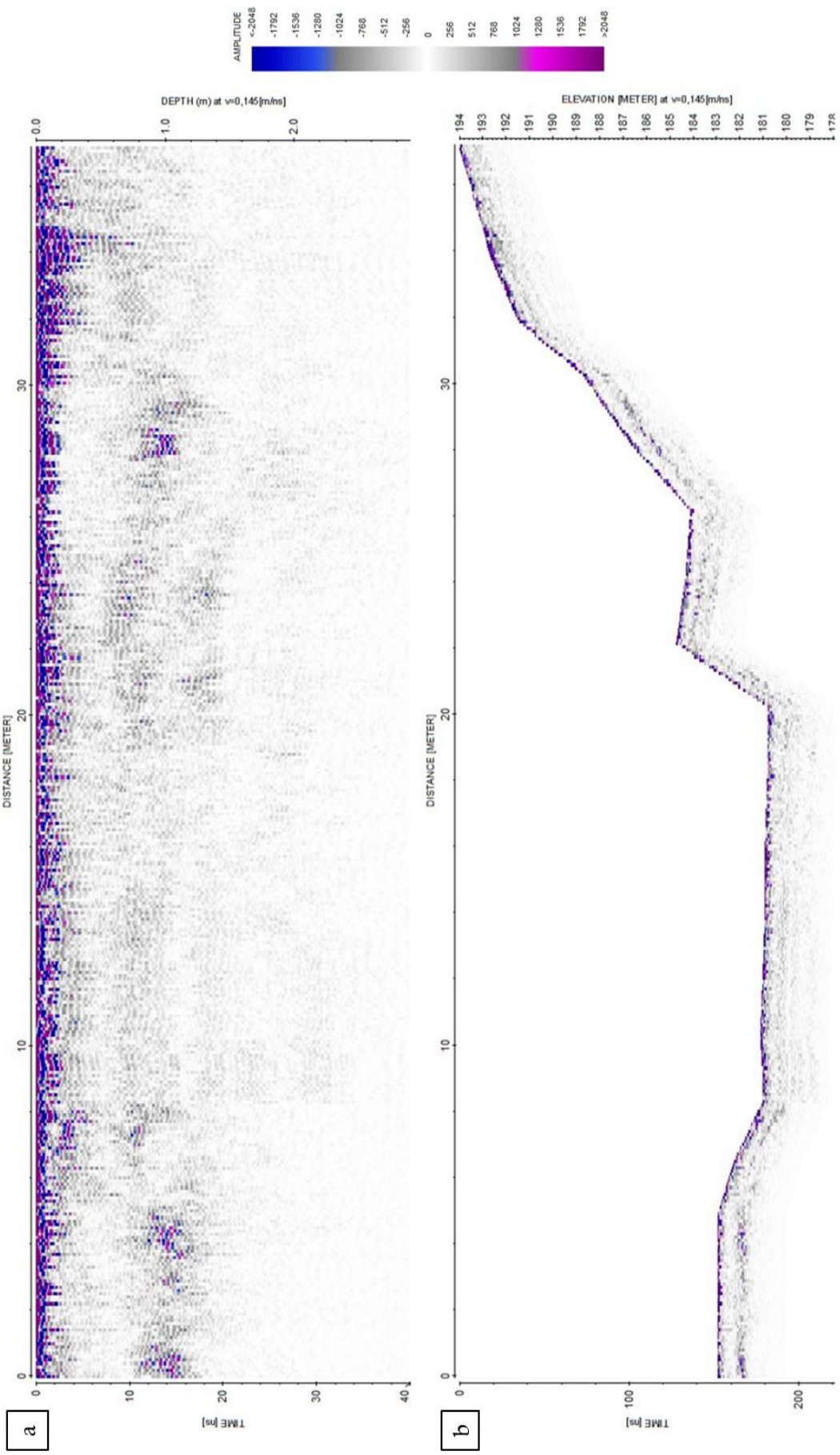

Figure 56: (a) GPR profile 9; (b) topographically corrected GPR profile 9. Elevation changes exaggerated due to erroneous accuracy of Z-coordinates.

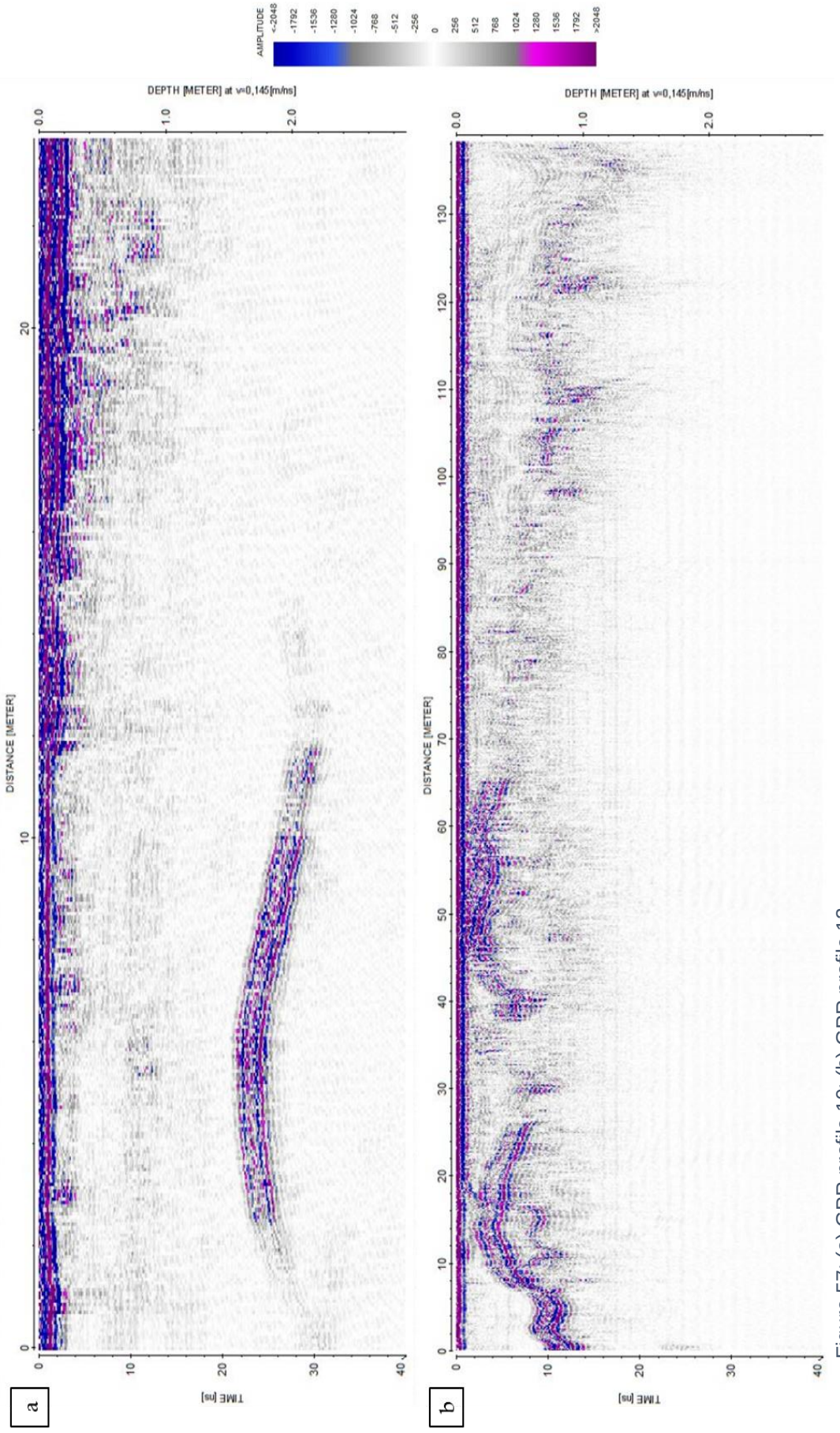

Figure 57: (a) GPR profile 10; (b) GPR profile 12.

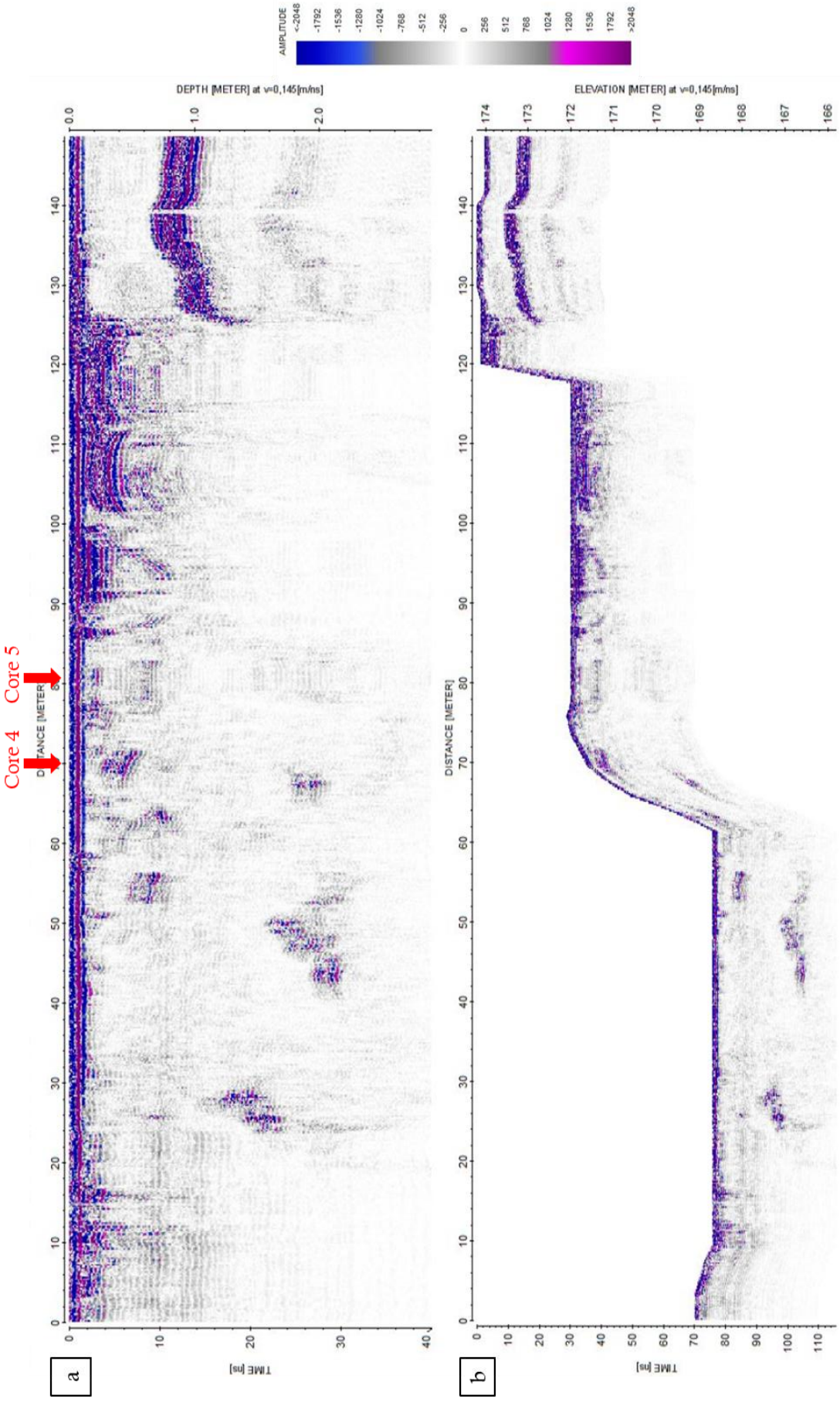

Figure 58: (a) GPR profile 11 with indication of ice core sample; (b) topographically corrected GPR profile 11. Elevation changes exaggerated due to erroneous accuracy of Z-coordinates.

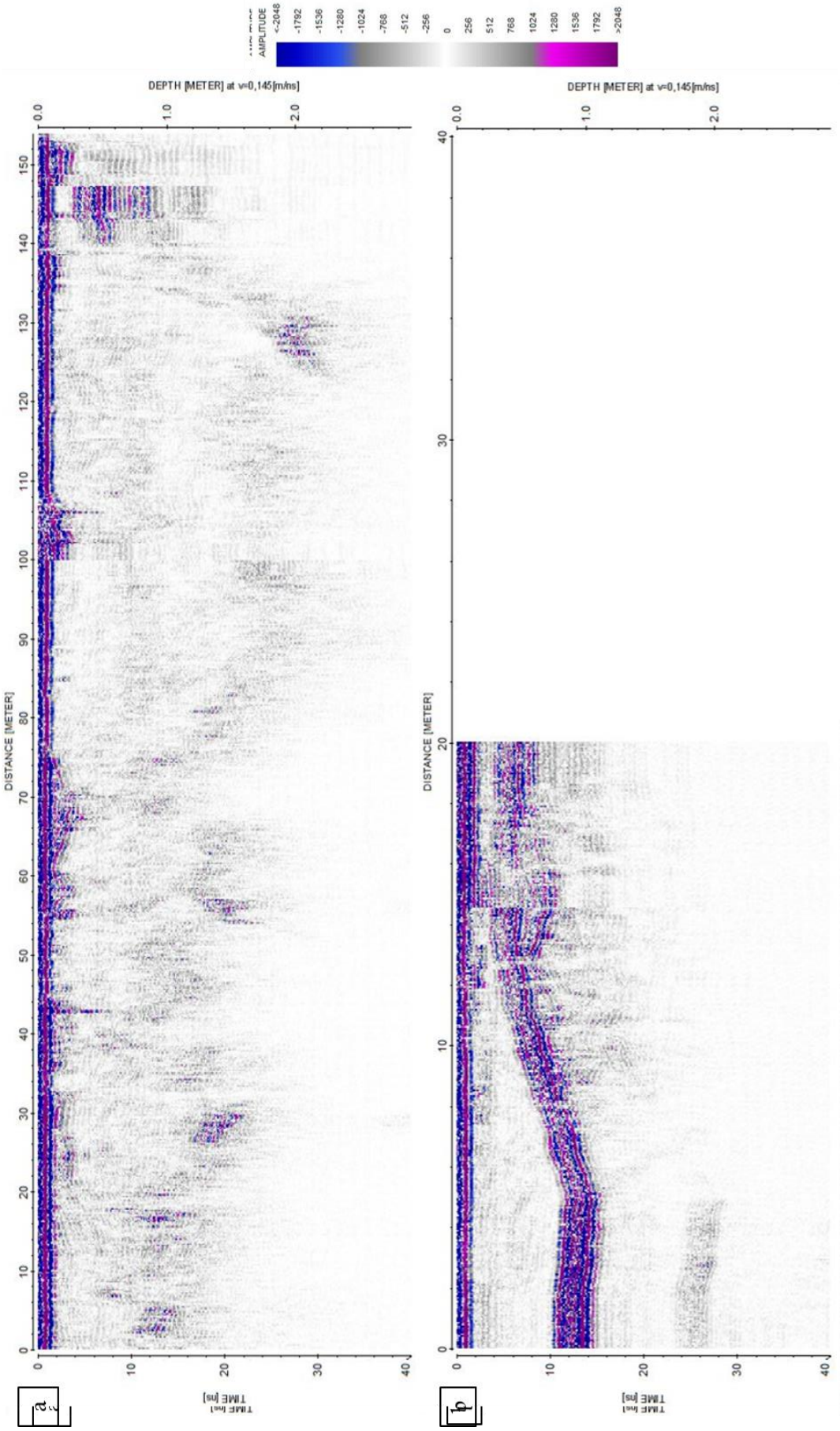

Figure 59: (a) GPR profile 13; (b) GPR profile 19.

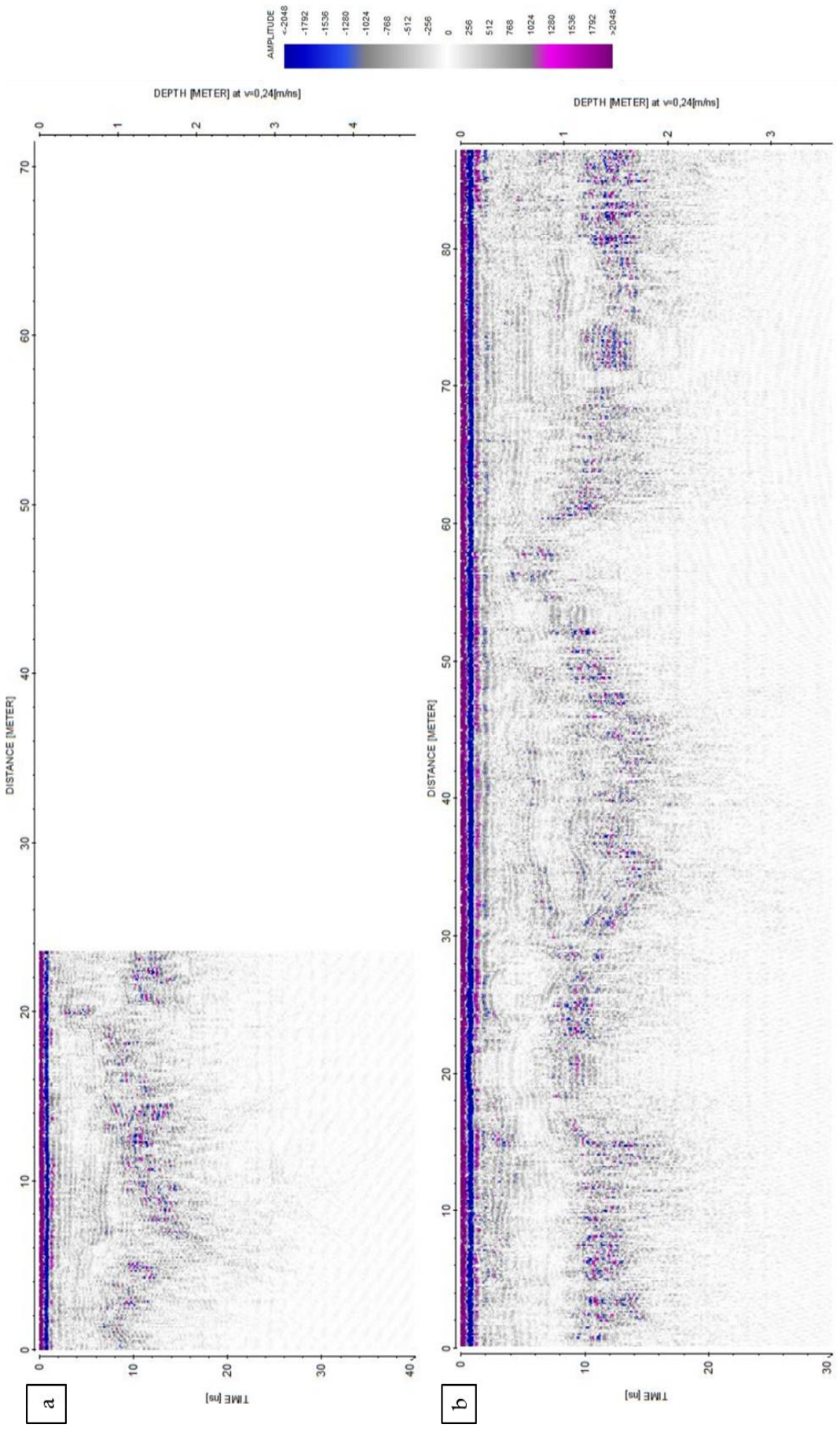

Figure 61: (a) GPR profile 16; (b) GPR profile 18.

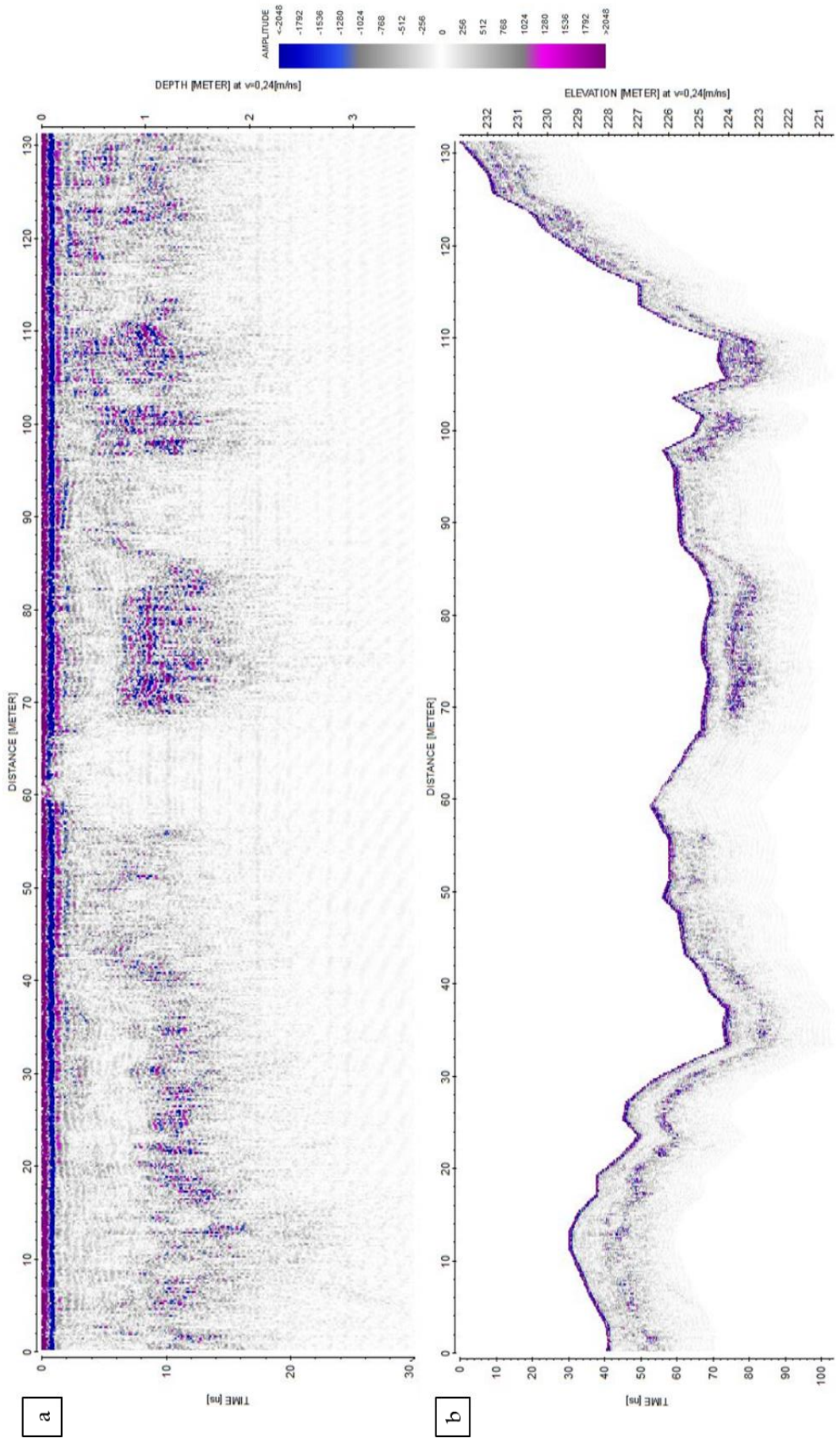

Figure 62: (a) GPR profile 17; (b) topographically corrected GPR profile 17. Elevation changes exaggerated due to erroneous accuracy of Z-coordinates.

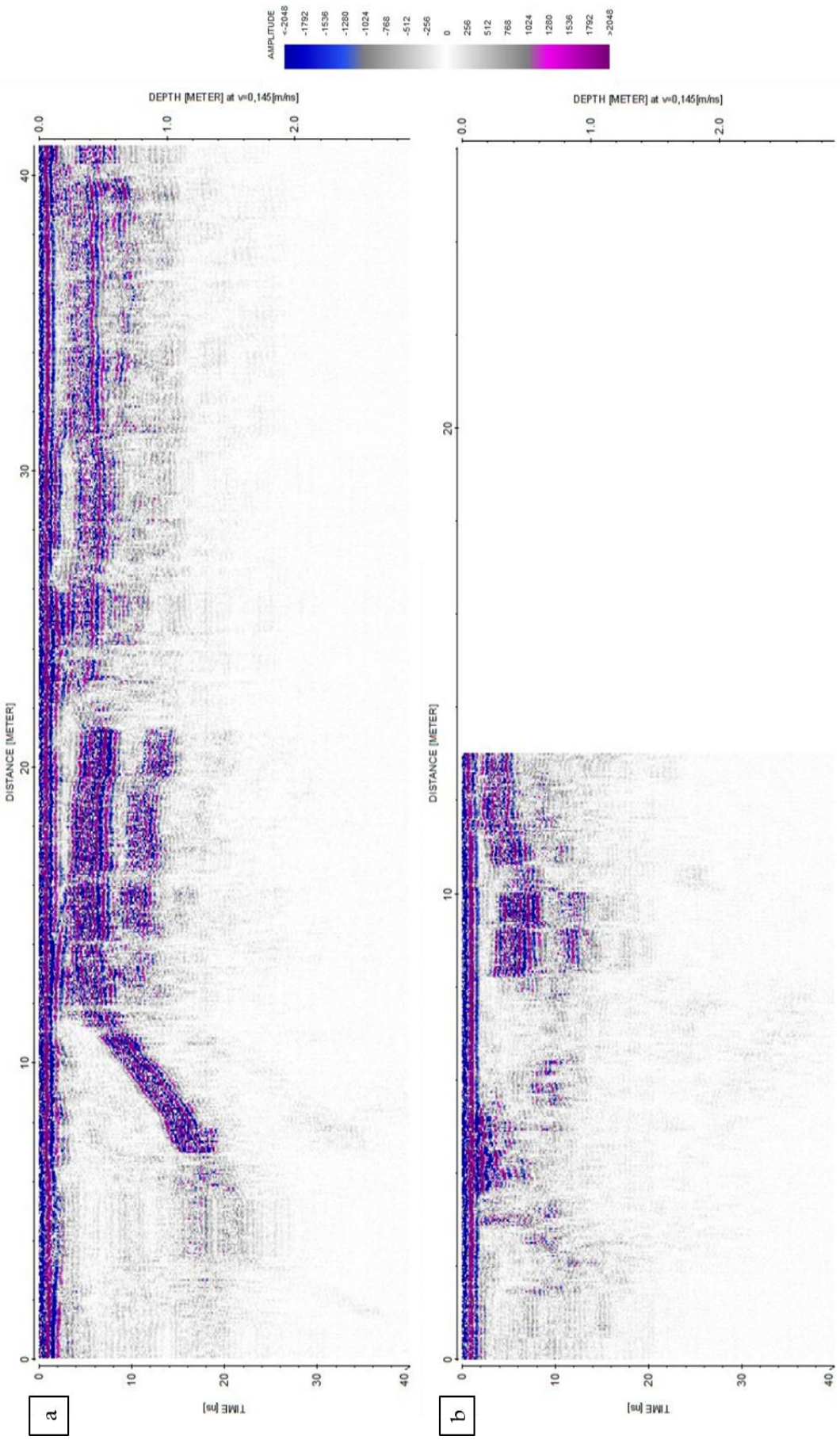

Figure 63: (a) GPR profile 20; (b) GPR profile 21.

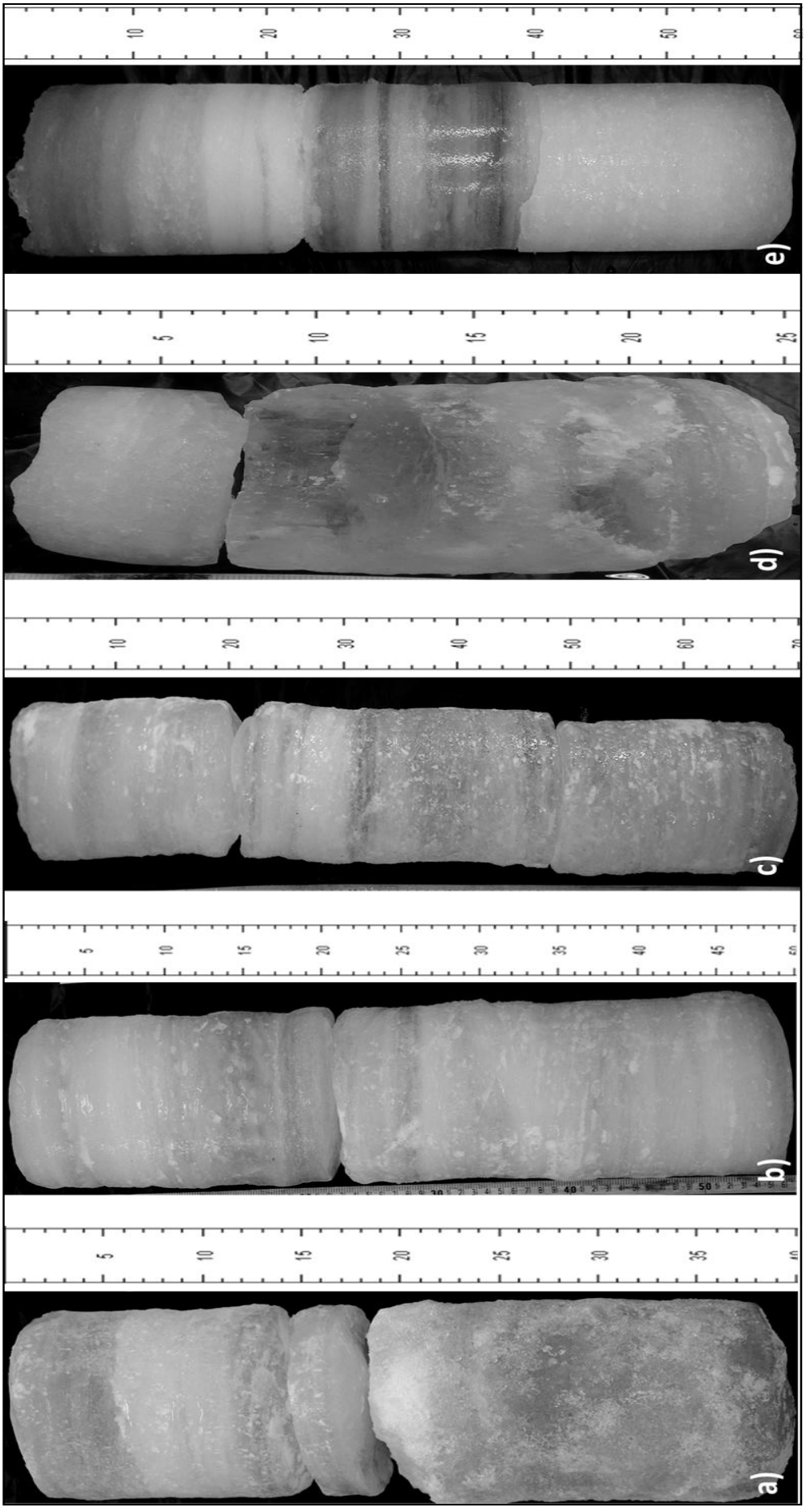

Figure 64: Photographs of ice cores 1 to 5 (a-e) sampled from the icing at the end of March. Light colours show bubble-rich ice layers whereas clear ice layers appear darker.

Table 12: (upper) Average ion concentration of ice cores and standard deviation in parentheses. DIC (measured) and DIC calculated from charge balance (CB) are listed (in mgC l^{-1}). TDS and CBE were calculated with DIC (from CB). EC gives the electrical conductivity corrected to 25°C. *SO_4^{2-} denotes the non-snowpack derived amount of SO_4^{2-} in % of total SO_4^{2-}. Absolute concentration in all subsamples are visualized in Figure 65 and listed in Table 13. (lower) Relative abundance of ions (in %TDS) calculated from concentrations averaged for whole ice cores (DIC from CB). Table 14 (appendix) lists the relative abundance of ions in all subsamples.

	all in mg l^{-1}																	
	NH_4^+	Si	Na^+	K^+	Mg^{2+}	Ca^{2+}	F^-	Cl^-	NO_3^-	SO_4^{2-}	DOC	DIC	DIC (CB)	TDS	CBE (%)	EC (µS cm^{-1})	pH	*SO_4^{2-}
core 1	0,07 (0,03)	0,14 (0,11)	15,70 (8,01)	1,51 (0,36)	4,28 (2,30)	19,49 (7,03)	0,49 (0,02)	5,55 (1,47)	0,59 (0,15)	32,47 (23,19)	1,71 (0,41)	9,26 (3,14)	13,92 (4,29)	94,21 (46,57)	11,66 (3,34)	179,84 (101,05)	8,52 (0,3)	96,67 (1,9)
core 2	0,05 (0,01)	1,01 (0,49)	41,04 (16,17)	1,65 (0,44)	9,60 (3,21)	31,67 (8,53)	0,48 (0,01)	8,68 (2,75)	0,41 (0,05)	86,76 (32,84)	1,81 (0,38)	15,57 (4,03)	25,07 (5,77)	206,21 (66,58)	11,26 (2,7)	419,31 (137,44)	8,90 (0,09)	98,67 (0,21)
core 3	0,03 (0,01)	0,29 (0,29)	19,70 (17,70)	0,80 (0,50)	5,14 (3,84)	21,06 (9,08)	0,47 (0,01)	5,11 (2,95)	0,39 (0,08)	41,48 (33,54)	0,56 (0,31)	9,61 (5,86)	15,56 (8,29)	109,89 (73,46)	14,19 (4,44)	201,57 (144,89)	8,86 (0,26)	97,90 (0,82)
core 4	0,08 (0,04)	0,40 (0,39)	22,49 (13,69)	1,27 (0,37)	4,99 (2,32)	15,35 (5,81)	0,49 (0)	5,85 (2,36)	0,32 (0,01)	31,26 (17,75)	1,28 (0,54)	9,92 (5,14)	16,13 (7,45)	98,30 (49,68)	15,40 (4,49)	193,47 (108,62)	8,33 (0,61)	96,85 (1,62)
core 5	0,04 (0,01)	0,81 (0,33)	32,50 (17,29)	0,90 (0,35)	6,72 (2,79)	24,31 (5,23)	0,52 (0,01)	6,67 (2,83)	0,33 (0,01)	52,80 (19,68)	0,91 (0,48)	14,42 (4,99)	22,49 (7,13)	147,75 (52,12)	12,25 (2,19)	286,49 (110,02)	8,73 (0,22)	98,42 (0,2)

	all in %											
	NH_4^+	Si	Na^+	K^+	Mg^{2+}	Ca^{2+}	F^-	Cl^-	NO_3^-	SO_4^{2-}	DOC	DIC
core 1	0,11	0,13	16,57	1,86	4,39	22,29	0,66	6,70	0,72	30,29	16,27	0,11
core 2	0,02	0,44	19,31	0,85	4,68	16,45	0,20	4,24	0,24	40,75	12,81	0,02
core 3	0,05	0,20	15,18	0,73	4,34	24,08	0,48	4,97	0,49	33,33	16,14	0,05
core 4	0,15	0,30	21,34	1,82	5,21	17,05	0,10	6,79	0,47	29,72	17,03	0,15
core 5	0,03	0,54	20,83	0,61	4,49	17,75	0,08	4,45	0,26	35,58	15,39	0,03

Table 13: Absolute concentration of ions in mg l^{-1}, measured DIC and DIC from charge balance (CB), total dissolved solids (TDS) calculated with DIC CB. Concentration of F^- below limit of quantification in some subsamples (-) Charge balance error (CBE) was calculated with measured DIC. *SO_4^{2-} denotes non-snowpack derived amount of SO_4^{2-} in % of total SO_4^{2-}. Ice types: 1 = clear ice, 2 = bubble-rich ice and 3 = mix of clear and bubble-rich ice.

		all in mg l^{-1}																		
	Sub-sample	NH_4^+	Si	Na^+	K^+	Mg^{2+}	Ca^{2+}	F^-	Cl^-	NO_3^-	SO_4^{2-}	DOC	DIC	DIC (CB)	TDS	CBE (%)	EC (µS cm^{-1})	pH	*SO_4^{2-}	Ice type
Core 1	1-1	0,08	0,05	11,14	1,28	3,81	16,13	0,54	4,89	0,63	22,63	1,69	8,70	11,69	72,87	8,3	127	8,9	97,28	1
	1-2	0,08	0,20	28,23	2,20	7,69	29,41	0,49	8,23	0,85	68,28	2,46	14,30	19,94	165,61	7,5	330	8,5	98,48	3
	1-3	0,03	0,33	21,72	1,55	6,01	26,33	0,49	5,92	0,55	50,54	1,75	11,10	18,12	131,59	11,8	268	8,3	98,52	2
	1-4	0,07	0,09	10,87	1,32	2,53	12,36	0,48	4,62	0,41	12,92	1,27	6,32	10,68	56,34	16,0	102	8,1	95,50	1
	1-5	0,11	0,03	6,57	1,21	1,35	13,20	0,46	4,07	0,49	7,97	1,39	5,87	9,17	44,62	14,7	72	8,8	93,56	1
Core 2	2-1	0,04	1,07	59,91	2,34	13,65	25,14	0,49	10,77	0,50	107,04	2,03	17,90	29,38	250,33	10,5	500	9	98,73	2
	2-2	0,03	0,08	13,85	1,00	4,14	19,32	0,47	3,84	0,40	28,04	1,13	7,73	14,26	85,43	16,6	167	8,9	98,27	1
	2-3	0,05	1,06	33,57	1,42	8,29	34,90	0,48	7,36	0,39	77,13	1,99	16,30	24,45	189,10	9,6	393	8,8	98,80	3
	2-4	0,05	1,50	44,97	1,63	10,95	35,27	-	10,68	0,41	98,89	1,70	16,80	27,04	231,39	10,2	474	9	98,64	2
	2-5	0,06	1,32	52,88	1,84	10,98	43,70	-	10,73	0,36	122,70	2,20	19,10	30,24	274,81	9,4	563	8,8	98,90	2
Core 3	3-1	0,02	0,74	52,36	1,54	11,37	22,51	0,48	10,14	0,39	80,00	0,95	18,90	28,40	207,94	10,0	395	8,8	98,40	2
	3-2	0,06	0,30	21,73	1,04	6,08	21,76	0,46	5,89	0,44	41,50	0,61	10,60	17,69	116,94	13,3	221	8,9	98,21	2
	3-3	0,04	0,06	3,90	0,34	1,19	14,81	0,46	2,24	0,31	8,06	0,39	4,96	8,88	40,27	19,5	63	9,1	96,50	2
	3-4	0,03	0,71	39,01	1,45	10,01	41,93	-	8,55	0,55	100,44	1,05	17,80	27,13	229,81	9,2	436	8,3	98,93	1
	3-5	0,02	0,07	5,77	0,29	1,95	13,85	0,47	2,70	0,34	13,37	0,11	4,59	8,53	47,37	17,7	75	9,1	97,45	1
	3-6	0,03	0,04	5,15	0,29	1,71	15,25	-	2,29	0,32	10,05	0,38	5,59	10,06	45,19	20,0	77	8,8	97,13	1
	3-7	0,04	0,08	10,01	0,65	3,68	17,28	0,48	3,96	0,38	36,93	0,43	4,85	8,24	81,73	9,7	143	9	98,65	1
Core 4	4-1	0,07	0,93	39,97	1,69	7,68	21,41	0,49	9,11	0,32	51,55	0,99	15,80	25,19	158,41	12,7	325	9,1	97,77	2
	4-2	0,13	0,02	6,54	1,33	2,02	7,52	-	3,59	0,33	8,32	2,03	3,27	6,95	36,75	21,7	59	7,6	94,57	1
	4-3	0,05	0,25	20,94	0,79	5,26	17,14	-	4,84	0,31	33,91	0,82	10,70	16,25	99,74	11,7	197	8,3	98,20	3
Core 5	5-1	0,04	0,97	56,41	1,49	11,35	21,79	0,51	11,38	0,32	72,54	1,41	19,75	31,51	208,30	12,2	422	8,7	98,02	2
	5-2	0,04	1,28	56,83	1,27	9,66	28,95	0,52	9,71	0,34	85,23	1,72	21,40	31,56	225,39	9,9	443	8,7	98,56	2
	5-3	0,03	0,52	20,58	0,61	4,48	19,34	-	4,41	0,35	36,44	0,56	9,87	16,01	102,76	13,0	189	8,9	98,47	3
	5-4	0,03	0,31	15,25	0,52	3,84	16,76	-	3,89	0,33	29,75	0,51	7,26	12,92	83,60	15,0	153	9	98,35	3
	5-5	0,04	1,04	24,95	0,81	5,82	30,09	-	5,68	0,34	45,75	0,63	14,00	23,23	137,74	14,4	273	8,8	98,43	2
	5-6	0,02	0,76	20,99	0,72	5,20	28,91	-	4,95	0,33	47,08	0,61	14,25	19,73	128,69	9,0	240	8,3	98,67	2
	min	0,02	0,02	3,90	0,29	1,19	7,52	0,46	2,24	0,31	7,97	0,11	3,27	6,95	36,75	7,5	59	7,60	93,56	
	max	0,13	1,50	59,91	2,34	13,65	43,70	0,54	11,38	0,85	122,70	2,46	21,40	31,56	274,81	21,7	563	9,10	98,93	
	avg	0,05	0,53	26,31	1,18	6,18	22,89	0,49	6,32	0,41	49,89	1,18	11,83	18,74	132,80	12,8	258	8,71	97,81	
	std	0,03	0,47	17,98	0,55	3,58	8,99	0,02	2,89	0,12	33,47	0,65	5,51	8,09	72,71	3,8	152	0,36	1,34	

Figure 65: Absolute abundance of ions in ice cores to visualize intra- and inter-core differences. Concentrations decrease from the top left to the bottom right diagram. Note the different scaling of the y-axes.

Table 14: Relative abundance of ions in % (DIC from CB). F^- <LOQ in some subsamples (-).

	Sub-sample	all in %											
		NH_4^+	Si	Na^+	K^+	Mg^{2+}	Ca^{2+}	F^-	Cl^-	NO_3^-	SO_4^{2-}	DIC
Core 1	1-1	0,11	0,07	15,29	1,76	5,23	22,13	0,74	6,71	0,87	31,05	16,04
	1-2	0,05	0,12	17,05	1,33	4,64	17,76	0,29	4,97	0,51	41,23	12,04
	1-3	0,02	0,25	16,50	1,18	4,57	20,01	0,37	4,50	0,42	38,41	13,77
	1-4	0,13	0,16	19,28	2,35	4,49	21,94	0,84	8,20	0,72	22,93	18,96
	1-5	0,24	0,07	14,71	2,70	3,02	29,59	1,04	9,12	1,09	17,85	20,55
Core 2	2-1	0,01	0,43	23,93	0,93	5,45	10,04	0,20	4,30	0,20	42,76	11,74
	2-2	0,04	0,10	16,21	1,17	4,85	22,61	0,55	4,50	0,47	32,82	16,70
	2-3	0,03	0,56	17,75	0,75	4,38	18,45	0,25	3,89	0,21	40,79	12,93
	2-4	0,02	0,65	19,43	0,71	4,73	15,24	-	4,61	0,18	42,74	11,69
	2-5	0,02	0,48	19,24	0,67	4,00	15,90	-	3,91	0,13	44,65	11,00
Core 3	3-1	0,01	0,36	25,18	0,74	5,47	10,83	0,23	4,88	0,19	38,47	13,66
	3-2	0,05	0,26	18,58	0,89	5,20	18,61	0,40	5,03	0,37	35,49	15,12
	3-3	0,09	0,15	9,69	0,83	2,95	36,77	1,14	5,55	0,76	20,01	22,05
	3-4	0,01	0,31	16,97	0,63	4,36	18,25	-	3,72	0,24	43,71	11,81
	3-5	0,05	0,15	12,19	0,61	4,11	29,24	0,99	5,71	0,71	28,23	18,01
	3-6	0,06	0,08	11,40	0,63	3,79	33,74	-	5,07	0,71	22,24	22,27
	3-7	0,05	0,09	12,24	0,79	4,50	21,15	0,59	4,84	0,47	45,19	10,09
Core 4	4-1	0,04	0,59	25,24	1,07	4,85	13,51	0,31	5,75	0,20	32,54	15,90
	4-2	0,36	0,06	17,80	3,61	5,51	20,45	-	9,76	0,91	22,64	18,91
	4-3	0,05	0,25	21,00	0,79	5,28	17,18	-	4,86	0,31	33,99	16,30
Core 5	5-1	0,02	0,46	27,08	0,71	5,45	10,46	0,25	5,46	0,15	34,83	15,13
	5-2	0,02	0,57	25,21	0,56	4,29	12,85	0,23	4,31	0,15	37,81	14,00
	5-3	0,03	0,50	20,02	0,60	4,35	18,82	-	4,29	0,34	35,46	15,58
	5-4	0,04	0,37	18,25	0,62	4,59	20,05	-	4,65	0,39	35,58	15,46
	5-5	0,03	0,75	18,11	0,59	4,22	21,85	-	4,13	0,25	33,21	16,86
	5-6	0,02	0,59	16,31	0,56	4,04	22,47	-	3,85	0,25	36,58	15,33
	min	0,0	0,1	9,7	0,6	2,9	10,0	0,0	3,7	0,1	17,9	10,1
	max	0,4	0,8	27,1	3,6	5,5	36,8	1,1	9,8	1,1	45,2	22,3
	avg	0,1	0,3	18,3	1,1	4,6	20,0	0,3	5,3	0,4	34,3	15,5
	std	0,1	0,2	4,4	0,7	0,7	6,5	0,4	1,5	0,3	7,7	3,2

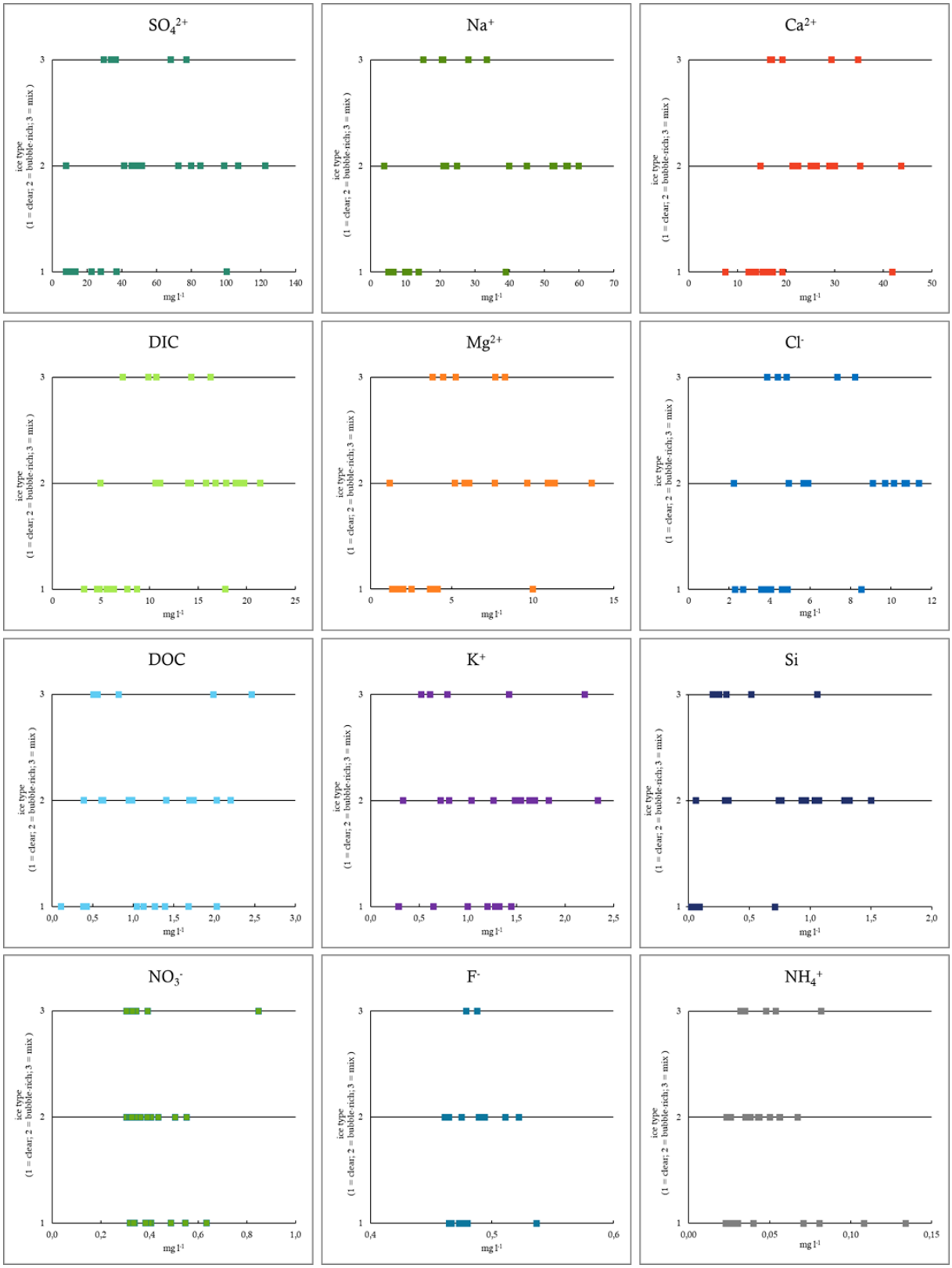

Figure 66: Correlation between ion species and main ice type of subsample as defined in Table 13 (1 = clear ice; 2 = bubble-rich ice; 3 = mix).

Table 15: Ion concentration in water samples from spring 1 and 2 (April 18th and June 13th) and lake (July 10th). Concentrations of NO_3^- and PO_4^{3-} given in mgN l^{-1} and mgP l^{-1}, respectively. DIC as HCO_3^- was calculated from charge balance. "<LOQ" indicates ion species with concentration below the limit of quantification. Total dissolved solids (TDS) was calculated as sum of all analysed ion species. The value for S 2.2 is an underestimate due to erroneous concentrations of Na^+, K^+, Mg^{2+} and Ca^{2+} which were excluded from further analyses (-). CBE (in %) was calculated after Eq. 13 and pCO_2 with Eq. 11.

		S1.1 (18.4)	S1.2 (18/4)	S2.1 (18/4)	S2.2 (18/4)	S1.1 (13/6)	S1.2 (13/6)	S2.1 (13/6)	S2.2 (13/6)	LA (10/7)
mg l-1	NH_4^+	0,03	0,03	0,03	0,03	0,05	0,04	0,04	0,04	0,04
	Si	2,11	2,11	2,11	2,11	0,78	0,77	0,45	0,45	1,44
	Na^+	121,24	119,47	145,13	133,57	11,50	10,60	10,09	-	9,26
	K^+	3,33	3,45	4,07	3,65	0,96	0,65	0,62	-	2,81
	Mg^{2+}	18,50	18,31	26,37	21,12	7,45	4,35	2,13	-	24,56
	Ca^{2+}	56,69	56,06	61,84	63,20	16,54	10,96	5,29	-	61,11
	F^-	0,46	0,43	0,44	0,41	0,56	0,53	n.a.	1,08	0,11
	Cl^-	28,03	26,93	29,10	30,79	10,15	9,97	2,70	2,56	1,96
	SO_4^{2-}	199,59	195,22	222,72	226,84	31,84	30,30	11,88	11,97	257,56
	NO_3^-	<LOQ	<LOQ	<LOQ	<LOQ	2,02	3,41	0,00	0,37	0,00
	PO_4^{3-}	52,95	51,71	66,28	60,18	<LOQ	0,00	0,00	<LOQ	0,00
	DIC	62,81	61,96	75,70	69,16	6,47	5,47	5,40	-	4,59
	S	52,95	51,71	66,28	60,18	15,83	12,86	5,12	3,66	83,38
	Al	0,59	1,57	0,94	0,60	0,02	0,00	0,01	0,00	0,04
	Mn	62,05	66,85	50,76	32,16	<LOQ	<LOQ	<LOQ	<LOQ	<LOQ
	Fe	44,20	59,67	65,45	51,54	0,07	0,06	0,04	0,06	0,20
	Co	0,12	0,12	0,18	0,09	0,02	0,02	0,01	0,01	0,09
	Cu	<LOQ	0,46	2,68	<LOQ	0,00	0,00	0,00	0,00	0,01
	Zn	6,78	31,22	17,64	7,45	<LOQ	<LOQ	<LOQ	<LOQ	<LOQ
	As	<LOQ	<LOQ	<LOQ	<LOQ	0,01	0,01	0,01	0,01	0,03
	Sr^{2-}	2,06	2,14	2,32	2,37	0,41	0,37	0,17	0,11	1,36
	U	0,30	0,29	0,31	0,34	<LOQ	<LOQ	<LOQ	<LOQ	<LOQ
	Pb	<LOQ	<LOQ	<LOQ	<LOQ	0,13	0,12	0,10	0,10	0,10
	V	<LOQ	<LOQ	<LOQ	<LOQ	0,03	0,02	0,01	0,01	0,12
	Ti	<LOQ	<LOQ	<LOQ	<LOQ	<LOQ	<LOQ	<LOQ	<LOQ	<LOQ
	Cr	<LOQ	<LOQ	0,63	<LOQ	<LOQ	<LOQ	<LOQ	<LOQ	<LOQ
	Ni	<LOQ	10,39	9,85	2,17	<LOQ	<LOQ	<LOQ	<LOQ	<LOQ
	Cd	<LOQ	<LOQ	<LOQ	<LOQ	<LOQ	<LOQ	<LOQ	<LOQ	0,10
	TDS	714,76	760,09	850,80	767,93	104,82	90,51	44,06	20,41	448,88
	CBE%	-2,52	-2,17	-0,52	-2,65	11,68	-2,39	7,32	-	-2,56
	pCO_2	-2,02	-2,02	-2,11	-2,15	-2,69	-2,76	-2,76	-	-3,63

Table 16: Relative abundance of analysed ion species in spring and lake samples in % TDS. Abundance of 0,00 due to concentrations <LOQ. Relative concentrations of ion species in S2.2 (13/6) were not included due to erroneous concentrations of Na^+, K^+, Mg^{2+} and Ca^2.

% TDS	S1.1 (18.4)	S1.2 (18/4)	S2.1 (18/4)	S2.2 (18/4)	S1.1 (13/6)	S1.2 (13/6)	S2.1 (13/6)	LA (10/7)
NH_4^+	0,00	0,00	0,00	0,00	0,05	0,05	0,09	0,01
Si	0,30	0,28	0,25	0,27	0,74	0,86	1,03	0,32
Na^+	16,96	15,72	17,06	17,39	10,97	11,71	22,89	2,06
K^+	0,47	0,45	0,48	0,48	0,92	0,72	1,40	0,63
Mg^{2+}	2,59	2,41	3,10	2,75	7,11	4,81	4,84	5,47
Ca^{2+}	7,93	7,38	7,27	8,23	15,78	12,10	12,01	13,61
F^-	0,06	0,06	0,05	0,05	0,53	0,58	0,00	0,02
Cl^-	3,92	3,54	3,42	4,01	9,68	11,01	6,12	0,44
SO_4^{2-}	27,92	25,68	26,18	29,54	30,37	33,48	26,97	57,38
NO_3^-	0,00	0,00	0,00	0,00	1,92	3,77	0,00	0,00
PO_4^{3-}	7,41	6,80	7,79	7,84	0,00	0,00	0,00	0,00
DIC	8,79	8,15	8,90	9,01	6,17	6,04	12,27	1,02
S	7,41	6,80	7,79	7,84	15,10	14,21	11,61	18,57
Al	0,08	0,21	0,11	0,08	0,02	0,00	0,03	0,01
Mn	8,68	8,79	5,97	4,19	0,00	0,00	0,00	0,00
Fe	6,18	7,85	7,69	6,71	0,07	0,07	0,08	0,04
Co	0,02	0,02	0,02	0,01	0,02	0,02	0,02	0,02
Cu	0,00	0,06	0,31	0,00	0,00	0,00	0,00	0,00
Zn	0,95	4,11	2,07	0,97	0,00	0,00	0,00	0,00
As	0,00	0,00	0,00	0,00	0,01	0,01	0,01	0,01
Sr^{2-}	0,29	0,28	0,27	0,31	0,39	0,41	0,38	0,30
U	0,04	0,04	0,04	0,04	0,00	0,00	0,00	0,00
Pb	0,00	0,00	0,00	0,00	0,13	0,13	0,22	0,02
V	0,00	0,00	0,00	0,00	0,03	0,02	0,03	0,03
Ti	0,00	0,00	0,00	0,00	0,00	0,00	0,00	0,00
Cr	0,00	0,00	0,07	0,00	0,00	0,00	0,00	0,00
Ni	0,00	1,37	1,16	0,28	0,00	0,00	0,00	0,00
Cd	0,00	0,00	0,00	0,00	0,00	0,00	0,00	0,02